Gamma ray tracking with the AGATA demonstrator
–
A novel approach for in-beam spectroscopy

Inaugural–Dissertation

zur

Erlangung des Doktorgrades

der Mathematisch-Naturwissenschaftlichen Fakultät

der Universiät zu Köln

vorgelegt von

Benedikt Birkenbach

aus Fulda

Köln 2014

Berichterstatter: Prof. Dr. Peter Reiter
(Gutachter) Prof. Dr. Jan Jolie

Tag der mündlichen Prüfung: 11. April 2014

Abstract

The Advanced GAmma Tracking Array (AGATA) employs the novel method of gamma-ray tracking (GRT), where all locations of energy depositions within the Ge crystal detector volume are used by computer algorithms to reconstruct the various simultaneous interactions of the measured γ radiation. The interaction positions are determined by Pulse Shape Analysis (PSA) algorithms that compare the measured and digitized signals with the information of a signal database comprising position dependent calculated sets of detector signals. The result of a detailed comparison between measured and calculated signals yields the position of each interaction point. The GRT algorithms rely on this precise position of the deposited energy as an input to reconstruct the initial γ-rays from the full sequence of the different interactions in the detector. Within this thesis a computer program library was developed, providing software routines to calculate the position dependent detector signals of the highly segmented HPGe detectors. The currently used signal databases of all AGATA detectors were generated by this software package and computer library. Part of the computing is based on individual detector properties which were deduced from detailed characterisation measurements. Details of the library, the used routines and the needed characteristics of the detector system are described, this includes a precise measurement of the crystal axis orientation of the AGATA HPGe crystals.

The second part of this thesis is dealing with the analysis of one of the first in-beam experiments performed with the AGATA demonstrator setup at the LNL in Italy. The experiment aimed for a spectroscopic investigation of neutron rich actinides from Thorium to Plutonium produced after multi-nucleon transfer reactions. For this purpose a ^{136}Xe beam with an energy of 1 GeV bombarded onto a ^{238}U target. The fast beam like particles after the transfer reactions were identified by the magnetic spectrometer PRISMA. The γ-rays were detected with the AGATA demonstrator consisting of five AGATA triple cluster detectors. An additional micro channel plate detector for particle detection was mounted inside the scattering chamber in order to request kinematic coincidences. The analysis procedures for the two complex sub-detectors AGATA and PRISMA were extended and ad-

apted to the specific requirements of this new approach for actinide spectroscopy. First the complex analysis of the magnetic spectrometer PRISMA and solutions for unexpected detector behaviour like time drifts and aberration corrections are described. As a result the individual isotopes of elements from Barium to Tellurium were identified confirming the very high quality of the PRISMA spectrometer and its design parameters.

The analysis of the γ-ray spectra comprised a detailed PSA and GRT analysis of the AGATA demonstrator. This analysis included also data analysis developments for the AGATA collaboration. The data of the AGATA demonstrator, the PRISMA spectrometer and the ancillary detectors were merged to obtain background free Doppler corrected spectra for the beam- and target-like reaction products. The simultaneous Doppler correction for beam and target-like ions included an elaborate optimization procedure for unobservable experimental parameters. The γ-ray spectra for the individual isotopes is consistent with the isotope identification of the PRISMA analysis. For the beam like particles γ-ray spectra of the isotopes $^{128-139}$Xe are presented and discussed. For the target like nuclei γ-ray spectra of the isotopes $^{236-240}$U are deduced. By gating on the remaining excitation energy after the multi-nucleon transfer reaction the neutron evaporation and fission of the excited actinide nuclei were suppressed. Coincidences between AGATA and PRISMA were exploited for the first time together with the particle coincidence between beam- and target-like nuclei. These triple coincidences allowed further background reduction. The results for the individual Xenon and Uranium isotopes demonstrate the successful operation of the AGATA demonstrator coupled to the PRSIMA spectrometer. The quality of the γ-ray spectra show clearly that the novel pulse shape analysis and γ-ray tracking methods fulfil expectations also for demanding in-beam γ-ray spectroscopy experiments.

Zusammenfassung

Das Advanced GAmma Tracking Array (AGATA) Spektrometer verwendet die neue Gamma-Ray Tracking (GRT) Methode. Diese rekonstruiert mithilfe von Computeralgorithmen und den Orten der Energiedepositionen die verschiedenen simultanen Interaktionen der gemessenen γ-Strahlung innerhalb der Germanium-Detektorkristalle. Die Interaktionsorte werden durch Impulsformanalyse-Algorithmen (PSA) bestimmt, welche die gemessenen und digitalisierten Signale mit den Informationen einer Signaldatenbank vergleichen. Diese Signaldatenbank besteht aus Sätzen von berechneten ortsabhängigen Detektorsignalen. Das Resultat eines detaillierten Vergleichs zwischen gemessenen und berechneten Signalen sind die Orte der jeweiligen Interaktionen. Die GRT-Algorithmen benötigen die präzisen Orte der Energiedepositionen um die ursprünglichen γ-Strahlen aus der vollen Sequenz unterschiedlicher Interaktionen im Detektor zu rekonstruieren. Im Rahmen der vorgelegten Arbeit wurde eine Programmbibliothek entwickelt, welche Softwareroutinen zur Berechnung der ortsabhängigen Signale von hochsegmentierten HPGe-Detektoren bereitstellt. Die aktuell genutzten Signaldatenbanken aller AGATA-Detektoren wurden durch Programme unter Verwendung dieses Softwarepaketes generiert. Teile der Berechnung basieren auf den individuellen Eigenschaften der Detektoren, welche durch detaillierte Messungen bestimmt wurden. Details der Programmbibliothek, die verwendeten Routinen und die benötigten Eigenschaften des Detektorsystems werden beschrieben und beinhalten eine präzise Messung der Orientierung der Kristallachsen der AGATA HPGe-Kristalle.

Der zweite Teil dieser Arbeit behandelt die Analyse eines der ersten In-Beam Experimente mit dem AGATA-Demonstrator am LNL in Italien. Das Ziel des Experimentes war die spektroskopische Untersuchung der neutronenreichen Actinoide von Thorium bis Plutonium nach Multi-Nucleon-Transfer-Reaktionen. Aus diesem Grund wurde ein ^{136}Xe-Strahl mit einer Energie von 1 GeV auf ein ^{238}U-Target geschossen. Die schnellen strahlähnlichen Teilchen wurden nach der Transfer-Reaktion mit Hilfe des magnetischen Spektrometers PRISMA identifiziert. Die γ-Strahlen wurden von dem AGATA-Demonstrator bestehend aus 5 AGATA-Tripel-Cluster-Detektoren detektiert.

Der innerhalb der Streukammer installierte zusätzlicher Micro-Channel-Plate-Detektor zur Teilchenmessung ermöglichte eine kinematische Koinzidenzmessung. Die Analyseprozeduren der beiden komplizierten Unterdetektoren AGATA und PRISMA wurden erweitert und an die spezifischen Anforderungen des neuen Ansatzes zur Spektroskopie der Actinoiden angepasst. Als Erstes wird die komplizierte Analyse des magnetischen Spektrometers PRISMA sowie Lösungen für unerwartetes Verhalten des Detektors, wie zeitabhängige Verschiebungen und Aberrationskorrekturen, beschrieben. Das Resultat ist die Identifikation verschiedener Isotope der Elemente Barium bis Tellur, welche die hohe Qualität des PRISMA-Spektrometers und seiner Designparameter verifiziert.

Die Analyse der Gamma-Spektren setzt eine detaillierte PSA und GRT-Analyse des AGATA-Demonstrators voraus. Die Entwicklungen zur Datenanalyse wurden in die AGATA-Gemeinschaft eingebracht. Die Daten des AGATA-Demonstrators, des PRISMA-Spektrometers und der Zusatzdetektoren wurden kombiniert um untergrund-freie, Doppler-korrigierte Spektren für strahl- und targetähnliche Reaktionsprodukte zu erhalten. Die simultane Doppler-Korrektur für strahl- und targetähnliche Ionen beinhaltet eine aufwändige Optimierungsprozedur für nicht beobachtbare experimentelle Parameter. Die γ-Spektren der einzelnen Isotope und die Identifikation der Isotope der PRISMA-Analyse sind konsistent. Für die strahlähnlichen Teilchen werden γ-Spektren der Isotope $^{128-139}$Xe vorgestellt und diskutiert. Für die targetähnlichen Atomkerne wurden γ-Spektren der Isotope $^{236-240}$U ermittelt. Mit einer Bedingung für die verbleibende Anregungsenergie nach der Multi-Nucleon-Transfer-Reaktion wurde die Abdampfung von Neutronen oder die Spaltung der angeregten Actinoidenkerne unterdrückt. Die Koinzidenz zwischen AGATA und PRISMA wurde erstmals um eine Teilchenkoinzidenz der strahl- und targetähnlichen Kerne erweitert. Diese dreifache Koinzidenz erlaubt weitere Untergrund-Reduktion. Die Resultate der einzelnen Xenon- und Uranisotope demonstrieren den erfolgreichen Betrieb des AGATA-Demonstrators im Verbund mit dem PRISMA-Spektrometer. Die Qualität der γ-Spektren zeigt deutlich, dass die neuen Methoden der PSA und des GRT die Erwartungen auch in anspruchsvollen In-Beam Spektroskopie-Experimenten erfüllen.

Contents

1. Introduction

The availability of energetic beams of short-lived nuclei opened a wide range for experiments in nuclear physics enlargening our knowledge on the structure and dynamics of nuclei under extreme conditions. The results are not only of highest importance for nuclear physics, but also address open questions in astrophysics, solid-state physics and the study of fundamental interactions. Several European facilities like FAIR (GSI, Darmstadt, Germany), HIE-ISOLDE (CERN, Geneva, Switzerland), SPIRAL2 (Caen, France) and SPES (INFN, Legnaro, Italy) will provide Radioactive Ion Beams (RIB) with new accelerator facilities. All these new facilities have in common, that the experimental conditions request a powerful detector system for in-beam γ-ray spectroscopy investigations. An excellent energy resolution, a wide energy range and a high efficiency combined with a good angular resolution and the ability to cope with high counting rates are the demands on such a spectrometer.

The quest for an optimal detector system fulfilling all the demands must be based on the basic principles of γ-ray interaction with matter which are the photoelectric effect, Compton scattering and pair production [1]. The photoelectric effect is dominant up to an energy of 200 keV. From here up to a few MeV the Compton scattering becomes the most probable interaction and for higher energies the pair production takes over. The cross-section of the photoelectric effect is proportional to Z^{4-5}, for the Compton scattering it is proportional to Z and for the pair production to Z^2, where Z is the atomic number of the absorbing material. Another important point is the size of the detectors and the density of the used material.

Scintillation detectors like NaI(Tl) or $LaBr_3$(Ce) allow for a large volume and a high Z resulting in detectors with highest efficiency. In general they have excellent timing properties. However their energy resolution is severely limited to a few percent of the deposited energy [1].

In contrast, semiconductor detectors provide a very high energy resolution as the energy needed to create an electron-hole pair are just a few eV. The atomic number of Germanium, the availability of large crystals with a volume up to 450 cm^3 and the small band gap of 0.7 eV

resulting in an excellent energy resolution makes Germanium the first choice for such a semiconductor based spectrometer. There are other materials that compete with Germanium. However, Silicon has only nearly half the atomic number making full absorption less probable. CdZnTe has a high Z and could be operated at room temperature, whereas Germanium detectors must be operated at liquid nitrogen temperature ($< 110\,\mathrm{K}$) due to their small band gap. Despite from three times worse energy resolution only small CdZnTe crystals can be produced and result in a low efficiency [2].

The first generation of Germanium detectors were very small, as the impurity concentration of the crystals were high. In the 1960s a process was developed to compensate the large space charge of the occurring p-type excess impurities in Germanium by the diffusion of Lithium. Now it was possible to grow large crystals with high efficiency. This development pushed the research on the structure of the atomic nucleus and provided the most powerful tool for high resolution γ-ray spectroscopy. Several detectors were combined to detector arrays enabling $\gamma\gamma$ coincidence experiments. In the late 1970s high purity Germanium (HPGe) detectors became commercially available and in the 1980s the production of the HPGe crystals advanced to a stage, where comparable large crystals were achieved and the Lithium drifted Germanium detectors became obsolete. National detector arrays like OSIRIS in Germany or TESSA in the UK were augmented with Bismuth Germanate (BGO) shields. These shields were operated in anti-coincidence and suppressed Compton scattered γ-rays escaping a detector. In this way a high peak to total ratio was achieved. The next generation of spectrometers were the 4π detector arrays GAMMASPHERE in the United States of America and EUROBALL in Europe. GAMMASPHERE consists of 110 cylindrical HPGe detectors each one surrounded by a hexagonal BGO shield. The EUROBALL array was build in several steps and variations and finally had the same efficiency and resolving power like GAMMASPHERE. A new mode of operation called add-back was introduced for the newly developed cluster detectors. In this mode the different coincident signals of neighbouring unshielded detectors inside a cluster were summed up to gain efficiency, especially at high energies. These huge detector systems pushed forward the sensitivity limit for nuclear

structure research. The evolution of Germanium detectors and arrays is well summarized in [2].

The technological progress in several fields paved the way for the development of position sensitive tracking detectors. The electrical segmentation of large volume HPGe detectors allows a position sensitive readout of the crystals. The outer contact of segmented crystals is divided by etching and each segment electrode is read out and the signal is amplified individually. With the availability of fast digital electronics not only the energy, but also the pulse shapes of all the detector signals are recorded. The advances in computing allow then the deconvolution and the storage of these signal traces. Pulse shape analysis (PSA) is utilized to determine the interaction position within one detector segment. Finally the track of the different interactions within the detector array can be reconstructed by tracking algorithms. First arrays of segmented HPGe detectors like the SeGa [3] or the MINIBALL [4] spectrometer were build. With the segmented detectors another new operation mode evolved: γ-ray imaging [5]. Due to the Compton scattering process the position of an emitting source with known energy can be located. Combined with the high energy resolution of a HPGe detector and the huge amount of available nuclear decay data a position and element sensitive detector can be build.

Actually new 4π gamma-ray tracking spectrometers are developed and constructed in order to cope with the demands introduced at the beginning. In the U.S. it is the GRETA [6] spectrometer and in Europe the Advanced Gamma Tracking Array (AGATA) [7, 8]. In this work new developments for the γ-ray tracking technique were advanced in order to increase the performance of the AGATA detectors and to achieve an improved position resolution of the new detector array. The analysis of a first experiment with AGATA demonstrates the successful implementation of these developments under demanding experimental conditions. Details of the technical design of AGATA are discussed in the following section.

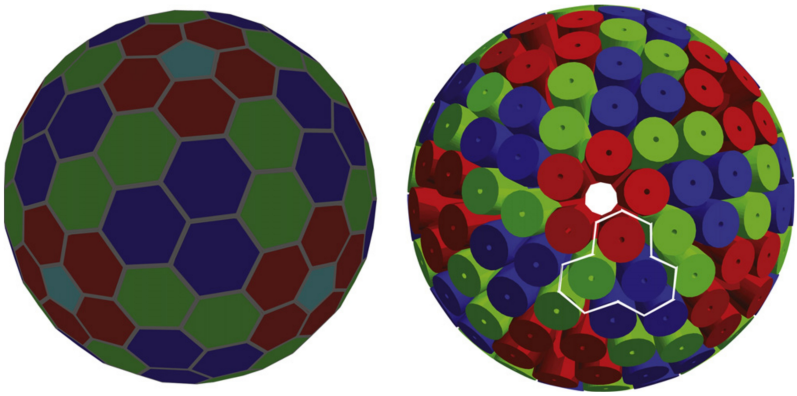

Figure 1: Design of the AGATA spectrometer. Computer aided design images of the tiling of the sphere (left) and the 180 crystal configuration (right). The cyrostats and the detector encapsulation are not shown. Taken from [8].

1.1. AGATA

AGATA is developed and financed by more than 40 institutions from 12 different countries and is based on the progress made within some precursor projects in Europe (e.g. EUROBALL and MINIBALL). AGATA is a flexible and mobile instrument operated at different European laboratories. After a first campaign at the Laboratori Nazionali di Legnaro (LNL) in Italy it was moved to the GSI facility in Germany in spring 2012. The next destination will be the GANIL laboratory in France and the move is scheduled for spring 2014. In future the spectrometer will be operated at the new radioactive beam facilities such as FAIR, SPIRAL2, SPES and HIE-ISOLDE. AGATA will have a large impact on nuclear physics research and the development of the device already was a considerable achievement implying technical advances in a wide range of other applications.

An overview of the complete AGATA system is given in [8]. The conceptual design of AGATA is described extensively in [9]. The maximisation of the detection efficiency and resolving power is the main goal of the new design. The result is an optimized configuration

consisting of 180 individual crystals with three different geometries resulting in nearly 4π solid angle coverage (figure 1). The inner radius is big enough to employ ancillary detector systems.

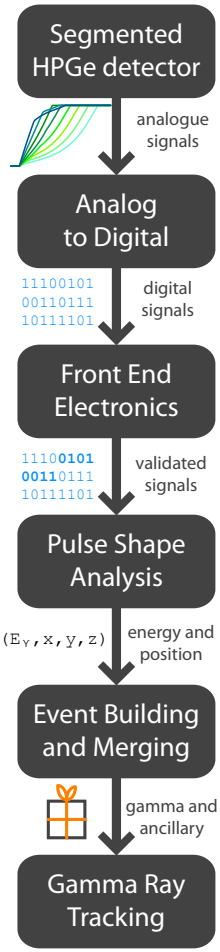

Figure 2

The AGATA detectors are based on encapsulated and electrically segmented closed-end coaxial n-type HPGe detectors. The crystals have a length of 90 mm, a rear diameter of 80 mm and a weight of about 2 kg. At the front they are tapered into a hexagonal shape with a slight asymmetry depending on the type of crystal geometry. Each detector has 36 segments and one central core contact. One detector of each geometry is housed in an AGATA triple cryostat [10]. The cryostat ensures the cooling to liquid nitrogen temperature of the detectors. To operate the detectors in reverse bias mode a high voltage of up to 5000 V is applied to the core electrode. The essential core electrode signal is read out by a so called dual core preamplifier[11] that allows two different amplification gains, a high and a low gain. All segment electrodes are connected to individual low noise charge sensitive preamplifiers [12] with a cold first feedback stage consisting of a field effect transistor (FET) situated nearby the cooled detector capsule. In its final configuration the number of signals will result in 6480 high resolution spectroscopy channels for the final stage of AGATA. The excellent performance of the first detectors is summarized in [13].

The data acquisition and processing scheme of AGATA is shown in figure 2. After reading out the analogue signals of the AGATA detectors they are sampled in custom made digitizers and transferred to the pre-processing electronics, where the trigger and the evaluation of good events reduces the amount of data. First timing, multiplicity and energy filters are ap-

plied to the digital signals. The complete data, including the signal trace, are transferred via optical links to a computer farm. Here the signals are calibrated and analyzed using PSA algorithms to determine the position of each interaction point with a higher precision. Latest investigations show a position resolution of 4 mm FWHM [14]. After the PSA an event builder consolidates the γ-ray and ancillary events. Finally a tracking algorithm reconstructs the initial γ-ray event. The algorithm is based on the probability for an interaction at a certain energy, its scattering angle and the penetration depth.Therefore the PSA is at the core of the new detection scheme and directly constitutes the over-all performance of the adjacent tracking algorithm. At the moment all the data of the experiments are written to disk in order to profit from future developments.

Within this thesis a software package for a realistic calculation of the signals of highly segmented HPGe detectors for γ-ray spectroscopy was developed. The input of the calculations is partially based on experimental measurements of the detector characteristics. The calculations are essential for AGATA, as the results are directly used to create signal databases for the PSA. The presented signal databases of AGATA detectors are exploited for in-beam spectroscopy experiments with AGATA.

One of the first experiments with the AGATA demonstrator coupled to the magnetic spectrometer PRISMA was analyzed within this thesis. The experiment aimed for the in-beam spectroscopy of neutron rich Thorium and Uranium nuclei after multi-nucleon reactions. As this was one of the first analysis done for an AGATA experiment, the performance of the PSA and the complete AGATA array was a major aspect and focus of the present work. Finally experimental results from in-beam spectroscopy of various Uranium and Xenon isotopes after multi-nucleon transfer reaction are presented.

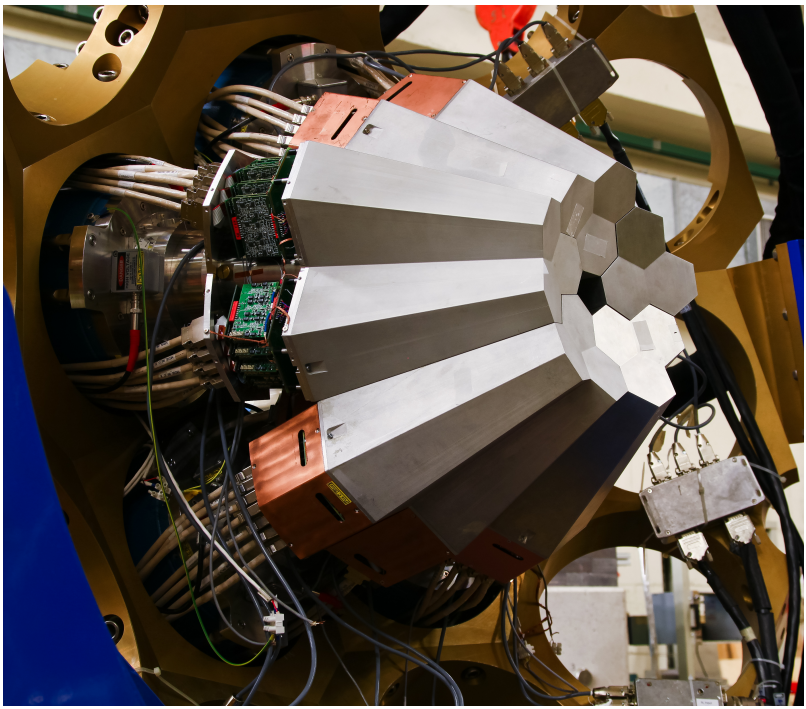

Figure 3: Picture of the AGATA demonstrator mounted at the Laboratori Nazionali die Legnaro (LNL) in Italy. The HPGe detectors are located in the triple canister with hexagonal shapes inside the grey Aluminium end caps. The first cold amplification stage is also sitting inside the end caps. After the commissioning phase of the new spectometer a series of experiments were performed in combination with the PRISMA spectrometer in the period from 2010 to 2012.

2. Characterisation of highly segmented HPGe detectors

2.1. Pulse shape analysis in AGATA

The AGATA spectrometer employs PSA to determine the positions of the interaction points with a much higher position resolution than the physical segmentation of the detector volume. A γ-ray will normally have a chain of interactions in the Germanium detectors (e.g. 3-4 at 1.3 MeV). There can be more than one interaction in one segment of a detector and / or the γ-ray can be scattered to another segment of the same crystal or to an adjacent detector. A high precision of the interaction positions is required in order to perform the gamma ray tracking process with high efficiency. The signals of every detector after the pre amplifier are digitized using a 14-bit analogue to digital converter with a rate of 100 MHz. This large dataset must be compared to an existing set of signal pulses. This comparison includes the signal of the core electrode, the signal of the hit segment electrode and the signals from the neighbouring segment electrodes for every interaction. This is needed because the transient signals induced in the neighbouring segment electrodes give important information for the angular and z position of the interaction.

As the PSA runs online and must be fast, a set of algorithms were developed, such as grid search [15], genetic algorithms [16], wavelet decomposition, a matrix method [17] and a particle swarm algorithm [18]. All algorithms compare the recorded pulses with a database that holds signal pulses of defined positions in the detector. At the moment only the grid search algorithm is implemented in the online analysis. The signal library includes all signal traces over a 2 mm grid. Before the search algorithm is applied the transfer function of the acquisition electronics and the differential crosstalk is folded in the signals of the library. The algorithm calculates for the nearest neighbours of the hit segment a figure of merit.

$$FOM = \sum_{\text{segments i}} \sum_{\text{timesteps j}} |v^m_{i,j} - v^d_{i,j}|^p$$

v^m are the measured signals and v^d are the signals within the database. p is a distance parameter defining a metric. For a gaussian distribution $p = 2$ would be the best choice. Investigations of the algorithm report a best position resolution with a $p = 0.3$ that is now used as a standard. The adaptive grid search is only capable of identifying single interactions within one segment of a crystal. Other algorithms, like the particle swarm algorithm [18], could identify more interactions within the same segment.

In order to generate a database for looking up the different positions different detector characterisation methods are used.

2.2. Characterisation methods

To characterise an AGATA like detector requires, that sets of core and segment signals for all the interaction points on a defined grid within the detector volume are determined. This vast amount of signals and the corresponding position information is stored in a library readable for the PSA algorithms. This can be achieved experimentally by measuring signals of defined positions. The technique developed at the University of Liverpool is a coincidence system [19, 20, 8], that puts a heavily collimated source ^{137}Cs (662 keV) in front of the detector. The x and y coordinate is defined by the position of the source, whereas the z coordinate is measured using a secondary collimation system perpendicular to the xy plane equipped with NaI(Tl) detectors. γ-rays that Compton scatter under 90° with an energy of 288 keV are measured in coincidence and determine the z position of the interaction. Another system based on the same principle but with a different secondary collimation and detector system was developed at the University of Orsay [21][8]. A third system based on the coincidence principle is build at the University of Salamanca [8]. Using the pulse shape comparison scan (PSCS) method [22] a new scanning system is developed at Strasbourg [8]. In this case only a collimated source is needed. The detector is rotated and the position is determined by comparing the pulse shapes of crossing beam lines. At GSI-Darmstadt the PSCS principle is extended with γ-ray imaging techniques based on positron annihilation [23][24][8].

A new method was proposed, in which the geometry of the crystals and the homogeneous distribution of γ-ray interactions from a source run is used to generate a dataset [25].

All scanning systems have in common, that every individual crystal needs to be scanned and that it takes time to prepare the measurement, to take and analyse the data. A complete different approach is on a calculated library of datasets which is based on the properties of the individual detectors. For this reason computer programs were developed to simulate and calculate the detector responses. Up to now three codes are available, the Multi Geometry Simulation (MGS) code [26], the Java AGATA Signal Simulation (JASS) toolkit [27] and the AGATA Data Library ADL which is part of this thesis.

2.3. The AGATA Detector Library ADL

The AGATA Detector Library (ADL) was developed to calculate signal databases for the PSA algorithms of the AGATA spectrometer. The library is written in the computer language C and is used for realistic simulations of semiconductor detectors in nuclear physics. In the following discussions the focus lies on highly segmented HPGe coaxial detectors, although many points can be transferred to different geometries or semiconductor materials.

2.3.1. Layout of the ADL software

In figure 4 a block diagram of the ADL is shown. The routines are coloured in green and the user provided input is coloured blue. The main routine called `Calculate Traces` consists of three subroutines and takes the interaction position as input. The first subroutine calculates the path of the charge carriers through the detector material for every time step. It needs the electrical field and a mobility model of the charge carriers as an input. The second subroutine calculates for every time step the induced charges in all electrodes. It needs the weighting potentials to do this. The last subroutine convolutes the signal with pre defined functions. The routines and their input parameters will be described in detail within the next sections.

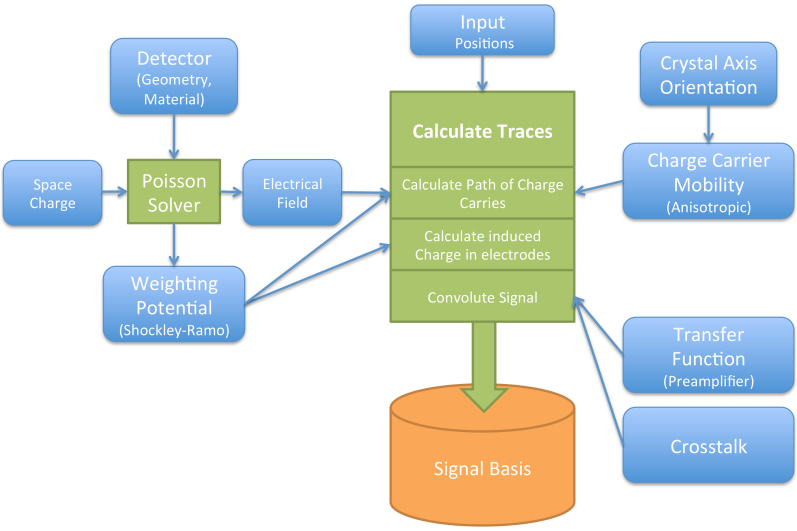

Figure 4: Block diagram of the routines (green) and the input (blue) for an ADL simulation

ADL intents to be flexible and extendible. The library has a special registration of the routines and input parameters controlled by template files. An overview of the parts of ADL is given in table 1.

To illustrate the working principle of the library the input and output (IO) of data is discussed. Three different possibilities are provided listed in table 2. To change the used IO routine the template file `Template_READWRITE.txt` has to be changed. The routine `ADL_Setup_READWRITE` implemented in `ADL_ReadWrite.c` reads in the template file and sets the right routines by linking the according function pointers. The `ADL_Status_READWRITE` routine implemented in `ADL_ReadWrite.c` reports the current status of this part of the library. The real work, like writing text files, is then implemented in the according source file. When adding routines, they have to implement the interface defined in `ADL_ReadWrite.h` and in `ADL_ReadWrite.c` the registration of the interface has to be added. In this way the complete library is structured. Routine implementation and definition are

Parts	Description
ADL	Main file setting up all other templates used in for the simulation
CONVOLUTION	Controls how to convolute the signals with a transfer function
DRIFT	Set up the drift process of the charge carriers inside the detector
EVENT	Basic event information
FIELDS	Geometries, weighting and electrical fields are set up
READWRITE	Input and output
TIME	Settings for the filter times and other timing
TRACES	Conditions and settings for the trace calculation
TRAPPING	Correction parameters for neutron correction

Table 1: Parts of the ADL controlled by template files

File	Description
`ADL_ReadWrite.h`	Header file describing routines for setting up IO routines
`ADL_ReadWrite.c`	Source file implementing routines for setting up IO routines
`ADL_ReadWrite_BIN.h`	Header file describing IO routines for binary data
`ADL_ReadWrite_BIN.c`	Source file implementing IO routines for binary data
`ADL_ReadWrite_TXT.h`	Header file describing IO routines for text data
`ADL_ReadWrite_TXT.c`	Source file implementing IO routines text data
`ADL_ReadWrite_TKT.h`	Header file describing IO routines for TKT
`ADL_ReadWrite_TKT.c`	Source file implementing IO routines for TkT
`Template_READWRITE.txt`	Template file controlling which routines to use

Table 2: ADL files implementing the in and output of data

written in the source and header files, control of the behaviour of the according routines is set up in the template files.

The important template files and routines, especially for HPGe detectors, will be discussed. A simple example program with its corresponding template files can be found in the appendix A.

2.3.2. Pulse shapes of HPGe detector signals

Radiation interacts with the active detector material by creating electron hole pairs. Depending on the type and the energy of the radiation the volume of the created charge cloud changes. For example a single interaction of a 1 MeV γ-ray in Germanium knocks out fast electrons that loose their energy by creating electron hole pairs resulting in a charge cloud with a radius of 0.5 mm [27]. Whereas cosmic muons interacting with the detector material form a line track of charges.

Once the charges are created inside the active Ge material, they travel along the electric field of the reversed biased semiconductor detector and induce a signal in the electrodes. In general semiconductors are described by the Van Roosbroek equations [28][29], that aside from the poisson equation for the electrical field, also comprise continuity equations for the electron and hole densities. The equations already assume a quasi static field approximation, such that the induced signals at all electrodes of the detector are instantaneously created. This approximation is valid, as the time needed to spread this information is the small distance in the detector divided by the speed of light. In our case of large volume detectors more valid approximations are applied to simplify the problem. A point like interaction for γ-ray spectroscopy is assumed, as the radius of the charge cloud is small and full photo events with energies above 1 MeV are unlikely. A partial shielding from the external field occurs in the detector, that causes a tiny time delay required to separate the electrons and holes. This shielding effect significantly affects the PSA for particle identification in Silicon detectors [30]. It roughly scales with the stopping power along the particle track and is inverse proportional to the external applied field. The time delay is small compared to the collection time of the charge carriers. The stopping power for electrons in Germanium is two orders of magnitude smaller than for alpha particles. Therefore this effect is neglected.

Depending on the geometry of the detector, the applied voltage and the impurity concentration of the semiconductor material the time until all charge carriers are collected changes. The initially formed charge clouds could change their shape as diffusion causes a transformation of a delta distribution into a Gaussian distribution. However

also this effect will be small and could be neglected in our case, although diffusion could play a small role at the segmentation lines of the segmented detectors. The two charge carriers have different anisotropic mobilities resulting in different collection times for electrons and holes depending on the orientation of the crystal axis [31, 32].

The two signals at the electrodes of a simple semiconductor detector, for example a planar Germanium detector, are identical despite from being inverted and small differences caused by the electronic noise. The requirement hereto is that the sum of both weighting potentials is one.

Segmentation of detectors is done by dividing the electrodes. This could be either just the cathode, like in AGATA, or both electrodes like in a double sided silicon strip detector. In these systems the signals of the hit segments look different depending on the position. Non hit segments show so called transient charge signals. While the amplitude of the hit segments is integrated over the feed back capacity, the transient charge signal vanishes after the collection process. Summing up anode segments and cathode segments to two signals results in the signals of a non segmented detector.

Different types of detectors need different processing of their signals for a good position resolution. A planar double sided strip detector has segments in the size of a few millimetres and it is sufficient for a good position resolution to use the segmentation information. However a large volume coaxial HPGe detector, like the AGATA detectors [10], needs pulse shape analysis to achieve a position resolution of a few millimetres.

2.3.3. The Ramo theorem

To calculate the induced charge Q_i in an electrode i for a unit charge placed at position $\vec{x}$ inside the active detector material the weighting potential $\phi_i(\vec{x})$ is used. It is defined by the following definition:

$$Q_i = -q\phi_i(\vec{x})$$

The Ramo theorem [33] is used to calculate the weighting potentials for all electrodes and positions inside the detector. The assumption of

a quasi static field is mandatory. As shown in [34] the Ramo theorem does not depend on the presence of space charge. The solution for the weighting potentials are obtained as a solution to the Laplace equation

$$\nabla^2\phi(\vec{x}) = 0$$

with the condition

$$\phi_i|S_j = \delta_{i,j}$$

for the boundary S_j. With the solution of the equation it is enough to evaluate the weighting potential at a given time and position of the charges for every electrode.

$$Q_i(t) = -\sum_q q\phi_i(\vec{x_q}(t)) \tag{1}$$

An example of the weighting potential calculated with ADL is shown in figure 6.

2.3.4. Calculating the weighting potentials and the electrical field

First the weighting potentials [33] and the electrical field have to be calculated. Depending on the geometry of the detector, this can be done analytical or numerical. An analytical example is the true coaxial detector[1]. The Possion equation

$$\Delta\phi = -\frac{\rho}{\epsilon} \tag{2}$$

in cylindrical coordinates becomes

$$\frac{d^2\phi}{dr^2} + \frac{1}{r}\frac{d\phi}{dr} = -\frac{\rho}{\epsilon}$$

The core electrode of a true coaxial detector defines the inner radius r_1 and the outer electrode the outer radius r_2. The boundary condition is the applied voltage V between the two electrodes $\phi(r_2) - \phi(r1) = V$. Solving the equation for $E(r) = -\frac{d\phi}{dr}$ results in

$$-E(r) = -\frac{\rho}{2\epsilon} + \frac{V + \left(\frac{\rho}{4\epsilon}\right)\left(r_2^2 - r_1^2\right)}{r\ln\frac{r_2}{r_1}}$$

[1] See for example [1] page 422

Assuming the space charge as constant.

The ADL library provides basic geometries like the true coaxial or a planar detector. More complex geometries are provided as SIMION[2] potential arrays. The user can easily add new geometries as SIMION potential arrays or implement new routines to add different formats.

The weighting potentials could be solved by any program. However a 3D Poisson solver is implemented in the library to calculate the fields. It is based on the established technique of successive over relaxation [35]. In principle the detector is split into many small cubes called voxels. Each voxel ν_i is either an electrode or active detector material. To calculate the weighing potential for one electrode, this electrode is set to 1 V and all other electrodes are set to 0 V. The solver now iterates over all voxels. If the voxel is active material, it takes the average of the values of the 6 neighbouring voxels as its new value plus some over relaxation parameter for faster convergence.

$$\begin{aligned}\nu_i^{\text{new}} =& \frac{\nu_{\text{top}} + \nu_{\text{bottom}} + \nu_{\text{left}} + \nu_{\text{right}} + \nu_{\text{front}} + \nu_{\text{back}}}{6} \\ &+ \Xi \cdot \left(\frac{\nu_{\text{top}} + \nu_{\text{bottom}} + \nu_{\text{left}} + \nu_{\text{right}} + \nu_{\text{front}} + \nu_{\text{back}}}{6} - \nu_i \right)\end{aligned}$$

The value of Ξ is changed after 10 iterations from 0.67 to 0.9. If the voxel is an electrode, it is not changed. The value change is monitored and if it becomes small enough the calculation stops.

The numerical solution of the solver is compared with the analytic one. Both simulations were calculate and the differences checked. The results are shown in figure 5. Only small deviations occur at the boundaries and are in the per mille range.

Different parameters can be adjusted in the template files depending on the type of input. For the analytical solvable geometries the applied high voltage, the impurity concentration, geometric details and the relative permittivity of the medium are set. For the SIMION files the different weighting potentials for all electrodes and the contribution of the impurity concentration must be set as file input.

[2]Documentation of and tools for the SIMION potential arrays can be found at http://simion.com/sl/

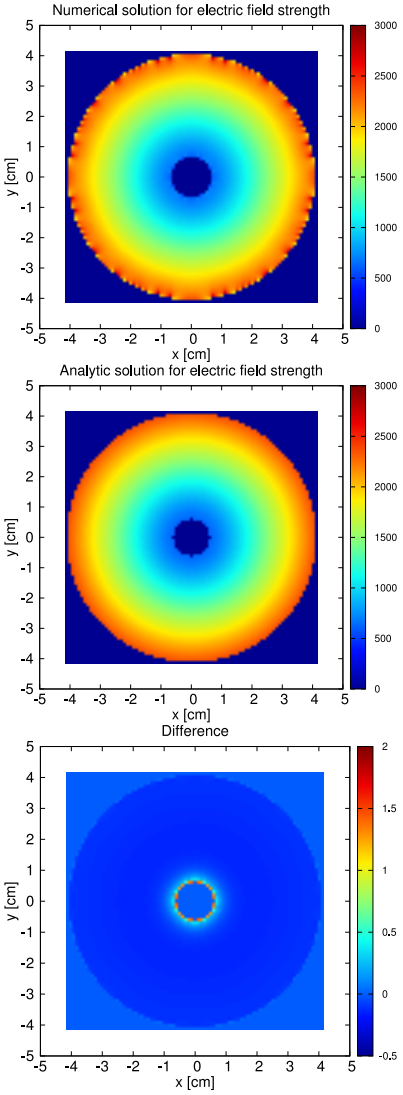

Figure 5: Electric field strength for a true coaxial HPGe detector. The numerical simulation (top) and the analytical (middle) show a good agreement, as indicated in the difference (bottom) between them. Only at the boundaries small deviations occur on 10^{-3} level.

For all AGATA geometries SIMION files were calculated and are available from the IKP AGATA webpage[3]. In figure 6 the weighting potential of the core and of the segment A4 are shown. To create a full simulation of an AGATA detector the weighting potential for all 36 segment and the core electrode were calculated.

The electrical field is the weighting potential of the core electrode scaled by the applied bias voltage plus the space charge contribution. The space charge is the uncompensated impurity of the germanium material and can be measured [36][37]. The contribution of the space charge to the electrical field is the calculated electrical field of the distribution for the boundary electrodes set to 0 V.

For the AGATA detectors the manufacturer[4] provides information on the impurity profile of the detectors. These information were verified by independent pulser measurements for the first asymmetric detector systems [38]. The analysis described in [39] was adapted for asymmetric detector systems by changing the mean radii of the cylindrical approximation depending on the asymmetry of the detector.

2.3.5. Calculation of the signals

The simulation is based on the interaction positions and the deposited energy as an input. This is implemented in a simple event structure that is controlled by the event template. Here the maximum number of simultaneous interactions per event and the number of segments has to be set. Furthermore the number of time steps and the time resolution is controlled by the template. It is also possible to read events from text or binary files.

At the interaction position two point like charges (the electrons and the holes) are generated and travel along the electric field depending on their mobility. Different models are provided by the library for the mobility. A basic model assumes a constant mobility. Another implemented model, see [1] p. 434, assumes an empirical dependence of the drift velocities with the electrical field strength. However, recent publications [31, 32] show that the mobilities of electrons and holes in the

[3] http://www.ikp.uni-koeln.de/agata
[4] CANBERRA Industries Inc.

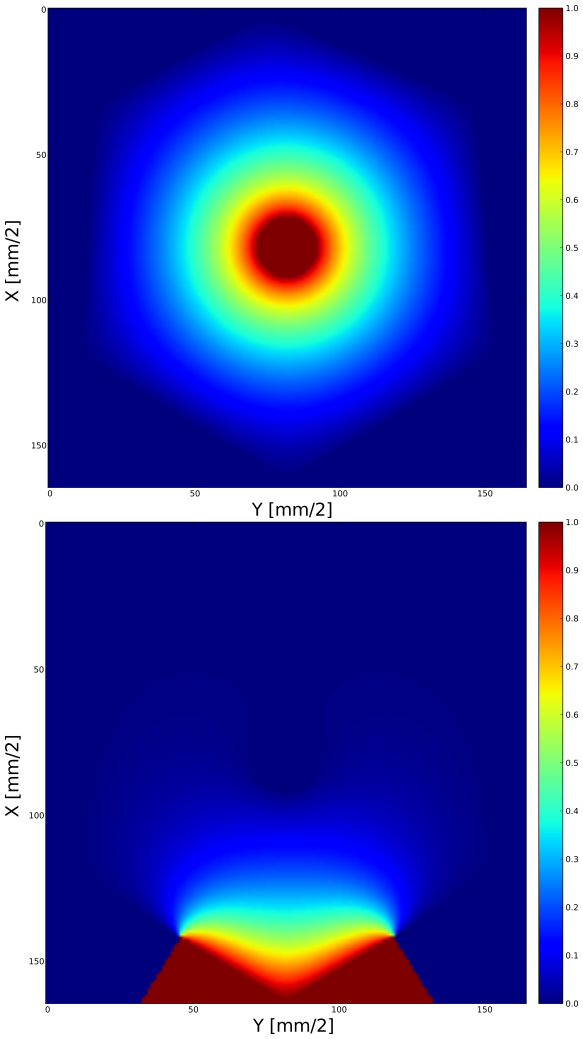

Figure 6: Weighting potentials for the core electrode (top) and segment electrode A4 (bottom) of detector A001. The complete region outside the active Germanium material are marked as electrodes with a fix potential of 1 V. The units of the z-scale are Volt.

Crystal axis orientation			
ϕ	0.7853981633		
θ	0.0		
ψ	0.0		
Electron mobility parameters			
Mobility in $\langle 100 \rangle$		Inter valley scattering rate	
E_0	507.7	E_0	1200
β	0.80422	ν_0	0.459
μ_0	0.0371654	ν_1	0.0294
μ_n	-0.0001447	ν_2	0.000054
Hole mobility parameters			
Mobility in $\langle 100 \rangle$		Mobility in $\langle 111 \rangle$	
E_0	181.9	E_0	143.9
β	0.73526	β	0.7488
μ	0.062934	μ	0.062383

Table 3: Parameters for the mobility of electrons and holes in Germanium according to the parametrization given in [31].

Germanium material are not isotropic, but depend on the orientation of the crystallographic axis of the cubic centred Ge crystal structure with respect to the electric field . This realistic description of the mobility inside Germanium crystals is implemented in `ADL_Drift_Ge.c` and set up with the template file `Template_DRIFT_GE.txt`. Here the orientation of the crystal axis and the parameters described in [31] are configured. The used parameters are listed in table 3. The axis orientation is given as the orientation of the $\langle 100 \rangle$ axis in Euler angles.

The orientation of the asymmetric AGATA crystals were measured [40]. The method is based on the use of a collimated 400 kBq ^{241}Am source emitting 60 keV γ-rays in combination with a small lead collimator of 1.5 mm radius and 1 cm length. The low energy γ-rays deposit their energy within a few millimetres of the active detector material. The created holes are collected immediately and only the drifting electrons form the signal. The crystal is scanned from the front over a circle with a fixed radius of 2.35 cm. The differences in

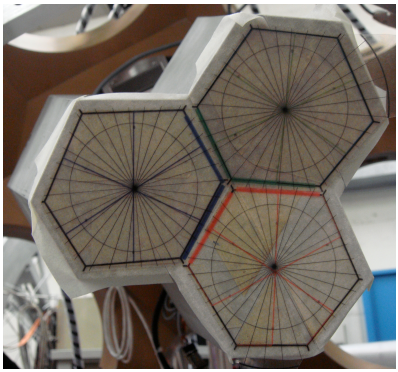

Figure 7: Aligned masks for scanning the crystal axis

rise time between different angles result mainly from the crystal internal structure. The impact of the hexagonal shape of the crystals is reduced. A mask, see figure 7, indicating 32 different scanning angles was placed at the front face of the detector. The mask was aligned by requesting that the count rates of two neighbouring segments are equal when the collimated source is placed on the corresponding segmentation line and that at the centre of the mask all front segments showed nearly equal count rates. The data acquisition recorded the energy and the full trace signals of every event. In the analysis the signals were filtered for total energy deposition and an average trace was build for every scan position. The resulting 10 % to 90 % rise times are summarized in figure 8. The applied fit function is

$$T_{10}^{90}(\theta) = A \cdot (1 + R_4 \cdot \cos(4 \cdot (\theta - \theta_4))) \cdot (1 + R_2 \cdot \cos(2 \cdot (\theta - \theta_2)))$$

with A, R_4, R_2, θ_4 and θ_2 as fit parameters. The largest contribution comes from the second factor that models the 4 fold symmetry of the anisotropic mobility. θ_4 describes the crystal orientation. The third factor was added to correct for observed deviations of the 4 fold symmetry. The results show clearly the orientation of the axis, especially that it is constant through all detectors.

In figure 9 the magnitude of the electron drift velocity is shown for the analytical solved true coaxial detector. The left plot assumes an

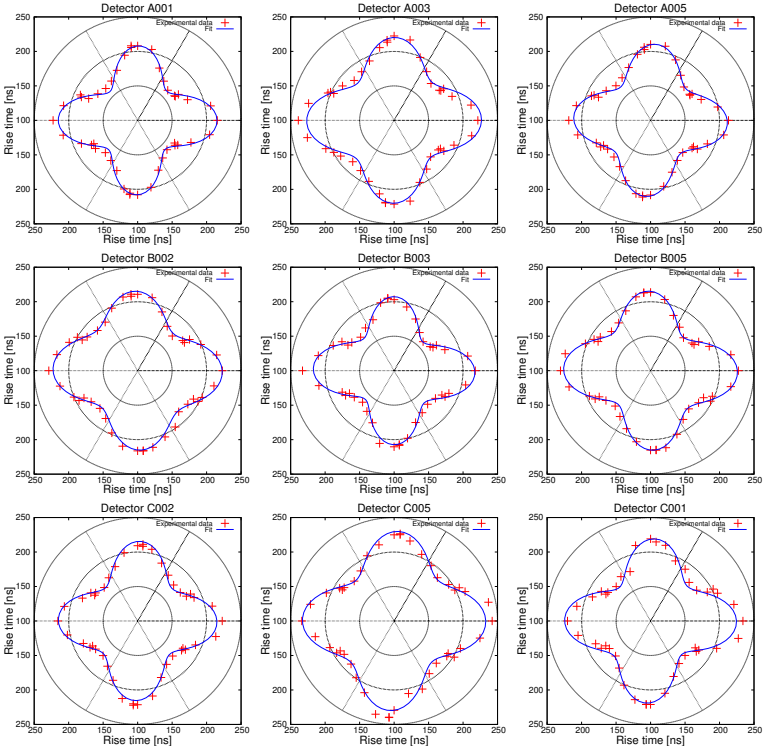

Figure 8: Rise times depending on the angle of the interaction for nine asymmetric AGATA detectors.

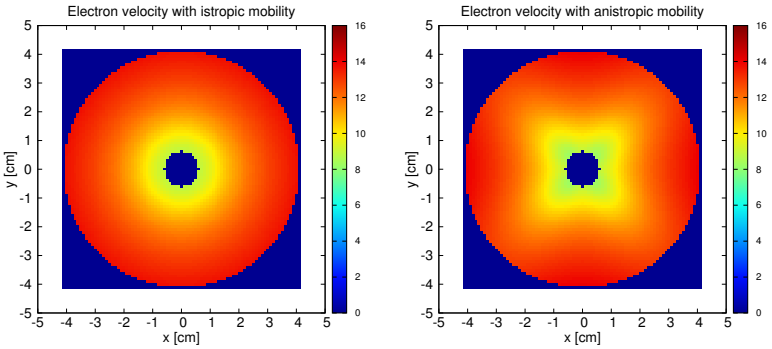

Figure 9: Simulation with isotropic (left) and anisotropic (right) mobility for the analytic solution of the true coaxial detector

isotropic drift mobility. The right plot an anisotropic mobility. The four fold symmetry of the velocity results in different rise times of the signals and reproduces the measured behaviour.

The routines that calculate the path of the charge carriers along the electrical field are implemented in `ADL_Traces_NUMRES.c` and configured in the according template `Template_TRACES_NUMRES.txt`. The calculation is based on the 5th-order Runge Kutta integration method with adaptive step size control[5]. The induced signals for every electrode of the detector are calculated depending on the drift of the electrons and holes to the electrodes. For every time step and for each interaction the weighting field evaluated at the position of the electrons is subtracted from the weighting field evaluated at the position of the holes. These differences are multiplied by the charge produced at the individual interaction, see formula (1). The sum of all interactions results in the signal set for the given event.

Finally these traces are convoluted with realistic behaviour of the detector system. The different polarity of the pre amplifiers are set up as a convolution function. The transfer function of the pre amplifier or the cross talk of segmented crystals could be taken into account.

[5] from [35] (Chapter 16.2 p.714)

Actually in the online analysis of AGATA these functions are folded in the signals of the library, as they could vary for different detector and digitizer configurations.

Additionally the library provides routines to calculate the trapping rates relevant for neutron damage correction as described in [41]. The rates are added to the PSA bases and are used in the neutron damage correction of the AGATA online analysis.

2.3.6. Simulations for AGATA PSA bases

The computer program that calculates a PSA base for AGATA iterates over the active detector volume with a defined grid size. The latest PSA bases for the AGATA detectors are available through the AGATA web page of the IKP[6].

In the following example a simulation for the detector A001 is described. In AGATA a 3D grid size of 2 mm is used. For an A type detector 47156 positions inside the detector volume are calculated. The template files with the precise values for all routines are summarized in appendix B. The potential arrays for the different geometries are available at the AGATA web page of the IKP. The complete set consists of 36 segment weighting potentials and one core weighting potential. Furthermore 5 files for the electrical field are given. The first one is the weighting potential for the core and represents the electric field in the detector without any space charge. It is scaled by the applied voltage, that is for detector A001 5000 V. The other files include refined space charge distributions that must be scaled according to the data reported by the manufacturer. To calculate the charge collection process the anisotropic mobility model is used including the measured axis orientation. Single interactions are calculated with an energy deposition of 1 keV. The trace length is set to 600 ns with a 5 ns step width. In addition to the trace signals the trapping rates for the online neutron damage correction are calculated for every position.

In figure 10 the simulated traces for this AGATA detector are shown. In the top plot the core signal for different interaction radii are shown. The effect of the different mobilities of electrons and holes is clearly

[6] http://www.ikp.uni-koeln.de/agata

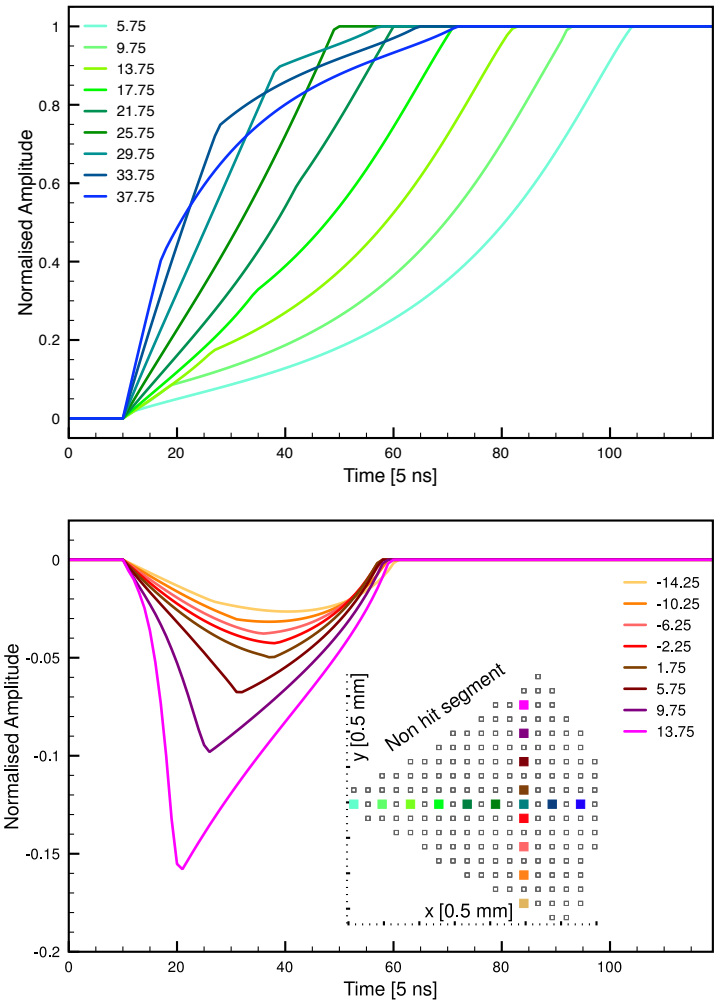

Figure 10: Simulated traces for an AGATA detector. Top shows the core signal for different radii and bottom shows the transient signals induced in a non hit neighbouring segment. Colour code as indicated in the bottom graph.

visible. For small radii the faster electrons are collected immediately while the slower holes still have to drift to the segment electrode. The shortest rise time occurs at an intermediate position, where the collection process for both signals is equal. Then for larger radii the time of the electrons to be collected is longer than for the holes, as they have to drift to the core electrode. In the bottom plot of figure 10 the transient signals in a segment next to the hit segment are shown. Depending on the distance of the interaction to the non hit electrode, the amplitude of the transient signal varies.

The PSA bases sets used in the AGATA online and offline analysis are generated by simulations based on ADL. In figure 11 the simulated traces are compared to a measurement with a ^{60}Co source after the PSA. The top of the plot shows an event with a γ-ray energy of 1172 keV deposited in segment A1. The middle of the plot shows an event with a γ-ray energy of 1332 keV. The energy was distributed over the segments C3, E1 and E3. In the two bottom graph the distribution of hits for different z slices are shown.

The position resolution depends on the quality of the calculated signal bases. To obtain a position resolution different techniques were employed and up to now a final position resolution below 5 mm (FWHM) is obtained for a gamma energy above 1 MeV. The first result is described in [42]. The technique compares a Monte Carlo simulations of the detector response with an experiment performed at the IKP Cologne. In the experiment a ^{48}Ti beam with 100 MeV impinged on a deuterated titanium target. The reaction ^{48}Ti(d, p)^{49}Ti was investigated in inverse kinematics. The γ-rays were measured with the first symmetric AGATA triple. To reconstruct the velocity vector of the scattered nucleus a double-sided silicon strip detector (DSSSD) was used to detect the emitted proton. The performance of the Doppler correction was compared to simulations taking into account the different contributions that cause a broadening of the peak. The final position resolution is of the order of 5 mm at an energy of 1382 keV. This result is adequate to reach the design performance of AGATA.

Another technique uses the imaging capability of AGATA to determine the position resolution of a single AGATA detector [43] and assesses a mean position resolution of 5 mm in an energy range from 300 keV to 1 MeV.

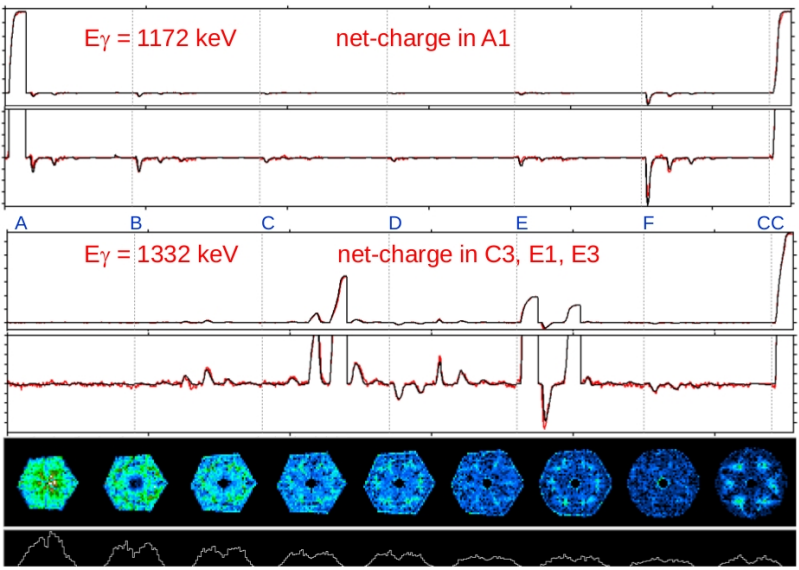

Figure 11: Simulated signals (black) compared to measured signals (red) of a ^{60}Co source for two events with a γ-ray energy of 1172 keV and 1332 keV. The induced charge of all segments (A-F) and the core (CC). Distribution of hits in the detector (bottom) for different z slices.

A third approach uses the annihilation of the positron emitted by a ^{22}Na source to extract the position resolution [44]. As the two γ-rays emitted by the annihilation process have opposite directions two AGATA detectors at different positions were used to perform a source measurement. The collected and analysed data was then compared to Monte Carlo simulations and position resolution of 3.5 mm was determined for an energy of 511 keV . The latest publication uses a comparable method to the first one [14]. The experiment was one of the first commissioning experiments performed at the AGATA setup at LNL. The results show that the FWHM of the interaction position resolution varies roughly linearly as a function of γ-ray energy. For a γ-ray with 250 keV the position resolution is 8.5 mm going down

to 4 mm at 1.5 MeV. Above 1.5 MeV the value stays constant up to 4 MeV.

3. Spectroscopy of neutron rich Th and U nuclei after multi-nucleon reactions

During the AGATA campaign from February 2010 to December 2011 a variety of physics experiments were performed at the LNL (INFN Legnaro, Italy)[45]. A complete list of experiments can be found in the appendix, page 235. The experiment on spectroscopy of neutron rich actinides was performed and analysed as part of this thesis.

3.1. Introduction

The heavy nuclei beyond the last double magic nucleus ^{208}Pb in the actinide region from Radium to Nobelium show a variety of shapes in the ground state and at higher excitation energies. The experimental results from in-beam γ-ray spectroscopy on excited states are either obtained in the vicinity of the few isotopes suited as target material in this mass region or have been measured after fusion evaporation reactions. In both cases mainly neutron deficient actinide nuclei were investigated. Another more recent approach is based on multi-nucleon transfer reactions as a tool for spectroscopy of heavy nuclei. These experiments rely on the high resolving power of a powerful γ-ray detector array to separate the γ-rays from the multitude of reaction products [46].

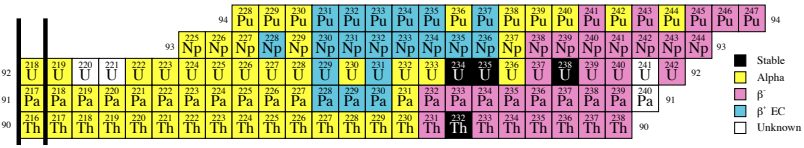

Figure 12: Chart of nuclei for the region of interest. Colour code is the major decay branch of the ground state.

The nuclear shapes and the transition between the different shapes in the actinides are subject of several recent theoretical investigations. The ground-state energies, first excited states and deformation parameters of a wide range of heavy nuclei from Ra up to the super heavy

region are calculated in a macroscopic-microscopic approach. The Yukawa-plus exponential model is taken for the macroscopic part of the energy and the Strutinski shell correction is used for the microscopic part. Detailed predictions for the even isotope chains $^{226-236}$Th and $^{226-242}$U are given in [47] with a minimum of excitation energy of the first 2^+ state and a maximum of deformation energy at N=144,146 exactly at the border where experimental data are available.

The ground state band and low-lying alternative parity bands in the heaviest nuclei are also predicted within a cluster model [48]. The model is based on the assumption that reflection asymmetric shapes are produced by the motion of the nuclear system in the mass asymmetry coordinate. For the lightest N=148 isotones including ^{240}U detailed results on the levels of the ground-state rotational band and states of the alternating parity band are obtained. This includes transitional electric dipole D0, quadrupole Q2, and octupole Q3 moments for the transitions from the ground state to the states of alternating parity band.

A very extensive theoretical study in the region from thorium to nobelium isotopes covered nearly all aspects of these heavy nuclei [49]. As part of the analysis collective rotational excitations in the even–even nuclei $^{226-236}$Th and $^{228-242}$U were determined employing the Gogny D1S force together with the constrained Hartree-Fock-Bogolyubov (HFB) mean field method as well as the configuration mixing, blocking, and cranking HFB approaches. The theoretical values for kinetic moments of inertia for the yrast normal deformed bands of even–even Th and U isotopes as functions of rotational frequency can be directly compared with an experimental measurement.

The most recent theoretical results on sequences of heavy nuclei from Th to No are obtained within self-consistent relativistic Hartee-Bogolyubov mean-field calculations which provide a unified description of particle-hole (ph) and particle-particle (pp) correlations on a mean-field level [50]. The two parts of the mean field are determined by a relativistic density functional in the ph channel, and a new separable pairing interaction in the pp channel. As one result of many others several predictions are made on unknown ground-state axial quadrupole and hexadecapole moments along the isotopic chains of Th, U, Pu, Cm, Cf, Fm and No.

A second study which is based on a reflection asymmetric relativistic mean-field theory concentrated on the shape evolution of even-even Th isotopes [51]. The calculated deformations, matter density distributions, and potential energy surfaces demonstrate that Th isotopes undergo two types of shape transition when the neutron number increases from N = 126 to the very hypothetical N = 156. One is the well investigated transition from spherical to octupole deformed around N = 134. The second transition is predicted to happen at the extreme neutron-rich side around N = 150 and would change from octupole to quadrupole deformed. Also the results of this study include e.g. quadrupole-, octupole-, and hexadecupole deformation values along the full Th chain which await experimental verification.

In recent years γ-ray spectroscopy studies of unexplored actinide nuclei were based on transfer and multi-nucleon transfer reactions. One group of experiments is performed with thick actinide targets to produce the heavy reaction products, to stop the target- and beam-like reaction products, to do spectroscopy of γ-rays emitted at rest with the most efficient spectrometers available. The technique depends on available cross coincidences with known γ-ray transitions of the beam like reaction partners in order to identify unknown transitions. The feasibility of these measurements was demonstrated in Rn and Ra nuclei which were produced in a series of experiments with different beams on heavy ^{232}Th targets. The measured cross sections as a function of different beam-target combinations and the populated high spin range are described in [46]. In agreement with older reaction studies performed at Berkeley [52] heavy projectile allow for highest production yields, excited states at angular momentum up to $30\hbar$. The region of the final reaction products is mainly determined by the available beam energy and the Q value for the different reaction channels.

A second group of measurements rely on few nucleon transfer reactions with light oxygen beams and were successfully exploited to detect excited states e.g. in neutron rich ^{236}Th, ^{240,242}U isotopes [53, 54]. γ-rays were detected in coincidence with the outgoing transfer products. For the most neutron rich cases the rotational ground state band was detected up to spin 8 to $10\hbar$.

In two experiments presented in [55] the magnetic spectrometer PRISMA combined with the clover array (CLARA) were employed to measure the multi nucleon transfer reactions ^{70}Zn(^{238}U,U')Zn' and ^{136}Xe(^{238}U,U')Xe'. The successful production of neutron rich U and especially Th isotopes motivated us to measure the ^{136}Xe(^{238}U,U')Xe' reaction with the AGATA demonstrator.

Our new experiment for spectroscopy of neutron rich Th and U nuclei after multi-nucleon transfer reactions was conducted in October 2011 at LNL. It combines the multi-nucleon transfer reactions induced by a heavy ion beam on a U-target and a coincident measurement detecting γ-rays and beam like reaction products. It exploited the AGATA demonstrator [7] in combination with the magnetic PRISMA spectrometer [56, 57] for particle identification. Inside the target chamber the position sensitive particle detector DANTE [58] was installed and used to detect outgoing heavy beam-like reaction products. In this way kinematical coincidences between different reaction products and γ-rays were detected. This method solves the problem of high γ-ray background from excited fission fragments after fission of highly excited actinide reaction products. To produce the nuclei of interest a ^{238}U target was bombarded with a 1 GeV ^{136}Xe beam from the Tandem-PIAVE-ALPI accelerator complex. The details of the setup are summarized in table 4. A schematic drawing of the setup is shown in figure 13.

projectile	$^{136}_{54}$Xe
beam energy	1 GeV
beam current	$\sim$ 2 pnA
effective beam time	97 h
PRISMA angle	50°
target	$^{238}_{92}$U
target angle	45°
target thickness	1.0 and 2.0 mg/cm^2
target backing	$^{93}_{41}$Nb
backing thickness	1.3 mg/cm^2

Table 4: Details of the beam, target and experimental setup

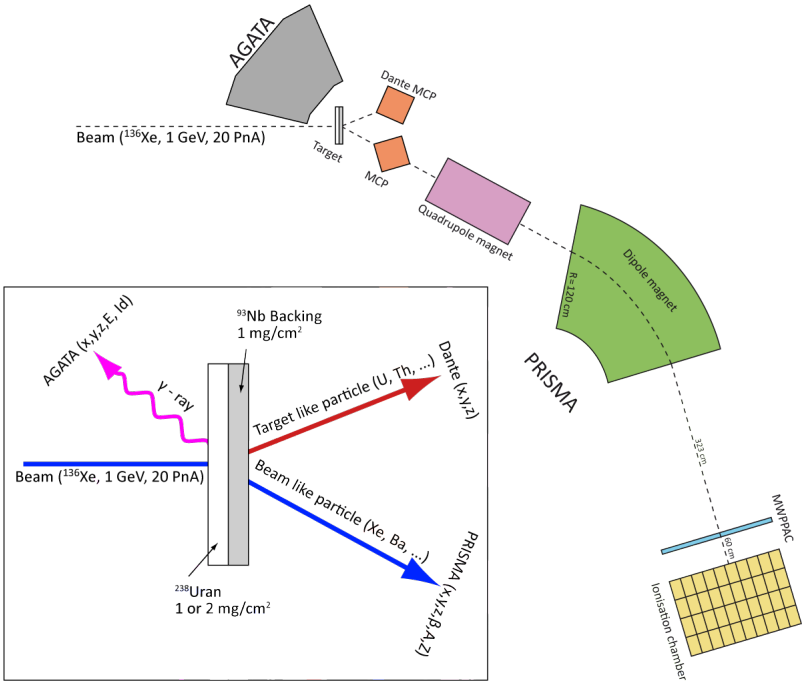

Figure 13: Schematic drawing of the experimental setup. Details of the target and the measurable outgoing particles are given in inset down left.

3.2. Detector systems

3.2.1. AGATA Demonstrator

The AGATA Demonstrator [8] is used to measure γ-rays with good efficiency and high energy resolution. It consists of 15 large volume electronically segmented high purity Germanium detectors comprised in 5 similar triple cryostats [13][10]. It is the first detector configuration of the AGATA spectrometer described in the introduction. Details of the experimental setup and of the AGATA demonstrator installed at the LNL are described in [45]. The conceptual design and the infrastructure needed for the demonstrator is summarized in [59].

Details of the processing electronics and the analysis will be discussed in the following chapters.

3.2.2. PRISMA magnetic spectrometer

The various reaction products and their velocity vectors are identified by the PRISMA magnetic spectrometer [56, 57]. PRISMA is designed for the mass region $A = 100$–200 and an energy range from 5 to 10 MeV per nucleon. The main features of the spectrometer are a large solid–angle coverage ($\sim$ 80 msr, $\pm 6^\circ$ for θ and $\pm 11^\circ$ for φ), a momentum acceptance of $\pm 10\%$, a mass resolution up to $\frac{1}{300}$ via time-of-flight, an energy resolution up to $\frac{1}{1000}$ and the possibility to be rotatable in a wide angular range from -20° to $+130^\circ$. A picture of the PRISMA spectrometer coupled to the AGATA demonstrator is shown in figure 14.

The spectrometer consists of different detectors. In figure 13 a schematic overview of the detector assembly is shown. The beam like ions scatter into the entrance window of PRISMA. Here their position and a timing signal are detected by the entrance multi channel plate (MCP) detector in Chevron configuration with a size of $80 \times 100\,\mathrm{mm}^2$ [60]. It is placed 25 cm behind the reaction chamber and has a position resolution of 1 mm and a time resolution of 400 ps. The following quadrupole magnet focuses the ions onto the x plane of the dipole magnet. The scattered ion passes through the adjacent dipole magnet on different trajectories depending on its velocity, its mass, its charge

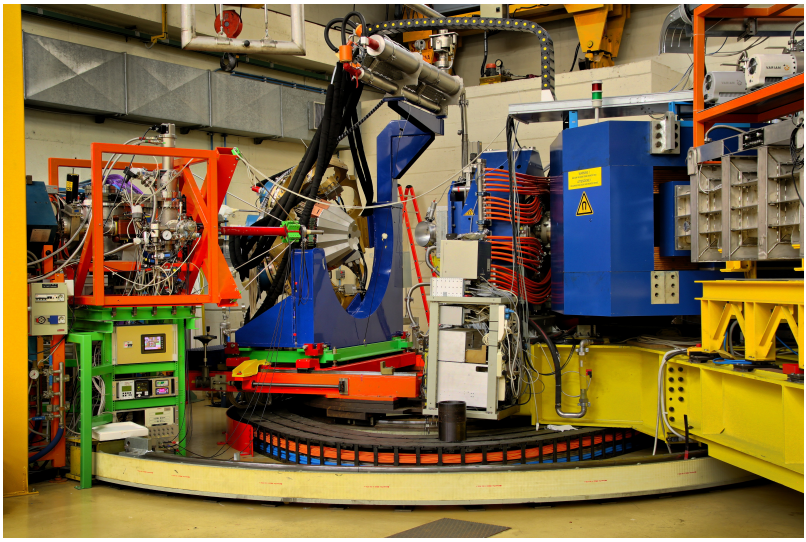

Figure 14: The AGATA demonstrator coupled to the magnetic spectrometer PRISMA

and the strength or rigidity of the magnetic dipole field. The position sensitive Multi Wire Parallel Plates Avalanche Counter (MWPPAC) [61] provides the second timing signal (first from the MCP) needed for the time of flight (TOF) measurement of the fast moving reaction products. The kinetic energy is deposited in the ionization chamber (IC). The IC is segmented in 40 segments, 10 segments per row (0–9) and four segments per layer (A–D). Veto detectors next to row 0 and 9 reject ions leaving the active detector volume of the ionization chamber. The gas pressure of the ionization chamber was adjusted in such a way, that the ions loose nearly all their energy in the first three layers A, B and C. The details of the settings of PRISMA are summarized in table 5.

PRISMA angle	50°
Magnetic dipole field strength	0.783272 T
Magnetic quadrupole field strength	0.857744 T
Fill gas	CH_4
Gas pressure	≈ 84 mbar

Table 5: PRISMA settings

3.2.3. DANTE particle detectors

The Detector Array for multi-Nucleon Transfer Ejectiles (DANTE) [58] is a position sensitive detector based on Micro Channel Plates (MCP) for detection of energetic heavy ions. A mylar foil is used as an entrance window. Energetic ions generate electrons which are amplified by two MCPs of dimensions $40 \times 60\,\mathrm{mm}^2$ mounted in Chevron configuration. The position-sensitive anode consists of two orthogonal delay lines connected to low-noise differential preamplifiers. The x and y position is derived from the arrival time of the corresponding delay line with respect to a fast reference signal generated by a capacitor formed with the second MCP. The position resolution was expected to be better than 1 mm and the timing resolution to be about 130 ps. The detectors were mounted in the 58° ring at the positions 1, 3 and 4, see picture 15. In the analysis of the experiment it became

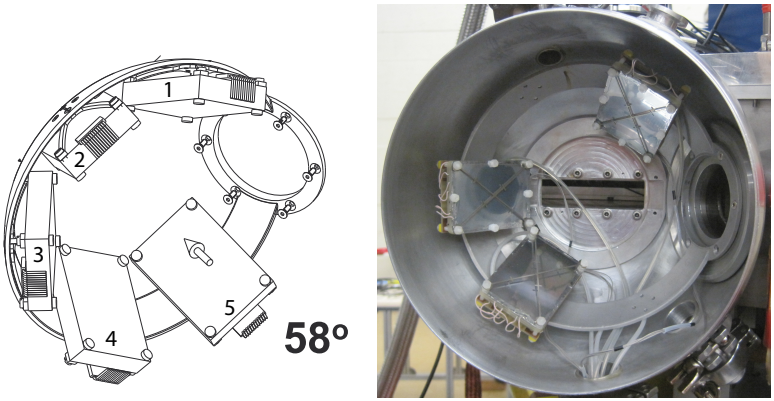

Figure 15: The Dante detectors, left picture modified taken from [59]

clear, that the position information of the DANTE detectors were not working properly and only the time information was usable for the data analysis.

3.3. Trigger, data acquisition and data processing

A huge amount of data is generated by the 15 highly segmented AGATA detector and the PRISMA detectors which request a selective trigger and a suitable data acquisition system especially for AGATA. The main objective of the AGATA front-end electronics (FEE) is to digitize all the signals from each crystal and to process them in real time. The FEE consists of pre-processing electronics and a trigger system. The processed data is then passed to a computer farm where the PSA, the event building including the ancillary detectors and the tracking is done online and all relevant data for a complete replay of the experiment is written to disk. The data of the ancillary detectors was passed via the AGATA VME interface AGAVA [8]. After the pre-processing electronics the data is transferred to a computer farm where all the information is stored on hard disk for further data processing.

3.3.1. Trigger

The Global Trigger and Synchronisation (GTS) system [8] provides the central clock[7] of the spectrometer. It synchronizes the AGATA detectors and the ancillary detectors and distributes a global time stamp to the events passing the system. It is organized in a tree structure where every AGATA detector or an ancillary detector like DANTE can generate a trigger request. A custom build fully programmable trigger processor validates the incoming requests. In the experimental setup discussed here the following trigger conditions were used: PRISMA (MWPPAC) or DANTE 1 and DANTE 4 and AGATA or DANTE 3 and PRISMA (MCP) and AGATA. The PRISMA (MWPPAC) trigger is the most important trigger for the experiment. Only ions that have reached the focal plane of PRISMA can be identified. In this trigger the coincidence with AGATA was not requested. The two other triggers are very similar. By knowing the interaction position of both ions on the MCPs of DANTE or PRISMA a basic Doppler correction could be performed and the additional statistics could be used in a $\gamma\gamma$ analysis. Depending on the time resolution even an assignment of beam or target like ions could be possible.

3.3.2. Front end electronics

The signals of the 15 AGATA HPGe detectors are passed to the FEE via mini-D ribbon (MDR) cables. The signals are digitized in the digitizer [8](one for each detector) with a sampling rate of 100 MHz using 14-bit analog to digital converter (ADC). The signal is now a data set, that is serialized by a field programmable gate array (FPGA) and sent to the pre-processing electronics via optical fibres. The FPGA of the digitizer implements a fast constant fraction discriminator (CFD) algorithm to generate a fast timing signal needed for the trigger system.

In a second step the data is processed by the pre-processing electronics [8]. The data from the digitizers is reduced by a factor of 100 by selecting only detectors that registered a relevant signal. Conditions from the trigger system can be implemented into the selection of events at this stage. Furthermore a moving window deconvolution

[7] 100 MHz digital clock with a 48-bit time stamp

(MWD) algorithm is used to determine the energy deposited in each detector. The raw trace data, the energy information and the time stamp is then passed to the computer system.

The ancillary detectors, PRISMA and DANTE, are read out using standard electronics housed in Versa Module Eurocard-bus (VME) crates. The bridge between VME and the AGATA GTS / FEE is a VME module named AGATA VME Adapter (AGAVA)[8].

3.3.3. Online processing and computer systems

Based on the trigger conditions the data is transported via optical fibre channels to the computer farm. Here a framework developed in the computer language ADA for parallel processing of data named NARVAL [62] processes and stores the data. NARVAL is a highly distributed data acquisition system running across a network and acting like a single program. The data is passed from and to so called actors running as individual processes on a computer. The different processes run on different computer nodes and the data is distributed over the network. The different actors talk a common language of data description based on the AGATA Data Flow (ADF) framework [63]. In figure 16 the topology used in the experiment is shown. All relevant data is written to disk, in this way the whole experiment, including the PSA, can be reconstructed on a computer system after the experiment. This allows to improve PSA and Tracking algorithms and to perform recalibration of time and energy. All actors are capable of writing spectra of interest in a simple binary format. A summary of all spectra and their meaning can be found in the appendix D.

The first actor is the crystal producer. It either reads the data from the disk[8] as indicated in figure 16 or online from the mezzanine system. The crystal producer formats the data and passes it to the pre-processing actor.

The pre-processing actor is capable to set energy gates, thresholds and multiplicity gates on the number of segments firing. It corrects for crosstalk [64]. Moreover, it is able to determine the core energy

[8]The producer is capable of reading and writing different compressed event data as described in [7]

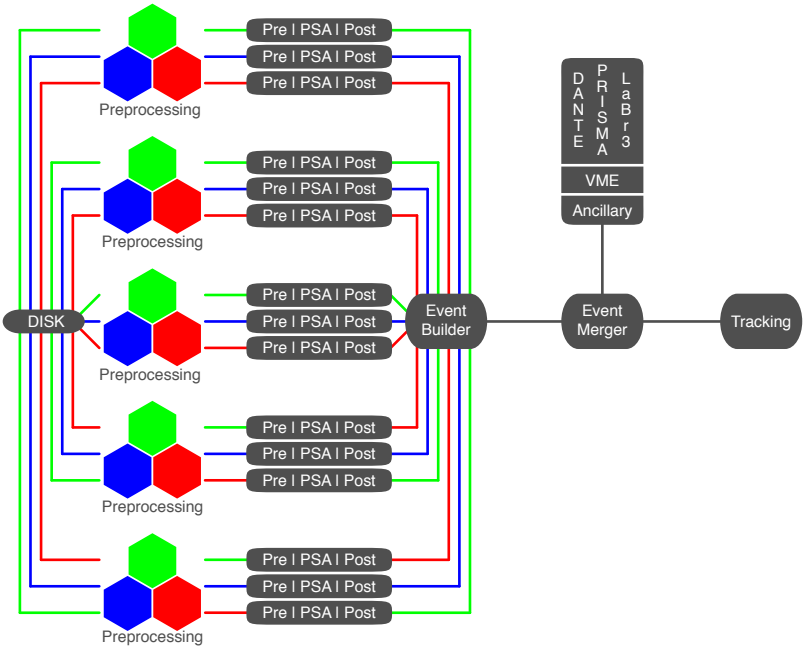

Figure 16: Topology of the NARVAL system

from the crosstalk contributions in the detector in case of events with very high energy deposition. The actor derives the time information of the HPGe-detector signals inside the trace window with a standard leading edge filter or by a linear fit on the combination of segment and core signals[9]. A routine is available to restore the energy information of one broken or unstable segment by comparing core and remaining segment energies. Energy calibrations of cores and segments are applied and a time shift of the trace signals is performed. As a result the actor produces data from the HPGe detectors which is energy calibrated and time aligned on the crystal level.

Next comes the multi threaded PSA actor. It handles different search types and settings for the comparison of the traces with the signal database; details are given in section 2.1 on page 17. The transfer function of the acquisition system and a function describing the differential crosstalk is folded with the information of the pre-calculated ADL bases. During the experiment and also later for the replay of the data the adaptive grid search algorithm was used [15]. The actor is able to reconstruct the information of segments where the signal is missing[10]. After this stage the full signal trace information is not needed any more. The deposited energy and the corresponding information on the interaction position is transferred to the next actor.

The post PSA actor is able to set gates on the core energy, the segment fold and the hit fold. The energy of core and segments can be recalibrated and the different core time signals can be shifted. Depending of the interaction position a correction for electron and hole trapping caused by neutron induced defects of the crystal was applied [41].

The data of all AGATA crystals is then merged by the event builder utilizing the time stamps as a coincidence condition. Again the filter can be used to set gates on the minimum fold of the event.

The next actor merges the data from the ancillary detectors into the data flow utilizing again the time stamps. The event merger actor may ask for a coincidence between AGATA and the ancillaries.

[9] see also chapter 3.6.1

[10] The main reason for a missing segment is a broken cable or not working preamplifier

The last actor is the tracking filter. It performs the tracking of the different hits in the array. The algorithm has to determine how the γ-ray(s) interacted within the full detector comprising all five cluster detectors. A detailed description and discussion of different tracking methods are given in [65, 66, 67]. Some information of the experimental setup have to be passed to the filter like the number of detectors and the position of the source or the target. A narrow time window for coincidences between AGATA and the ancillaries is utilized to reduce unwanted background contributions.

All the filters are processed online on a computer farm housing several systems and the data is written on high capacity disk servers utilizing a parallel file system[11]. After the experiment all the data is stored on the GRID[12] and could be accessed from different sites. Approximately 7 TByte of data where collected during the experiment.

3.4. Replay and analysis programs

To replay the data the NARVAL system in offline mode [62] or an emulator called femul[13] is used. Both systems use the same user libraries for the actors. The emulator is easier to set up, but it is limited to one single computer. After the development of multi core central processing units (CPU), this is not a strong limitation any more. For the offline data analysis a standard server machine with 2 CPUs each one providing 8 cores and 16 threads and a CentOS Linux system was employed.

The data of the experiment is split in different runs[14]. Due to tests and calibrations during the experiment not all runs contribute information and statistics for the analysis of the physics results. During the experiment a problem with the ancillary site could only be solved by taking the ancillary data separately. For these runs the data sets of

[11] At the time of the experiment IBM x3550 server and SUN Storage Tek system was in use with IBMs General Parallel File System (GPFS)

[12] The AGATA collaboration is represented as a virtual organization in the WLCG GRID [68]

[13] femul is avaiable from svn://gamm01.lnl.infn.it/agata

[14] In total there are 133 runs including calibration and test runs

ancillary and AGATA detectors have to be merged offline, that is another reason to replay the data set. Bash[15] scripts were programmed to control the replay with different configurations.

The result of the replay is either stored in ADF files that could be analysed using the software package gammaware or as ROOT trees [69]. For this analysis the ROOT trees (AGATREE) were used as an input for a second stage of analysis. In figure 17 the different analysis steps are schematically shown. The computer program treegen was developed within this work to control the PRISMA analysis and to perform the Doppler corrections. The treegen code extracts the raw data of the ancillary detectors stored in the AGATREE and uses the PRISMA Manager[16] and adapted routines to do the PRISMA analysis and the calculation of the binary partner as described in section 3.6.6. Finally all the calibrated and analysed data from AGATA, PRISMA and DANTE is stored in one ROOT tree (ANATREE). The treegen program is able to reduce the amount of data stored in the trees by asking on an event by event basis for fulfilled conditions. For example it is possible to generate trees, where the mass and Z number of all events were successfully identified. By storing the data in ROOT trees all functions and methods implemented in ROOT are available for the analysis.

Figure 17: Different steps for the analysis with the developed programs treegen and PostAnalysis

The final step in the analysis is the PostAnalysis program that generates spectra and matrices out of the ANATREE. The possible histograms are:

[15] The Bourne Again SHell
[16] A C++ library providing tools to analyse data from the PRISMA by E. Farnea

- γ-ray spectra and $\gamma\gamma$ matrices (ROOT histograms and MFILE[17] spectra)
- mass and charge state spectra (ROOT histograms and MFILE spectra)
- time spectra (ROOT histograms)
- spectra for the aberration correction (see section 3.5.4) (ROOT histograms)
- IC and ΔE-E spectra and matrices (ROOT histograms)

The PostAnalysis program is capable of doing an optimization of the Doppler correction described in section 3.6.7.

[17] MFILE is the data format usable with tv and hdtv

3.5. PRISMA analysis for particle identification, tracking and kinematics

The PRISMA analysis comprises the calibration of the different detectors, the reconstruction of the ion trajectory through the spectrometer, the selection of right data sections in different graphs and the configuration of correction routines. In the following sections these steps will be described. The PRISMA analysis is an iterative process as many selections and corrections request to be rerun for the complete analysis. Here only the final states are described and remarks on problems and dependencies will be given as a comment in the text.

3.5.1. Calibration of the entrance MCP

The first PRISMA detector to calibrate is the entrance MCP. It provides the first interaction point and therefore the direction of the ions velocity and a time signal for the time of flight (TOF) measurement. The TOF alignment is described later. In front of the MCP a cross with four flags is mounted as position calibration points. The positions of these flag marks are well-known. A matrix method described in [70] is used to achieve a mixed linear calibration of the two dimensional surface resulting in six parameters.

$$f_x(x,y) = a_x + b_x x + c_x y$$

$$f_y(x,y) = a_y + b_y x + c_y y$$

These parameters are input values for the PRISMA manager library. To eliminate noise contributions a 2D gate on the MCP plane is set. The raw position data and the calibrated MCP plane are shown in the figures 18 and 19.

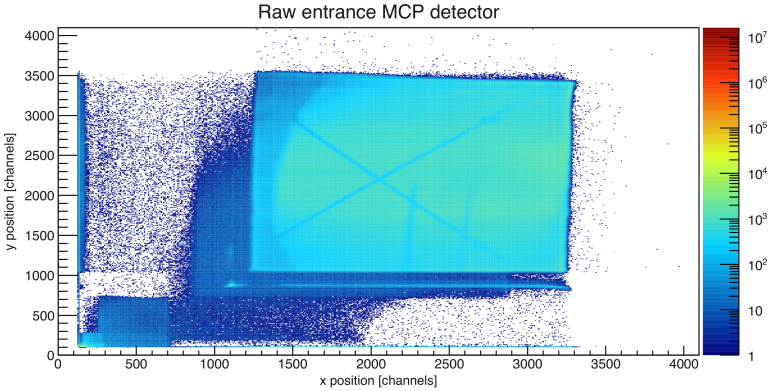

Figure 18: MCP entrance detector plane. The position distribution of incoming ions without calibration is shown.

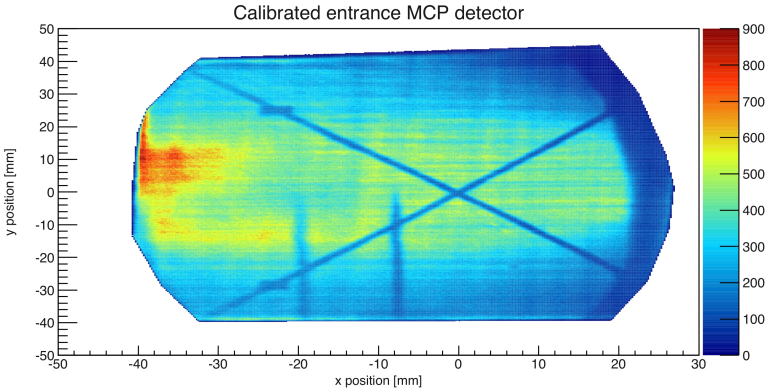

Figure 19: MCP entrance detector plane. The calibrated position distribution of incoming ions is shown.

3.5.2. Selection of Z

The data of the segmented ionization chamber (IC) of PRISMA is analyzed to determine the chemical element via the atomic charge Z of the beam like reaction product. The Bethe–Bloch formula[18] describes the specific energy loss of an incident particle in an absorber:

$$-\frac{dE}{dx} = 2\pi N_a r_e^2 m_e c^2 \rho_a \frac{Z_a}{A_a}\frac{z^2}{\beta^2}\left[\ln\left(\frac{2m_e\gamma^2 v^2 W_{\max}}{I^2}\right) - 2\beta^2 - \delta - 2\frac{C}{Z}\right]$$

with $2\pi N_a r_e^2 m_e c^2 = 0.1535\,\mathrm{MeVcm^2/g}$, Z_a the atomic number, A_a the atomic weight and ρ_a the density of the absorbing material, z is the charge of the incident particle in units of the electronic charge. $\beta = \frac{v}{c}$ with v as the velocity of the incident particle and c the speed of light. γ is defined as $\gamma = \frac{1}{\sqrt{1-\beta^2}}$ and $W_{\max}$ is the maximum energy transfer in a single collision. δ is the density correction and C is the shell correction as described in [71]. After the reaction the ions have different charge states around $z \sim 28$. By entering the IC the ions pass through a window that separates the vacuum from the gas. Here most electrons are stripped from the nuclei. When they finally run through the gas, the rest of the electrons are stripped and in a good approximation $z = Z$ with Z the atomic number of the incident particle is valid.

The IC is segmented; the CH_4 absorber gas and its pressure in the chamber was set in a way, that the ions were stopped within the four segment layers of the IC (see figure 13). The energy loss in the first or in the first two layers versus the full energy deposited in the IC is plotted to identify the chemical elements.

First the IC needs a proper calibration of all its 40 segments. Before the start of the experiment an electron gun was installed to fire electrons with four different energies in every segment of the IC [72]. However the analysis of this data did not result in a well calibrated IC. Therefore another method to calibrate the IC was used. It is assumed that the dominant contribution of ions arriving in PRISMA are beam like particles and that for a given velocity ratio $\beta = v/c$, the deposition of energy in the segments of layer A is equal. The

[18] See for example page 24 in [71]

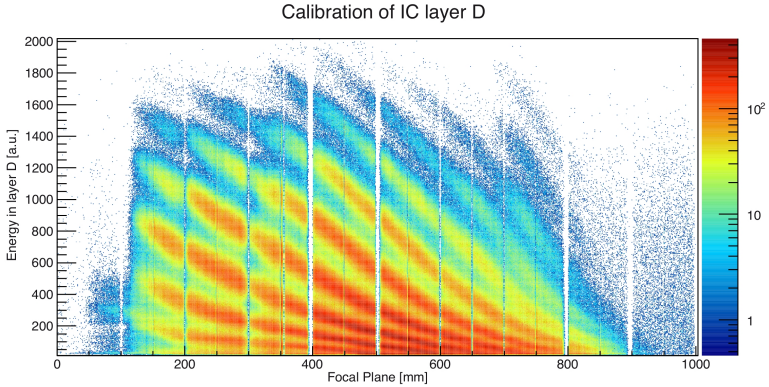

Figure 20: Histogram for energy of layer D segments versus the focal plane of the MWPPAC with a cut on $Z = 54$

same argument holds for the segments of layers B and C. A cut with a high beta value was now used to generate spectra and to calibrate the IC segments relative to one segment from one layer. Here the 5^{th} segment was used as its spectra are well aligned between the different layers. The relationship between the different layers could therefore be taken from the original calibration. An upper threshold was applied to get rid of noise in the last channels of the IC. The last layer D could not be calibrated in the same way as only a small fraction of rest energy is deposited here. A 2D histogram with the energy on the y axis versus the focal plane of the MWPPAC on the x axis is used for the calibration. The corresponding graph is shown in figure 20.

The different IC segments were shifted relative to the 5^{th} segment of the layer. The different lines in figure 20 are the different charge states of the ions. For each line the beta values of the different sections were checked in overlapping regions to make sure that the lines are aligned in the right way. The uncalibrated and calibrated spectra of all IC segments are shown in 21. The energy of segment C1 was missing.

After the calibration the different Z values were selected by applying graphical 2D cuts. Two different 2D spectra were generated for this purpose, (i) the energy released in the first layer A of the IC versus

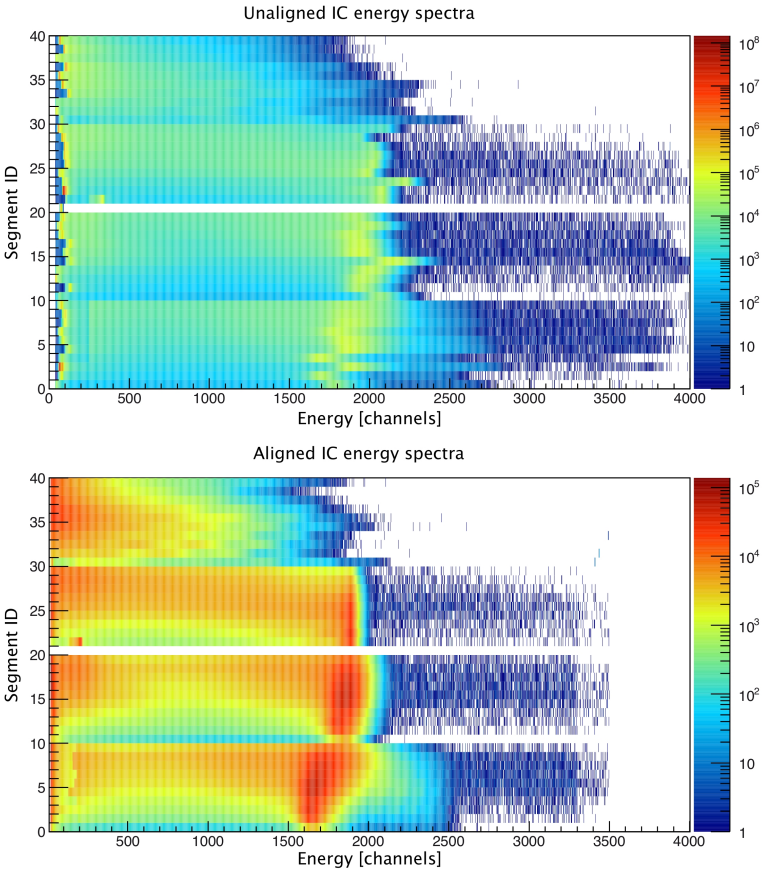

Figure 21: Unaligned and aligned spectra for the IC. The scales of the intensities in the two plots are different. The high intensity in the top plot results from the pedestals that were used as a zero reference in the described alignment procedure.

Barium	1.79×10^6	16.0%
Caesium	3.71×10^6	33.2%
Xenon	11.17×10^6	100%
Iodine	4.10×10^6	36.7%
Tellurium	2.07×10^6	18.5%

Table 6: Relative intensity distribution of measured elements

the total deposited energy and (ii) the energy deposited in the first two layers A and B versus the total energy. Two different sets of cuts were applied for the two spectra. The plot for the first two layers A and B is shown in figure 22. The top plot in figure 22 shows the energy loss related to the total energy deposited in a logarithmic scale. In the bottom plot in figure 22 the selected events are coloured proportional to the number of events, while the not selected events are grey. On the left side of the plot the selected events from the cuts on the energy loss only in layer A are visible. In the top plot of figure 23 the energy loss in the layer A related to the total energy is shown in a logarithmic scale. In the bottom plot the selected events using 2D cuts are coloured, while the not selected events are grey. On the right side of the bottom plot events from the selection of the cuts on the energy loss in the two layers A and B are visible. Although the resolution of the energy loss in only one layer is not as good as in the two layer approach, the selected events are important for the analysis as ions with lower kinetic energy could be resolved and identified.

The relative intensity distribution of the measured elements is listed in table 6. Especially in the one proton transfer and pickup channels contaminations of Xenon isotopes are observed.

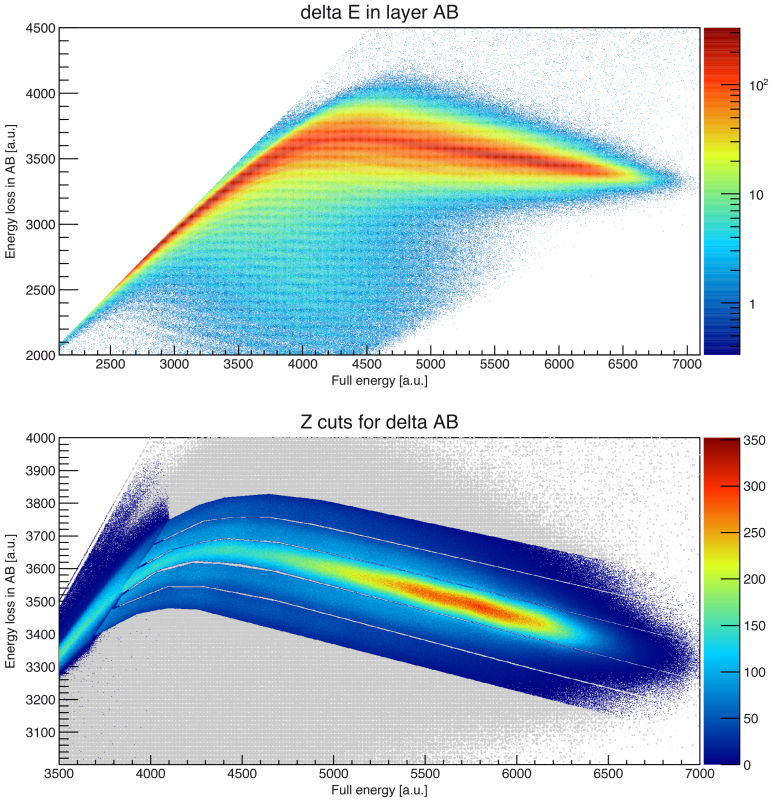

Figure 22: Energy loss versus full energy is used for selection of different Z values. Energy loss in the first two IC layers A and B versus to the total energy loss in a logarithmic scale (top). Selection of the elements Barium, Caesium, Xenon, Iodine and Tellurium (bottom) by applying a 2D cuts. Excluded events are shaded grey.

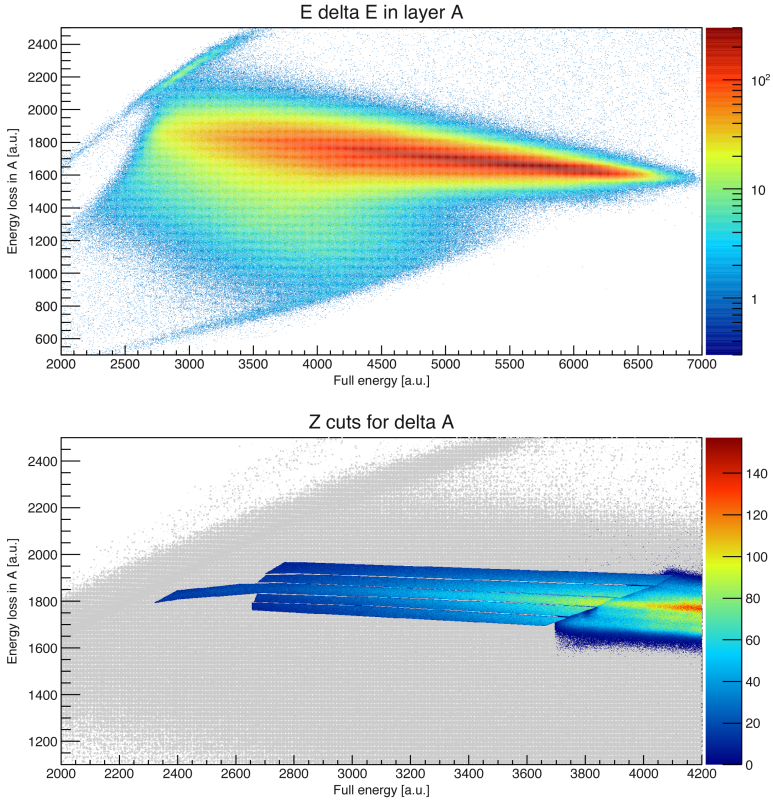

Figure 23: Energy loss versus full energy is used for selection of different Z values. Energy loss in the first IC layer A related to the total energy loss in a logarithmic scale (top). Selection by 2D cuts for the elements Barium, Caesium, Xenon, Iodine and Tellurium (bottom) by applying 2D cuts. Excluded events are shaded grey.

3.5.3. Time of flight (TOF) alignment

The time of flight (TOF) of the reaction products through PRISMA provides very important information for the complete analysis. It is mandatory for the mass and charge state identification. Moreover the velocity is deduced from TOF and used for the Doppler correction of the γ-rays. TOF is measured by ten time to amplitude converters (TAC). The TAC start signal is caused by the MWPPAC at the focal plane of the PRISMA detectors. The delayed entrance MCP signal is used for the TAC stop signal. A tedious and time consuming problem of the data analysis occurred due to instabilities and shifts of detectors and electronics as a function of the beam time. The mass resolution achieved for a small set of data which corresponds to a short measuring period could not be reproduced for the complete data set of the full beam time. Consequently even mixing of masses and charge states were observed. The problem is illustrated in the 2D histogram showing the A over Q values as a function of the running time stamp number of the AGATA events. Depending on the time stamp number or the real time of the experiment the A over Q ratios showed instabilities and shifts during the experiment as shown in figure 24 for the TAC of section 3 of the MWPPAC.

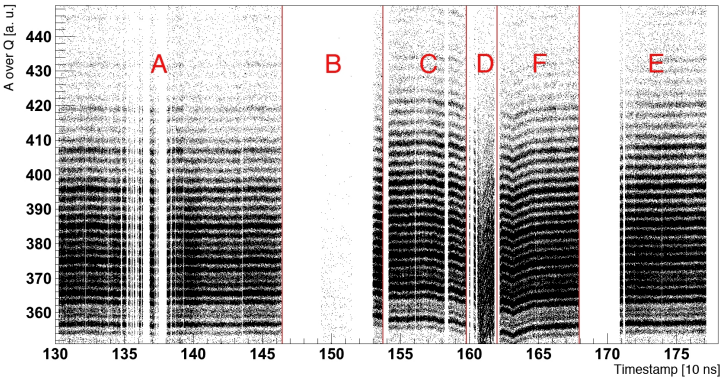

Figure 24: A over Q ratio for section 3 of the MWPPAC as function of the measuring time which is proportional to the AGATA time stamp.

In order to correct for this unexpected time dependent behaviour the runs were split in different time periods or sections indicated with A,B,C,D,F,E in figure 24. The short sections B and D were not analyzed. The sections A, C, F and E had to be analysed separately implying different calibration procedures and long term stabilization as a function of measuring time.

For best mass resolution the ten TACs have to be aligned relative to each other. Looking at the raw TOF values there are no obvious peaks for the time alignment available. For a distance of 100 mm along the MWPPAC one TAC gives the time information. Depending on the position the different TACs are identified along the focal plane. With the mass number A and the charge state Q, the trajectory of an ion through the detector is characterized by the formula

$$\frac{A}{Q} = B \cdot R\frac{t}{l}$$

where B is the rigidity of the magnetic field, R is the radius of curvature of the trajectory, t the TOF and l the path length of the trajectory. B is a constant given by the setting of the dipole magnet. R and l are calculated by reconstructing the ions path done by the PRISMA manager software. The alignment of the ten different TACs is inspected by a 2D histogram of TOF and position on the focal plane. The different A over Q values are smeared out for different path lengths of the ions. A cut on a small region of l shows then the different A over Q values as straight lines depending on R, see figure 25.

To align the different TACs a 2D cut on one A over Q line for the different sections of the MWPPAC were employed. A root script calculates for a given number of bins in x direction the mean y value for the entries in one line and the mean error of the distribution. These numbers are then plotted and a straight line is fitted to the data using gnuplot [73]. A residual plot showing the difference between the fit and the data is plotted in figure 26 for the section E. The upper plot shows the spread of the lines before the alignment and the lower one after the alignment is done. This procedure had to be repeated for every section of the data set. The final precision of the alignment is about ± 0.4 ns.

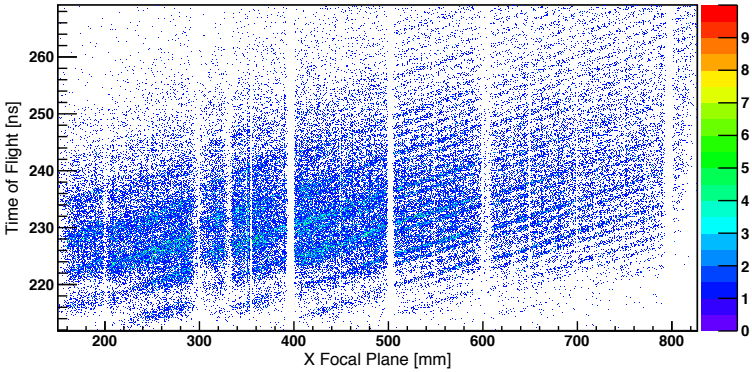

Figure 25: TOF versus position x at the focal plane, atomic charge number Z=54 and a path length interval between 6.1 and 6.12 m. Poor alignment can be seen between section 1 and 2 at position 200 mm, section 2 and 3 at position 300 mm and section 6 and 7 at position 600 mm.

The absolute shift is done at a later stage resulting in an absolute time difference and therefore corrected velocity and beta value. A small absolute offset does not cause an effect on the mass resolution but of course is relevant for the Doppler correction of the γ-rays emitted in flight.

3.5.4. Aberration corrections

After the successful alignement of the TACs a closer look at the A over Q values reveal systematic dependencies of the A over Q ratios and the position of the start MCP and the position on the focal plane MWPPAC detector. These aberrations are caused by imperfections of the magnetic field and approximations for the properties of the magnetic lenses. In figure 27 the effects are illustrated for the Xenon ions $Z = 54$.

The PRISMA manager software provides several routines to correct for these effects in a phenomenological way. The routines rely on a

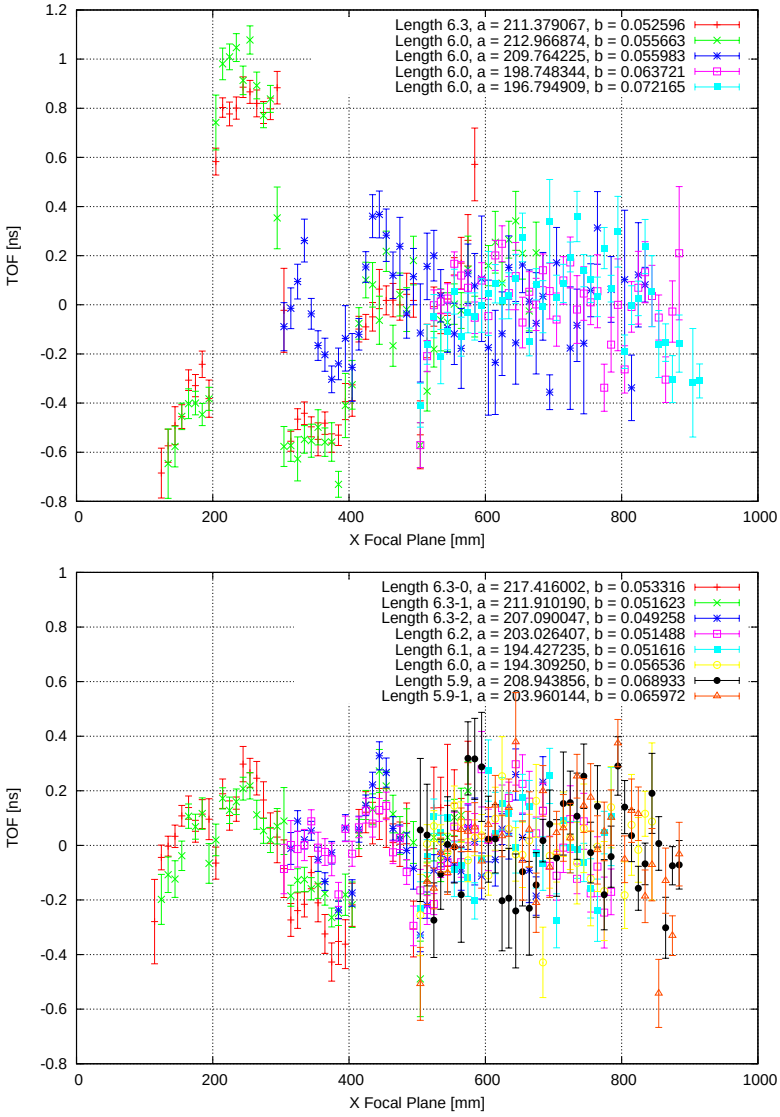

Figure 26: TOF versus the ion position at the focal plane. Top graph before the alignment and bottom graph after the alignment.

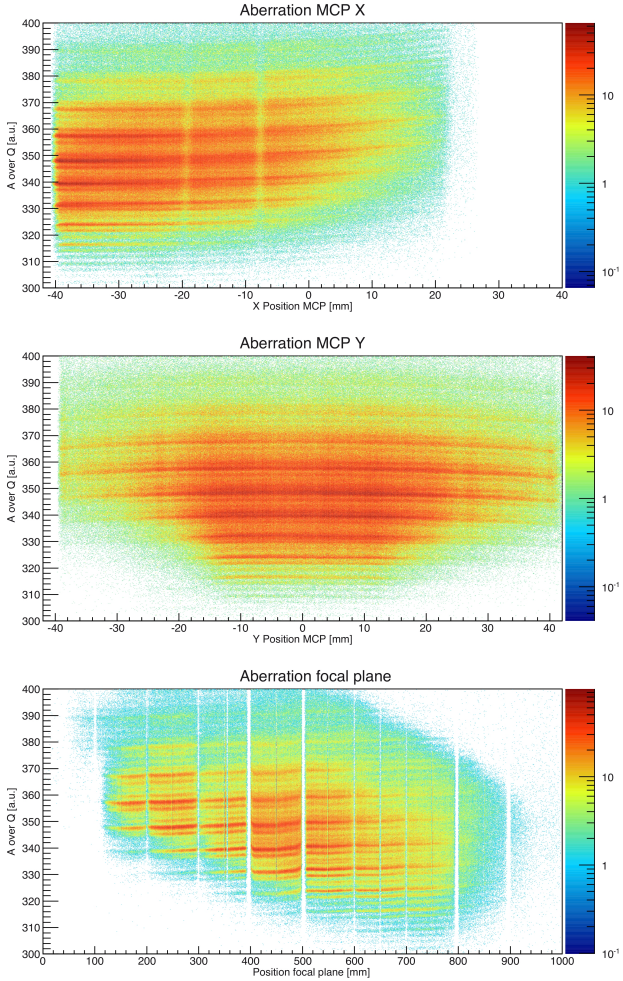

Figure 27: Aberrations are the reason for non-linear distortions in the 2D distributions of A over Q versus the X position on the MCP (top), A over Q versus the Y position on the MCP (middle) and A over Q versus the position on the focal plane MWPPAC detector (bottom) for $Z = 54$

polynomial function as input to correct the deviations. A 2D cut on one A over Q line from the plots in figure 27 is used to generate the input data. A root script, similar to the TOF alignment from the last section, was used to determine the slope of the 2D cut. The gnuplot program [73] fits a polynomial with degree 5 for MCP X and Y and a polynomial degree 7 for the position on the focal plane. In some cases additional points at the boundaries were used to make the fit results more stable. The procedure must be done step by step for the three aberrations, as they affect each other. The first correction is the correction for MCP X, then MCP Y and finally for X focal plane. The data points and the fit function are shown for section A in figure 28.

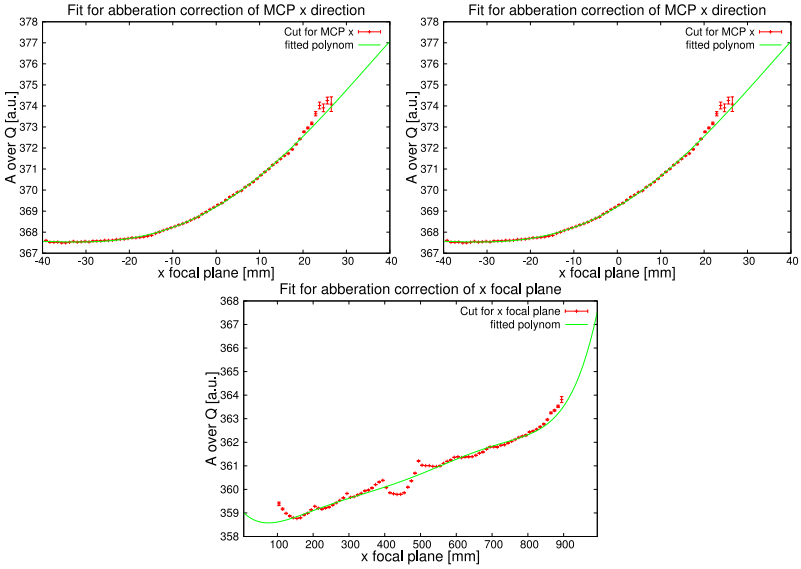

Figure 28: Polynomial fit for one A over Q value versus the X position on the MCP (top left), the Y position of the MCP (top right) and the position on the focal plane (bottom) for Z equal 54

This procedure was done for all different sections of the analysis in-

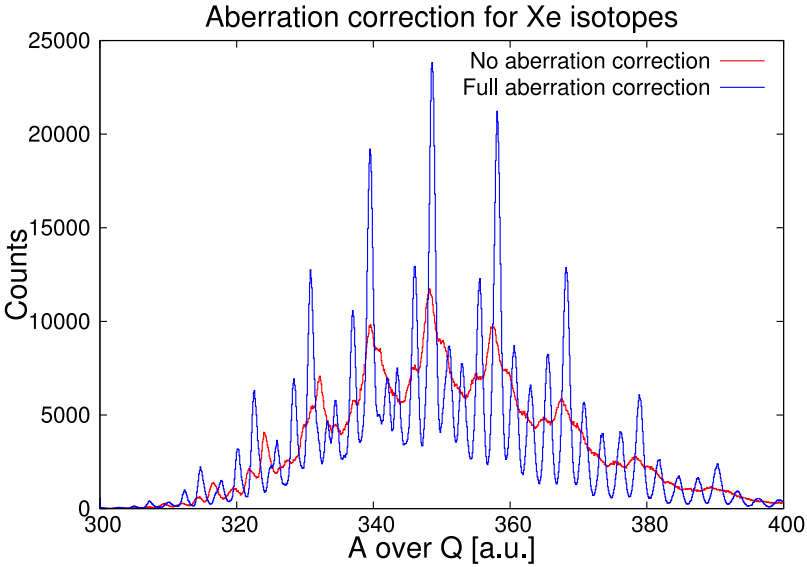

Figure 29: A over Q spectra before and after aberration correction for Xe isotopes.

dependently. The corrections were also done for every individual Z value. The importance of these aberration corrections and the improved mass separation is obvious from the two A over Q spectra shown in figure 29 where corrected and uncorrected results are compared.

3.5.5. Charge state identification

To identify the different isotopes of one chemical element the charge state Q of the atom passing the dipole magnet is multiplied to the A over Q value determined in the last section. The relation

$$\frac{E}{R\beta} \sim Q$$

with E as the total kinetic energy deposited in the ionization chamber is derived in [72] chapter 3. A 2D histogram relating the $E/R\beta$ ratio

shows different straight lines each one representing one charge state. Such a plot is shown in figure 30. The lines are not straight as the

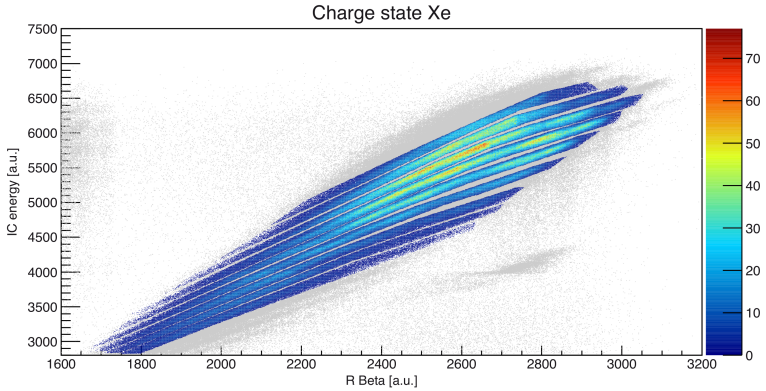

Figure 30: $R \cdot \beta$ related to E with a cut on Xe isotopes. The shown data is taken from the analysis section E. Grey points were outside the cuts.

aberration correction is affecting directly the A over Q value and not the trajectory reconstruction of the PRISMA manager. Nevertheless the lines are separated and the 2D cuts shown in figure 30 are used for the charge state identification.

3.5.6. Mass identification

In general the charge state Q is multiplied to the A over Q value event by event resulting in a mass distribution. This procedure did not result in a sufficient mass resolution as there is also a non linear behaviour visible. Therefore for each charge state the position of the beam like ^{136}Xe isotope was identified by the isotope γ signature and a linear fit between A over Q values and the mass numbers was done. In this way for every charge state Q two parameters were fitted and the corresponding A over Q value was transferred using a function like

$$M = a + b \cdot \frac{A}{Q}$$

The needed routines to do such an transfer were added to the PRISMA manager software. A over Q spectra for three different charge states from section C and the according fits are shown in figure 31.

As each charge states Q number is fitted it does not have to be the real charge of the ion, but an index that makes it unique. The ^{136}Xe signal is dominating the spectra, although for lower charge states the spectra are more balanced. The A over Q spectra for the different sections are slightly different, so the fits must be done for all Z numbers and sections separately. The calibrated mass spectra are shown in figure 32.

Section	$\frac{M}{\Delta M}$	FWHM
A	266.7 ± 0.3	0.5100 ± 0.0005
C	242.6 ± 0.4	0.5605 ± 0.0008
E	252.0 ± 0.3	0.5396 ± 0.0007
F	186.1 ± 0.3	0.7310 ± 0.0013

Table 7: Mass resolution values for ^{136}Xe detected at all position of the focal plane

Section	$\frac{M}{\Delta M}$	FWHM
A	349.4 ± 0.7	0.3892 ± 0.0008
C	315.4 ± 1.0	0.431 ± 0.001
E	295.4 ± 0.8	0.460 ± 0.001
F	278.4 ± 0.8	0.489 ± 0.001

Table 8: Mass resolution for ^{136}Xe for events with a position between 500 and 600 mm of the focal plane

Although the aberration correction improved the A over Q spectra and therefore the mass spectra a lot, there is still a strong relationship between the mass value and the focal plane position. Taking the best performing TAC of the MWPPAC (focal plane position 500 to 600 mm) the improvement of the mass resolution is up to 50 %. The mass resolution values are listed in table 7 for the complete MWPPAC

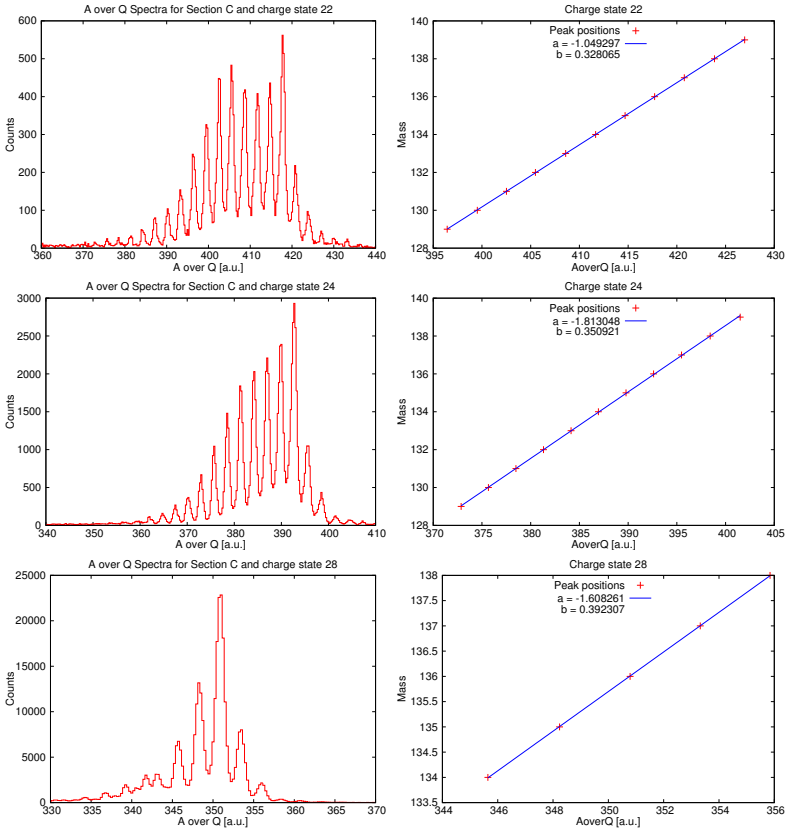

Figure 31: *A* over *Q* spectra (left) and the according fits to the mass number (right) for charge state 22 (top), 24 (middle) and 28 (bottom)

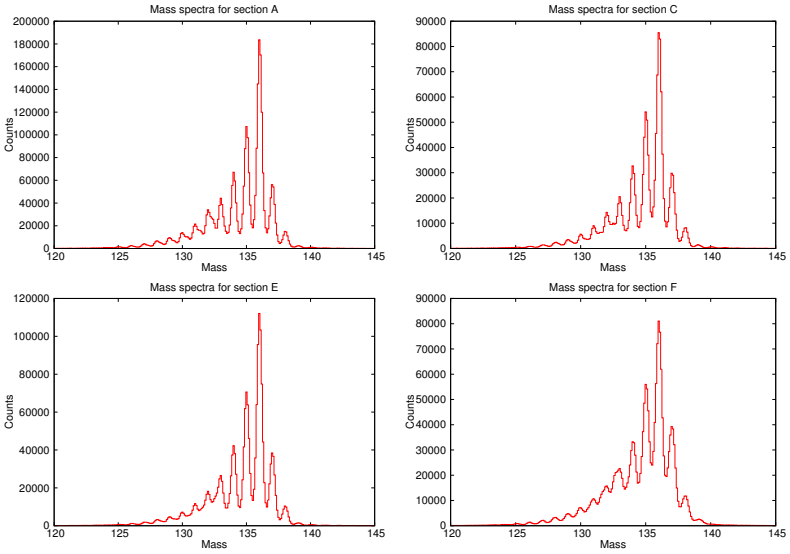

Figure 32: Mass spectra for Section A (top left), C (top right), E (bottom left) and F (bottom right)

and in table 8 for the best section of the MWPPAC. In histogram figure 33 the mass measurement is shown as a function of the position on the focal plane. Some sections of the MWPPAC are effected by bending or distortions. By utilizing 2D cuts, the total mass resolution is comparable to the best section of the MWPPAC.

In the region below mass $A = 133$ in figure 33 the resolution gets worse and a double structure appears. The same effect can be seen in the 1D mass spectrum in figure 32 as tailing of the peaks.

The final distribution of Xenon isotopes is listed and shown in table 9. The pickup of neutrons by the beam like particle drops rapidly and already for ^{139}Xe only a fraction of 0.6% with respect to the beam isotope ^{136}Xe were identified. The transfer of neutrons from the beam nuclei to the target nuclei is clearly favoured. For example for ^{128}Xe, that is 8 neutrons away from the initial isotope, still 2.1% were identified.

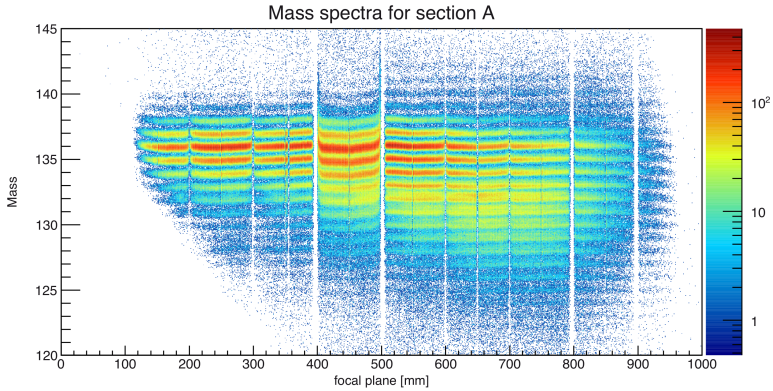

Figure 33: Mass function related to the position of the focal plane with a cut on Xe isotopes. This spectrum is used to select the masses by applying 2D cuts.

After the full identification of the single ions passing PRISMA the following information is available for the further analysis:

- the direction and the magnitude of the velocity vector
- the A and Z number of the ion
- the energy of the ion

This information will be used in the following chapters to analyse the data related to the AGATA demonstrator and in-beam γ-ray spectroscopy.

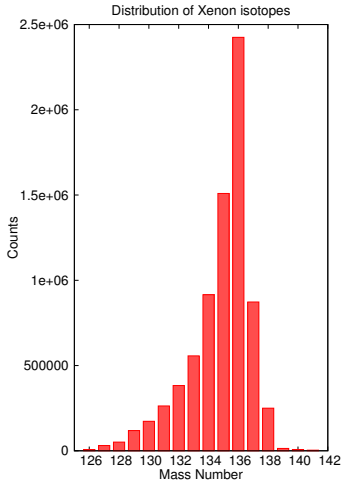

Xe isotope	Counts	Proportion
126	7300	0.3
127	30833	1.3
128	50935	2.1
129	118278	4.9
130	173048	7.1
131	263162	10.9
132	382781	15.8
133	556940	23.0
134	915442	37.7
135	1509140	62.2
136	2425030	100.0
137	872634	36.0
138	250071	10.3
139	13973	0.6
140	7536	0.3
141	3689	0.2

Table 9: Mass distribution for the beam like Xe isotopes after the complete PRISMA analysis

3.6. In-beam spectroscopy with AGATA

AGATA is the first γ-ray spectrometer based on digital pulse shape processing. It does not acquire the same information like spectrometers with analogue electronics and therefore needs new and special routines to process the data. The pre-processing electronics [8] applies the moving window deconvolution (MWD) algorithm [74, 75] on the incoming data streams from the digitizer to determine the γ-ray energy deposited in each segment and the whole crystal. The energy calibration is then done in the producer actor of the NARVAL system.

The time information have to be extracted from the digital signals. It is important for the event building, the γ-ray tracking and for the coincidences of particles and multiple γ-rays. The signals are not shaped, because the information needed for the PSA is in the leading edge of the detector signals. There is an inherent problem to acquire time information from signals which are not shaped with the techniques known from analogue electronics. The digitizer samples with a 10 ns interval and leading edge timing of the digitized signals is not sufficient. Therefore new techniques were developed and used to determine the time information of the signals. The different time signals have to be aligned at different points of the analysis. This is done by changing the configuration files of the different actors of the NARVAL system.

Different types of event multiplicity can be defined in a highly segmented detector array with PSA and γ-ray tracking. Four types are available: (i) the number of gamma rays determined by the γ-ray tracking algorithm, (ii) the number of hits determined by the PSA algorithm, (iii) the number of hit segments and (iv) the number of hit detectors. The PSA is described in section 2.1 on page 17. The Doppler correction for the beam and target like particles is done by the treegen program and the optimization of the Doppler correction with the PostAnalysis program.

3.6.1. Time alignment of the array

A good time resolution for the prompt coincidence between the ancillary detectors and AGATA is needed to suppress background radiation. The observed count rates during the experiment were up to

50 kHz per crystal. Most of the measured radiation was background from Coulomb excitation and fission of the ^{238}U target. Furthermore a good timing is important for the event building, the γ-ray tracking and for the $\gamma\gamma$ analysis. The huge amount of signals require robust procedures for an efficient time calibration of the complete array. Three different steps are needed to get the optimal time resolution of the AGATA detectors: (i) Alignment of segment and core signals, (ii) alignment of detector signals to the PSA database and (iii) alignment between the different AGATA detectors.

The first step is the alignment of the segment signals to the core signal for every detector on a detector level. The calibration run with a ^{60}Co source is replayed and the pre processing filter generates the time signals for segment and core electrodes using a simple leading edge filter[19]. This first step is needed to get a coarse alignment of the different signals. Then all the time peaks of the segments are fitted and shifted, so that the peak centroid of the distributions lie upon each other. This procedure is repeated with a new time filter. The filter adds the net charge signals of the core and the segments. Due to the segmentation of the detector the leading edge of the core and segment signals have a different bending. The sum of the hit segment and the core electrodes is in a good approximation a straight line. This line is fitted and the crossing point of the line with the base line is taken as time zero. This methods gives a better time information than the 10 ns binning of the sampled signals. In a first order it is also independent of the energy. In figure 34 an example of the time spectra relative to the core of each detector in ATC 2 are shown. The time signals of the segments of the different detector types are in red (A type), green (B type) and blue (C type).

In the second step the comparison between simulated data of the PSA libraries and the experimental data is investigated. In order to find the best match, the PSA algorithm shifts all the experimental data in time until the best agreement is found. This procedure is important, as the PSA relies on a minimized FOM value, which should not depend on time offsets of the signals. The shift value is reported for every event. Histograms showing the shift value for every segment give a good hint, how off the experimental data is compared to the simulated data. To

[19] See for example [1] page 681

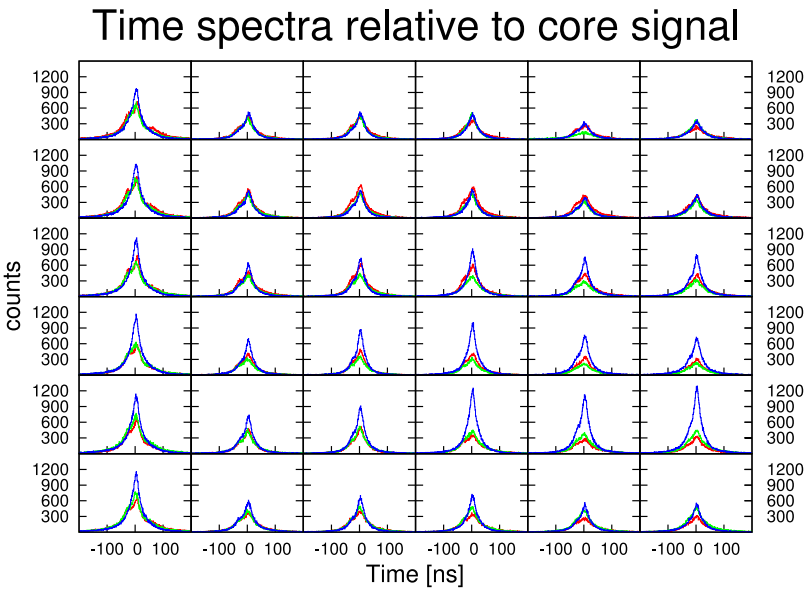

Figure 34: Time spectra for the segments of the detectors in ATC 2 relative to the core signal. The red, green and blue lines correspond to the A, B and C type detectors in the ATC 2.

find a minimal shift the complete signal set including all segments and the core signals are moved in time and the same histograms are generated again. In the right plot of figure 35 the peak centroid position of these histograms for different total time shifts are plotted for all segments of the red (A type) detector in ATC 2. In the left plot of figure 35 a mean value of the peak centroids of segment signals is calculated and plotted. A shift value of zero is interpolated by a linear fit for every detector. This value is then used as a parameter for the configuration. The PSA algorithm will still try to find an optimal match, but with this configuration it is assured, that the starting conditions are optimal.

The last step aligns the different core signals after the PSA. A sophisticated procedure [76] is applied to match all 15 detectors. The

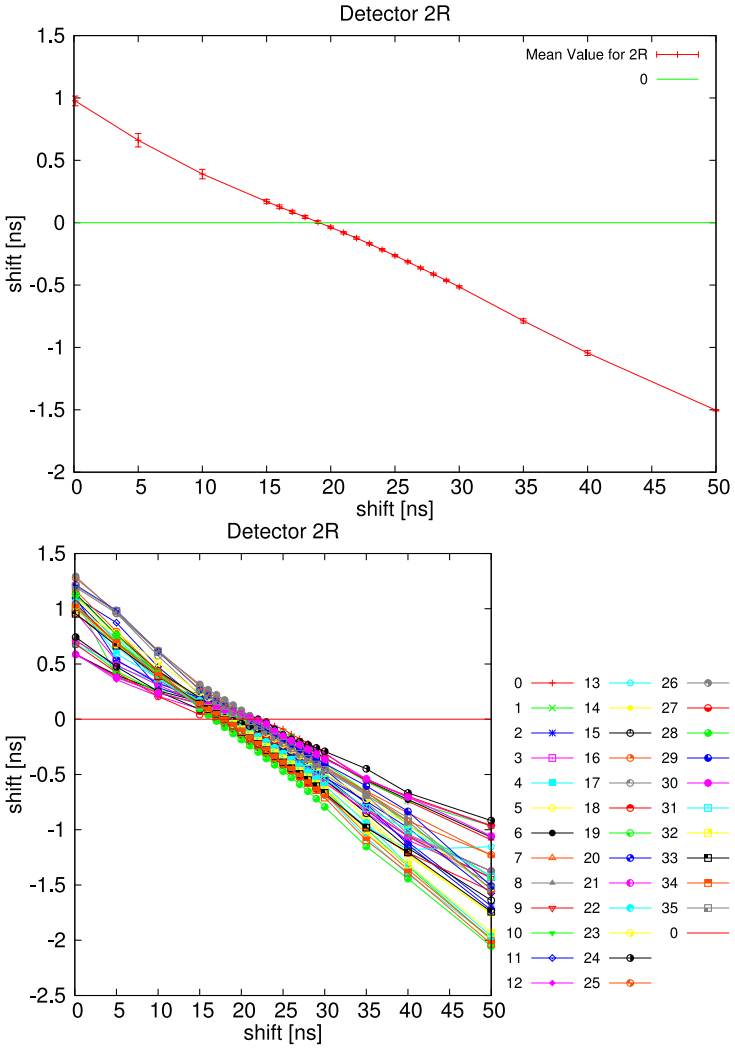

Figure 35: Time shift applied to the segment times by the PSA alogrithm in relation to the shift time sift for the red (A type) detector in ATC 2. In the right plot all segments are shown individually, in the left plot a mean value of all segments is plotted.

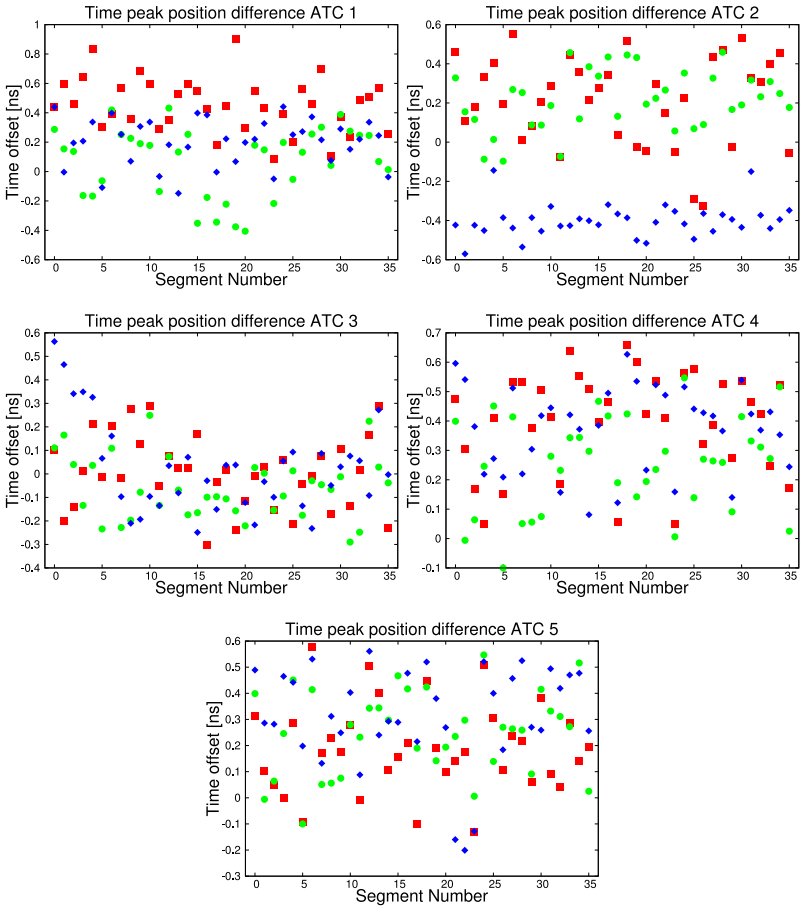

Figure 36: Offset of time peak centroid positions for the segments relative to the aligned cores for all ATCs. The red, green and blue lines correspond to the A, B and C type detectors in the ATC.

time signal of each core against the other ones are summed in 225 spectra. A fit to get the peak position is then put in a 15×15 matrix D. The matrix D is extended by one row where all entries are 1.0. This results in a control sum in the 16^{th} entry of $\vec{B}$. The vector $B_j = \frac{\left(\sum_i^{15} D_{ji} - \sum_i^{15} D_{ij}\right)}{2}$ is used to fit a least square solution of the linear matrix equation

$$\begin{pmatrix} -14.0 & 1.0 & ... & 1.0 \\ 1.0 & -14.0 & ... & 1.0 \\ \vdots & ... & \ddots & \vdots \\ 1.0 & 1.0 & ... & -14.0 \\ 1.0 & 1.0 & ... & 1.0 \end{pmatrix} \times \begin{pmatrix} x_1 \\ x_2 \\ \vdots \\ x_{15} \end{pmatrix} = \begin{pmatrix} B_1 \\ B_2 \\ \vdots \\ B_{15} \\ SUM \end{pmatrix}$$

utilising a computer program. The resulting vector $\vec{x}$ is the global time shift for every core signal. This information is then written in the configuration needed for the replay. The total time offset of every segment signal in relation to the aligned core values is shown in figure 36.

The iterative time alignment procedure improved the prompt timing peak between AGATA and PRISMA as shown in figure 37. The shown peak is already corrected for the time of flight inside the PRISMA spectrometer and for a shift in the trigger system, where three out of ten MWPPAC sections triggered 20 ns later. The FWHM of the red peak is 28.9 ns and of the blue peak 24.0 ns. A similar plot is generated by only taking events, where the A and Z number was identified in PRISMA. For the time resolution a value of 15.7 ns (FWHM) was finally achieved for the analysis.

3.6.2. Energy calibration

Calibration measurements are needed to acquire the right calibration parameters and to get energy resolutions as a standard for the comparison with in-beam data. The calibration procedure is inflated by the number of energy signals of the system (570). The energy calibration depends on the digital filter settings which needed to be changed during the experiment to achieve an optimal energy resolution of the system. The shaping time of the Moving Window Deconvolution (MWD) algorithm was changed during the experiment from

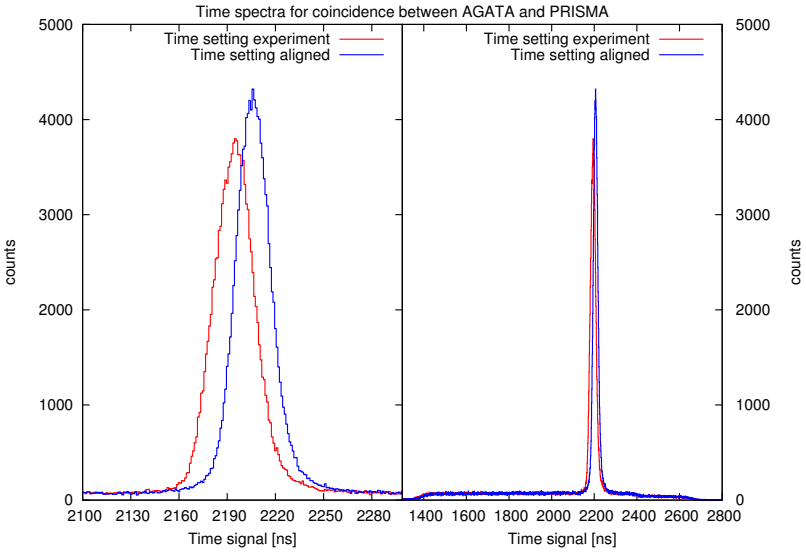

Figure 37: Prompt time signal between AGATA and PRISMA corrected for time of flight for the initial and final alignment of AGATA

2.5 μs to 5 μs. A correction for neutron damage was applied with the parameters adapted from the online analysis. The resolution of two source runs done after the experiment with PSA and tracking is shown in figure 38. The lines correspond to a measurement with a ^{152}Eu source and the dots to a measurement with a ^{60}Co source. The red line is the energy resolution (FWHM) of the tracked spectrum when only the segment energy information is taken into account. The highly segmented detectors show very small signal amplitudes below the threshold which distort the line shape and reduce the energy resolution. A simple solution to avoid this behaviour is to force the energy sum of the segments within one detector to the energy registered in the corresponding core electrode. The missing energy is distributed between the hit segments. This improves the energy resolution of the tracked spectrum as shown by the green data. Some not well cali-

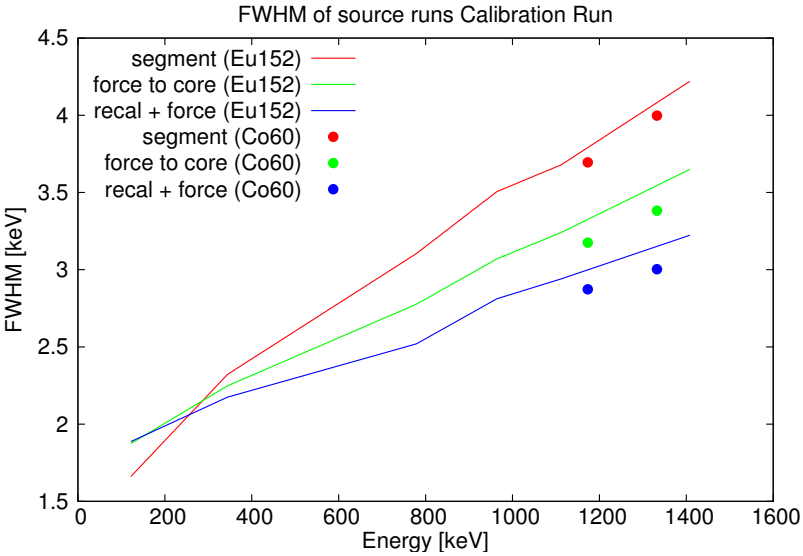

Figure 38: Energy resolution (FWHM) of a source run with ^{152}Eu (line) and ^{60}Co. The red data is tracking with the segment energy information. The green data forces the segment sum in the tracking to the core energy value. The blue data was generated using the same algorithm as the green data but with a recalibration of some segments and cores.

brated cores and segments were adjusted to the right values resulting in the energy resolution (FWHM) shown in blue.

The energy resolution in the final spectra of the experiment was worse after applying the method of forcing the energy of the core than for the simple segment tracking. This was due to the high count rate during the experiment that causes a worse energy resolution of the core. Finally the recalibrated channels with the tracking using only the segment energy information resulted in the best resolution for the analysis of the experiment.

3.6.3. Relative efficiency

In order to quantify the intensities of γ-rays one needs an energy dependent efficiency calibration. For this reason a measurement with a ^{152}Eu source was done just after the experiment. In the spectrum of the source run many lines and random background from activated material shows up. To reduce the influence of the background, background peaks near or within the ^{152}Eu lines were fitted simultaneously with the ^{152}Eu lines. The major lines of the ^{152}Eu source after passing the tracking actor were fitted twice with different background treatment. The first fit takes a broader fit area with many background peaks, the second one takes a small fit area. The difference between the two areas calculated by the fit is then taken as an error estimation. To calculate the relative efficiency the area calculated by the first fit is divided by the area of the peak at 1408 keV and multiplied by the relative intensity taken from [77].

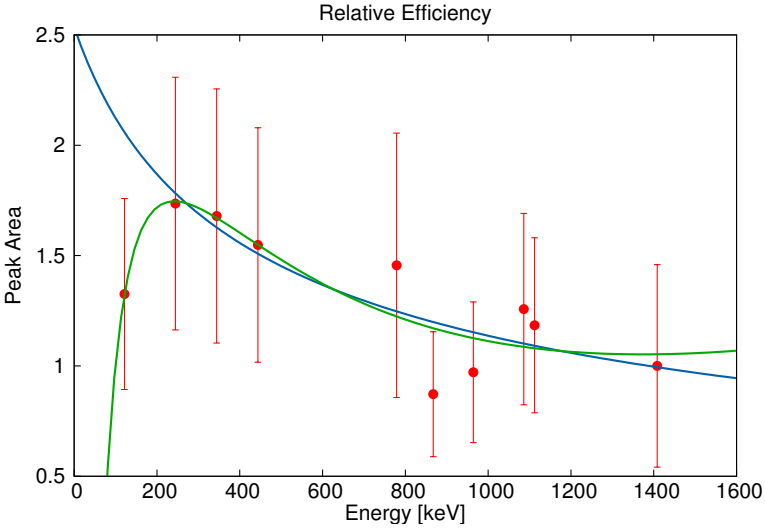

Figure 39: Relative intensity normalized to 1408 keV of ^{152}Eu after tracking. The blue line corresponds to a fit of the function (3), the green line to a fit of the function (4).

In this way the peak at 1408 keV shows up as a one in the plot shown in figure 39. A first function

$$\epsilon(E_\gamma) = \kappa E_\gamma^b + c \tag{3}$$

colored in blue and a more complex second function

$$\epsilon(E_\gamma) = \sum_{i=0}^{4} a_i (\ln E_\gamma)^i \tag{4}$$

were fitted to the data and are shown in figure 39. It is clear that function (3) is not able to treat the low energy part, however it seems to behave more realistic at higher energies. Function (4) treats the low energy part better, but at higher energies it rises again. However, values from this energy region were not used for this analysis. The absolute efficiency of the array was measured in [78] for the lines of a ^{60}Co source.

3.6.4. Gamma multiplicity

In the AGATA analysis four different types of multiplicities are generated. The first one is the number of crystals that registered a coincident energy deposition. It is comparable to a classic definition of multiplicity in detector arrays where only core electrodes were read out. A second one is the number of hit segments. A third one is the number of hits passed to the tracking algorithm. For the used PSA algorithm this number is equal to the number of segments that registered a coincident γ-ray. However with PSA algorithms capable of detecting multiple interactions within one segment, the number of hits could be greater than the number of segments with energy depositions. The fourth type of multiplicity is the most interesting one. It is the number of gamma rays emitted by the source that were measured by the detector system. This number is determined by the tracking algorithm, where multiple interactions in the detector are combined to different γ-rays. The tracking algorithm rejects not well reconstructed events.

In figure 40 the multiplicity distribution of the experiment is shown. The left plot shows the complete experiment without any gates or

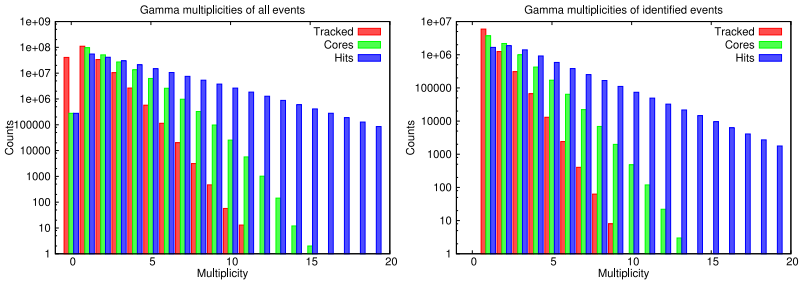

Figure 40: Multiplicity of γ events for the complete experiment (left) and for the events identified in PRISMA (right). Tracked (red) data is the multiplicity after the PSA and tracking, Core (green) data is the number of core electrodes with coincident interactions and Hits (blue) the number of coincident hits after the PSA

cuts. The multiplicity after PSA and tracking is shown in red, the hit multiplicity after PSA in blue and the multiplicity of core signals in green. The right plot shows the multiplicity of events that were identified in the PRISMA analysis. Here the events without any γ after the tracking are sorted out. In the PRISMA trigger events with no γ-rays were also accepted to have more statistic available for the PRISMA analysis and to be independent from the AGATA efficiency. Although a condition in the replay asked for a coincidence between AGATA and the ancillary detectors some events without a γ-ray were taken. However it can be seen, that many events are rejected by the tracking algorithm, as the number of zero γ-ray multiplicity rises in the tracked multiplicity compared to the core and hit multiplicity. There are more 1-fold events in the tracking multiplicity as in the core or hit multiplicity. These are events, where the tracking algorithm successfully identified Compton scattering, even over the single detector boundaries. There are also more 1-fold events for the core compared to the hits. These are events where due to Compton scattering the energy was deposited in more than one segment of a single detector. For the 2-fold events the core and hit multiplicities already have more events than the tracking multiplicity. In the 3-fold events

the hit multiplicity shows more events than the core multiplicity. The core multiplicity drops down and stops at 15, as only 15 detectors were used. The hit multiplicity constantly drops down to 40. The highest tracking multiplicity is 11 for the complete experiment and 9 for the events identified in PRISMA.

3.6.5. Doppler correction

γ-rays emitted in flight by fast moving particles are shifted in their energy in the laboratory frame due to the Doppler effect. The Doppler shift of the energy depends on the velocity β of the particle and the emission angle θ of the γ-ray with respect to the velocity vector of the particle.

$$E_\gamma = E_{\gamma_0} \frac{\sqrt{1-\beta^2}}{1-\beta\cos\theta}$$

E_γ is the energy registered by the detector in the laboratory system and E_{γ_0} is the transition energy in the center of mass system of the nucleus neglecting a small recoil energy of the nucleus. The Doppler correction requires θ, β and E_γ. These three quantities are determined for every event from the PRISMA spectrometer and AGATA. The velocity vector of the emitting ions is measured by the reconstruction of the path the ion takes through the spectrometer and the time difference between the entrance MCP and the MWPPAC. An improved Doppler correction is possible in this experiment due to the position sensitivity of the AGATA detectors. The angle between the emitted γ-ray and the flight direction of the ion is given by the first interaction of the γ-ray with AGATA determined by the PSA and tracking algorithm and the interaction position of the ion on the entrance MCP of PRISMA. In this way the remaining Doppler broadening due to the unknown opening angle of the emission cone is limited in the AGATA detectors by the overall position resolution of the PSA and tracking method. The result of the energy resolution after Doppler correction is one of the most sensitive measures to prove the position sensitivity and its quality from the remaining Doppler broadening. Consequently very great care was given to a detailed analysis of the Doppler correction in order to understand and to improve the PSA and γ-ray

tracking procedure under real experimental conditions at high velocities and considerable Doppler shifts in the following section.

3.6.6. Kinematics of binary reactions

In this experiment a binary reaction of the target material and the beam is investigated. The lighter beam like Xe particle is called ejectile and the heavier target like U particle is called recoil. The ejectiles are identified in PRISMA and have a mean value of $\beta = 0.087$. The recoils have a mean value of $\beta = 0.049$. So for both reaction products a different Doppler correction has to be applied to correct for γ-rays emitted from one of the two different reaction partners.

The velocity vector for the ejectile is just given by the line between the target position and the interaction point on the MCP with a magnitude proportional to β. For the target or recoil nucleus a kinematic calculation has to be done. The beam (B) is shot on the target (T) particle and the resulting particles are the light ejectile (E) and the heavy recoil (R) scattered in the reaction plane. In the following calculation θ is the angle between the ejectile and the beam axis. φ is the angle between the recoil and the beam axis. Classical momentum conservation results in the following equalities:

$$\begin{aligned} p_\mathrm{B} &= p_\mathrm{E}\cos\theta + p_\mathrm{R}\cos\varphi \\ p_\mathrm{T} = 0 &= p_\mathrm{E}\sin\theta + p_\mathrm{R}\sin\varphi \end{aligned} \tag{5}$$

and energy conservation yields:

$$E_\mathrm{B} + Q = E_\mathrm{E} + E_\mathrm{R} + E_x \tag{6}$$

with $Q = m_\mathrm{B} + m_\mathrm{T} - m_\mathrm{E} - m_\mathrm{R}$ as the Q-value of the reaction between the ground state configurations and E_x as the excitation energy of the particles after the reaction. Squaring, rearranging and adding equation (5) results in

$$p_\mathrm{B}^2 + p_\mathrm{E}^2 - 2p_\mathrm{B}p_\mathrm{E}\cos\theta = p_\mathrm{R}^2$$

Using the kinetic energy

$$E_\mathrm{B} + Q - E_x - \frac{p_\mathrm{E}^2}{2m_\mathrm{E}} = \frac{p_\mathrm{R}^2}{2m_\mathrm{R}}$$

and combining the last two equations a quadratic equation is obtained

$$p_{\mathrm{E}}^2\left(1+\frac{m_{\mathrm{R}}}{m_{\mathrm{E}}}\right)-2p_{\mathrm{E}}p_{\mathrm{B}}\cos\theta+(p_{\mathrm{B}}^2-2m_{\mathrm{R}}(E_{\mathrm{B}}+Q-E_x))=0$$

which shows the following two solutions:

$$p_{\mathrm{E}}=\frac{2p_{\mathrm{B}}\cos\theta\pm\sqrt{4p_{\mathrm{B}}^2\cos^2\theta-4\left(1+\frac{m_{\mathrm{R}}}{m_{\mathrm{E}}}\right)(p_{\mathrm{B}}^2-2m_{\mathrm{R}}(E_{\mathrm{B}}+Q-E_x)}}{2\left(1+\frac{m_{\mathrm{R}}}{m_{\mathrm{E}}}\right)} \tag{7}$$

$$E_{\mathrm{E}}=\frac{p_{\mathrm{E}}^2}{2m_{\mathrm{E}}} \tag{8}$$

$$\varphi=\arcsin\left(\frac{p_{\mathrm{E}}}{p_{\mathrm{R}}}\sin\theta\right) \tag{9}$$

$$E_{\mathrm{R}}=E_{\mathrm{B}}+Q-E_x-E_{\mathrm{E}} \tag{10}$$

$$p_{\mathrm{R}}=\sqrt{2m_{\mathrm{R}}E_{\mathrm{R}}} \tag{11}$$

As a crude assumption one may neglect the excitation energy E_x to calculate the velocity and the angle for the Doppler correction of the recoil. However, the β of the ejectile and the angle θ is measured by PRISMA. With this experimental information (the angle θ, the β value, the known Q-value) from PRISMA the excitation E_x can be determined experimentally.

The PRISMA manager library has a built in routine to calculate the binary partner[20]. This routine has some more features. It uses the relativistic version of the formulas that were derived above. Furthermore it simulates the energy loss of the ions through material (the target, some windows of PRISMA) and it calculates an effective Q_r value. The calculation of the Q_r value is similar to the one proposed in [79].

$$Q_r=\frac{m_{\mathrm{R}}+m_{\mathrm{E}}}{2m_{\mathrm{R}}m_{\mathrm{E}}}p_{\mathrm{E}}^2-\frac{m_{\mathrm{R}}-m_{\mathrm{B}}}{m_{\mathrm{R}}}E_{\mathrm{B}}-\frac{1}{m_{\mathrm{R}}}\sqrt{2m_{\mathrm{B}}E_{\mathrm{B}}}p_{\mathrm{E}}\cos\theta$$

with the momentum p. In this analysis the routines from the PRISMA manager were used.

[20] Added by Philip John

3.6.7. Optimization of the Doppler correction

Based on the PRISMA data for the measured ejectile and the binary partner calculation a Doppler correction can be done. After a first analysis without any optimization the energy resolutions of the AGATA detectors after Doppler correction was completely insufficient and even the peak centroid position after correction was not right. For example in the analysis of beam time section C the energy resolution was 7.24(33) keV (FWHM) and the peak centroid was shifted by 4 keV to 1317.27(14) keV compared to 1313.02 keV from the literature. It became obvious that some experimental values related to the position and geometry of the experimental set up were not determined properly or modified before/after the experiment. From the PRISMA data analysis it became clear that moving the MCP position could improve the result of the Doppler correction. The β value given by PRISMA is well aligned, however an absolute time off-set cannot be excluded due to shifts in the measuring electronics. Furthermore the position of the PRISMA windows potentially also shifts the β values slightly. The overall distance (the z position) of the AGATA array with respect to the incoming beam axis was not controlled carefully after each target change and could also be slightly off. The detector is moveable in this direction and already small deviations distort the Doppler correction significantly. In summary the following four parameters were crucial for best energy resolution after the Doppler correction:

1. The position measured by the MCP in x direction
2. The position measured by the MCP in y direction
3. The β value measured by PRISMA
4. The z position of AGATA

Even more uncertainties, like the position of the beam on the target or the angle and energy straggling of the recoiling nuclei passing the target and backing material do affect the Doppler correction but cannot be varied and optimized.

To perform the best Doppler correction a small variation of these parameters within reasonable limits was done to extract an optimal parameter set of these four values. To illustrate the behaviour of

the spectra the dependence of the Doppler correction on the parameters are illustrated in figure 41. Only events with ^{136}Xe identified in PRISMA were taken into account. The region around the decay of the first 2+ state of ^{136}Xe with an energy of 1313.02 keV is zoomed. By varying the x value of the PRISMA MCP mainly the energy resolution (FWHM) of the peak is affected and only small shifts in the energy are visible. The same effect, but less pronounced, is visible for the y value of the PRISMA MCP. Changing the z position of AGATA is not affecting the energy resolution (FWHM) strongly. But the position

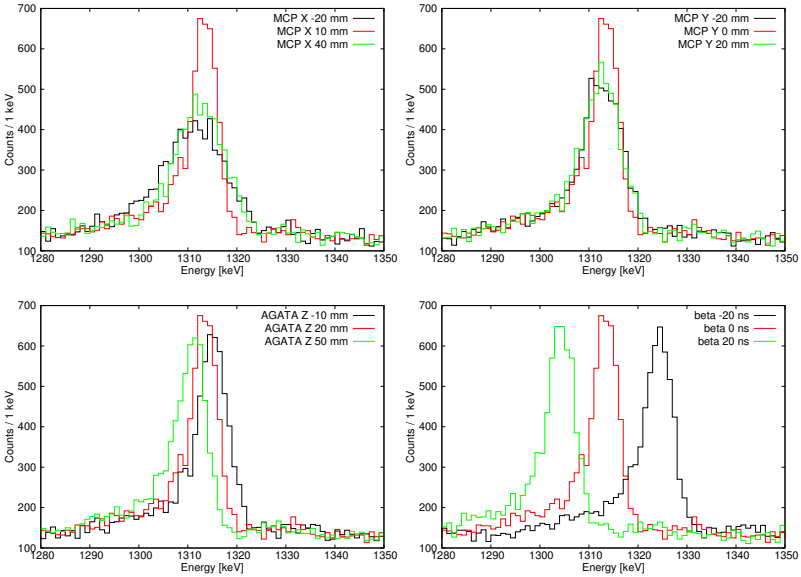

Figure 41: The Doppler corrected γ-ray spectra of ^{136}Xe identified in PRISMA is plotted for different parameters. The region around the decay of the first 2+ state with an energy of 1313.02 keV is zoomed. The behaviour of the Doppler correction for a variation of the x value of the PRISMA MCP (top right), the y value of the PRISMA MCP (top left), the z position of AGATA (bottom left) and the β determined by PRISMA (bottom right) is shown.

of the peaks are shifted. The variation of the β value is shifting the peak position a lot, while the energy resolution (FWHM) is changing only slightly.

The first 2+ state of ^{136}Xe decays emitting a γ of 1313.02 keV. This peak position and its width is used as a reference, to determine the quality of the Doppler correction for the ejectile. The target is made of ^{238}U that emits γ-rays with 158.8 keV, 211 keV, 257.8 keV and 300.6 keV. These peaks are well present in the spectra and used as a reference for the target like particles. For the optimization not only the position should be reproduced, but simultaneously the energy resolution of the peak has to be minimized.

The four parameters can be varied and the parameters depend on each other. This requires a sorting code, that changes the parameter and calculates the resulting corrected γ energy on an event-by-event basis. The sorting code was set up only to look at events that are identified by PRISMA as ^{136}Xe. The code loops for every event over any combination of shifts, that are fed into the system by defining a range and a number of steps this range is divided into. For every combination a spectrum is hold in memory and filled with the results of the Doppler correction for the ejectile like particles and the target like particles. This can be done in parallel, as the results are independent. A normal run was divided for every parameter into 21 steps and therefore $21^4 = 194481$ different combinations were investigated. As the code could run in parallel a locking mechanism for accessing the spectra is implemented. Tests with one lock for write access for the spectra did not perform well, as all threads were waiting for access. Therefore a lock for every spectra is generated. The probability to access a locked spectra drops as there are 194481 spectra but only a maximum number of 32 threads. The scalability of the code was tested for different numbers of used threads on a server node with 2 Intel(R) Xeon(R) CPU E5-2670 each providing 8 cores and 16 threads. For 0.2 million events the code was run with 2, 4, 8, 16 and 32 threads to test its performance. The result is shown in figure 42. The relative time is the number of threads multiplied with the real time divided by twice the time needed with 2 threads. The more threads are used the faster runs the program, but at a certain number of threads the time needed for waiting and locking is so long, that the performance

becomes constant. However the gain of time for the first 16 threads is high and made it possible to do calculations within reasonable times.

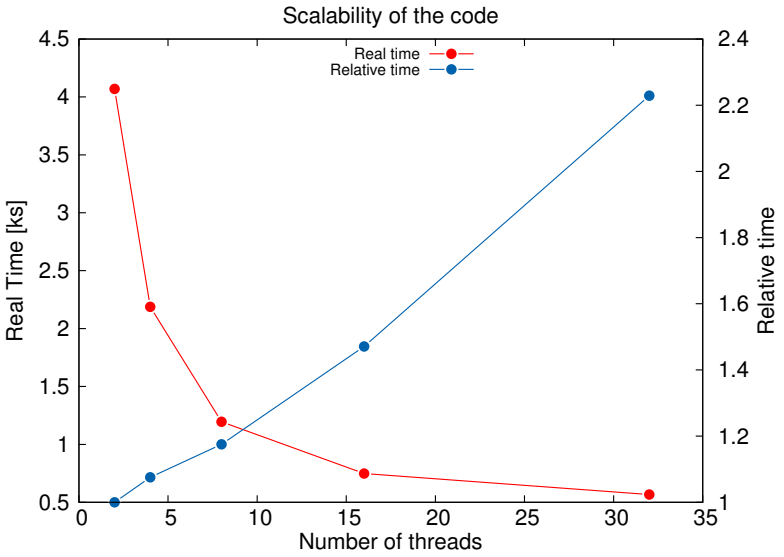

Figure 42: Scalability of the code for parallel processing of 0.2 million events

Once the calculation was finished the resulting spectra were analysed. A fit program [76] capable of searching a peak in a provided region of the spectra was used. The program fits the peak and calculates the shift of the peak centroid with respect to a given energy. The results are long lists for five peaks each one containing all the data of the fit. If the peak is shifted out of the provided region or if it cannot be fitted, the program does not report it. In order to analyse and to look at the data it has to be visualized. This is done by a developed program that generates ROOT trees out of the results. The ROOT trees can then be plotted and analysed with the methods and routines available in ROOT [69].

To find the optimal parameters a first run takes a wide range of shifts as listed in table 10. The results are illustrated in figure 43. By

parameter	index	range	steps
x_{MCP}	I	$-100 \rightarrow 100\,\mathrm{mm}$	21
y_{MCP}	J	$-100 \rightarrow 100\,\mathrm{mm}$	21
z_{AGATA}	K	$-100 \rightarrow 100\,\mathrm{mm}$	21
TOF_{PRISMA}	J	$-100 \rightarrow 100\,\mathrm{ns}$	21

Table 10: Parameters for the first calculation with very extended regions

fixing two parameters the variation of the other two parameters and the resulting FWHM are shown. In the top left plot the variation of the x and y position measured by the entrance MCP of PRISMA is shown. A shift of the x parameter improves the FWHM. However it is not enough to look at the energy resolution. The top left plot in figure 44 shows the absolute deviation of the peak center compared to the literature value. It is clear, that the parameters resulting in the minimum FWHM do not result in the right energy. To solve this problem the other parameters have to be varied too.

The same analysis has to be done for the recoil spectra. Here not only the Doppler correction but also the kinematic calculation is introducing a new source for errors. To find an optimal parameter set the data from the recoil and ejectile calculation were combined and only those parameter combinations with an energy shift below 0.5 keV are taken into account. The FWHM also depends on the energy of the γ-ray, but only the error from the Doppler correction is interesting. Therefore an estimated error from the energy and the electronic noise [13] are subtracted from the FWHM.

$$\mathrm{FWHM}_D = \mathrm{FWHM} - \sqrt{(2.355 \cdot \sqrt{F \cdot E_{\mathrm{EH}} \cdot E_\gamma})^2 + E_{\mathrm{N}}^2} \qquad (12)$$

Here $F = 0.129$ is the Fano factor, $E_{\mathrm{EH}} = 2.96\,\mathrm{eV}$ is the mean energy needed to create an electron hole pair in the Germanium detector and $E_{\mathrm{N}} = 1\,\mathrm{keV}$ is the contribution from the electronic noise. This is the theoretical limit of the energy resolution. In an in-beam experiment

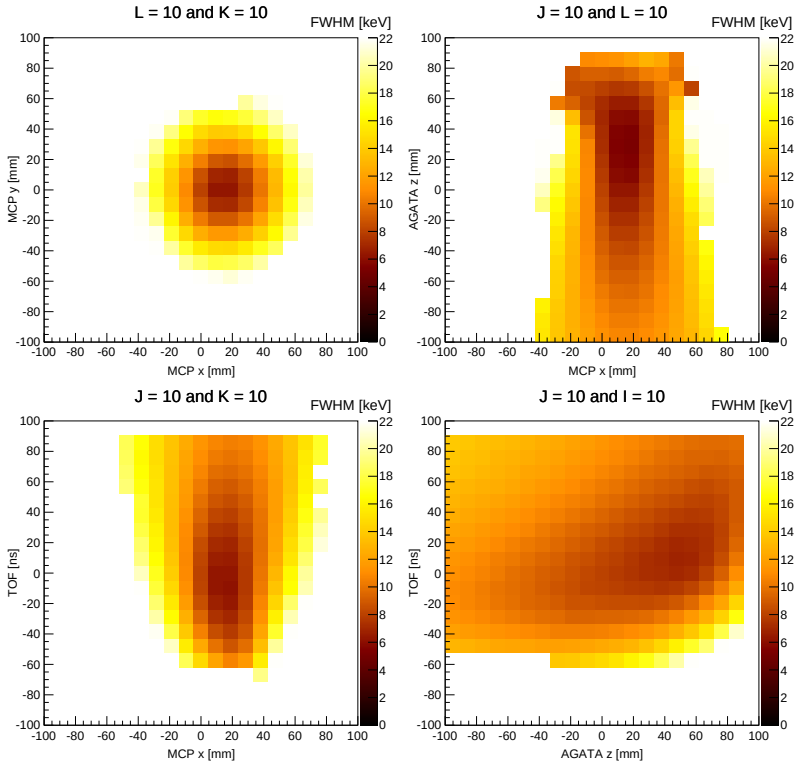

Figure 43: 2D plots showing the FWHM of the ^{136}Xe peak depending on the variation of the parameters for section A

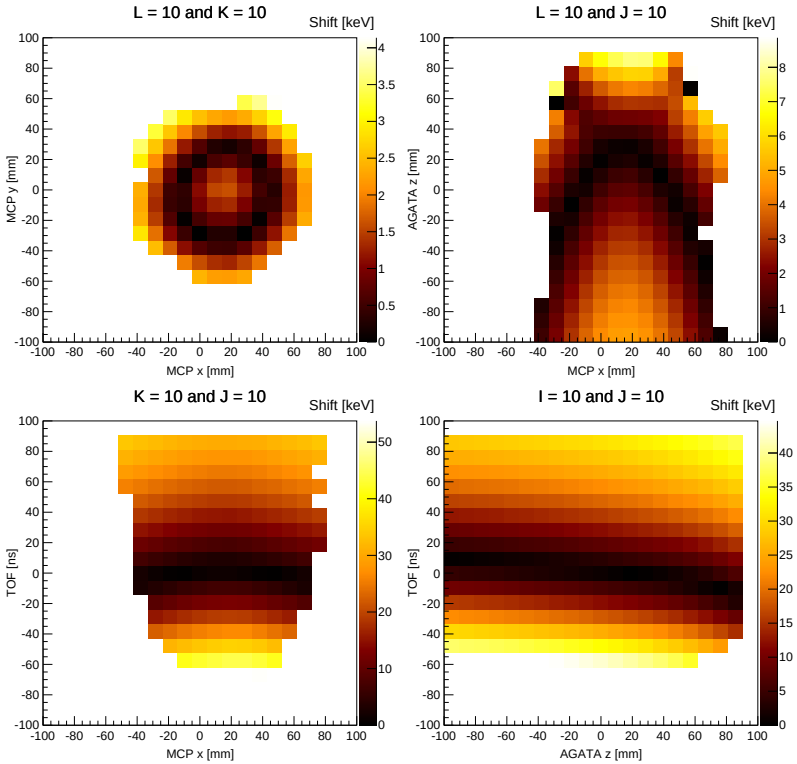

Figure 44: 2D plots showing the absolute shift of the ^{136}Xe peak depending on the variation of the parameters for section A

with high count rates the FWHM will be worse. Furthermore the energy is in general the sum of multiple interactions in the detector. As described in the energy calibration section this is worsening the resolution. To combine the results the FWHM_D values of the recoil and of the ejectile are added and a minimum of this sum was searched in the data. The results of the first iteration for the minima are listed in table 11.

parameter	section	index	value	section	index	value
x_{MCP}	A	11	10 mm	E	11	10 mm
y_{MCP}	A	10	0 mm	E	10	0 mm
z_{AGATA}	A	13	30 mm	E	11	10 mm
TOF_{PRISMA}	A	10	0 ns	E	10	0 ns
x_{MCP}	C	11	10 mm	F	11	10 mm
y_{MCP}	C	10	0 mm	F	10	0 mm
z_{AGATA}	C	12	20 mm	F	13	30 mm
TOF_{PRISMA}	C	10	0 ns	F	10	0 ns

Table 11: Results of the first iteration

Finally the procedure was iterated with a narrow parameter range. The new ranges are listed in table 12. The regions were adjusted according to the results of the first iteration. A smaller region with a constant number of steps results in a smaller differences between two step points.

parameter	index	range	steps
x_{MCP}	I	$-20 \rightarrow 40$ mm	21
y_{MCP}	J	$-20 \rightarrow 20$ mm	21
z_{AGATA}	K	$-10 \rightarrow 50$ mm	21
TOF_{PRISMA}	J	$-20 \rightarrow 20$ ns	21

Table 12: Parameters for the second iteration with smaller regions

In order to see the best results a minimum for every peak was searched. The results are summarized in table 13 for all sections. The energy

I	J	K	L	section	peak [keV]	^{136}Xe [keV] FWHM	^{136}Xe [keV] energy	^{238}U [keV] FWHM	^{238}U [keV] energy
11	11	8	11	A	mean	5.81	1312.70	3.29	257.87
12	11	13	10	A	Xe 1313.02	5.31	1312.70	3.43	257.92
2	9	14	2	A	U 158.8	15.6	1318.70	2.89	257.19
3	11	9	20	A	U 211.0	24.2	1275.53	2.77	258.19
0	9	11	11	A	U 257.8	11.4	1303.00	2.97	257.60
0	8	13	10	A	U 300.6	15.0	1310.00	2.78	257.68
11	12	9	11	C	mean	5.39	1313.90	2.97	258.16
11	11	15	10	C	Xe 1313.02	5.12	1312.90	3.2	258.15
5	8	13	2	C	U 158.8	8.70	1321.32	2.85	257.45
4	8	15	16	C	U 211.0	9.10	1306.66	2.78	258.31
0	8	16	7	C	U 257.8	16.4	1313.33	2.75	257.70
0	7	14	8	C	U 300.6	16.7	1312.75	2.80	257.90
9	9	9	10	E	mean	5.51	1313.10	2.69	258.12
10	9	12	10	E	Xe 1313.02	5.10	1312.57	2.82	258.16
4	9	16	2	E	U 158.8	9.57	1319.50	2.69	257.54
4	6	10	11	E	U 211.0	8.82	1311.1	2.62	258.08
0	6	18	5	E	U 257.8	17.2	1313.51	2.60	257.70
0	6	19	6	E	U 300.6	17.15	1312.18	2.64	257.79
10	9	12	11	F	mean	5.50	1311.86	2.86	258.10
10	10	13	10	F	Xe 1313.02	5.46	1312.67	2.99	258.03
0	11	17	4	F	U 158.8	17.0	1315.50	2.67	257.50
8	5	9	15	F	U 211.0	7.50	1308.06	2.75	258.27
1	10	14	6	F	U 257.8	13.2	1314.76	2.64	257.65
1	4	16	8	F	U 300.6	14.5	1311.81	2.69	257.78

Table 13: Results of the first iteration

resolution and the energy for the peak position of ^{136}Xe at 1313.02 keV and for the peak of ^{238}U at 257.8 keV are listed. The indices I, J, K and L correspond to the parameters as listed in table 12. The last column reports for which peak a minimum FWHM with a good energy was found. The entry "mean" stands for the combined minimum derived with formula (12). In cases the automatic fit routine did not work properly the fits were done with hdtv [80] and controlled individually. The fits included a left tail of the peak shape. There might be small deviations of ± 0.1 keV between the fit results of the automatic fit. The result of the fit done with hdtv depends on the selected fit and background regions, therefore the regions were kept constant for the individual peaks of the different analysis sections.

The data in table 13 shows that the parameters for the best resolution for the recoils result in an insufficient energy resolution and peak energy for the ejectiles. For example the best FWHM of the Doppler correction for recoils in section A is 2.77 keV, but the result for the ejectile is 24.2 keV. This shows that a minimum at one side, is not automatically the minimum of the other. Only the combined calculation delivers an acceptable result which is not the very best when looking at ejectiles and recoils individually.

parameter	index	range	steps
x_{MCP}	I	$1 \rightarrow 19$ mm	21
y_{MCP}	J	$-6 \rightarrow 8$ mm	21
z_{AGATA}	K	$8 \rightarrow 32$ mm	21
TOF_{PRISMA}	J	$-2 \rightarrow 6$ ns	21

Table 14: Parameters for the third calculation with smaller parameter ranges

The third and last iteration had again smaller step regions summarized in table 14. The variation of energy resolution and peak position is getting smaller. Again the combination of the ejectile and recoil peaks was used to find a minimum in the data. The positions of the minima are listed in table 15. The result of the fits are listed in table 16. For the ejectile Doppler correction other peaks with smaller energies of ^{136}Xe were fitted to make sure the correction works reasonably

parameter	section	index	value	section	index	value
x_{MCP}	A	14	13.6 mm	E	11	7.3 mm
y_{MCP}	A	10	2.4 mm	E	10	−2.5 mm
z_{AGATA}	A	13	16.4 mm	E	11	21.2 mm
TOF_{PRISMA}	A	10	0.8 ns	E	10	−0.4 ns
x_{MCP}	C	11	8.2 mm	F	11	7.3 mm
y_{MCP}	C	10	−0.4 mm	F	10	−0.4 mm
z_{AGATA}	C	12	29.6 mm	F	13	21.2 mm
TOF_{PRISMA}	C	10	0 ns	F	10	1.2 ns

Table 15: Final results after the last iteration for the experimental parameters

at lower energies.

For different runs slightly different optimal values for the four parameters can be observed. Although it was tried to keep the setup constant during the beam time, small changes during the experiment happened. The difference of x_{MCP} between section A and the other sections can be explained by an additional offset of 2.5 mm in the configuration file of section A. The differences in the TOF_{PRISMA} values result from the alignment of the different sections and the drift of the TACs as mentioned before.

Section A					
^{136}Xe [keV]			^{238}U [keV]		
E_{ex}	E_{li}	FWHM	E_{ex}	E_{li}	FWHM
370.15	369.81	3.10	158.98	158.80	2.37
380.76	381.36	2.68	210.60	211.00	2.70
813.11	812.63	3.53	257.91	257.80	3.15
1313.23	1313.02	5.69	300.69	300.60	3.36
Section C					
^{136}Xe [keV]			^{238}U [keV]		
E_{ex}	E_{li}	FWHM	E_{ex}	E_{li}	FWHM
370.22	369.81	3.34	159.02	158.80	2.43
380.71	381.36	1.84	210.74	211.00	2.51
813.07	812.63	3.66	258.05	257.80	2.96
1313.16	1313.02	5.06	300.79	300.60	3.29
Section E					
^{136}Xe [keV]			^{238}U [keV]		
E_{ex}	E_{li}	FWHM	E_{ex}	E_{li}	FWHM
369.95	369.81	3.34	159.08	158.80	2.37
380.78	381.36	2.53	210.81	211.00	2.32
812.76	812.63	3.28	258.12	257.80	2.78
1312.94	1313.02	5.10	300.84	300.60	2.95
Section F					
^{136}Xe [keV]			^{238}U [keV]		
E_{ex}	E_{li}	FWHM	E_{ex}	E_{li}	FWHM
369.91	369.81	3.08	158.98	158.80	2.37
381.11	381.36	1.55	210.74	211.00	2.46
812.15	812.63	4.23	258.05	257.80	2.76
1312.6	1313.02	5.35	300.71	300.60	3.06

Table 16: Results of the final iteration for the resolution and peak position for the different sections. E_{ex} is the value from this experiment, E_{li} is the literature value taken from [81] and [55], FWHM is the full width half maximum of the peak.

3.6.8. Impact of PSA algorithm

Finally the energy resolution after the Doppler correction was scrutinized with respect to different PSA algorithms. The quality of these PSA algorithms is directly reflected by the final Doppler broadening of the lines. An even simpler method, which is not based on PSA, places the interaction in the middle of the hit segment. The normal PSA algorithm is the adaptive grid search method. Lately this algorithm was extended to include also two interactions within one segment. This new version is still under development and was only used for this comparison. For comparison also the result is shown for an algorithm that places the first interaction point randomly in the segment volume. In figure 45 the results of the algorithms are illustrated by the line from the 2^+ decay of ^{136}Xe with an energy of 1313 keV. Only data from the analysis section C was taken. The data from the fits for the peaks are summarized in table 17.

algorithm	FWHM [keV]	peak area
PSA	5.05 (21)	4241 (76)
PSA with 2 hits per segment	5.11 (22)	4388 (78)
Random	6.40 (26)	4109 (77)
Segment center	6.05 (24)	4179 (76)

Table 17: Results for different PSA algorithms.

By utilizing the Gaussian error propagation formula a coarse determination of the position resolution can be done. The mean Doppler angle is 154.1° and the mean β value 0.0889. The energy resolution (FWHM) of the detectors after tracking is approximately 4 keV. This value is taken from the 1.33 MeV line of the ^{60}Co source run. The angular resolution of the PRISMA MCP is 0.23°. The angular straggling in the target is 0.005°and was calculated utilizing the methods of [82]. The error of the β value is small around 2%. The position resolution deduced from the remaining contribution to the observed energy resolution corresponds to an energy resolution of about 6 mm for the adaptive grid search algorithm.

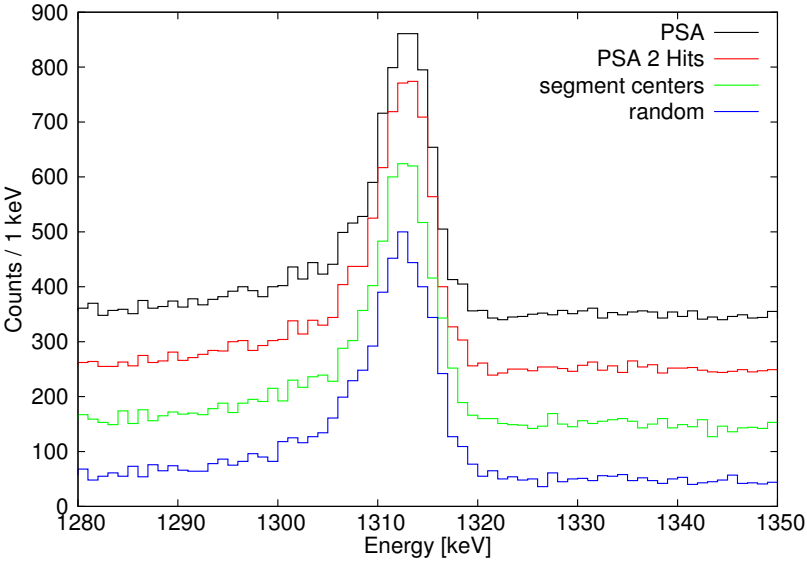

Figure 45: The results of the different PSA algorithm are illustrated for the 2^+ decay of ^{136}Xe with an energy of 1313 keV. The black line used the PSA algorithm that was used in this analysis. The red line uses the latest extension that enables the search for two interactions within one segment. The green line was generated by using only the segment center of the hit segment and the blue line is a random distribution of hits within the hit segment. The different results are shifted each 100 counts for better comparison.

3.7. Gamma ray spectra

The quality of the final γ-ray spectra of the AGATA demonstrator will be discussed first for the Xenon and Uranium isotopes. A short summary is given to remind again the multiple steps which are needed in the data analysis of the AGATA demonstrator and PRISMA spectrometer to create the final spectra. The tracking algorithm is based on the energy and position information of all coincident interactions recorded in the AGATA detectors after the PSA. The results of the tracking algorithm are the reconstructed γ-rays with the energy and the position of the first and (possibly) second and more interaction point. The first interaction is needed for the Doppler correction. The second interaction can be used for polarization measurements [83].

In figure 46 three γ-ray spectra are shown without any cuts on the prompt time. To generate these spectra all events of the complete experiment were taken. The red spectrum named "Core electrodes" shows the sum of the individual core spectra; corresponding to a single spectrum of an array with unsegmented detectors. The green spectrum named "Segment electrodes" is the sum of the individual segment signal spectra and the blue one named "Tracked" is the spectrum after the PSA and the tracking algorithm.

To compare these spectra the number of counts in the spectra and the area of four background peaks from unshifted lines are listed in table 18. The background peaks were chosen, as the γ-rays from target and beam like particles need to be Doppler corrected. The line at 511 keV results from the annihilation of a positron, where two γ-rays with 511 keV are emitted in opposite directions. The line at 563 keV results from a neutron induced reaction in ^{76}Ge and the line at 1014 keV from a neutron induced reaction in ^{27}Al. The line at 1434 keV was taken for comparison at higher energies.

The segments see more low energy events, as it is very likely that γ-rays interacting with Compton scattering will scatter out of the hit segment. The interaction of neutrons with ^{72}Ge at an energy around 700 keV are discriminated well, they are not seen in the tracked spectrum. A zoom on the region of the neutron line is shown in figure 47. The 0^+ decay of the ^{72}Ge has a half life of 444.2 ns and the tracking algorithm will not identify the energy deposition of the recoiling ^{72}Ge

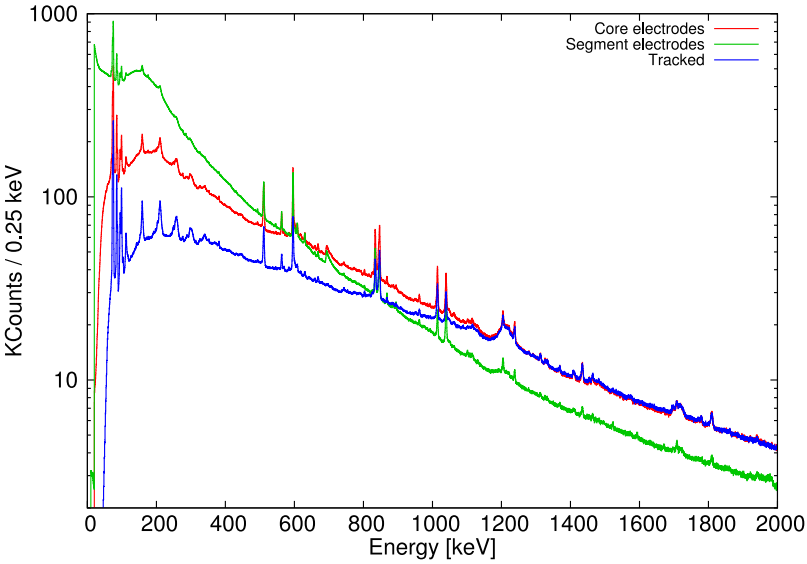

Figure 46: γ-ray spectra of the complete experiment without prompt time coincidence condition. Spectra of core electrodes (red), segment electrodes (green) and after the tracking algorithm (blue)

atom and the emitted electron as one interaction. Around 830 keV the intensity of the segment spectrum is below the intensity of the tracked spectrum and at an energy around 1.2 MeV the intensity of the core spectrum drops slightly below the tracked one. The tracking efficiency is defined as the ratio between the peak area for the tracked and the core spectra. The measured value of 87% for the peak at 1434 keV is very close to the value of 84.5% at 1332.5 keV reported in [8].

	Peak area at			
	511 keV	563 keV	1014 keV	1434 keV
Core	189653 (100)	52768 (100)	68115 (100)	13201 (100)
Segment	157935 (83)	46586 (88)	23516 (35)	3475 (26)
Tracked	105597 (56)	29489 (56)	50922 (75)	11476 (87)

	Total
Core	3.9×10^8 (100)
Segment	6.8×10^8 (175)
Tracked	2.2×10^8 (57)

Table 18: Overview for the spectra in figure 46, number in parenthesis is the percentage with respect to the value from the core spectrum.

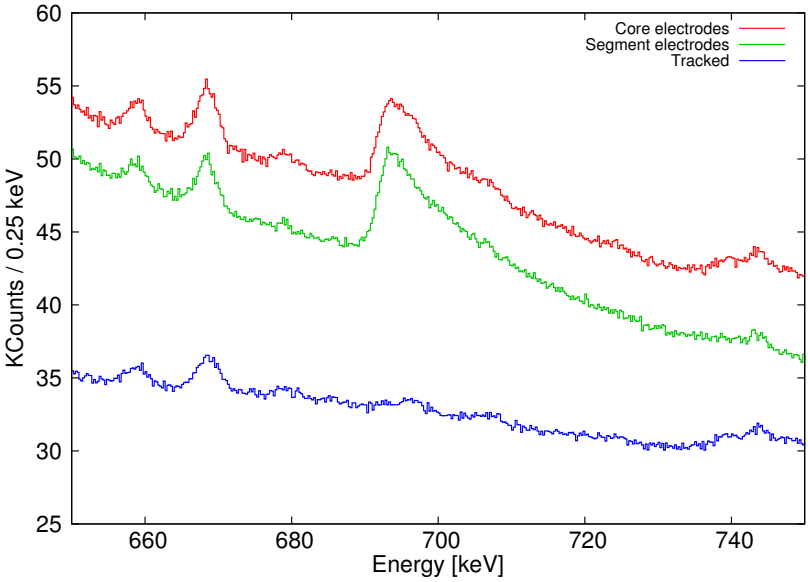

Figure 47: Zoomed γ-ray spectra of core electrodes, segment electrodes and after the tracking algorithm.

3.7.1. Cuts on Elements

The next step is to require the successful identification of a specific element via the PRISMA spectrometer. As described before the selection of Z is done by placing 2D gates on the energy loss spectra of the ionization chamber. In this analysis gates on the five elements with the highest yields (Xenon (100%), Iodine (37%), Caesium (33%), Tellurium (19%) and Barium (16%)) were placed. At this point the quality of the spectrum does not change, however the number of counts drops down to 13.6% of the tracked spectrum without conditions.

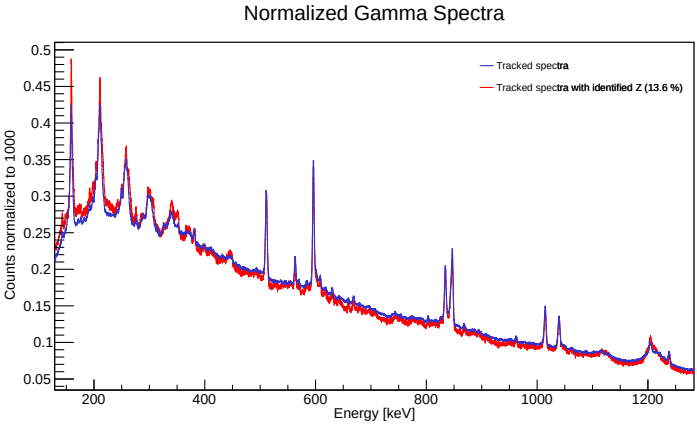

Figure 48: Normalized γ-ray spectra after GRT with and without a cut on identified Z numbers

After normalizing the two spectra with and without the cut on the element identification of figure 48 the differences become clear. The background drops and the peaks of the Uranium and of Xenon are getting more pronounced. Both spectra were normalized to 1000 counts. The next steps are (i) to gate on the prompt time peak between AGATA and PRISMA shown in figure 37 and (ii) to gate on the different isotopes.

3.7.2. Background radiation

The prompt time condition between AGATA and PRISMA eliminates uncorrelated contributions from background radiation in the spectra. The tracked spectrum, where all Xenon nuclei are taken without the Doppler correction, is shown in figure 49. The green spectrum is without any prompt time condition. In the blue spectrum a prompt time condition between AGATA and PRISMA was applied. The red spectrum is the prompt spectrum minus a spectrum generated with two cuts on half the time period of the prompt peak before and after the prompt peak. The improvement of the prompt time cut is obvious. About 40% of the events were caused by background (see final number of the red spectrum of figure 49). For example the peak at 511 keV resulting from positron annihilation is going down to 47% in the prompt spectrum and down to 42% in the corrected one.

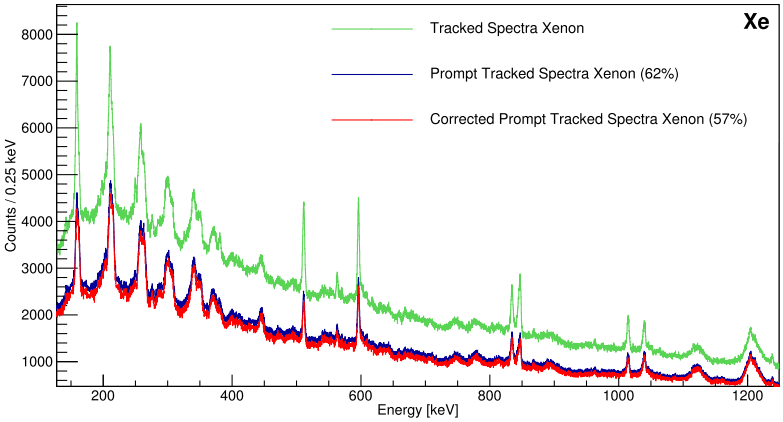

Figure 49: γ-ray spectra for Xenon isotopes with a cut on the prompt time peak between AGATA and PRISMA and a background correction. The number of counts relative to the spectrum without a time condition are indicated in the legend.

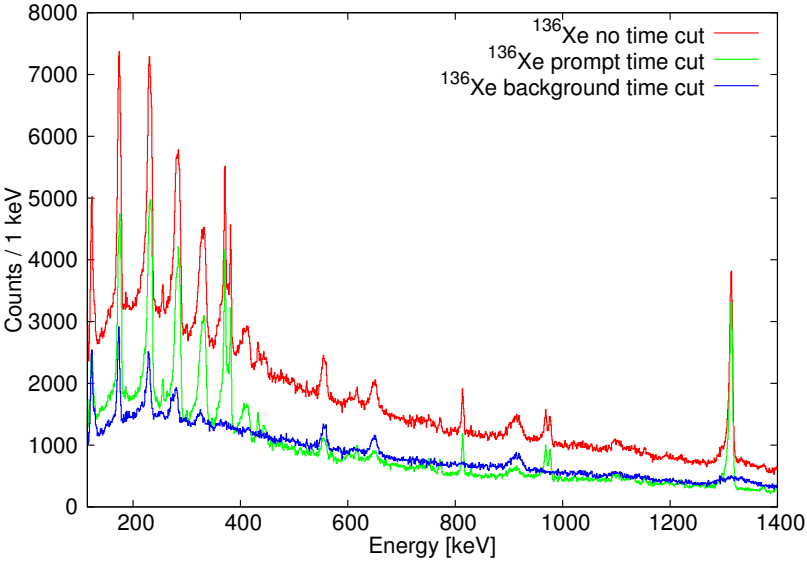

Figure 50: Doppler corrected γ-ray spectra of ^{136}Xe. In the red spectrum no time cut is applied. In the green spectrum a time cut on the prompt time peak between AGATA and PRISMA was applied. The blue spectrum is the difference between the red and the green spectra.

The effect of the prompt time condition between AGATA and PRISMA is even better demonstrated in the Doppler corrected spectra of ^{136}Xe and ^{238}U. The ^{136}Xe spectra are shown in figure 50. The red spectrum corresponds to no time condition, the green spectrum to a prompt time condition and the blue spectrum is the difference between the red and green spectra. The blue spectrum does not show clear lines of ^{136}Xe. Only peaks with a wrong Doppler correction from the background and target excitations can be seen. The area of the peak at 1313 keV in the green spectrum is a bit smaller (89%). A small bump is visible in the blue spectrum around 1313 keV. This bump adds extra counts to red spectrum. The ^{238}U spectra are shown in figure 51. A similar color code is used as in the ^{136}Xe figure 50, but in this figure the blue spectrum is not Doppler corrected. In the spectra

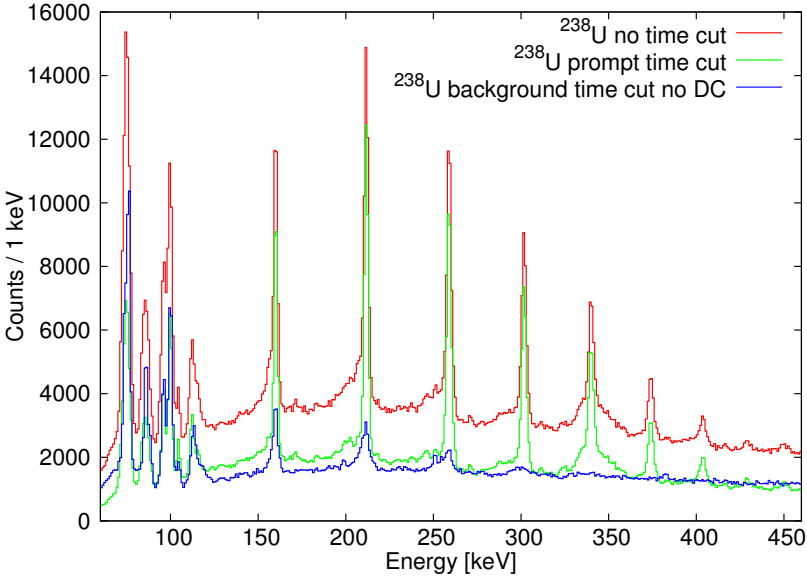

Figure 51: Doppler corrected γ-ray spectra of ^{238}U. In the red spectrum no time cut is applied. In the green spectrum a time cut on the prompt peak between AGATA and PRISMA was applied. The blue spectrum is the difference between the red and the green spectra.

also the x-rays are shown. The condition on the prompt time reduces the x-ray background. The x-ray lines of ^{238}U visible in the spectra are: $K_{\alpha 1} = 98.434\,\text{keV}$, $K_{\alpha 2} = 94.654\,\text{keV}$, $K_{\beta 1} = 111.298\,\text{keV}$ and $K_{\beta 2} = 114.455\,\text{keV}$ [84]. In the blue and the green spectra the x-ray energies are not smeared out. This demonstrates that the ^{238}U atoms were moving in the events accumulated in the green spectrum, while the ions in the blue spectrum emitted the x-rays in rest. A similar effect is visible for the γ-rays of ^{238}U. Therefore most of the ^{238}U nuclei that contribute to the blue spectrum were produced by Coulomb excitation, an abundant background reaction with high cross sections.

The different γ-rays emitted as a function of time were investigated by sorting a 2D histogram with the prompt timing signal vs. the γ

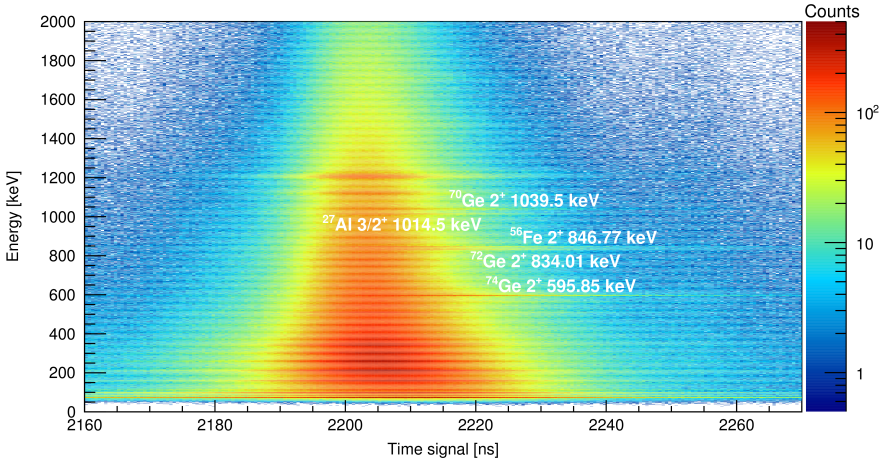

Figure 52: Tracked γ-ray energy versus prompt time signal for Z = 54 identified in PRISMA

energy. Such a plot is shown in figure 52. The fast neutron induced delayed γ-ray lines are seen in the energy spectrum and compare well to background lines reported in [1], page 463. These lines are indicated in the 2D plot. In the time spectrum they are delayed due to the longer time-of-flight of the neutrons. The interactions of neutrons inside HPGe detectors, especially AGATA detectors, are described in [85]. The edge that shows up in the core and segment sum spectra in figure 47 around 700 keV is the decay of the first 0^+ of ^{72}Ge to the ground state at an energy of 689.6 plus the energy of the recoiling ^{72}Ge atom. The E0 decay is only possible by internal conversion. The emitted electron will not travel far in the detector and it is very likely that it is seen as a sum peak. For the decay of the first 2^+ state this is different. The probability that the energy deposition of the ^{72}Ge atom and of the γ-ray from the decay will happen in two different detectors is high. A sharp peak in the sum of the single core electrodes is seen. For the segment sum this is even more probable, as the segments are smaller. For the decays of the 2^+ of ^{70}Ge and ^{74}Ge the same explanation holds. The target chamber, the end caps of the cryostats, the beam line and many other components are made

of Aluminium. The large dipole magnet of PRISMA consists mainly of Iron and many construction parts are made of steel. This explains the extra background lines of ^{27}Al and ^{56}Fe in the spectra.

The focus of the experiment are deep inelastic reactions after neutron and proton transfer reactions producing highly excited reaction products which may evaporate neutrons. Therefore background contributions are studied more carefully. It is assumed that the neutrons missing in the ejectile are transfered to the target material. However, it is possible that some neutrons will be directly evaporated by the target nucleus. These neutrons will then interact with the surrounding detectors. Therefore it is expected, that in the channels where neutrons from the ejectile were transferred, more neutrons react with the surrounding HPGe detectors.

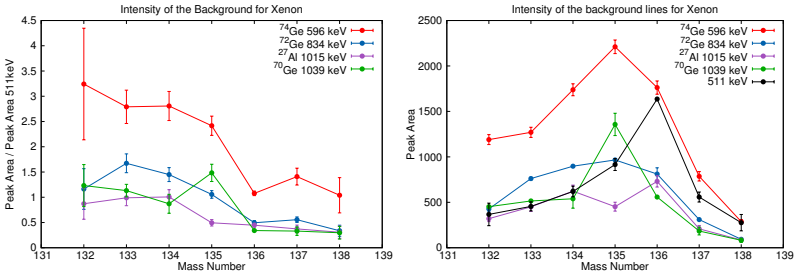

Figure 53: γ-ray intensities of background radiation for different isotopes (right) and intensities divided by the intensity of the 511 keV line (left).

To proof this, tracked γ-ray spectra with cuts on the individual isotopes and a time cut on the prompt time signal were generated. The gate on the time cut was opened at 2205 ns and closed at 2270 ns to take an extra focus on the delayed part of the spectra. The area of the peaks at 511 keV, 595.85 keV, 834 keV, 1014 keV and 1039.5 keV were fitted in each spectrum. In the right plot of figure 53 the absolute values of the area are given. It reproduces mainly the statistics of the distribution. The peak at 511 keV does not depend on the neutrons, but the area of the peak gives a good value to compare the distribution of the isotopes. The result is shown in figure 53 and the

expected behavior is observed. Therefore the areas of the different neutron induced lines are divided by the area of the 511 keV line. The left graph of figure 53 gives a clear indication that more neutron induced background reactions happen, if the ejectile looses more neutrons. The peak at 1039 keV in the spectrum of ^{135}Xe is on top of the uncorrected 1131.5 keV peak of ^{135}Xe. Therefore the area is too big and not reliable.

3.7.3. Q_r value

The PRISMA spectrometer provides not only the velocity vector of the recoil. Depending on the β value and the reaction products the Q_r value of the reaction is calculated according to [79]. By gating on the Q_r value the excitation energy of the excited recoil nucleus can be restricted and suppress the neutron evaporation of the actinide reaction product. To investigate this behaviour the delayed neutron induced radiation of ^{74}Ge at an energy of 596 keV is taken. In figure 53 the decay of the ^{74}Ge is more likely for reactions where the beam like particles transfers a neutron. In figure 54 the right plot shows the ratio of the ^{74}Ge line and the 511 keV line from positron annihilation for different ranges of Q_r values. To determine the area of the peak two different spectrum analyser programs were used as the systematic uncertainties varied. However, the hypothesis that for higher Q_r values less neutron evaporation can be seen is proven right. In both fits the area of the ^{74}Ge peak goes down, demonstrating that less neutrons are emitted.

Another way to demonstrate the Q_r value dependence of neutron emission probability is given by the recoil spectra of ^{239}U. These are obtained by gating on ^{135}Xe identified in PRISMA and applying the Doppler correction for the recoil nuclei. In the resulting spectra also the lines of the rotational band of ^{238}U are seen, because the excited ^{239}U nucleus decays above the neutron separation energy also via neutron emission. By gating on different Q_r values different spectra were generated and the ratio of the intensity of the peak of ^{239}U at 250 keV and the peak of ^{238}U at 258 keV were determined. The result is shown in the left plot of figure 54. The relative area is rising with higher Q_r value implying less neutrons are released from ^{239}U.

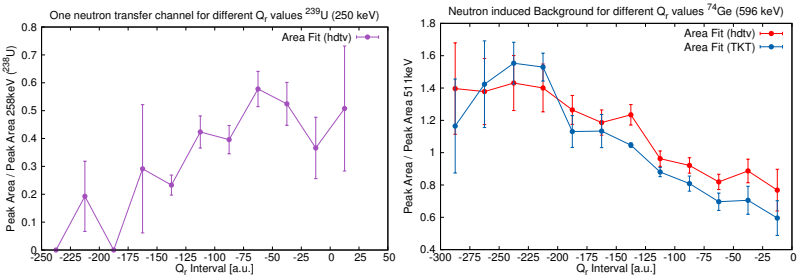

Figure 54: γ-ray intensities for different Q_r value ranges indicated by the tics of the axis. In the left graph the intensity of the radiation of the one neutron transfer nuclei ^{239}U at 250 keV divided by the intensity of the line of ^{238}U at 258 keV is shown. In the right graph the intensity of the radiation of ^{74}Ge divided by the intensity of the 511 keV line is shown. Two different spectra viewers were used to measure the peak area (hdtv[80] and TKT[76]).

These observations illustrate the possibility of the Q_r value cut. Especially events with a higher value favour reaction products with lower excitation energy and reduced neutron emission. However this parameter has to be adjusted for each reaction channel.

3.7.4. Particle coincidence

As described above one DANTE detector was mounted at the opposite site of the entrance MCP of PRISMA. Two other DANTE detectors were placed in a similar arrangement but rotated around the beam axis (see figure 15 on 47). Both pairs of detectors were connected to TACs allowing to gate on coincident particles hitting the detectors. The time spectra are shown in figure 55. The statistics are listed in table 19.

By comparing the left and right plot it is obvious that the number of entries for the identified Xenon isotopes (blue lines) are very small in the DANTE DANTE spectrum, while in the DANTE MCP PRISMA spectrum more events are registered. Two peaks around channel 3500

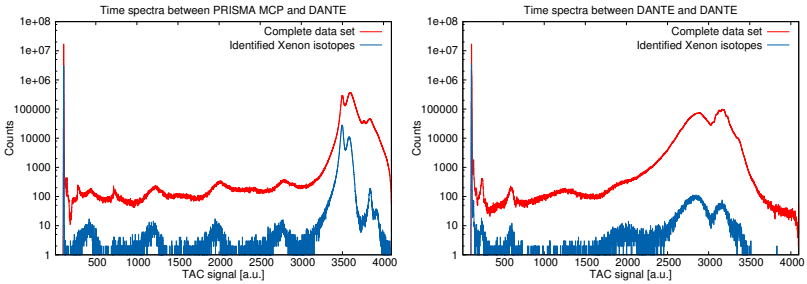

Figure 55: Particle coincidence between entrance MCP of PRISMA and DANTE (left) and between two DANTE detectors (right) in logarithmic scale for the complete data set and for Xenon isotopes identified in PRISMA.

	Number of entries $\times 10^7$		
	Total	TAC PD	TAC DD
Complete data set	19.8	5.68	3.72
Identified Xenon Isotopes	0.758	0.166	0.0039

Table 19: Statistics for particle coincidence with PRISMA DANTE (PD) and DANTE DANTE (DD).

can be seen in figure 55. To analyze this in more detail, γ-ray spectra of ^{135}Xe are employed. The Doppler corrected spectra for recoils and ejectiles gated on the left and on the right peak are shown in figure 56 for ^{239}U and in figure 57 for ^{135}Xe. For the recoil only the left peak shows meaningful contributions in the spectrum. For the ejectile this is not clear. The two peaks at 298 keV and 309 keV are well seen in the spectrum gated on the right peak of the TAC specrum. These peaks are identified as decays of the excited ^{135}Xe nucleus (table 22 on page 132). The line at 1131 keV is also a decay of the ^{135}Xe nucleus (table 22 on page 132), but it is mainly seen in the spectrum gated on the left peak.

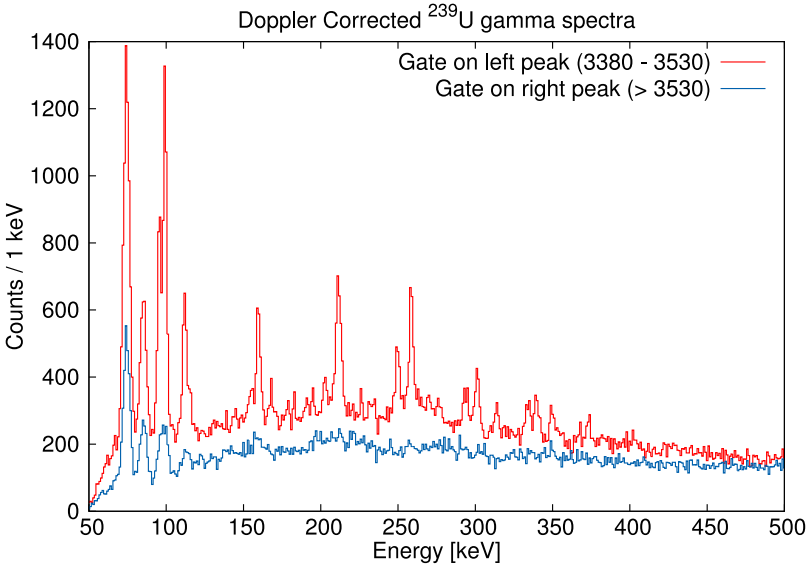

Figure 56: Doppler corrected spectra of ^{239}U with TAC gates

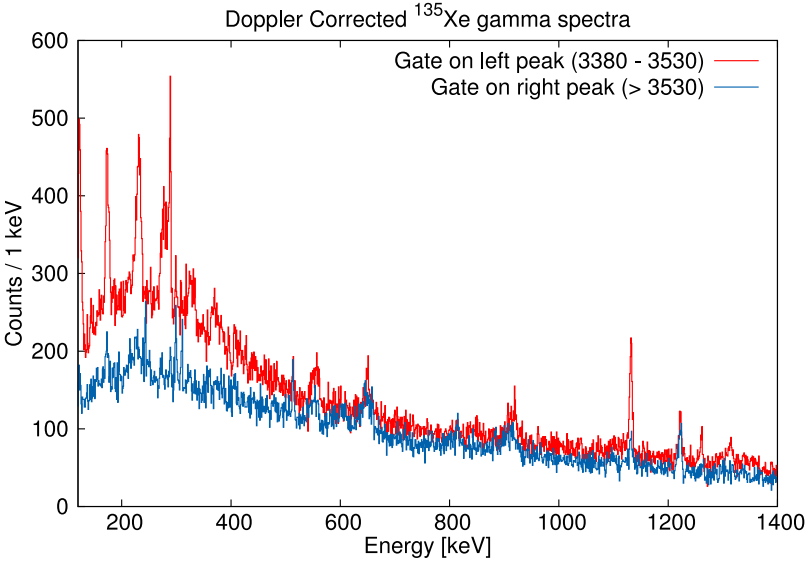

Figure 57: Doppler corrected spectra of ^{135}Xe with TAC gates

In figure 58 similar spectra for ^{238}U are shown. The mean ratio of the peak areas between the condition on the particle coincidence and without is 23.7% in the case of ^{238}U. This value is determined by a comparison of the lines at 158.8, 211.0, 257.8 and 300.6 keV. The effect of the two cuts on the left and right peaks in the TAC spectrum is similar to the case of ^{239}U. For the events in the left peak x-rays and γ-rays of excited ^{238}U ions and nuclei are visible, while in the right peak nearly no excitations can be seen. Two explanations are possible: either the coincidence in the right peak is caused by random background triggered by a faulty electronic module or the right peak results from fission of the target material. As a result from the reaction ^{136}Xe(^{238}U, $f\gamma$)^{136}Xe one of the two fission fragments cause a hit in the DANTE detector which is shifted in time due to the additional kinetic energy of the fission fragments. In figure 59 the area of the left (red) and the right peak (blue) divided by the absolute number of the different identified isotopes is shown. The relative area of left peak shows a maximum in the reaction where no neutrons are transferred. For the same isotope the relative area of the right peak shows a minimum. If the right peak would just be random background, the blue line in the plot should be constant. This indicats, that the events in the right peak are fission events where one of the fission products was registered in the DANTE detector.

As a summary different cuts can be applied while sorting and analyzing the data set. A cut on the prompt time peak between PRISMA and AGATA reduces the background in both ejectile and recoil spectra. Cuts on the Q_r value help to suppress the neutron evaporation in the actinide spectra. Cuts on the particle coincidence between PRISMA and DANTE clear the spectra of the recoils. Unfortunately the last condition decrease the total number of counts down dramatically by a factor of five. In the case of ^{238}U the number of events in the peaks is going down to 25%.

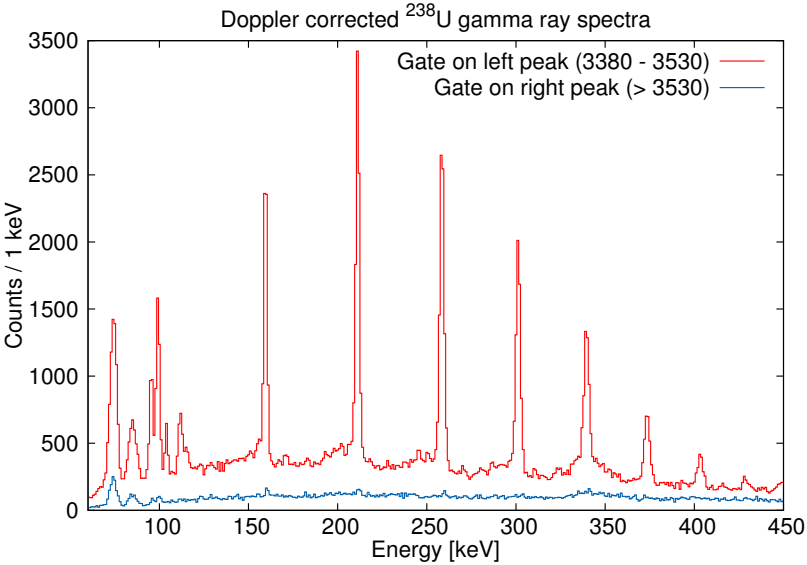

Figure 58: Doppler corrected spectra of ^{238}U with and without TAC gates

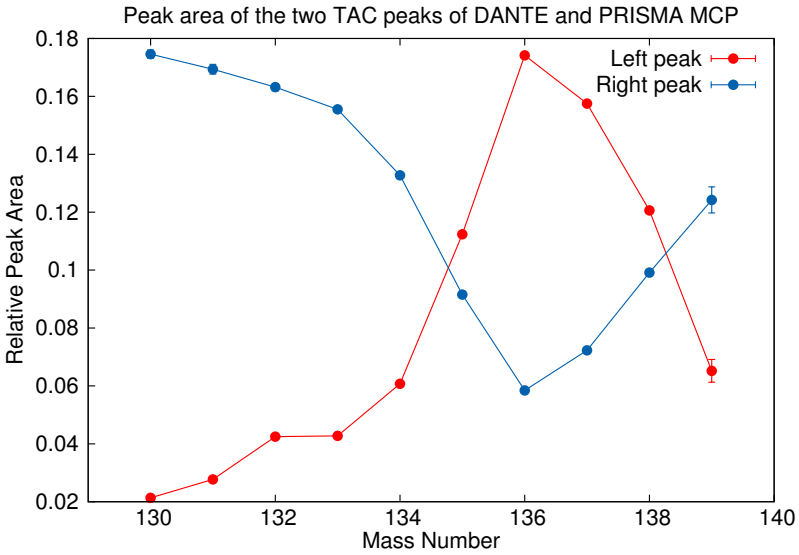

Figure 59: Area of the left (red) and right (blue) peak in the TAC spectrum between DANTE and PRISMA divided by the absolute number of the different identified isotopes. Both peaks were fitted simultaneously with left and right tails free to obtain the best fit result.

3.7.5. Gamma ray spectra of individual isotopes

The individual γ-ray spectra of the different reaction channels are described and discussed within this section. The section is divided by the different multi nucleon transfer reaction channels. In all following tables the error next to the measured energies are the errors from the fit program illustrating how well the fit routine describes the peak. In general this error is very small. The Doppler correction introduces a new source for systematic uncertainties and a more realistic error of 0.5 keV should be considered.

Inelastic scattering The channel with the highest number of recorded ions is the reaction where no neutrons or protons are transferred and inelastic scattering occurs at beam energies and scattering energies well above the Coulomb barrier.

$$^{136}\mathrm{Xe}(^{238}\mathrm{U},^{238}\,\mathrm{U'})^{136}\mathrm{Xe'}$$

The Doppler corrected spectrum of ^{136}Xe identified in PRISMA with an applied prompt time cut between AGATA and PRISMA is shown in figure 60. The observed lines and the according results are listed in table 20.

This Work			Literature [81]		
E_γ [keV]	FWHM [keV]	Peak area	E [keV]	E_γ [keV]	J^π
254.58 (13)	2.72 (24)	2294 (181)	3484.5 (3)	255.0 (3)	(10^+)
369.874 (41)	2.926 (92)	7392 (167)	2261.53 (3)	369.813 (23)	6^+
380.521 (46)	2.926 (92)	4947 (138)	1694.386 (13)	381.359 (7)	4^+
431.25 (14)	2.69 (31)	971 (94)	2125.68 (6)	431.38 (12)	$3^+, 4^+$
750.47 (24)	3.04 (60)	483 (79)	2444.39 (6)	750.05 (7)	5
771.16 (20)	4.26 (50)	816(82)	2465.03 (11)	770.75 (15)	(4^+)
813.199 (84)	3.69 (20)	2843 (99)	2125.68 (6)	812.63 (8)	$3^+, 4^+$
967.58 (14)	4.25 (26)	2766 (96)	3229.4 (3)	967.8 (3)	(8^+)
975.81 (13)	4.26 (26)	2698 (108)	2289.53 (9)	976.5 (2)	2^+
1313.35 (5)	5.7 (1)	25683 (187)	1313.027 (10)	1313.02 (1)	2^+
1373.29 (38)	6.12 (87)	558 (82)	4857.7 (5)	1373.2 (3)	(11^-)
2289.96 (42)	9.7 (12)	884 (63)	2289.53 (9)	2289.6 (2)	2^+
2415.8 (10)	7.8 (17)	650(74)	2414.74 (12)	2414.6 (2)	2^+

Table 20: γ-ray lines identified in the single spectrum of ^{136}Xe. Literature values are taken from [81].

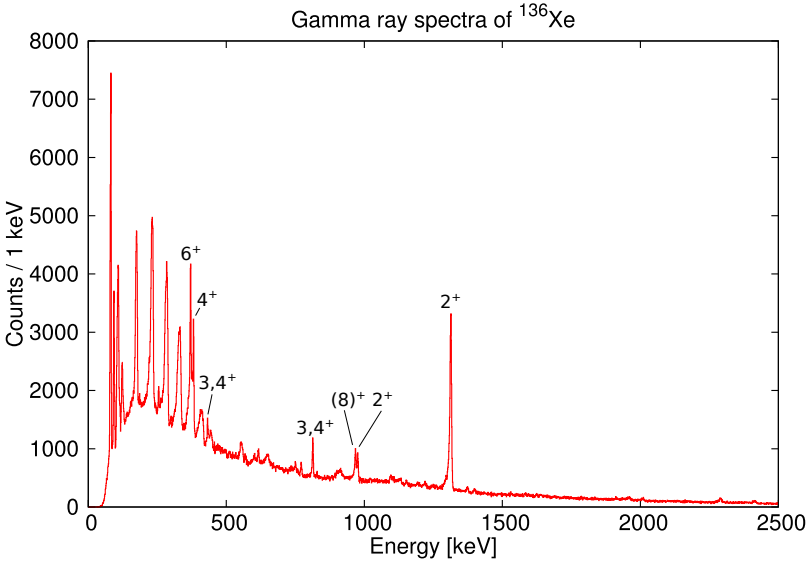

Figure 60: Doppler corrected γ-ray spectrum of ^{136}Xe with a time cut on the prompt peak between PRISMA and AGATA. The identified peaks are listed in table 20.

All the observed lines can be attributed to transitions in ^{136}Xe. The observed transitions are summarized in the level scheme taken from [81]. The decay sequences are shown in the level scheme in figure 61. The 6^+ state has a life time of 2.95 μs and its decay can not be observed in the spectrum with prompt time condition.

The simultaneously emitted γ-rays were analyzed by creating $\gamma\gamma$ matrices. To place cuts the matrix is projected to one of its axis. A γ-ray spectrum showing all the coincident γ-rays is produced by placing a gate at a region around a certain peak energy and a projection of this region onto the other axis. Background cuts can be placed in the same way and the generated spectra are weighted by the width of the background cut or the number of counts in the cut before they are subtracted from the original cut.

Two spectra are shown in figure 62, the left one shows a cut on the

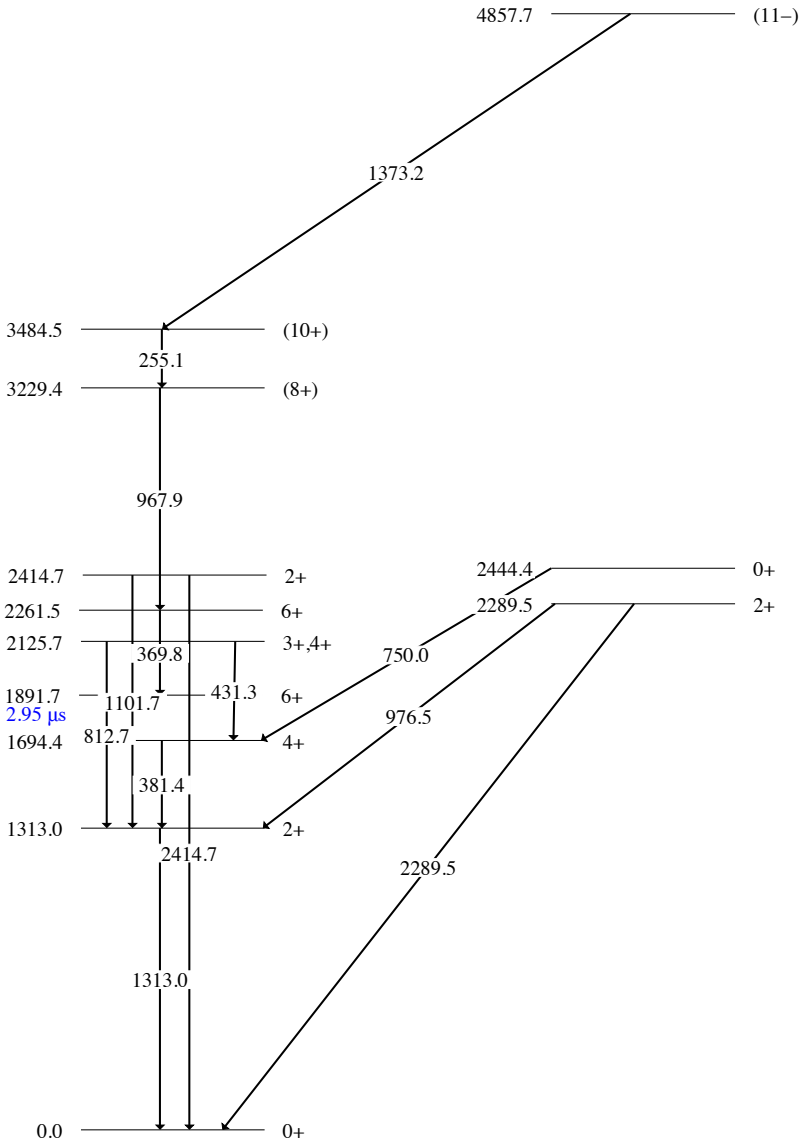

Figure 61: Level scheme for the observed γ-rays of the single spectrum of ^{136}Xe. . Literature values are taken from [81].

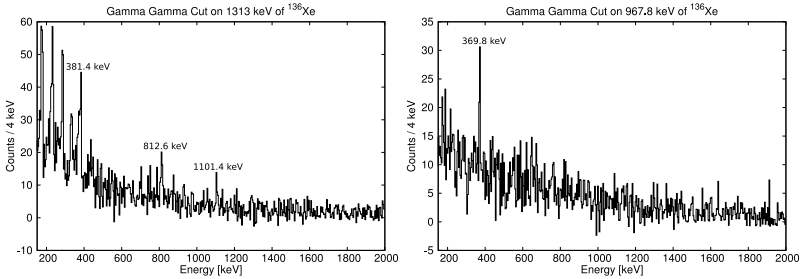

Figure 62: Time coincidence cut on the line at 1313 keV (left) and on the line at 967.8 keV (right) for ^{136}Xe

1313 keV line, the right one a cut on the line at 967.8 keV. In the left cut three lines can be seen. The peak at 381.4 keV is connected to the 4^+ state feeding the 2^+ of the 1313 keV line. The peak at 812.6 keV is connected to 3^+, 4^+ state at 2125.7 keV that decays to the 2^+ state at 1313 keV or to the 4^+ state at 1694.4 keV. The line at 1101.4 keV cannot be identified in the single spectrum, but in coincidence with the 1313 keV line it becomes visible. It is the decay of the 2^+ state at 2414.7 keV to the 2^+ at 1313 keV. It is also decaying directly to the ground state with a γ-ray of 2414.6 keV that was identified in the single spectrum. The right spectrum in figure 62 is a cut on the line with an energy of 967.8 keV connected to the (8^+) state at 3229.4 keV. In coincidence the line at 369.8 keV is seen. It is the decay of the 6^+ into the isomeric 6^+ state. All the decays and states are known and demonstrate that the $\gamma\gamma$ analysis works as expected.

The recoil nucleus of the inelastic scattering is the target material ^{238}U. A Doppler correction with calculated parameters for the kinematics of the target like recoils (see section 3.6.5) is performed to obtain the single spectrum shown in figure 63. The rotational ground state band of ^{238}U is prominent starting with the decay of the 4^+ up to the decay of the 22^+ state. The corresponding fit data is summarized in table 21 and the corresponding level scheme is shown in figure 64.

The $\gamma\gamma$ matrices demonstrate that the listed γ-rays are emitted in coincidence. The $\gamma\gamma$ cuts on the decays of the 6^+ up to the 20^+

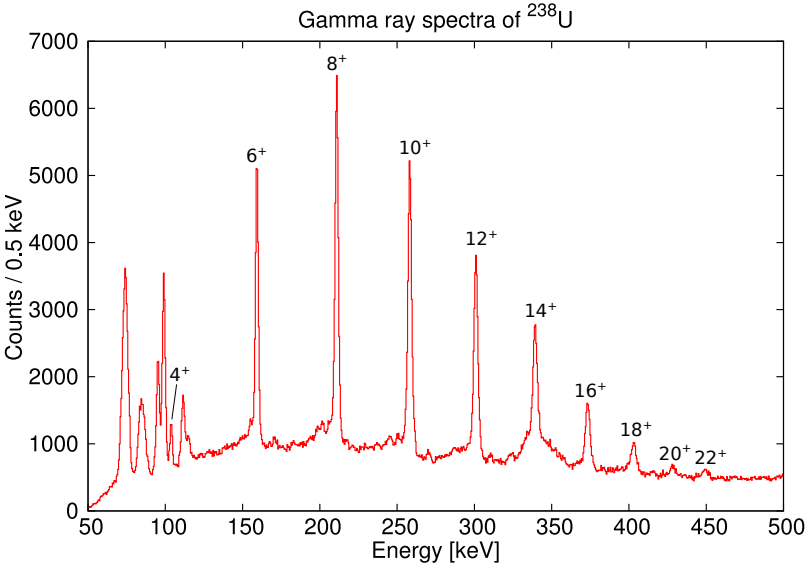

Figure 63: Doppler corrected γ-ray spectrum for ^{238}U with a cut on the prompt time peak between AGATA and PRISMA. Transitions of the ground state band of ^{238}U are indicated.

are shown in figure 65. It is notable that in the $\gamma\gamma$ cut on 159 keV nearly no x-ray background can be seen. This might be an effect of the tracking algorithms, which could reject combinations of γ-ray energies it cannot interpret well. However, with the shown spectra it is proven that the $\gamma\gamma$ analysis is also working for the undetected recoil particles.

The particle coincidence between DANTE and PRISMA MCP allows also direct detection of ^{238}U. The corresponding spectra with a Doppler correction for the recoil is shown in figure 66. The red spectrum shows a cut on the left peak of the TAC spectrum and the blue spectrum a cut on the right peak of the TAC spectrum. In the right peak of the TAC spectrum the Uranium lines are very suppressed, while in the left peak they dominate. It is worth to mention, that the FWHM of the peaks are approximately 0.2 keV smaller in the TAC

This Work			Literature [81]		
E_γ [keV]	FWHM [keV]	Peak area	E [keV]	E_γ [keV]	J^π
103.608 (35)	1.512 (77)	1833 (85)	148.38 (-)	103.50 (4)	4^+
159.050 (89)	2.223 (28)	20768 (192)	307.18 (8)	158.80 (8)	6^+
210.701 (11)	2.486 (26)	30784 (219)	518.1 (3)	211.0 (3)	8^+
257.987 (12)	2.926 (30)	27053 (208)	775.9 (4)	257.8 (4)	10^+
300.740 (16)	3.145 (39)	19994 (166)	1076.7 (5)	300.6 (9)	12^+
339.054 (26)	3.282 (67)	11982 (196)	1415.5 (6)	338.8 (4)	14^+
373.083 (41)	3.62 (11)	7656 (152)	1788.4 (6)	372.9 (4)	16^+
403.067 (96)	3.82 (26)	3984 (144)	2191.1 (7)	402.6 (4)	18^+
428.08 (17)	3.86 (46)	1275 (124)	2619.1 (8)	427.9 (4)	20^+
449.10 (24)	4.64 (65)	1262 (138)	3068.1 (9)	448.9 (4)	22^+

Table 21: γ-ray lines identified in the single spectrum of ^{238}U. Literature values are taken from [81].

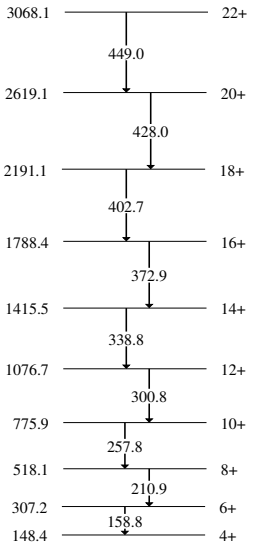

Figure 64: Level scheme for the γ-rays seen in the single spectrum of ^{238}U.

gated spectrum. The reason for this behavior is the combination of two effects: (i) the peak to total is better and (ii) the Coulomb excited ^{238}U isotopes, that are wrongly Doppler corrected, are suppressed.

The next step to clear the spectra is to ask for particle and $\gamma\gamma$ coincidence. This is done by only sorting those events into the $\gamma\gamma$ matrix that are within the TAC gate. For the ejectiles both peaks of the TAC signal are valid, while for the recoils only the left peak is taken as a validation. For the ejectiles this does not really improve the situation, but for the recoil nuclei the spectra become cleaner and show indications for lines not observed in the $\gamma\gamma$ analysis without particle coincidence.

In figure 67 the projection of the recoil Doppler corrected $\gamma\gamma$ matrix with particle coincidence for ^{238}U is shown. The cuts on the transitions of the 6^+ up to the 18^+ are summarized in figure 68. As expected the spectra show a similar behavior as the spectra of the $\gamma\gamma$ analysis without particle coincidence unfortunately with reduced statistics. In the cuts on 159, 258 and 402 keV some higher energy lines become visible that could not be identified. In the cut on 159 keV a line at 349.7 keV shows up. Two lines are reported in the vicinity of 349.7 keV, but they are either not connected to the 6^+ state or other coincident lines must be visible in the spectrum, that are not observed.

For this reaction we were able to identify the beam and target like nuclei by their emitted γ-rays without contaminations from other reaction channels. The combined AGATA-PRISMA analysis worked. For events with both reaction partners detected the $\gamma\gamma$ analysis worked and showed the expected results. The highest excitation energy of the ^{136}Xe isotope is 4857.7 keV and the highest identified spin is (11^-). For the ^{238}U the highest excitation energy is 3068.1 keV and the highest observed spin is 22^+. The condition on the particle coincidence cleaned up the spectra and even improved the energy resolution. For the ^{238}U recoil the particle and $\gamma\gamma$ coincidence analysis could be performed, although the statistic is getting unexpectedly low due to reduced efficiency of the DANTE detector.

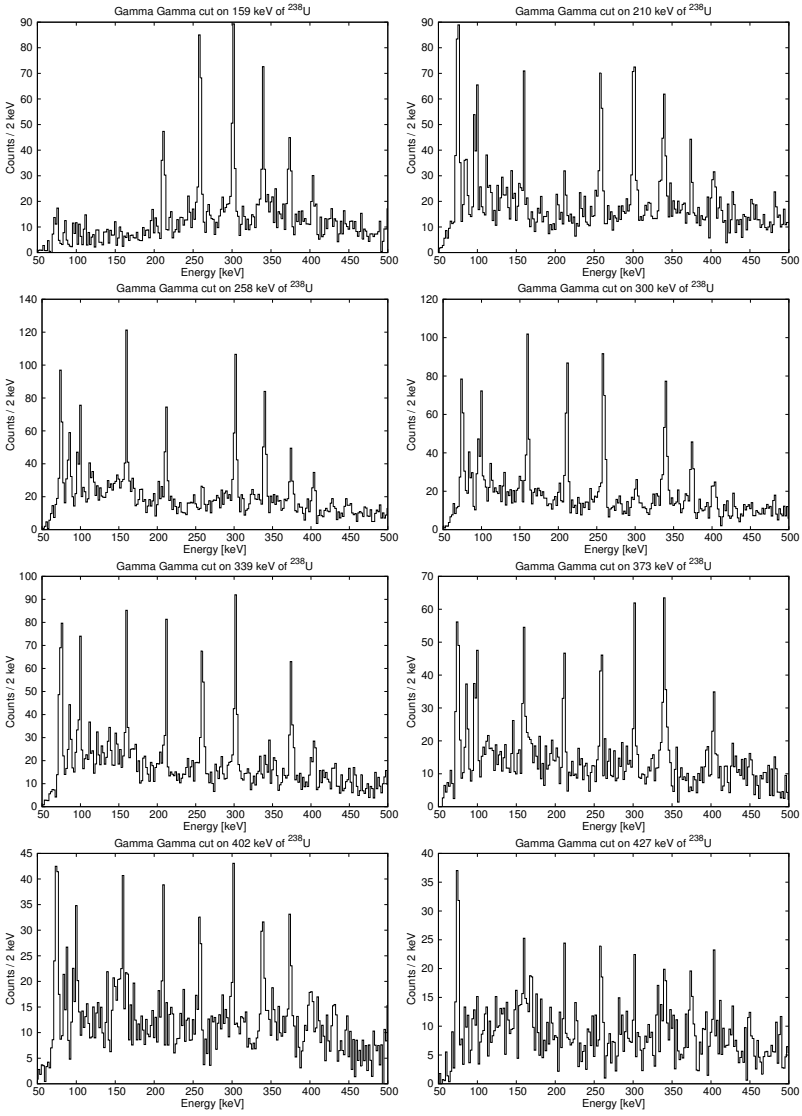

Figure 65: γ-ray coincidences for the indicated γ-ray energies for ^{238}U.

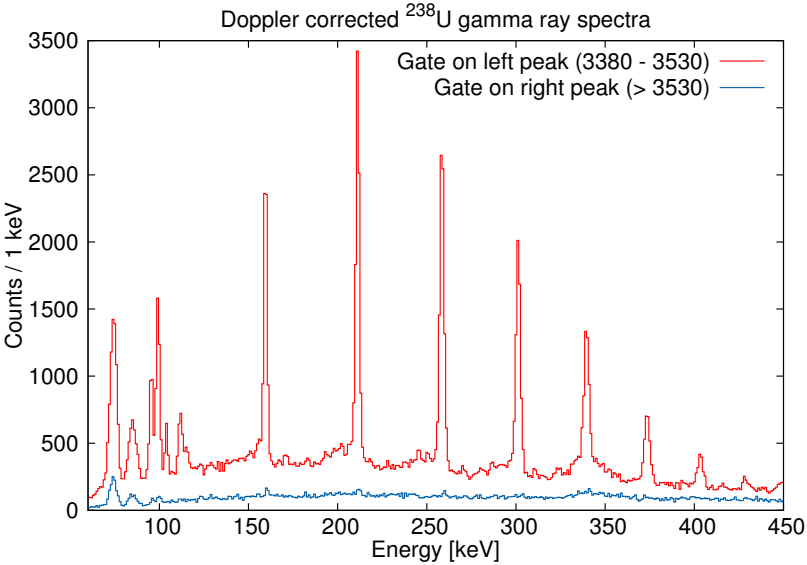

Figure 66: Doppler corrected spectra of ^{238}U with and without TAC gates

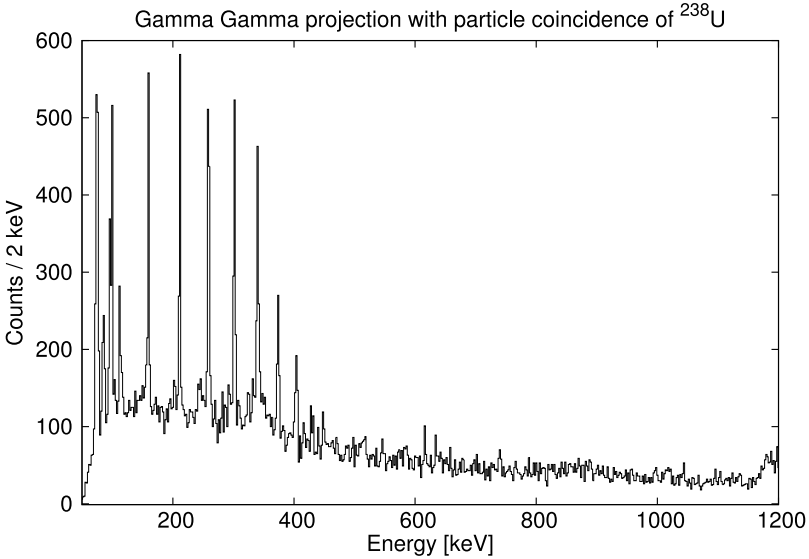

Figure 67: Projection of the recoil Doppler corrected $\gamma\gamma$ matrix with particle coincidence for ^{238}U

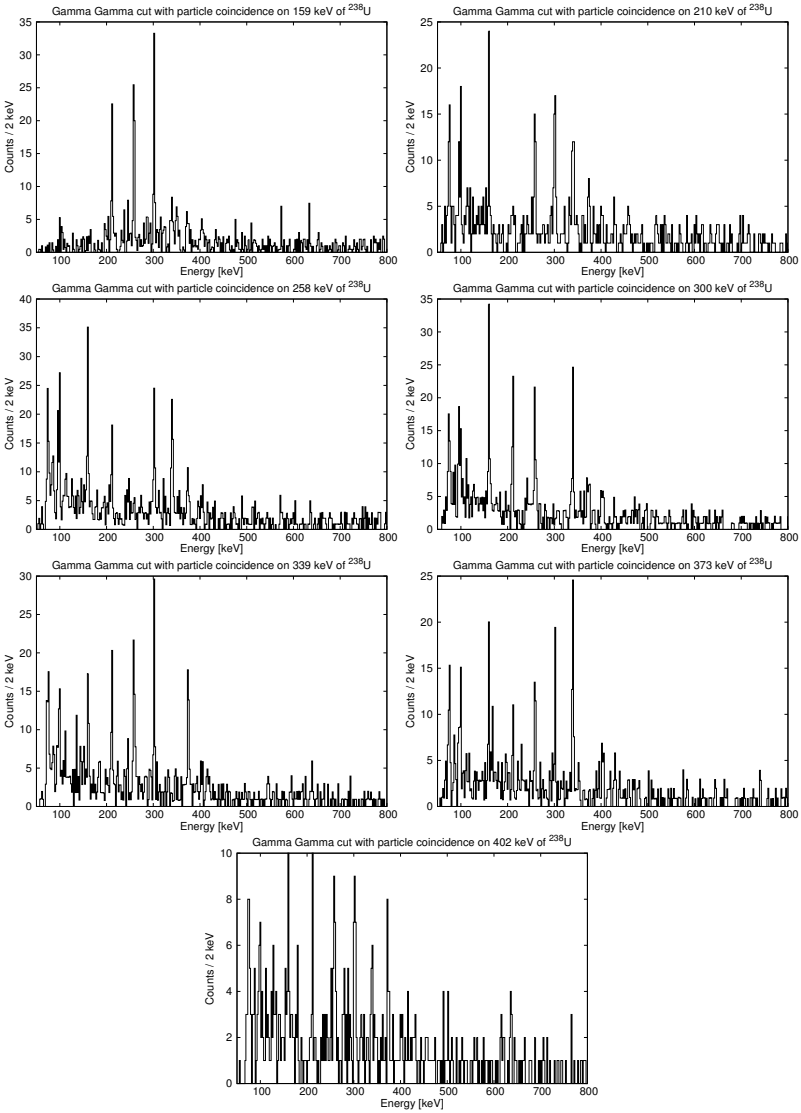

Figure 68: $\gamma\gamma$ coincidence spectra with particle coincidence for ^{238}U. The energies of the cuts are indicated in the title of the spectra.

One neutron transfer channel The one neutron transfer reaction channel

$$^{136}\mathrm{Xe}(^{238}\mathrm{U},^{239}\,\mathrm{U'})^{135}\mathrm{Xe'}$$

is the reaction with highest cross section with neutron transfer and neutron pickup. The unstable even–odd nucleus ^{135}Xe was identified in PRISMA. The survival of the complementary neutron pickup nucleus ^{239}U is not assured because the excited ^{239}U nucleus may decay instantaneously via neutron emission or fission, depending on the excitation energy with respect to the neutron separation energy and the fission barrier. The neutron separation energy S_n of ^{239}U is 4.81 MeV [84] and the fission barrier B_f is 6.21 MeV [86].

The peaks fitted in the Doppler corrected single spectrum of ^{135}Xe and the corresponding data is summarized in table 22. The single spectrum with a prompt time cut on AGATA and PRISMA is shown in figure 70. A level scheme for the identified peaks is drawn in figure 69. All known observed lines are connected or directly decay into the ground state or into the isomeric state at 526.6 keV with a lifetime of 15.3 minutes. The isomeric state could not be seen in the data.

This Work			Literature [81, 87]		
E_γ [keV]	FWHM [keV]	Peak area	E [keV]	E_γ [keV]	J^π
243.20 (96)	2.27 (17)	1016 (4)	-	-	-
250.20 (16)	2.27 (17)	500 (4)	-	-	-
288.737 (65)	2.22 (15)	3234 (163)	288.455 (15)	288.451 (16)	$\frac{1}{2}^+$
298.866 (72)	1.97 (28)	2158 (111)	2356.5 (8)	298.1 (6)	-
310.24 (11)	1.97 (28)	1314 (143)	2058.4 (6)	309.9 (4)	$\left(\frac{19}{2}^-\right)$
513.084 (78)	2.91 (18)	1495 (81)	2570.7 (8)	512.3 (6)	-
599.76 (15)	3.02 (30)	698 (69)	3169.9 (9)	599.2 (6)	-
609.32 (22)	2.98 (32)	544 (81)	-	-	-
650.60 (28)	5.29 (57)	1466 (184)	1781.39 (3)	649.84 (4)	$\left(\frac{11}{2}^+\right)$
813.79 (14)	4.62 (37)	1310 (89)	3169.9 (9)	813.4 (9)	-
1132.167 (93)	4.79 (21)	5731 (122)	1131.512 (11)	1131.511 (10)	$\frac{7}{2}^+$
1222.34 (17)	5.06 (39)	3792 (105)	1748.5 (3)	1221.9 (4)	$\left(\frac{15}{2}^-\right)$
1260.68 (33)	5.77 (80)	1373 (115)	1260.413 (13)	1260.409 (17)	$\frac{5}{2}^+$
1447.6 (15)	5.5 (13)	226 (134)	1448.36 (3)	1448.35 (10)	$\left(\frac{3}{2}^+\right)$
1457.37 (62)	5.5 (13)	1143 (190)	1457.566 (10)	1457.56 (10)	$\frac{5}{2}^+$

Table 22: γ-ray lines identified in the single spectrum of ^{135}Xe. Literature values are taken from [81, 87].

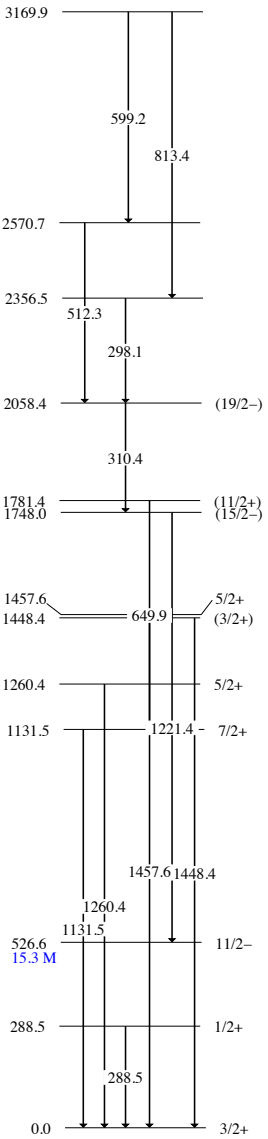

Figure 69: Level scheme for the γ-rays seen in the single spectrum of ^{135}Xe. Literature values are taken from [81, 87].

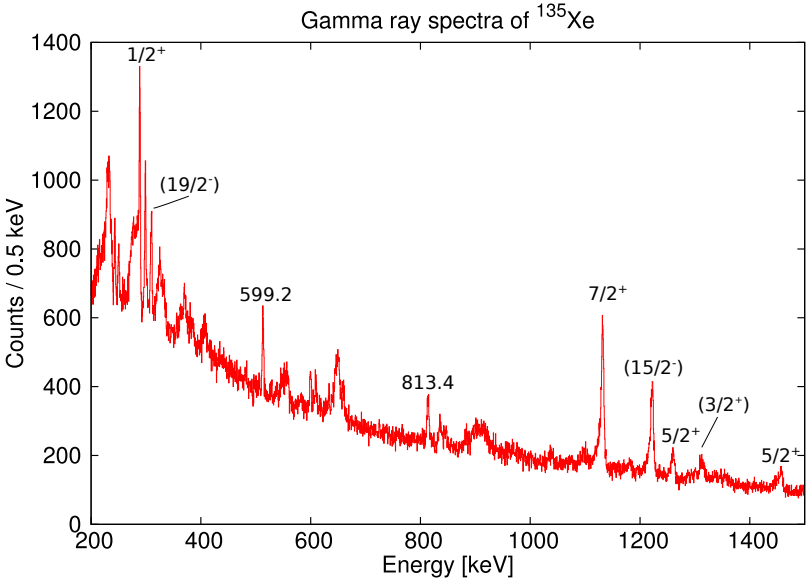

Figure 70: Doppler corrected γ-ray spectrum of ^{135}Xe with a time cut on the prompt peak between PRISMA and AGATA. The identified peaks are listed in table 22.

The peak at 650 keV is on top of a broader wrongly corrected background peak and could not be fitted very well. The unknown peaks at 243.2 keV, 250.2 keV and 609.32 keV are having reasonable energy resolutions (FWHM) and peak areas. The $\gamma\gamma$ analysis did not work properly for the unidentified transitions, as the statistics were to low.

The recoil nucleus of the reaction is ^{239}U. The fitted data from the single spectrum shown in figure 71 are listed in table 23. The corresponding level scheme is shown in figure 72. The even odd–nucleus has a multi-band structure and the reported transitions are most often found either in the x-ray region or at energies above 500 keV. In the spectrum lines of ^{238}U at the energies 159, 210, 258, 300, 339, 373 and 403 keV are visible. Many peaks of ^{238}U show a right tailing. This might result from a slightly wrong Doppler correction, as in the calculations the ^{239}U nuclei was assumed. In most other nuclei, where one could see a contamination of ^{238}U, this behaviour cannot be seen. In the listed data in table 23 at the energies of 210 and 300 keV a second peak was fitted close to the ^{238}U energies.The fits are marked with a $\star$ in the table.

A γ-ray spectrum with a cut on the particle coincidence registered between the DANTE detector and MCP of PRISMA is shown in figure 73. In the spectrum at the energy 210 keV and close to 303 keV two peaks close to the ^{238}U lines can be seen. This is another confirmation of the peaks marked with a $\star$ in table 23. A peak at 182.19(23) keV emerges from the background, that was not visible before.

As shown before the Q_r value might also clean the spectra, especially as the neutron separation value of 4.81 MeV is rather low. This was investigated by placing cuts for minimum Q_r values. The resulting spectra are shown in figure 74. In figure 75 the particle coincidence was request in addition to the minimum Q_r value. In both spectra the number of counts is normalized to the total number of counts in the spectrum multiplied with 1000 and the different spectra are shifted by 1 to be better visible. With the Q_r value cuts the peaks which were already visible in the single spectrum, are observed with an improved peak to total ratio. Results are given in table 24. The peak at 133.8 keV is the decay of an isomeric level with a half life of 780 ns. The peak at 194.74 is caused by the weakest decay branch of the level at 292.6 keV. To illustrate the behaviour of the peaks for

This Work			Literature [81]		
E_γ [keV]	FWHM [keV]	Peak area	E [keV]	E_γ [keV]	J^π
159.137 (37)	2.073 (85)	2858 (102)	^{238}U	-	-
167.49 (10)	1.30 (22)	445 (644)	-	-	-
189.89 (12)	1.05 (21)	285 (2)	-	-	-
201.97 (18)	2.82 (47)	901 (118)	-	-	-
210.677 (50) ⋆	2.34 (11)	4238 (187)	^{238}U	-	-
212.79 (10) ⋆	2.34 (11)	1894 (158)	-	-	-
249.506 (83)	2.03 (20)	2133 (124)	292.5872 (20)	250.072 (5)	$\left(\frac{7}{2}^-\right)$
258.094 (44)	3.06 (13)	5019 (160)	^{238}U	-	-
270.46 (20)	2.97 (50)	793 (141)	-	-	-
275.02 (20)	1.49 (22)	260 (2)	-	-	-
277.13 (14)	1.49 (22)	429 (2)	-	-	-
291.81 (37)	3.02 (22)	744 (154)	292.5872 (20)	292.587 (2)	$\left(\frac{7}{2}^-\right)$
294.42 (30)	3.02 (22)	1006 (155)	-	-	-
300.55 ⋆	3.02 (22)	2706 (292)	^{238}U	-	-
303.1 ⋆ (13)	3.02 (22)	295 (246)	-	-	-
313.51 (17)	2.04 (40)	679 (113)	-	-	-
333.21 (17)	3.90 (20)	1342 (96)	-	-	-
339.07 (13)	3.90 (20)	1728 (101)	^{238}U	-	-
349.84 (20)	3.48 (22)	980 (92)	-	-	-
367.12 (24)	3.48 (22)	654 (82)	-	-	-
373.14 (15)	3.48 (22)	1115 (88)	^{238}U	-	-
403.09 (37)	3.3 (17)	633 (175)	^{238}U	-	-

Table 23: γ-ray lines identified in the single spectrum of ^{239}U. Literature values are taken from [81]. Contaminations from ^{238}U are marked at the level energy with ^{238}U. Energies marked with a ⋆ were fitted with two close peaks simultaneously.

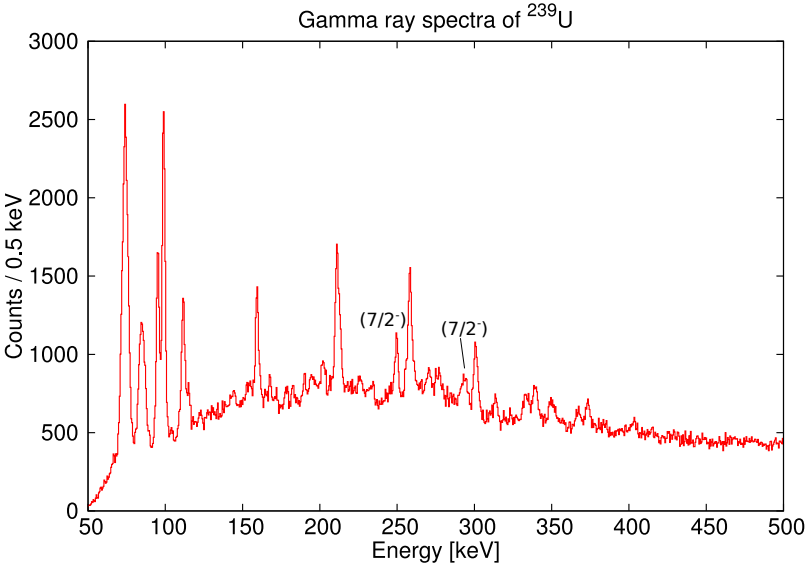

Figure 71: γ-ray spectrum of ^{239}U with a time cut on the prompt peak between PRISMA and AGATA. The identified peaks are listed in table 23.

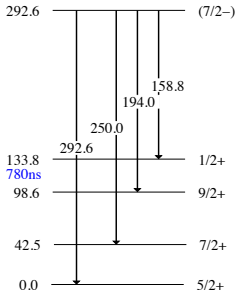

Figure 72: Level scheme for the γ-rays seen in the single spectrum of ^{239}U. The lines with an energy of 133.6 and 194.74 keV are only seen after a cut on the Q_r value.

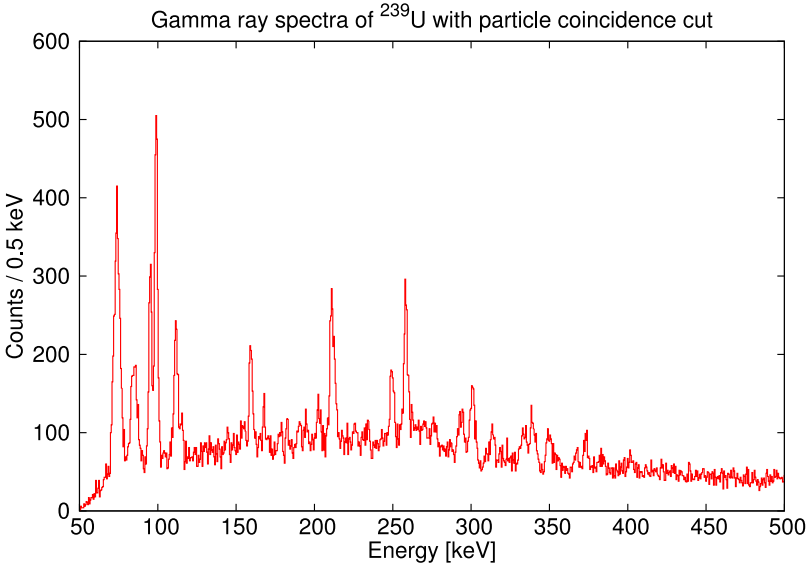

Figure 73: γ-ray spectrum of ^{239}U with a time cut on the prompt peak between PRISMA and AGATA and an additional cut on the coincidence between particles.

different Q_r values, the left plot of figure 76 shows the area of the peak at an energy of 250 keV depending on the condition on the Q_r value. In the right plot of figure 76 for the same cuts the peak to total ratio is shown. While the total number of counts in the peak decrease for higher Q_r values, the peak to total ratio rises. Three different conditions were applied: (i) no time cut (red), (ii) a cut on the prompt time peak between AGATA and PRISMA (blue) and (iii) an additional time cut on the particle coincidence (violet).

For both nuclei of the reaction the $\gamma\gamma$ analysis was not applicable anymore as the statistics were to low. This is also true for $\gamma\gamma$ matrices with applied Q_r value cuts. Due to low statistics no reliable results could be extracted.

Nearly all peaks in the single spectrum of ^{135}Xe were identified to be transitions of ^{135}Xe. Demonstrating that the PRISMA analysis

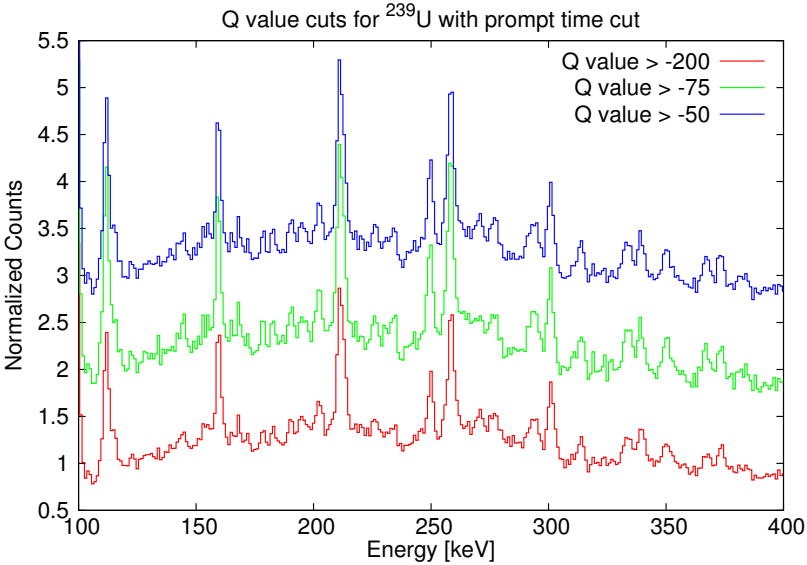

Figure 74: Cuts on the Q value for ^{239}U with a time cut on the prompt peak between AGATA and PRISMA

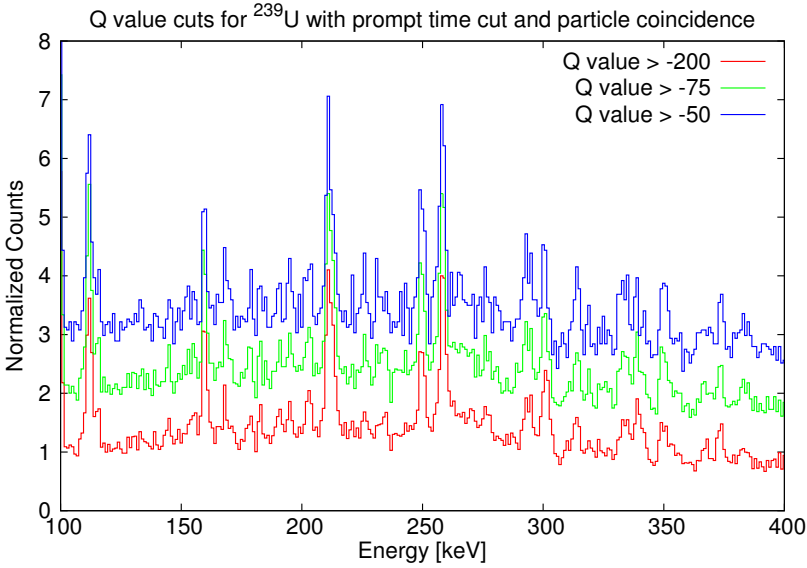

Figure 75: Cuts on the Q_r value for ^{239}U with a time cut on the prompt peak between AGATA and PRISMA and particle coincidence

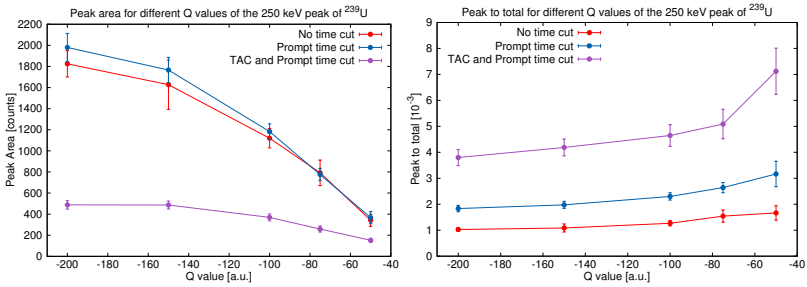

Figure 76: Peak area (left) and ratio of peak to total (right) of the peak at 250 keV of ^{239}U for different Q values and time cuts.

This Work			Literature [81]		
E_γ [keV]	FWHM [keV]	Peak area	E [keV]	E_γ [keV]	J^π
133.6 (21)	1 (-)	30 (141)	133.7990 (10)	133.799 (1)	$\frac{1}{2}^+$
144.20 (19)	1.75 (51)	226 (56)	-	-	-
177.98 (18)	1.74 (35)	175 (36)	-	-	-
182.19 (23)	1.74 (35)	174 (39)	-	-	-
194.74 (65)	4.4 (11)	281 (58)	292.5872 (20)	193.956 (25)	$\left(\frac{7}{2}^-\right)$
225.60 (25)	2.31 (26)	227 (41)	-	-	-
230.20 (36)	2.31 (26)	141 (40)	-	-	-
233.55 (23)	2.31 (26)	247 (41)	-	-	-

Table 24: γ-ray lines identified in the single spectrum of ^{239}U with applied Q_r value cut. Literature values are taken from [81].

worked fine. Only three lines could be identified as candidates for new transitions: 243.2 keV, 250.2 keV and 609.32 keV. The highest observed level energy is 3169.9 keV and the highest spin is $(19/2^-)$. For the neutron-odd reaction partner ^{239}U only a few transitions could be identified. This is expected due to the high level density, low transition energies favour in most cases decays via electron conversion. Cuts on the particle coincidence and the Q_r value cleaned the spectra and, especially for the cut on Q_r value, additional peaks show up in the spectra. The highest identified level energy is 292.6 keV and the highest spin is $(9/2^-)$.

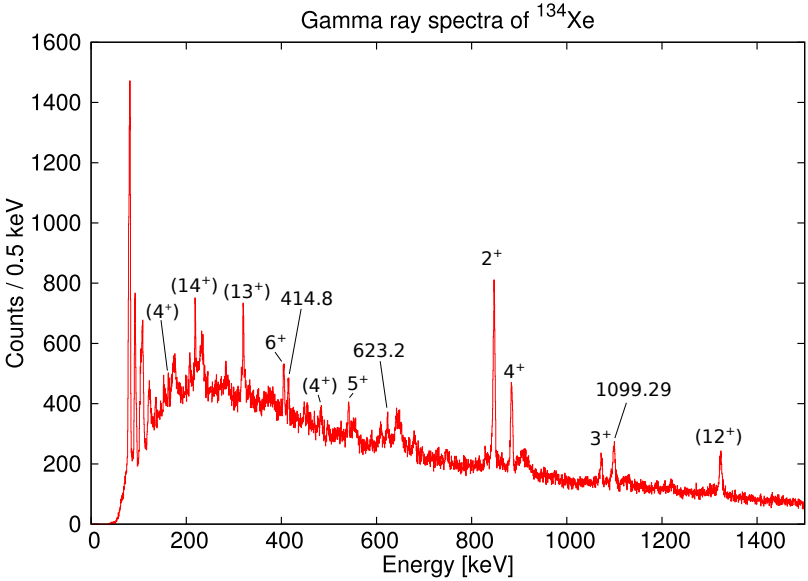

Figure 77: Doppler corrected γ-ray spectrum of ^{134}Xe with a time cut on the prompt peak between PRISMA and AGATA. The identified peaks are listed in table 25.

Two neutron transfer channel The transfer of two neutrons

$$^{136}\mathrm{Xe}(^{238}\mathrm{U},^{240}\,\mathrm{U'})^{134}\mathrm{Xe'}$$

is the reaction channel with the second highest cross section for neutron transfer. The stable even-even ^{134}Xe nucleus was identified in PRISMA. The survival of the complementary ^{240}U is not assured as the excited nucleus may decay instantaneously via neutron emission or fission. The neutron separation energy of ^{240}U is 5.93 Mev [84] and the fission barrier is 6.38 MeV [86]. The single spectrum of ^{134}Xe is shown in figure 77, the fitted peaks and the corresponding data are summarized in table 25, the partial level scheme is shown in figure 78.

The first transitions from the low lying states up to spin 6^+ and an excitation energy of 2272.0 keV are clearly observed. Intensities are in agreement with know literature values and the level scheme.

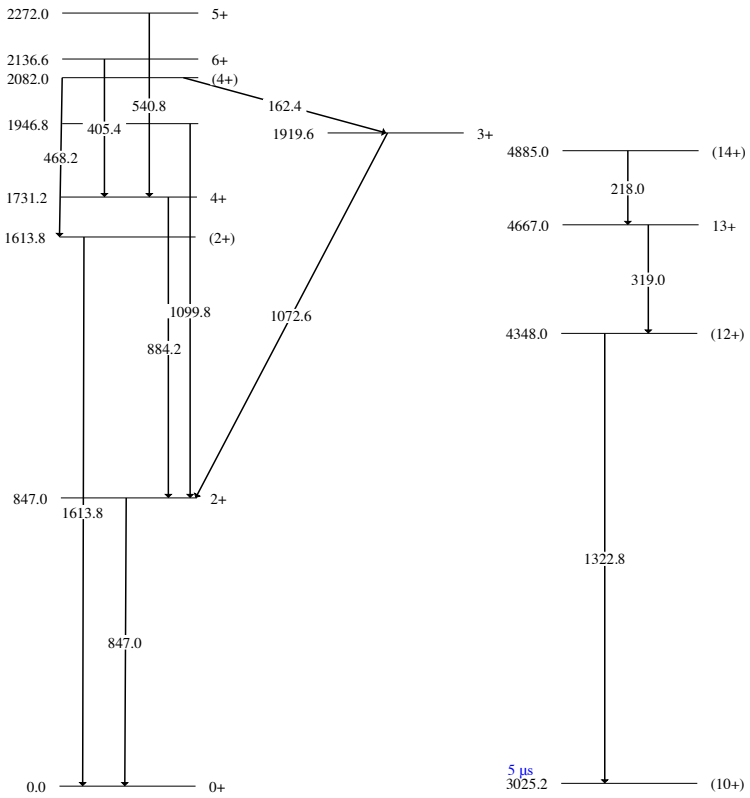

Figure 78: Level scheme of ^{134}Xe. Right plot shows the observed decays ending in the ground state [81]. Left plot shows the observed decays that stop at the not observed isomeric state at 3025 keV as proposed in [88].

The results on ^{134}Xe demonstrate the competitiveness of the actual measurement with other high efficient and selective experiments. The γ-ray lines at 218.8, 319.9 and 1323.83 keV were reported to be decays of states attributed to ^{135}Xe in [87] in 2007. The experiment is based on $\gamma\gamma$ coincidence of two reactions: fission of a ^{226}Th nucleus formed in a fusion-fission reaction and as an evaporation residue in the ^{136}Xe$(n, 2n\gamma)^{135}$Xe reaction. The γ-rays of the fusion-fission reaction were measured using the GAMMASPHERE array at the Lawrence Berkeley National Laboratory. The γ-rays of the evaporation reaction were measured with the GEANIE spectrometer [89] at the Los Alamos Neutron Science Center Weapons Neutron Research facility. In both experiments the γ-ray emitting nuclei were not directly identified and the assignment to ^{135}Xe was tentative. The authors reported even more γ rays from high spin states attributed to ^{135}Xe that are visible in the one neutron transfer channel of our experiment which are listed in table 22.

Two years later the γ-rays with an energy of 218, 320 and 1323 keV were reported to be decays of ^{134}Xe [88]. This time the γ-rays were measured with the EXOGAM Compton-suppressed segmented clover detectors. The reaction products of the fusion-fission reaction ^{12}C(^{238}U, ^{134}Xe)Ru were identified with the magnetic spectrometer VAMOS. However the statistics in this spectrum is rather limited and below the achieved results from our experiment. In this work the lines are well above the background level and the reaction products were clearly identified.

In the previous experiment from 2007 two more lines were reported to be in coincidence with the 1323 keV line: 323.1 and 541.8 keV. The 541.8 keV transition is expected to be in coincidence with the 319.9 keV and the 1323 keV transition. A cut on the 1323 keV line is shown in figure 79. The coincidence with the lines at 218 and 320 keV is visible in the $\gamma\gamma$ spectrum. The other two reported coincidence with lines at 323.1 keV and 541.9 keV are not observed. Gating on the line at 541 keV only shows a clear coincidence with the decay of the first 2^+ corroborating the assumption that the peak at 541.2 keV corresponds to the decay of the 5^+ state given in table 25.

The broad line at 323.1 keV in the single spectrum is shown in figure 80. It consists of a peak at 319.9 keV and a line at 323.4(3) keV. The

This Work			Literature [81, 88]		
E_γ [keV]	FWHM [keV]	Peak area	E [keV]	E_γ [keV]	J^π
162.40 (15)	1.55 (32)	308 (57)	2082.0 (6)	162.35 (-)	(4^+)
218.835 (70)	1.78 (15)	890 (7)	4885.0	218	(14^+)
319.934 (80)	2.97 (26)	1994 (109)	4348.0	320	(13^+)
405.13 (12)	3.08 (20)	1070 (77)	2136.61 (4)	405.451 (20)	6^+
414.78 (15)	3.08 (20)	751 (69)	-	-	-
448.25 (39)	2.83 (47)	361 (66)	-	-	-
454.36 (31)	2.83 (47)	280 (59)	-	-	-
469.43 (17)	1.07 (41)	132 (42)	2082.0 (6)	468.24 (-)	(4^+)
541.17 (15)	2.59 (33)	564 (64)	2272.01 (4)	540.825 (25)	5^+
623.20 (25)	2.5 (11)	550 (87)	2352.97 (3)	621.790 (25)	4^+
			2547.55 (4)	627.96 (3)	$4^+, 5^+$
847.173 (57)	4.33 (13)	5721 (109)	847.041 (23)	847.025 (25)	2^+
883.980 (70)	4.15 (14)	2365 (79)	1731.17 (3)	884.090 (25)	4^+
1072.67 (22)	3.91 (48)	803 (71)	1919.60 (3)	1072.55 (3)	3^+
1099.29 (17)	5.59 (45)	1742 (85)	1946.8 (7)	1099.77 (-)	-
1323.83 (21)	6.30 (56)	2296 (97)	4348.0	1323	(12^+)
1614.8 (13)	7.2 (48)	421 (124)	1613.80 (4)	1613.77 (3)	(2^+)

Table 25: γ-ray lines identified in the single spectrum of ^{134}Xe. Literature values are taken from [81, 88].

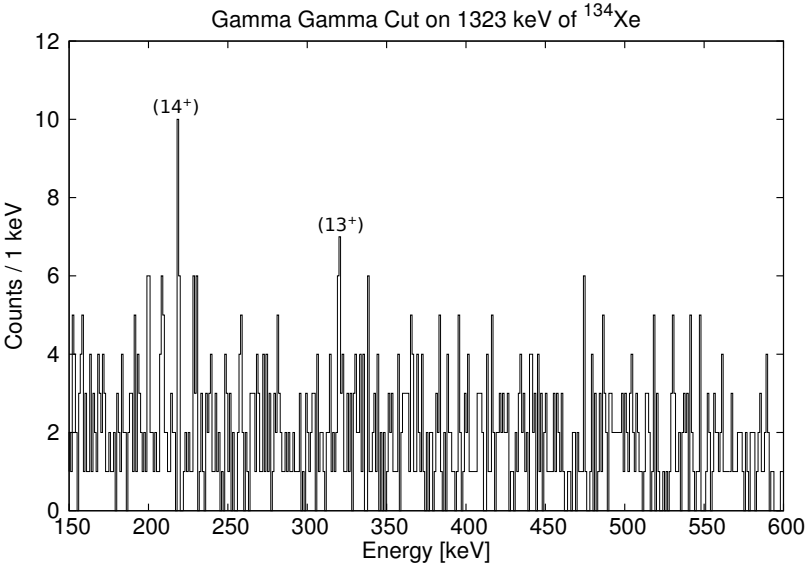

Figure 79: Time coincidence cut on the line at 1323 keV for ^{134}Xe

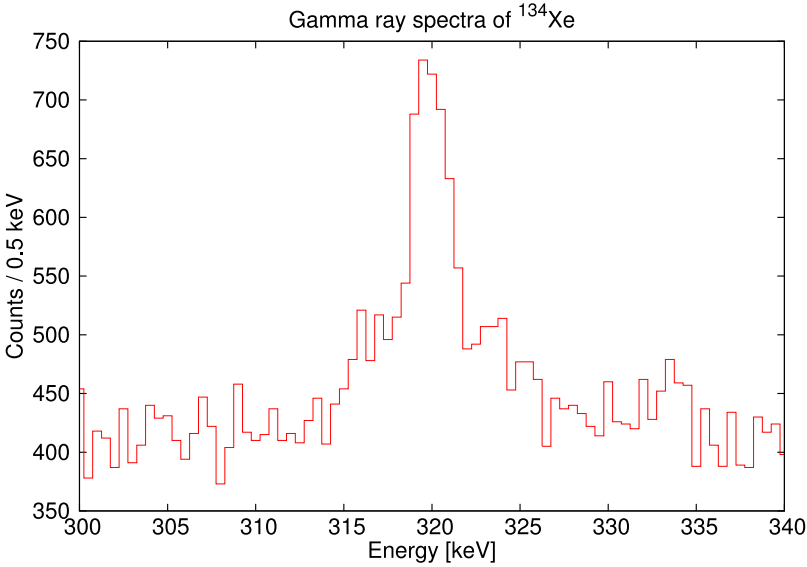

Figure 80: Doppler corrected γ-ray spectrum of ^{134}Xe with a time cut on the prompt peak between PRISMA and AGATA. Zoomed at the region around 320 keV.

line at 323.1 keV is expected to be in coincidence with 218.5 keV peak, but the cuts on the $\gamma\gamma$ matrix are not clean enough to verify this.

Although most of the lines were identified, some observed lines could not be found in the data. The unknown line at 414.78 keV shows a clear coincidence with the line at 1099.7 keV and a coincidence with the decay of the first 2^+ state. For the other two unidentified decays with energies of 448.3 and 454.4 kev the coincidences do not provide conclusive results.

The recoil nucleus of the reaction is ^{240}U. The single spectrum is shown in figure 81. The fitted peaks and the corresponding data of the single spectrum are listed in 26. The highest energies at 409.9 and 429.7 keV were only observable in a spectrum where conditions on the Q_r and particle coincidence were required. This will be described later. The contamination with lines from ^{238}U are not listed

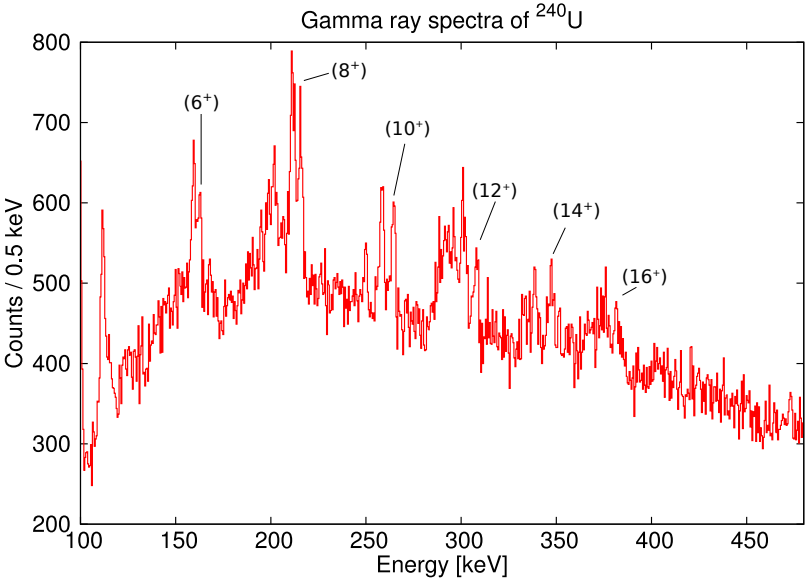

Figure 81: γ-ray spectrum of ^{240}U with a time cut on the prompt peak between PRISMA and AGATA.

in the table. The unknown lines at 201.40 and 249.86 keV are contaminations from ^{239}U caused by neutron evaporation from ^{240}U. A level scheme based on latest data from [81, 55, 53] is shown in figure 82. The excitation energies of the last four levels were calculated with the energies measured in this analysis.

Two additional conditions are applied in order to improve the peak to background ratio and to suppress the lines from the neighboring neutron evaporation channels. The first condition asks for a particle coincidence between DANTE and PRISMA. The second cut requires the Q_r value. The resulting spectra are shown in figure 83. The red spectrum is the normalized spectrum with the additional cuts. The blue spectrum is shifted 0.6 counts higher and is similar to the spectrum shown in 81. The better peak to total ratio is clearly visible. The lines of ^{238}U and ^{239}U are suppressed. In the red spectrum two new lines could be cleanly identified. At 275.45(20) keV a line with a

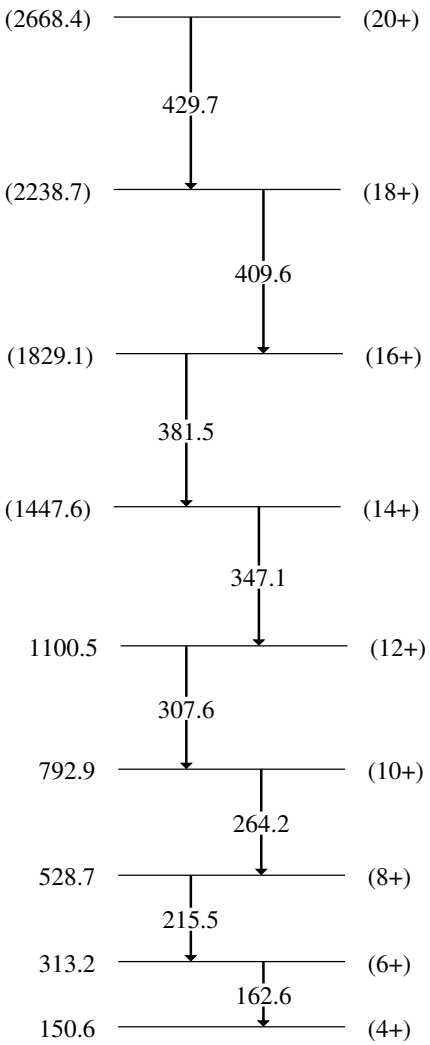

Figure 82: Level scheme of ^{240}U with data taken from [81, 55, 53]. The energies of the last four levels were recalculated with the energies measured in this analysis.

This Work			Literature [81], [55]		
E_γ [keV]	FWHM [keV]	Peak area	E [keV]	E_γ [keV]	J^π
162.23 (15)	2.09 (18)	500 (63)	313.19 (14)	162.6 (1)	(6^+)
201.40 (28)	2.40 (95)	380 (109)	-	-	-
215.32 (12)	2.55 (15)	892 (80)	528.69 (18)	215.5 (1)	(8^+)
249.86 (53)	1.2 (11)	378 (81)	-	-	-
264.50 (16)	1.54 (32)	897 (90)	792.9 (3)	264.1 (2)	(10^+)
307.66 (25)	2.29 (30)	267 (60)	1100.5 (4)	307.6 (3)	(12^+)
347.14 (20)	2.35 (43)	532 (80)	1441 (-)	345.3 (10)	(14^+)
381.25 (25)	1.65 (70)	192 (62)	1821 (-)	379.6 (10)	(16^+)
409.91 (65)	2.98 (94)	25 (11)	2238.7 (-)	409.91 (65)	(18^+)
429.68 (48)	2.39 (77)	25 (10)	2668.4 (-)	429.68 (48)	(20^+)

Table 26: γ-ray lines identified in the single spectrum of ^{240}U. Literature values are taken from [81, 55]. The last two energies could not be identified in the single spectrum, but in the spectrum where conditions on the Q_r and particle coincidence were set shown in figure 83.

36 (10) counts and at 337.26(29) keV another line with 30 (2) counts can be fitted. There are indications for lines at 431 and 445 keV, which are candidates for levels with higher spins of the ground state band. The $\gamma\gamma$ matrix has not enough statistics for firm conclusions.

The relationship between the γ-rays of the reaction products and the identification of the beam like particle in PRISMA could be clearly demonstrated for this reaction channel. For the ejectile nucleus the lines at 1323.2, 319.1 218.5, 323.1 and 541.8 are related to ^{134}Xe. In [87] these decays were tentatively reported to be decays of ^{135}Xe. However the results were revised in [88] and the lines were associated with ^{134}Xe transitions like in our analysis. For the recoil nucleus ^{240}U the first measurements of decays of the 14^+ to the 20^+ reported in [55] are confirmed with slightly different energies. Analysis conditions on the particle coincidence and the Q_r value improved the spectrum quality and suppressed the lines of ^{238}U and ^{239}U caused by neutron evaporation.

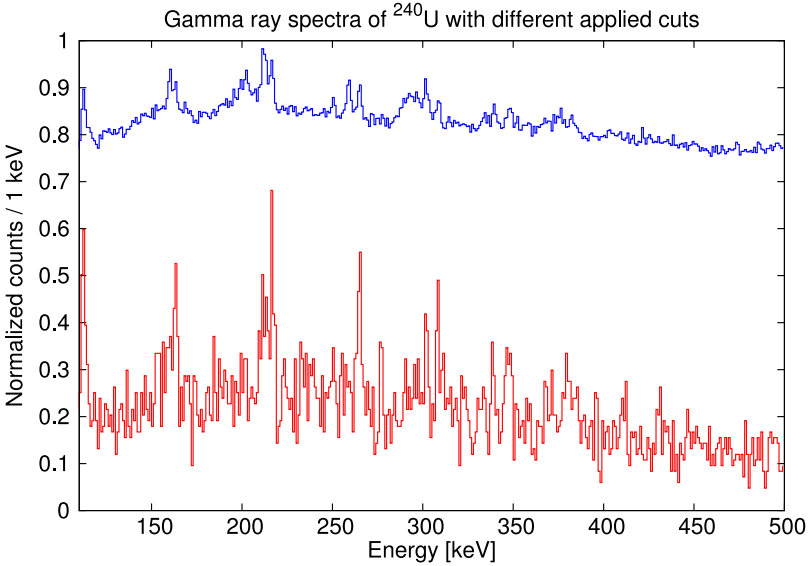

Figure 83: Normalized γ-ray spectra of ^{240}U with a time cut on the prompt peak between PRISMA and AGATA (blue) and with additional cuts on the particle coincidence and the Q_r value (red). The blue spectrum is shifted 0.6 counts above the red spectrum for a better comparison.

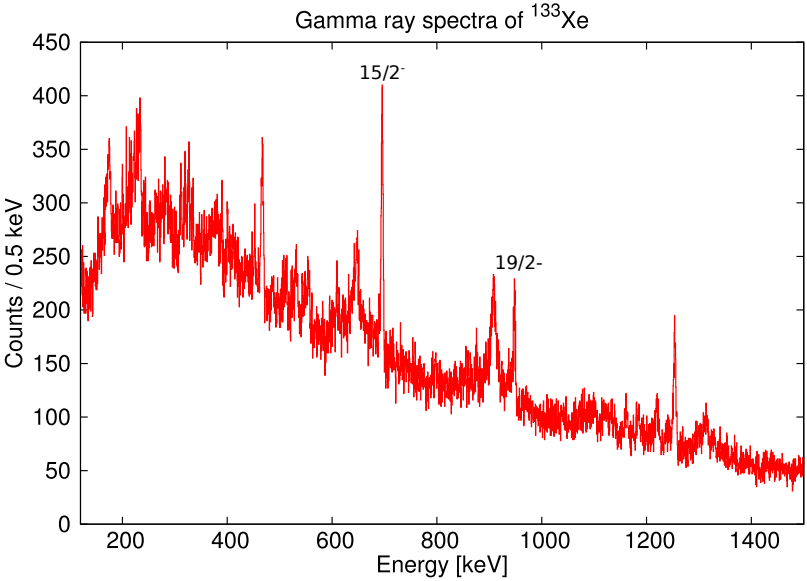

Figure 84: Doppler corrected γ-ray spectrum of ^{133}Xe with a time cut on the prompt peak between PRISMA and AGATA. The identified peaks are listed in table 27.

Three neutron transfer channel The three neutron transfer channel

$$^{136}\mathrm{Xe}(^{238}\mathrm{U},^{241}\,\mathrm{U'})^{133}\mathrm{Xe'}$$

populates the even-odd nucleus ^{133}Xe and excited states of the even-odd nucleus ^{241}U are expected to be accessible. Excited states of ^{241}U have not been observed yet. ^{133}Xe is an unstable nucleus decaying by β^- emission with a half life of 5.25 days. The single spectrum of ^{133}Xe with a cut on the prompt coincidence between AGATA and PRISMA is shown in figure 84, the data of the fitted peaks is summarized in table 27, a level scheme based on the available data [81] is given in figure 85.

The line at 452.53 keV has a similar energy as a decay of the $13/2^+$, however no other lines from the decay of the $13/2^+$ state are visible in the single spectrum. The strong line at 467.10 keV is coincident with

This Work			Literature [81]		
E_γ [keV]	FWHM [keV]	Peak area	E [keV]	E_γ [keV]	J^π
311.67 (25)	2.65 (47)	293 (2)	-	-	-
389.90 (18)	1.56 (38)	204 (46)	-	-	-
452.53 (28)	4.48 (85)	237	-	-	-
467.10 (20)	3.96 (47)	1492 (92)	-	-	-
531.54 (38)	5.38 (98)	519	-	-	-
554.94 (81)	4.1 (14)	939 (156)	-	-	-
695.539 (71)	4.01 (14)	1976 (2)	928.52 (20)	695.3 (2)	$\frac{15}{2}^-$
947.63 (15)	4.47 (32)	867 (51)	1876.3 (3)	947.8 (2)	$\frac{19}{2}^-$
1161.88 (54)	5.06 (45)	402 (44)	-	-	-
1184.56 (56)	5.06 (45)	395 (49)	-	-	-
1220.36 (42)	5.06 (45)	625 (53)	-	-	-
1253.99 (21)	5.06 (45)	1413 (66)	-	-	-

Table 27: γ-ray lines identified in the single spectrum of ^{133}Xe. Literature values are taken from [81].

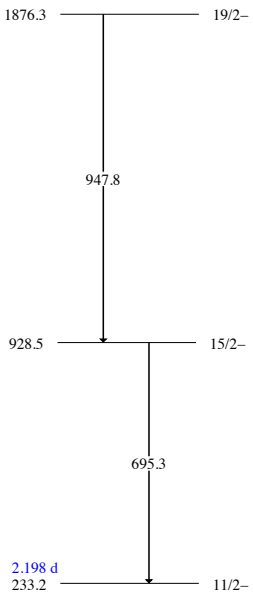

Figure 85: Level scheme for the γ-rays seen in the single spectrum of ^{133}Xe based on data taken from [81]

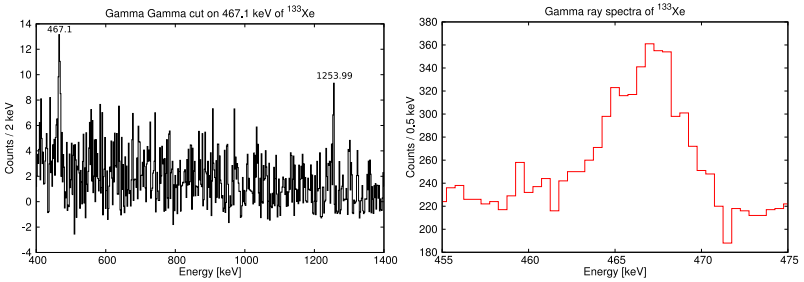

Figure 86: Doppler corrected coincident $\gamma\gamma$ spectrum of ^{133}Xe with an energy cut on 467.1 keV (left). Zoomed region of the spectrum shown in figure 84.

itself and with the line at 1253.99 keV. In the left picture of figure 86 the corresponding plot is shown. The single spectrum shown in the right plot of figure 86 shows a double structure of the peak. The fit routine yields peaks at 465.00(49) and 467.49(26) keV which explains the self coincidence. The line at 1253.99 keV is not known from decays of state of ^{133}Xe. The peak intensity at 554.94 keV is low and in the $\gamma\gamma$ analysis no coincidences are observed. The same is true for the other smaller peaks. Only the line at 1253.99 keV is in coincidence with a γ-ray with an energy of 467.1 keV.

Compared to the previous isotope where many decays especially with high spins were assigned only two lines in the spectrum of ^{133}Xe could be assigned properly. The highest excitation energy is 1876.3 and the highest spin is $\frac{19}{2}^-$.

Decays from the odd-neutron recoil nucleus ^{241}U has not been observed yet. There is no indication that it was produced in this experiment from the observed single γ-ray spectrum. The Doppler corrected spectrum for the recoils do mainly show transitions from ^{238}U, ^{239}U and ^{240}U which are expected from one- to three neutron evaporation of excited neutron transfer products. After applying Q_r value and particle coincidences the spectrum shown in figure 87 is obtained. The γ-ray lines at energies 144.5 keV, 238.5 keV and 287.5 keV indicated in the spectrum are strong and convincing candidates for transitions of ^{241}U. However, the line at 144.20 keV is also visible in the Q_r value

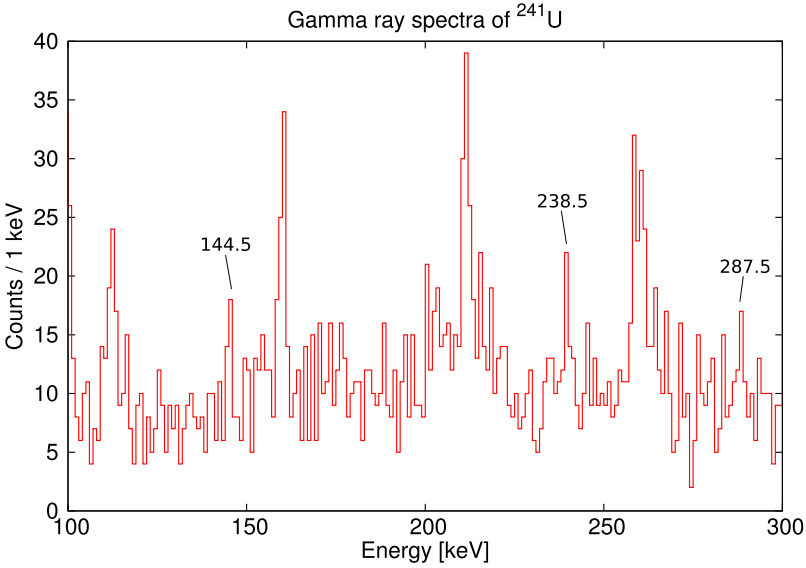

Figure 87: Doppler corrected γ-ray spectrum of ^{241}U with a time cut on the prompt peak between PRISMA and AGATA and additional cuts on particle coincidence and Q_r value

gated spectrum of ^{239}U. As the lines have low statistics and the nucleus ^{241}U has not been seen in any experiment this result should be taken as an indication.

Four neutron transfer channel The four neutron transfer channel

$$^{136}\mathrm{Xe}(^{238}\mathrm{U},^{242}\,\mathrm{U'})^{132}\mathrm{Xe'}$$

is selected by gating on the stable even-even nucleus ^{132}Xe identified in PRISMA. The recoil nucleus would be ^{242}U, where first results were reported in [54]. The neutron separation energy is not known and the fission barrier is 7.1 MeV [86]. The single spectrum of ^{132}Xe is shown in figure 88. The fitted peaks and the corresponding data is summarized in table 28. A level scheme is shown in figure 89.

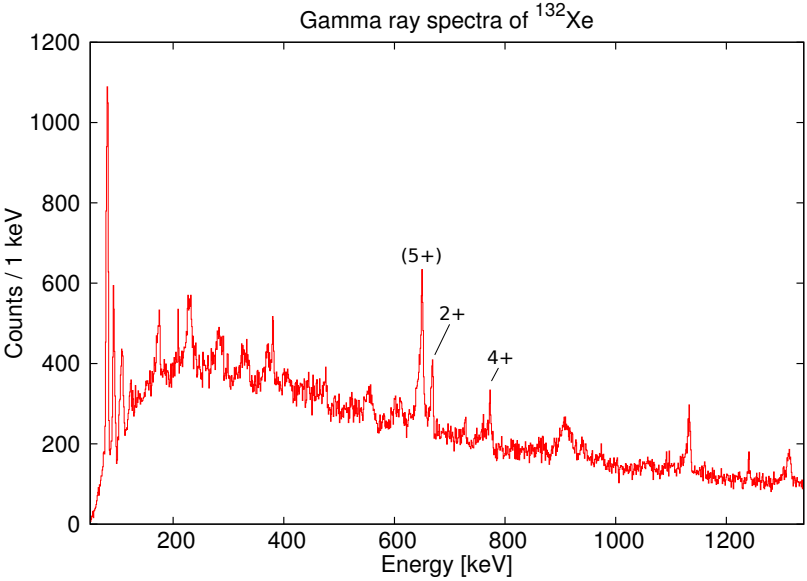

Figure 88: Doppler corrected γ-ray spectrum of ^{132}Xe with a time cut on the prompt peak between PRISMA and AGATA. The identified peaks are listed in table 28.

Only two connected lines could be identified in ^{132}Xe. The γ-rays with an energy of 380 and 1313.76 keV are contaminations from ^{136}Xe. The lines at 298.25 keV and 1133.15 keV are contaminations from ^{135}Xe. The line at 380.25 keV is identified to be the known decay of a 5^+ (see table 28). The corresponding peak area is large. The energy is similar to a wrongly Doppler corrected background line adding extra counts to the peak volume. If the assignment to the decay of the 5^+ level is right, another line with a similar intensity should be observed at 809.5 keV. However this line is not visible and therefore the assignment is tentative.

The unknown line at an energy of 1240.37 keV could correspond to a reported line at 1242.6(7) keV with a rather large error. However the reported level decays with a 5 time higher probability by emitting a γ-ray with an energy of 1049.6 keV. This transition is not observed in the spectrum.

This Work			Literature [81]		
E_γ [keV]	FWHM [keV]	Peak area	E [keV]	E_γ [keV]	J^π
208.93 (13)	1.38 (21)	237 (2)	-	-	-
298.25 (23)	1.64 (79)	130 (42)	-	-	-
380.25 (22)	2.74 (53)	647 (78)	-	-	-
649.97 (16)	4.45 (38)	2634 (135)	2613.45 (9)	650.5 (2)	5^+
668.09 (23)	4.45 (38)	1066 (74)	667.715 (2)	667.714 (2)	2^+
772.51 (26)	4.70 (79)	485 (14)	1440.323 (10)	772.60 (1)	4^+
1133.16 (26)	4.46 (57)	1273 (76)	-	-	-
1240.37 (22)	2.7 (11)	179 (39)	-	-	-
1313.76 (64)	7.1 (14)	1005 (78)	-	-	-

Table 28: γ-ray lines identified in the single spectrum of ^{132}Xe. Literature values are taken from [81].

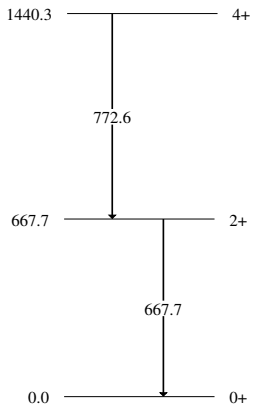

Figure 89: Level scheme for the γ-rays seen in the single spectrum of ^{132}Xe based on data taken from [81]

The highest excitation energy is 1440 keV and the highest observed spin is 4^+.

For the recoil nucleus ^{242}U two decays were reported in [54]. They are measured at an energy of 169.3 and 224.7 keV. In our spectra these decays cannot be observed and no other peaks are visible, despite contaminations of ^{238}U. Cuts on Q_r value and particle coincidence do not improve the results.

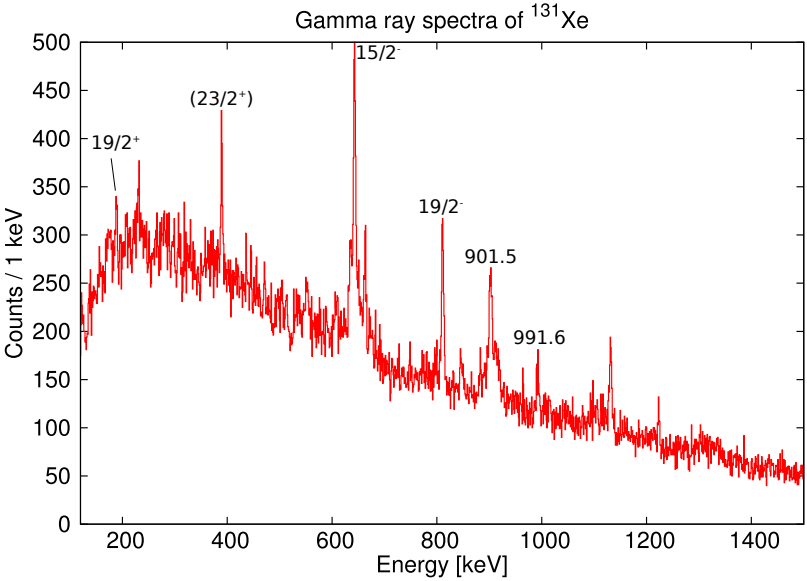

Figure 90: Doppler corrected γ-ray spectrum of ^{131}Xe with a time cut on the prompt peak between PRISMA and AGATA. The identified peaks are listed in table 29.

Five neutron transfer channel In the five neutron transfer channel

$$^{136}\mathrm{Xe}(^{238}\mathrm{U},^{243}\,\mathrm{U'})^{131}\mathrm{Xe'}$$

the stable even-odd nucleus ^{131}Xe was populated and identified by PRISMA. The $_\gamma$-ray spectrum with a gate on the prompt time peak between AGATA and PRISMA is shown in figure 90. The fitted peaks found in the single spectrum and the corresponding data is summarized in table 29. The level scheme based on the data from [81] is shown in figure 91.

In figure 92 the zoomed energy spectra around 642 and 901 keV are shown: left plots show the situation around 642 keV and the right plots around 901 keV. The top plots are the single spectra with a gate on the prompt coincidence between PRISMA and AGATA; for the bottom plots an extra condition was requested for the coincidence

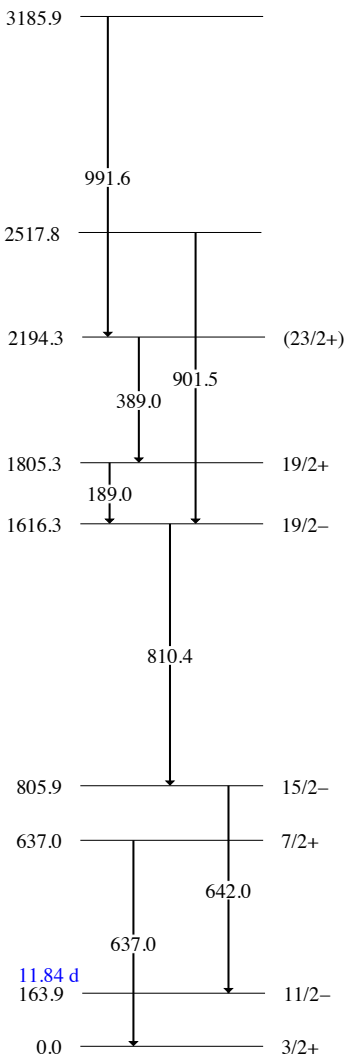

Figure 91: Level scheme for the γ-rays seen in the single spectrum of ^{131}Xe based on data taken from [81]

This Work			Literature [81]		
E_γ [keV]	FWHM [keV]	Peak area	E [keV]	E_γ [keV]	J^π
188.45 (43)	3.13 (83)	259 (80)	1805.3 (3)	189.1 (2)	$\frac{19}{2}^+$
389.18 (15)	3.36 (44)	551 (53)	2194.3 (5)	389.0 (3)	$\left(\frac{23}{2}^+\right)$
634.41 (32)	4.88 (34)	489 (66)	636.990 (4)	636.989 (4)	$\frac{7}{2}^+$
642.74 (12)	4.88 (34)	1779 (66)	805.93 (20)	642.0 (2)	$\frac{15}{2}^-$
650.41 (42)	4.88 (34)	473 (58)	1621.02 (24)	649.8 (2)	-
662.78 (26)	4.88 (34)	678 (56)	-	-	-
810.79 (15)	4.75 (38)	880 (56)	1616.3 (3)	810.4 (2)	$\frac{19}{2}^-$
900.90 (41)	4.25 (76)	419 (73)	2517.8 (4)	901.5 (3)	-
904.52 (48)	4.25 (76)	327 (65)	-	-	-
992.04 (46)	5.5 (11)	246 (42)	3185.9 (6)	991.6 (3)	-
1131.27 (26)	4.52 (70)	500 (48)	-	-	-
1222.88 (32)	3.18 (68)	135 (27)	-	-	-

Table 29: γ-ray lines identified in the single spectrum of ^{131}Xe. Literature values are taken from [81].

between DANTE and PRISMA. The line at 642.74 is a dublett with a second smaller peak at the left side with an energy of 634.34(41) keV. The lines at 900.9 and 904.52 keV also form a close dublett. The energy resolutions (FWHM) of the two lines compare well with the other decays.

Most of the lines listed in table 29 were identified to belong to ^{131}Xe. The decay of the $15/2^-$ level with the corresponding line at 642.74 keV to the long-lived isomeric state at 163.9 keV is clearly visible in the spectrum. The other observed decays of levels above the $15/2^-$ level are connected in the level scheme up to an excitation energy of 3185.9 keV. This excitation energy is the highest yet observed excitation energy for this nucleus according to [81]. The highest observed spin is $(23/2^+)$.

The unknown transition with an energy of 662.78 keV observed in the single spectrum can be associated with ^{131}Xe via the coincidence relationship with the decay of the $15/2^-$ level at an energy of 642.0 keV. As mentioned above the line at 637.0 keV is a small peak close to the line at 642.74 keV. The measured energy is 2.5 keV away from the value of the assigned transition. The not assigned γ-rays with an energy of 650.41 keV, 1131.27 keV and 1222.88 keV could be contaminations or candidates for new transitions in ^{131}Xe.

The recoil nucleus ^{243}U had not been observed yet and there are no hints for lines in the corresponding spectrum.

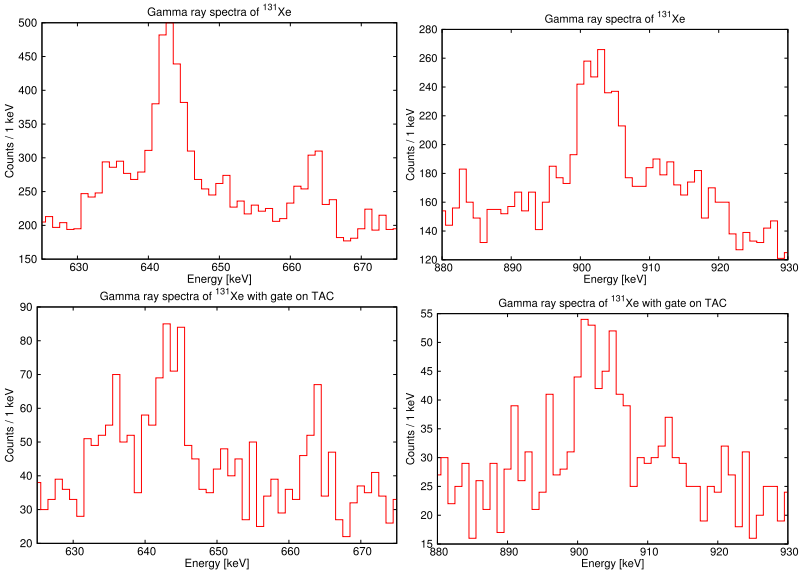

Figure 92: Doppler corrected γ-ray spectra of ^{131}Xe with a time cut on the prompt peak between PRISMA and AGATA (top). Additional cuts on the right peak of the TAC between PRISMA and DANTE are requested (bottom).

Six neutron transfer channel The γ-ray spectrum of the stable even-even nucleus ^{130}Xe produced via the reaction

$$^{136}\mathrm{Xe}(^{238}\mathrm{U},^{244}\,\mathrm{U'})^{130}\mathrm{Xe'}$$

is shown in figure 93. The corresponding data is summarized in table 30. A level scheme connecting the identified transitions is given in figure 94. The transitions from the first 2^+ state up to spin (14^+) are visible in the spectrum. In addition transitions from states with negative parity with spins from (5^-) to (15^-) are observed. The line at 431.73 keV fits for two transitions. It is possibly the superposition of two decays as both levels are visible. The highest excitation energy is 4.97 MeV and the highest spin is (15^-).

Only the weak line at 643.41 keV can not be associated to known transitions. The line has low statistics and sits together with the close-lying peak at 647.94 keV on a wrongly Doppler corrected background peak.

The numerous assigned transitions in the case of ^{130}Xe demonstrate the high quality of the mass separation capability of the PRISMA spectrometer. No indications for new lines could be identified in the recoil gated spectra.

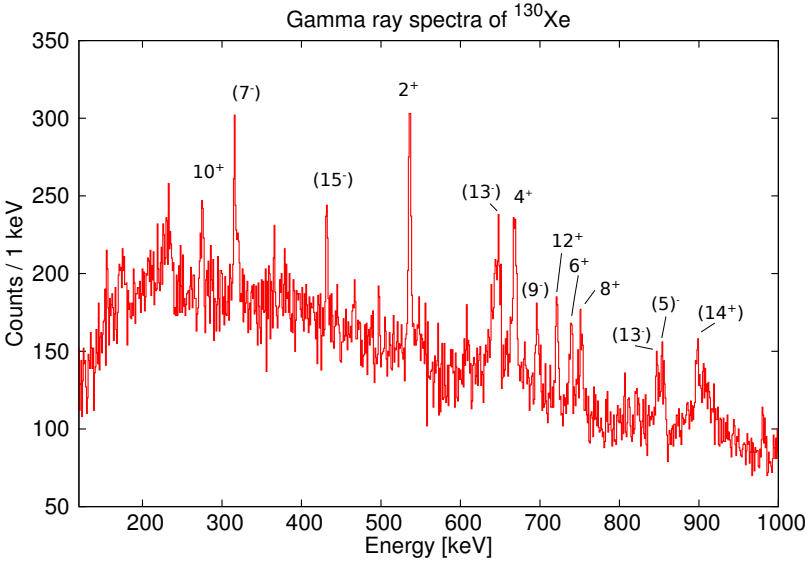

Figure 93: Doppler corrected γ-ray spectrum of ^{130}Xe with a time cut on the prompt peak between PRISMA and AGATA. The identified peaks are listed in table 30.

This Work			Literature [81]		
E_γ [keV]	FWHM [keV]	Peak area	E [keV]	E_γ [keV]	J^π
275.39 (46)	2.22 (84)	265 (57)	2972.41 (15)	275.42 (12)	10^+
315.53 (14)	1.57 (27)	172 (26)	2375.21 (10)	315.52 (11)	$\left(7^-\right)$
431.73 (24)	2.78 (49)	228 (36)	4971.6 (3)	431.5 (2)	$\left(15^-\right)$
			2375.21 (10)	431.3 (2)	$\left(7^-\right)$
536.07 (12)	3.72 (29)	651 (44)	536.068 (6)	536.066 (6)	2^+
643.41 (44)	4.10 (57)	254 (40)	4184.7 (3)	642.5 (2)	-
647.94 (34)	4.10 (57)	316 (44)	4540.13 (20)	646.8 (2)	$\left(13^-\right)$
668.21 (27)	4.74 (61)	528 (54)	1204.614 (16)	668.536 (9)	4^+
696.47 (45)	5.0 (14)	243 (54)	3071.49 (16)	696.2 (2)	$\left(9^-\right)$
721.20 (22)	3.66 (44)	278 (2)	3693.27 (18)	720.84 (13)	12^+
738.91 (33)	3.76 (71)	211 (35)	1944.140 (12)	739.512 (10)	6^+
752.6 (15)	6.7 (38)	347 (171)	2696.95 (12)	752.77 (14)	8^+
821.70 (56)	4.6 (11)	94 (34)	3893.35 (19)	821.9 (2)	$\left(11^-\right)$
847.05 (52)	4.91 (66)	180 (35)	4540.13 (20)	846.8 (2)	$\left(13^-\right)$
853.86 (52)	4.91 (66)	208 (34)	2059.60 (5)	854.99 (10)	$(5)^-$
898.00 (51)	5.4 (12)	230 (40)	4590.5 (3)	897.2 (2)	$\left(14^+\right)$

Table 30: γ-ray lines identified in the single spectrum of ^{130}Xe. Literature values are taken from [81].

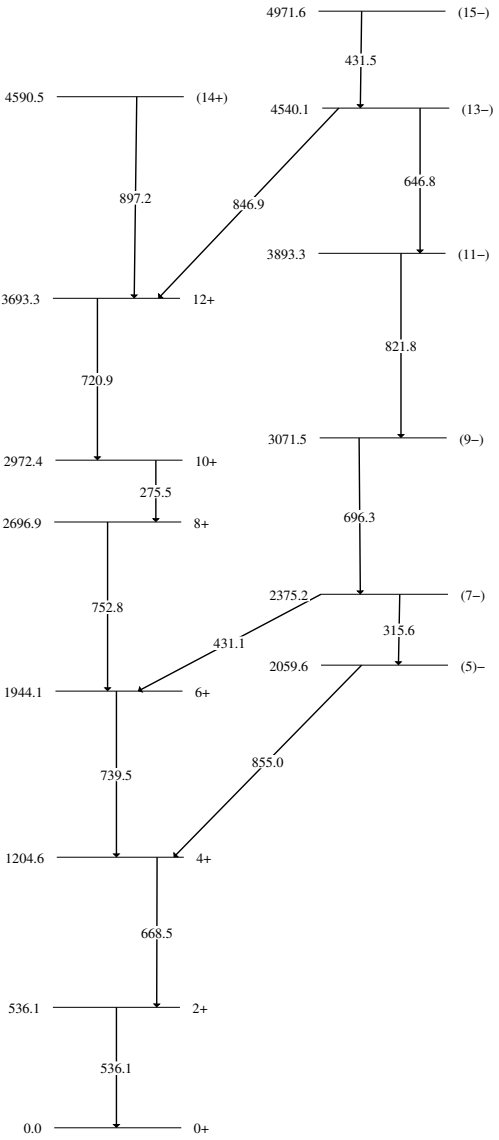

Figure 94: Level scheme for the γ-rays seen in the single spectrum of ^{130}Xe based on data taken from [81].

Seven neutron transfer channel In the seven neutron transfer channel

$$^{136}\mathrm{Xe}(^{238}\mathrm{U},^{245}\,\mathrm{U'})^{129}\mathrm{Xe'}$$

γ-ray lines of the decays of the stable even-odd nucleus ^{129}Xe can be identified in the γ-ray spectrum shown in figure 95. As in the other spectra before, a cut on the prompt time peak between AGATA and PRISMA was applied. The fits and the corresponding data is summarized in table 31. A partial level scheme is shown in figure 96. The transition from the $(19/2^-)$ to the $(15/2^-)$ is clearly observed as well as the transition from the $(15/2^-)$ to the isomeric $(11/2^-)$ state. There are some indication for lines at 233.1, 407, 447.5 and 467.5 keV. The 407 keV line is reported to be the decay of a level at 2586.2 keV, the highest yet observed energy level in this nucleus. The highest excitation energy identified in this reaction channel is 1888.5 keV and the highest observed spin is $(19/2^-)$.

In the recoil spectra no peaks could be identified.

This Work			Literature [81]		
E_γ [keV]	FWHM [keV]	Peak area	E [keV]	E_γ [keV]	J^π
587.45 (22)	3.90 (55)	298 (34)	823.31 (18)	587.2 (2)	$\left(\frac{15}{2}^-\right)$
695.61 (22)	2.55 (56)	159 (26)	1888.5 (3)	694.0 (3)	-
752.44 (22)	2.75 (60)	184 (26)	1576.0 (3)	752.7 (2)	$\left(\frac{19}{2}^-\right)$

Table 31: γ-ray lines identified in the single spectrum of ^{129}Xe. Literature values are taken from [81].

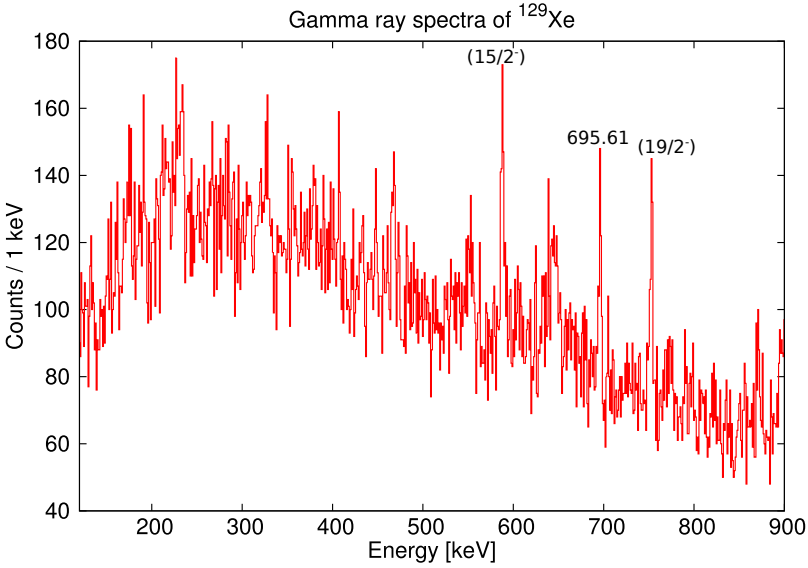

Figure 95: Doppler corrected γ-ray spectrum of ^{129}Xe with a time cut on the prompt peak between PRISMA and AGATA. The identified peaks are listed in table 31.

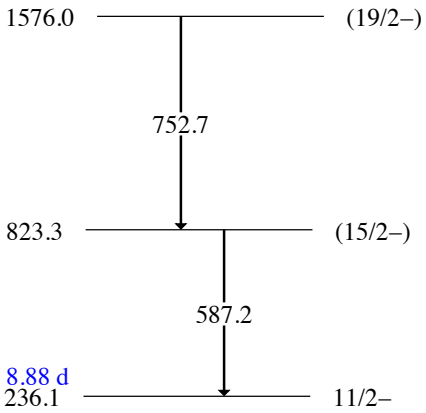

Figure 96: Level scheme for the γ-rays seen in the single spectrum of ^{129}Xe based on data taken from [81].

Eight neutron transfer channel The last neutron transfer channel populating neutron-deficient reaction products is

$$^{136}\mathrm{Xe}(^{238}\mathrm{U},^{246}\mathrm{U'})^{128}\mathrm{Xe'}$$

where eight neutrons were transferred from the incoming beam particle away. The spectrum of the identified even–even nucleus ^{128}Xe is shown in figure 97. The fits and the corresponding data is summarized in table 32. A level scheme is given in figure 98. The transitions from the 2^+ of ^{128}Xe is visible in the spectra providing clear evidence for the identification of the isotope measured with PRISMA. Weaker evidence is found for four other transitions expected from the known levels of and their decay properties. The line at 1132 keV can be assigned to two transitions. $\gamma\gamma$ coincidences do not deliver conclusive results. The highest excitation energy level identified in this reaction channel is at 2165.9 keV and the highest observed spin is 4^+.

No lines could be observed in the recoil spectra except contaminations of ^{238}U.

This Work			Literature [81]		
E_γ [keV]	FWHM [keV]	Peak area	E [keV]	E_γ [keV]	J^π
443.23 (20)	3.06 (43)	167 (22)	442.911 9()	442.901 (10)	2^+
590.20 (49)	2.5 (19)	77 (21)	1033.147 (19)	590.24 (2)	4^+
649.89 (62)	6.4 (1.3)	338 (48)	3113.4 (4)	650.8 (8)	-
1132.74 (39)	5.5 (17)	117 (23)	2165.9 (4)	1132.7 (5)	(4)
			2736.7 (6)	1133.2 (5)	-

Table 32: γ-ray lines identified in the single spectrum of ^{128}Xe. Literature values are taken from [81].

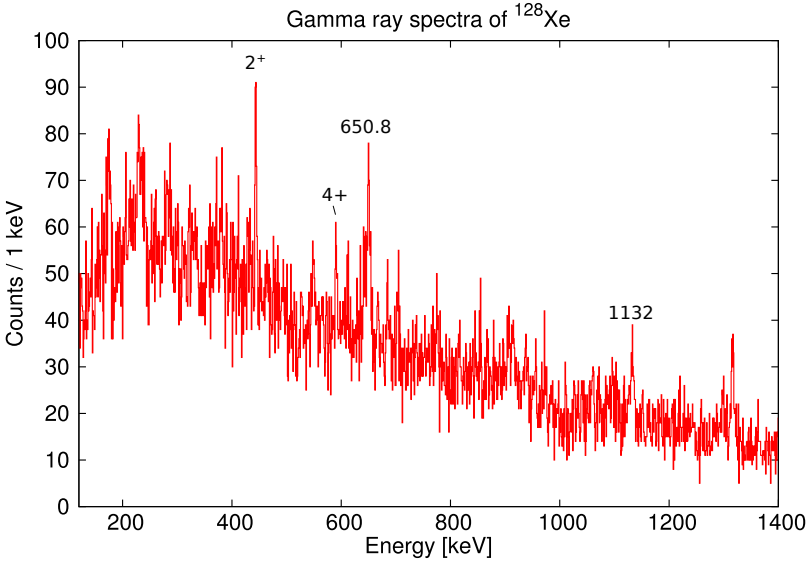

Figure 97: Doppler corrected γ-ray spectrum of ^{128}Xe with a time cut on the prompt peak between PRISMA and AGATA. The identified peaks are listed in table 32.

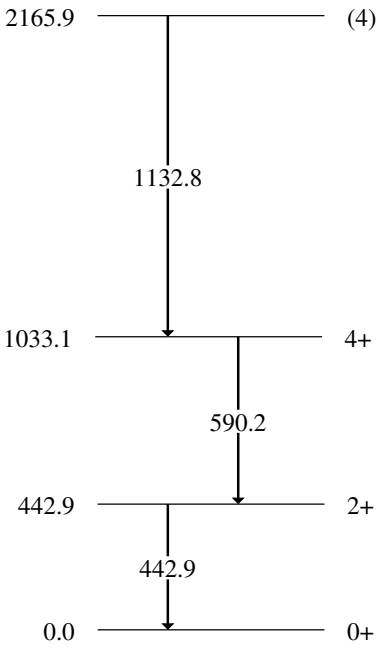

Figure 98: Level scheme for the γ-rays seen in the single spectrum of ^{128}Xe based on data taken from [81].

One neutron pickup channel The one neutron pickup channel is populating via the

$$^{136}\mathrm{Xe}(^{238}\mathrm{U},^{237}\,\mathrm{U'})^{137}\mathrm{Xe'}$$

reaction ^{137}Xe and ^{237}U. It has the highest cross section for neutron pickup of the beam like particle. The peaks fitted in the single spectrum are shown in figure 99 and the corresponding data is summarized in table 33. A level scheme with the listed lines is shown in figure 100. The two lines at 1218.66 and 1220.79 keV have very similar energies. The fit of the peak with a single line is not acceptable with the expected energy resolution, therefore a dublett fit with two lines was used.

Transitions from the ground state up to a $(27/2^-)$ state are observed in the spectrum 99. As shown in the level scheme additional transitions from levels with $3/2^-$, $9/2^-$ and $(13/2^+)$ were identified. All lines could be identified with existing data, except the transition at 1183.79 keV. It was inspected by placing a $\gamma\gamma$ cut, but no related decays could be identified. The highest excitation energy identified in this reaction channel is 3291.6 keV and the highest observed spin is $(27/2^-)$.

The numerous identified transitions of ^{137}Xe show, that the PRISMA analysis also provides reliable results for the neutron pickup reactions.

This Work			Literature [81, 90]		
E_γ [keV]	FWHM [keV]	Peak area	E [keV]	E_γ [keV]	J^π
270.50 (12)	2.99 (24)	960 (2)	2204.0 (6)	269.7 (3)	$\left(\frac{19}{2}^-\right)$
312.7 (17)	4.1 (25)	955 (1840)	3291.6 (11)	311.6 (3)	$\left(\frac{27}{2}^-\right)$
314.3 (17)	4.1 (25)	383 (1867)	1935.2 (3)	314.10 (10)	$\frac{19}{2}^-$
400.1 (12)	3.7 (21)	3858 (94)	1621.1 (2)	400.10 (10)	$\frac{15}{2}^-$
532.94 (13)	3.57 (35)	916 (74)	1752.56 (16)	532.49 (10)	$\left(\frac{13}{2}^+\right)$
601.55 (14)	3.12 (34)	1223 (80)	601.05 (7)	601.05 (7)	$\frac{3}{2}^-$
1045.80 (37)	5.6 (10)	561 (78)	2980.0 (6)	1045.8 (3)	$\left(\frac{23}{2}^-\right)$
1183.79 (41)	3.7 (11)	415 (89)	-	-	-
1218.66 (54)	5.04 (56)	4636 (1547)	1218.00 (10)	1218.00 (10)	$\frac{9}{2}^-$
1220.79 (19)	5.04 (56)	3840 (1594)	1220.07 (15)	1220.07 (15)	$\frac{11}{2}^-$

Table 33: γ-ray lines identified in the single spectrum of ^{137}Xe. Literature values are taken from [81, 90].

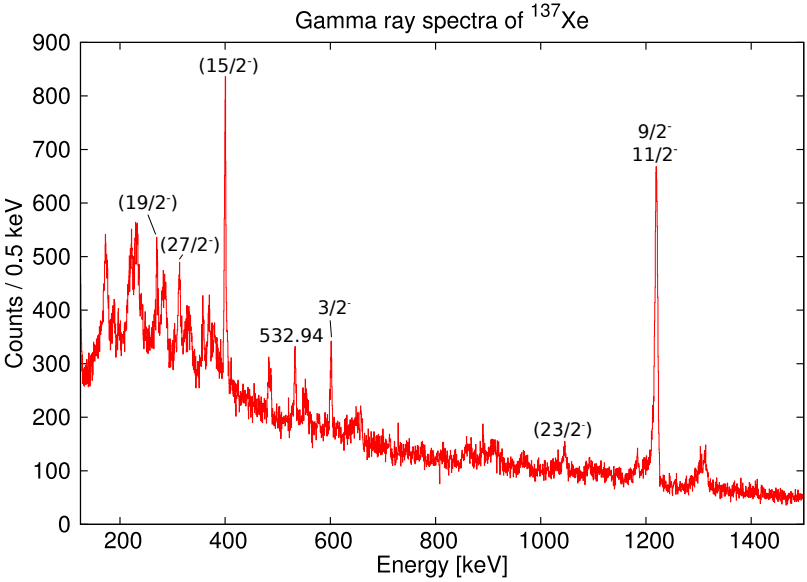

Figure 99: Doppler corrected γ-ray spectrum of ^{137}Xe with a time cut on the prompt peak between PRISMA and AGATA. The identified peaks are listed in table 33.

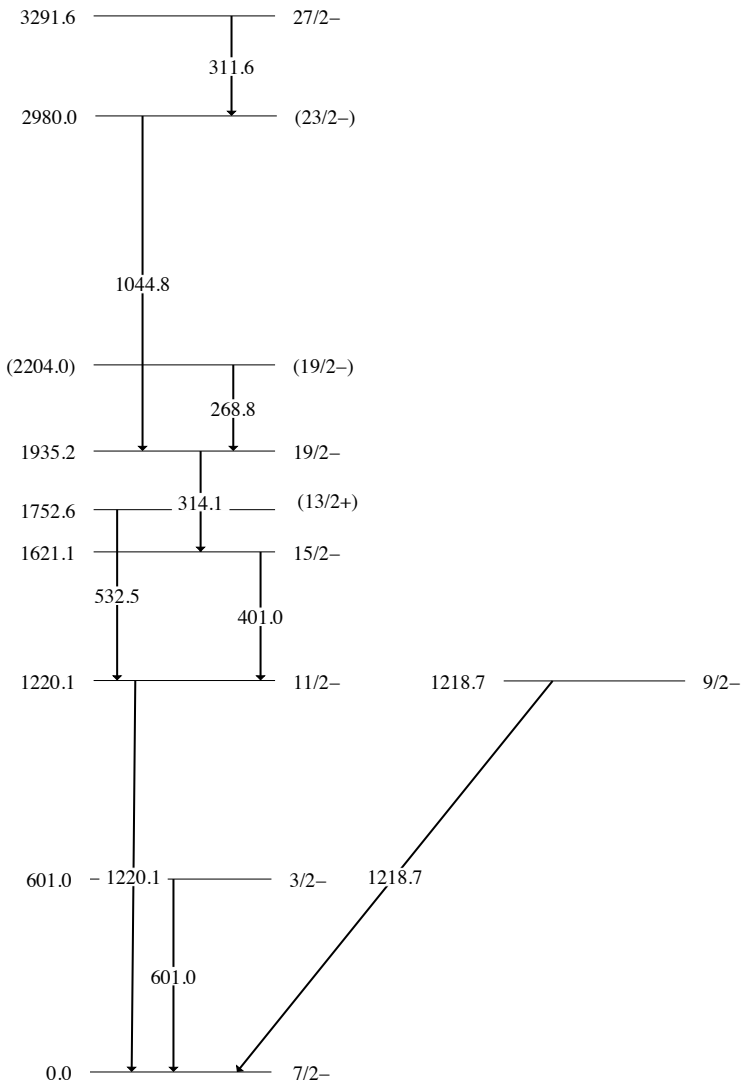

Figure 100: Level scheme for the γ-rays seen in the single spectrum of ^{137}Xe based on data taken from [81, 90].

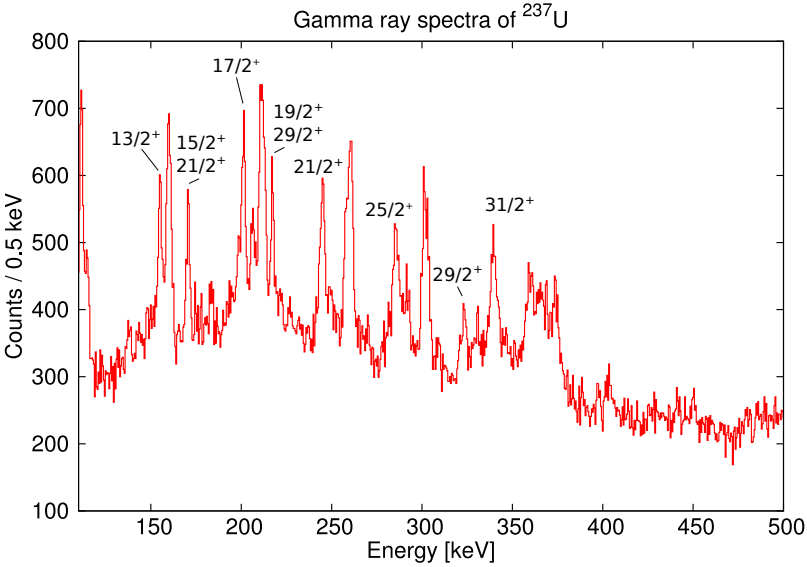

Figure 101: Doppler corrected γ-ray spectrum of ^{237}U with a time cut on the prompt peak between PRISMA and AGATA. The identified peaks are listed in table 34.

The corresponding recoil nucleus is ^{237}U. It has a neutron separation energy of 5.126 MeV [84] and a fission barrier of 5.43 MeV [86]. The vast amount of possible γ decays makes it hard to identify the individual lines that show up in the spectrum of figure 101. Only a cut on the prompt coincidence between AGATA and PRISMA was requested to create the spectra. All the fitted lines are listed in table 34 combined with already reported energy levels and decays [81]. A corresponding level scheme is shown in figure 102. In a comparable experiment described in [55] similar results were obtained.

The peaks of transitions from the neighbouring ^{238}U show a broadening and a larger FWHM as a fit result. This could be the result of a wrong Doppler correction or because there are two peaks. Furthermore it is possible that the ^{237}U evaporated a neutron and similar lines coming from ^{236}U can be seen. ^{236}U has very similar decay en-

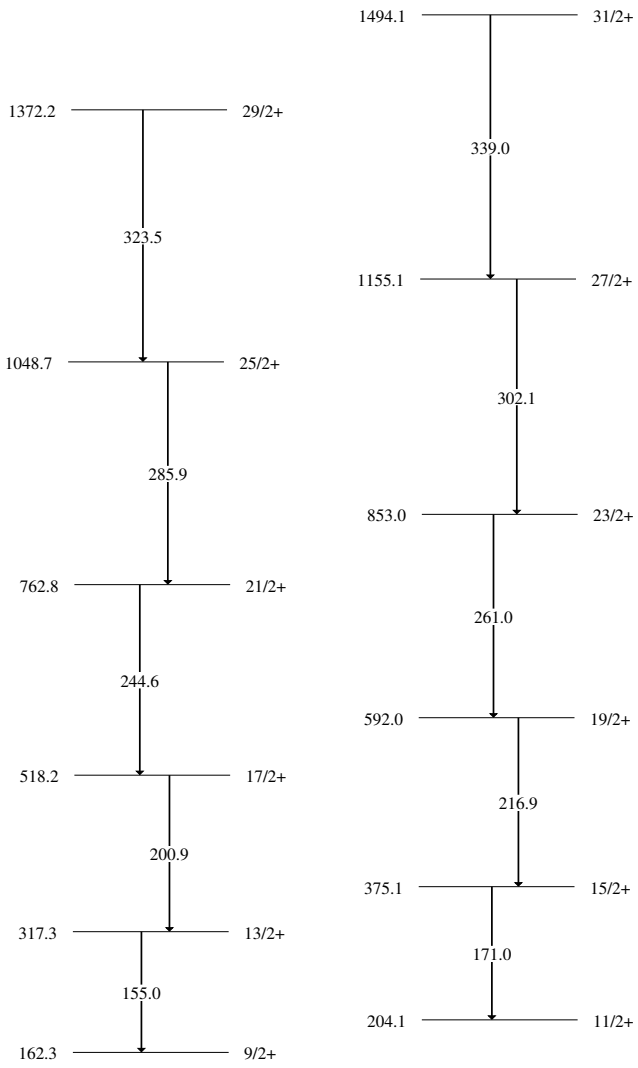

Figure 102: Level scheme for the γ-rays seen in the single spectrum of ^{237}U based on data taken from [81].

ergies as ^{238}U. It is discussed in the next paragraph. The $\gamma\gamma$ data does not show significant peaks due to low statistics. For some peaks two transitions were used for the fit and the corresponding results are marked with a $\star$ in table 34.

The transitions of the first band with signature $\alpha = \frac{1}{2}$ could be seen in the single spectrum and the partner band with signature $\alpha = -\frac{1}{2}$ as well. The lines at 217 and 170 keV are expected to be also transitions between these two signature partner bands. A $\gamma\gamma$ analysis would clarify this situation and establish γ intensities, but due to low statistics it was not conclusive.

One decay with an energy at 198 keV is assigned to a known third rotational band. There are indications for other decays of this band. At 148,keV a small bump is visible and the energy resolution (FWHM) of the 244 keV line is enlarged. This could be related to the transitions with a reported energy of 243 and 150 keV. The last identified band has negative parity and connects all the three found lines with negative parity. They are not included in the level scheme. The line at 212 keV cannot be identified and might just result from a wrong Doppler correction of ^{238}U as it was fitted simultaneously with the line at 211 keV.

Conditions on the Q_r value and the particle coincidence improve the peak to background ratio. The corresponding spectrum is shown in figure 103. In the spectrum there are indications for a number of lines, but as the lines are very dense and the background becomes fluctuating due to low statistics, the fit routines do provide only results with huge uncertainty.

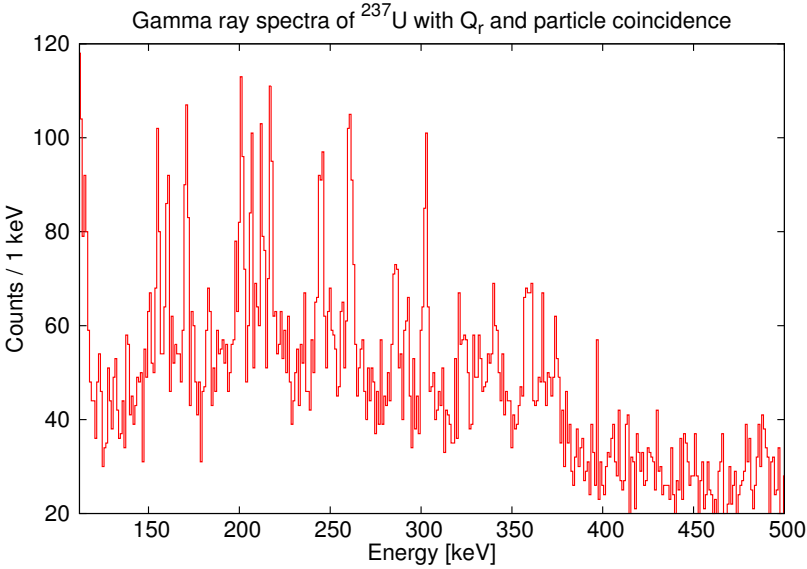

Figure 103: Spectrum of ^{237}U with applied cuts on the Q_r value, the prompt peak between AGATA and PRISMA and particle coincidence

This Work			Literature [81]		
E_γ [keV]	FWHM [keV]	Peak area	E [keV]	E_γ [keV]	J^π
154.860(81)	2.22 (10)	1074 (86)	317.3 (16)	155 (-)	$\frac{13}{2}^+$
			^{238}U		
159.10 (21) ⋆	2.22 (10)	1138 (246)			
160.53 (24) ⋆	2.22 (10)	919 (242)	592 (3)	160 (-)	$\left(\frac{17}{2}^-\right)$
			^{236}U		
170.367 (82)	2.06 (19)	826 (66)	375.1 (11)	171	$\frac{15}{2}^+$
			762.8 (14)	171 (-)	$\frac{21}{2}^+$
198.16 (25)	2.29 (16)	397 (84)	607.7 (12)	198 (-)	$\left(\frac{17}{2}^+\right)$
			2191.0 (19)	198 (-)	$\left(\frac{35}{2}^+\right)$
			^{236}U		
201.086 (79)	2.29 (16)	1497 (91)	518.2 (13)	201 (-)	$\frac{17}{2}^+$
206.5 (13)	2.29 (12)	790 (67)	798.0 (24)	206 (-)	$\left(\frac{21}{2}^-\right)$
210.54 (13) ⋆	2.29 (16)	1515 (133)	^{238}U		
212.45 (14) ⋆	2.29 (12)	1214 (136)	^{236}U		
217.018 (91)	2.29 (12)	987 (71)	592 (3)	217 (-)	$\frac{19}{2}^+$
			1372.2 (15)	217	$\frac{29}{2}^+$
244.76 (91)	2.89 (39)	1463 (92)	762.8 (14)	245 (-)	$\frac{21}{2}^+$
			^{236}U		
257.86 (13) ⋆	2.50 (15)	919 (78)	^{238}U		
260.470 (86) ⋆	2.50 (15)	1508 (88)	853 (14)	261 (-)	$\frac{23}{2}^+$
			^{236}U		
285.10 (19)	2.96 (28)	1046 (119)	1048.7 (14)	286 (-)	$\frac{25}{2}^+$
291.55 (25)	2.96 (28)	501 (68)	1340.0 (24)	292 (-)	$\left(\frac{25}{2}^-\right)$
300.93 (11) ⋆	2.1 (25)	1106 (96)	^{238}U		
303.06 (13) ⋆	2.1 (25)	844 (92)	1155.1 (15)	302 (-)	$\frac{27}{2}^+$
			^{236}U		
322.66 (26)	2.93 (48)	484 (3)	1372.2 (15)	324 (-)	$\frac{29}{2}^+$
339.48 (14)	3.86 (35)	1193 (111)	1494.(16)	339 (-)	$\frac{31}{2}^+$
			^{238}U		
			^{236}U		

Table 34: γ-ray lines identified in the single spectrum of ^{237}U. Literature values are taken from [81]. Energies marked with a ⋆ were fitted with two close peaks simultaneously.

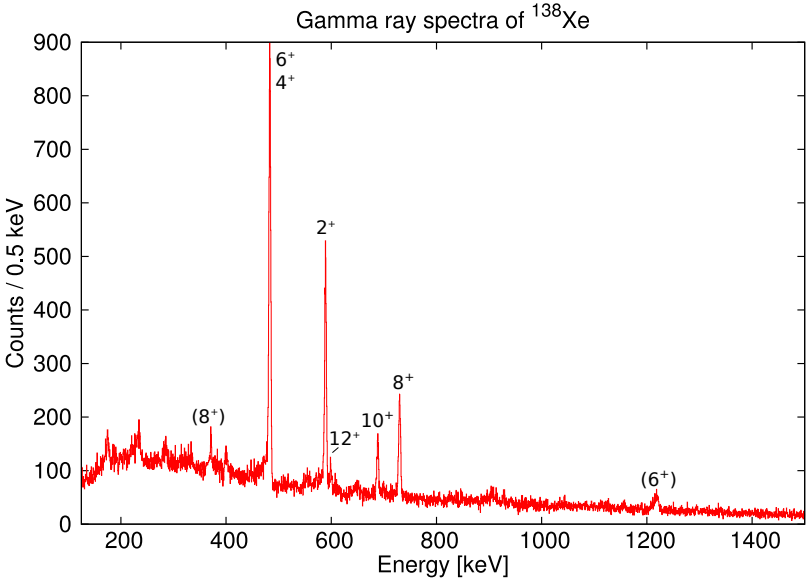

Figure 104: Doppler corrected γ-ray spectrum of ^{138}Xe with a time cut on the prompt peak between PRISMA and AGATA. The identified peaks are listed in table 35.

Two neutron pickup channel In this paragraph the observed γ-rays from the reaction

$$^{136}\mathrm{Xe}(^{238}\mathrm{U},^{236}\,\mathrm{U'})^{138}\mathrm{Xe'}$$

are described. The single spectrum of ^{138}Xe gated on the prompt peak between AGATA and PRISMA with prominent peaks is shown in figure 104. The corresponding data is summarized in table 35. All observed peaks are consistent with the existing data. A level scheme connecting all the observed transitions is shown in figure 105. The transitions from the 2^+ up to the 12^+ level are visible in the single spectrum. The highest excitation energy identified in this reaction channel is at 3571.3 keV and the highest observed spin is 12^+.

The corresponding recoil nucleus is ^{236}U. This is the only actinide nucleus where in the γ-ray spectrum transitions of the ground state

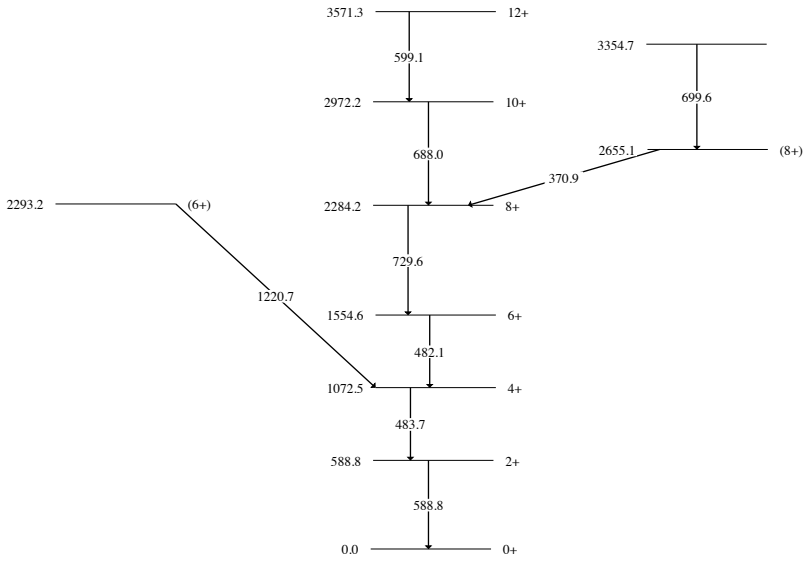

Figure 105: Level scheme for the γ-rays seen in the single spectrum of ^{138}Xe based on data taken from [81].

This Work			Literature [81]		
E_γ [keV]	FWHM [keV]	Peak area	E [keV]	E_γ [keV]	J^π
371.40 (22)	2.58 (53)	414 (59)	2655.1 (12)	370.9 (-)	(8^+)
482.67 (16)	3.22 (29)	3846 (689)	1554.6 (9)	482.1 (-)	6^+
484.16 (31)	3.22 (29)	3046 (683)	1072.53 (3)	483.700 (24)	4^+
589.147 (47)	3.57 (11)	3575 (74)	588.827 (18)	588.825 (18)	2^+
599.08 (19)	2.90 (53)	277 (45)	3571.3 (15)	599.0 (-)	12^+
688.33 (10)	3.94 (23)	846 (107)	2972.2 (14)	687.9 (-)	10^+
699.29 (49)	1.75 (40)	95 (2)	3354.7 (13)	699.5 (-)	-
729.997 (85)	4.27 (20)	1716 (56)	2284.2 (12)	729.6 (-)	8^+
1219.8 (12)	6.7 (18)	401 (287)	2293.2 (9)	1220.7 (-)	(6^+)

Table 35: γ-ray lines identified in the single spectrum of ^{138}Xe. Literature values are taken from [81].

rotational band and of the odd parity rotational band can be identified. The results from the fitted lines of spectrum 106 are listed in table 36. The level scheme is shown in figure 107.

This Work			Literature [81]		
E_γ [keV]	FWHM [keV]	Peak area	E [keV]	E_γ [keV]	J^π
104.49 (18)	1.27 (20)	199 (2)	149.477 (6)	104.233 (5)	4^+
152.30 (55)	2.7 (12)	235 (86)	999.6 (9)	151.5 (5)	7^-
160.13 (12)	2.57 (23)	997 (88)	309.785 (7)	160.308 (2)	6^+
199.55 (52)	3.8 (14)	393 (118)	1198.4 (10)	198.8 (3)	9^-
212.288 (97)	2.66 (22)	1347 (98)	522.25 (5)	212.46 (5)	8^+
244.23 (20)	1.82 (53)	315 (72)	1443.4 (11)	245.0 (5)	11^-
260.33 (12)	2.64 (28)	1118 (99)	782.3 (5)	260.1 (5)	10^+
303.04 (27)	4.68 (94)	1064 (152)	1085.3 (7)	303.0 (5)	12^+
341.70 (18)	2.21 (46)	461 (79)	1426.3 (9)	341.0 (5)	14^+

Table 36: γ-ray lines identified in the single spectrum of ^{236}U. Literature values are taken from [81].

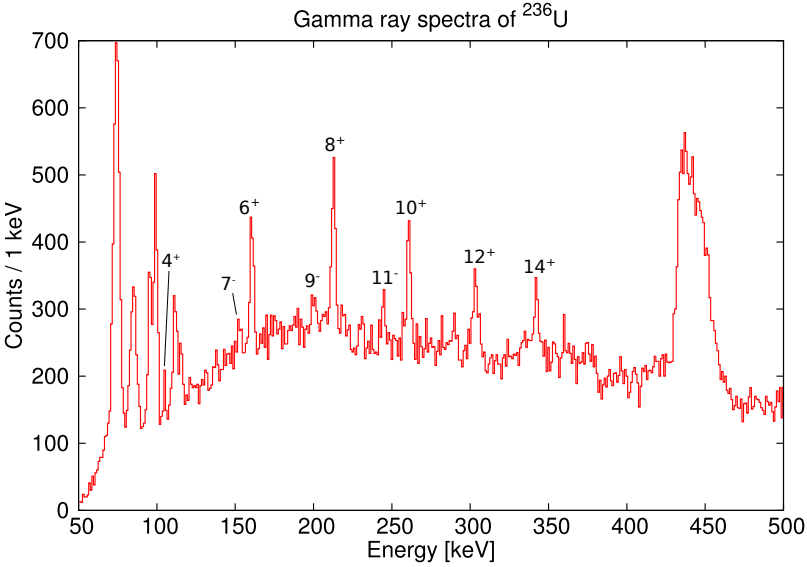

Figure 106: Doppler corrected γ-ray spectrum of ^{236}U with a time cut on the prompt peak between PRISMA and AGATA. The identified peaks are listed in table 36.

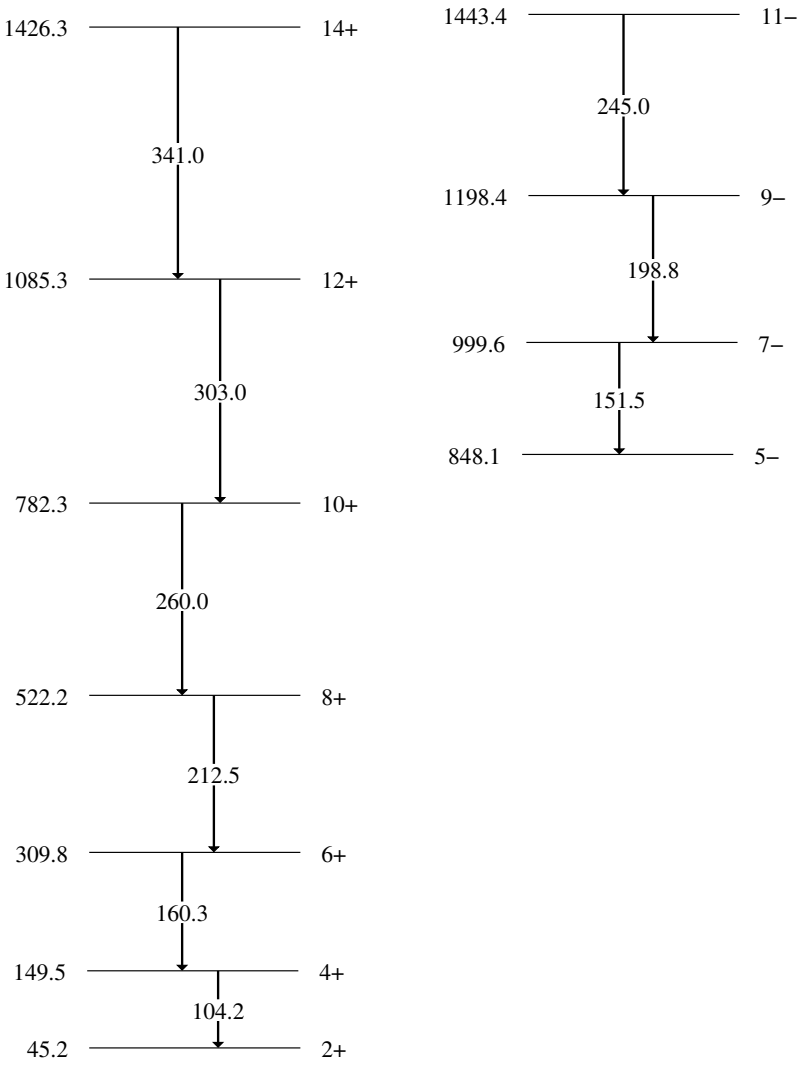

Figure 107: Level scheme for the observed γ-rays from the single spectrum of ^{236}U based on data taken from [81].

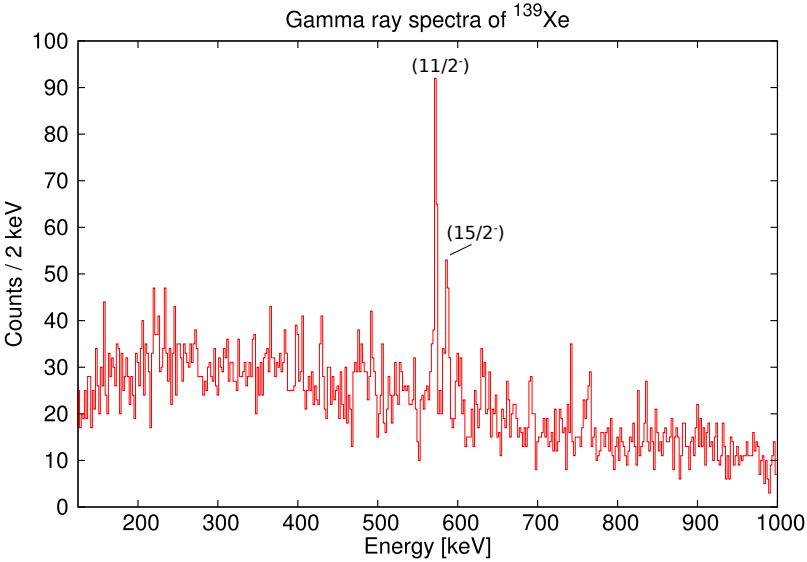

Figure 108: Doppler corrected γ-ray spectrum of ^{139}Xe with a time cut on the prompt peak between PRISMA and AGATA. The identified peaks are listed in table 37.

Three neutron pickup channel In the three neutron pickup channel

$$^{136}\mathrm{Xe}(^{238}\mathrm{U},^{235}\,\mathrm{U'})^{139}\mathrm{Xe'}$$

the even-odd unstable nucleus ^{139}Xe was identified in PRISMA. It is the last pickup channel showing γ-rays that could be identified with transitions of the corresponding isotope. The fit results and the data are summarized in table 37. The spectrum is shown in figure 108 and the level scheme in figure 109. The highest excitation energy identified in this reaction channel is 1179.6 keV and the highest observed spin is $(15/2^-)$.

The recoil spectra does not show any peaks with reasonable statistics.

This Work			Literature [81]		
E_γ [keV]	FWHM [keV]	Peak area	E [keV]	E_γ [keV]	J^π
571.72 (15)	2.84 (28)	117 (13)	594.28 (15)	571.2 (3)	$\left(\frac{11}{2}^-\right)$
585.57 (46)	2.84 (28)	48 (10)	1179.6 (4)	585.4 (-)	$\left(\frac{15}{2}^-\right)$

Table 37: γ-ray lines identified in the single spectrum of ^{139}Xe. Literature values are taken from [81].

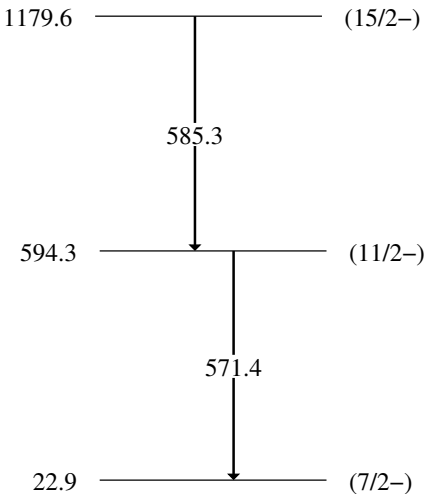

Figure 109: Level scheme for the γ-rays seen in the single spectrum of ^{139}Xe based on data taken from [81].

Summary In all mass gated reaction channels the Xenon isotopes could be identified by their characteristic γ-ray signature confirming the right identification with the PRISMA spectrometer. In the case of $^{130,131,134-138}$Xe levels with high spins and excitation energies up to 4.8 MeV were observed. The results from isotopes ^{128,129,139} show reduced statistics and only few transitions are observed. The case of ^{132,133}Xe is a bit different. Also here only few decays could be identified, although the statistics are higher than for ^{130,131}Xe. The highest observed excitation energy of these two isotopes is 1.87 MeV. For some Xe isotopes the statistics was sufficient for a $\gamma\gamma$ analysis showing consistent results.

The Uranium isotopes $^{236-240}$U were identified based on the assumption that neutrons were transferred from the beam like particle to the target like particle. Indications for additional neutron evaporation from excited states after the transfer reaction are clearly observed. The γ-ray yield for the actinide reaction product is reduced due to fission of the transfer products. Background from excited fission fragments in the spectra can be suppressed by requiring a PRISMA-DANTE coincidence. However this reduces the yield again dramatically. Consequently the $\gamma\gamma$ coincidence analysis is working as shown in the case of ^{238}U. However in most of the neighbouring reaction channels the matrices lack statistics. The particle coincidences between the PRISMA start MCP and the DANTE detector helps to reduce the background and to get a better peak to total ratio, but it also decreases the number of counts significantly. The Q_r value cuts can be applied to reduce the effect of evaporated neutrons by the produced actinide nuclei.

The high quality of the ^{238}U spectra demonstrates that the PSA and GRT works nicely for the reconstruction of the scattered target like nuclei. The improved peak to total ratio by gating on the coincidence between the DANTE and PRISMA detectors demonstrates, that the suggested method of particle coincidence is applicable. However the reduced efficiency of the DANTE detector would have required longer beam times or higher beam intensities. As the high count rate during the experiment was already close to the design limit of AGATA only longer beam times could have improved the final result. In future a more robust detector or different detection principle for the

surviving recoil nucleus should be taken into account to improve the experimental situation and to gain more statistics.

As the neutron separation energy of Uranium isotopes with A $>$ 239 is not measured yet, the question if U isotopes with A $>$ 240 could be produced in the presented reaction can not be clearly answered. Despite small indications for ^{241}U no γ-ray transitions were observed for neutron-rich U isotopes with A $>$ 241.

The future analysis of this experiment will focus on the proton pickup and transfer channels employing the techniques and methods developed within this analysis in order to generate and analyze the spectra of the remaining other target and beam like isotopes.

4. Conclusion

The development phase of the AGATA demonstrator and the first in-beam experiments required a variety of new solutions and contributions for the γ-ray tracking (GRT) method. During the installation phase the PSA technique was lacking reliable position sensitive pulse shape libraries for comparison with the measured pulses. Therefore the AGATA Detector Library ADL was an essential step towards the implementation of PSA and GRT in the AGATA demonstrator. The PSA signal databases of all currently used AGATA detectors were created by simulations based on the routines of ADL combined with the important measurements on the crystal axis orientation and earlier measurements on the drift velocities [31, 32, 33] and the impurity concentration of the crystals [36, 64, 38, 39]. Up to know the individual ADL for each detector are employed for the online and offline analysis of all AGATA experiments. As demonstrated in several publications [14, 44] the position resolution achieved with the PSA algorithms based on the ADL signal databases reach the specifications and design performance of the AGATA detectors under experimental conditions. Although alternative characterization techniques are available, like the coincidence scan of the crystals [19, 20, 8], only the simulations deliver up to now usable and reliable signal databases for the in-beam spectroscopy with AGATA. Since then the GRT results obtained with the AGATA demonstrator at LNL and GSI utilized the ADL based signal databases for the PSA of experiments and contribute to the successful operation of the spectrometer.

In the analysis of the experiment for spectroscopy of neutron rich Th and U nuclei after multi-nucleon transfer reactions the novel GRT method was adapted to a demanding in-beam γ-ray spectroscopy experiment which also required special developments of digital signal processing. Finally clean γ-ray spectra of high quality for a wide range of nuclei were extracted and demonstrate the implementation of the complete analysis procedure. Newly developed software tools were combined with the software packages available from the AGATA community in order to extract the events of interest. To profit also from the latest developments for the PRISMA spectrometer it was manadatory to merge the ancillary PRISMA and DANTE data with the AGATA data for the complete experiment. Only the combined in-

formation from the PRISMA and DANTE detectors and the AGATA demonstrator allowed the successful generation of Doppler corrected γ-ray spectra including the PSA and the GRT. Moreover instabilities during the long beam time required unforeseen difficulties with long-term stabilities which were overcome by additional computer programs to control the PRISMA analysis, the Doppler correction and the creation of the resulting spectra. In addition several obstacles needed to be overcome like aberration corrections and invalid calibrations of the PRISMA detectors beside the time dependent behaviour of sub detector systems. The final mass resolution after the PRISMA analysis allowed the identification of individual Xenon isotopes over a wide range from ^{126}Xe up to ^{141}Xe with the high mass resolution of the PRISMA design parameters. Based on this work the analysis will be extended in the near future also to the neighboring isotopes in order to investigate the transfer and pickup channels with protons and neutrons.

The basic AGATA analysis, like the energy calibration and the time alignment of the signals, were partially rewritten and optimized to obtain the best results with the combined information of three detector subsystems (PRISMA, DANTE, AGATA). The background radiation during the experiment was considerable due to high Xe beam intensities and huge cross sections for Coulomb excitation, fission and atomic processes at 1 GeV beam energy in the actinide target. The background was successfully suppressed by gating on narrow prompt time coincidences between the different detector systems. The full potential of the position sensitive AGATA spectrometer was demonstrated by the optimization of the Doppler correction for beam and target like nuclei. Superior energy resolutions in the Doppler corrected spectra were achieved for beam and target like nuclei after a newly written four-dimensional optimization procedure. As a final result it could be shown for the ^{238}U results that the quality of the final γ-ray spectra especially the peak to total ratio becomes comparable to Compton suppressed spectrometers.

For the $^{128-139}$Xe isotopes the Doppler corrected γ-ray spectra are clean and consistent with available nuclear structure data due to the unambiguous correlation after the PRISMA identification. In the case of $^{134/135}$Xe isotopes a very recent open discrepancy in the data of [87]

and [88] was found about excited states at higher spin in these nuclei. The new data set of this analysis clearly confirms with higher statistics the more recent and more sensitive experimental results of [88] which were also obtained with a mass separator. This demonstrates the competitiveness of the new experiment in comparison with the most advanced spectrometers.

The Doppler correction parameters of the target like nuclei, the angle and the velocity vector, were calculated and the Doppler corrected γ-ray spectra of the recoiling target nuclei show very good values for energy and energy resolution (FWHM). Based on the extracted Doppler corrected γ-ray spectra the production of $^{236-240}$U was verified and the results of earlier measurements [55] were reproduced and extended. The neutron evaporation of the produced actinide nuclei could be suppressed by gating on the Q_r value of the reaction. The good quality of the ^{238}U spectra demonstrates that the principle of PSA and GRT is also applicable for the reconstruction of the unobserved scattered target like nuclei. An improved peak to total ratio after fission background suppression is obtained by gating on the coincidence between the DANTE and PRISMA detectors. Unfortunately the reduced efficiency of the DANTE detectors hampered the finally available statistics and would have required longer beam time or higher beam intensities. However, the high count rate of the Ge detectors during the experiment was already close to the design limit of AGATA and only longer beam times would have improved the situation.

As the neutron separation energy of Uranium isotopes for A $>$ 239 are unknown, the question to which extent the more neutron-rich Uranium isotopes with A $>$ 240 could be produced in the present reaction could not be clearly resolved by searching γ-rays and x-rays emitted from these nuclei. Despite some indication for ^{241}U no γ-ray lines are observed for U isotopes with A $>$ 240. In [55] it was shown that the reaction ^{70}Zn(^{238}U,U')Zn' showed clean spectra for $^{236-240}$U, however there were only indications for the population of neutron rich Th isotopes. Therefore the different Q-values for the ^{136}Xe(^{238}U,U')Xe' reaction was used for the new experiment and the final results for the Th isotopes will be available very soon. For an improved investigation of neutron rich U isotopes it may be concluded that the Zn based multi-nucleon reaction may still be favorable.

5. Outlook

The AGATA demonstrator, as a first step towards the full AGATA spectrometer, was successfully implemented at the LNL in Italy. The performed experiments, including the measurements performed and analyzed within this thesis, demonstrate the good performance of the array. The system is, already in its demonstration phase, a powerful spectrometer for nuclear structure investigations under extreme conditions. The new approach of γ-ray tracking based on position sensitive detection of gamma radiation is working. The individual parts of the system, starting from the detectors and cryostats up to the computer algorithms for the reconstruction of the events, show reliable performance. New technologies, especially in information processing and capturing, will provide new options to improve the AGATA detector system in the near future. One should have in mind that AGATA has just exceeded its starting phase. Improved methods and features are expected to appear within the realization of more powerful detector configurations up to the finalization of the spectrometer system with its nearly complete full solid angle coverage.

The new highly segmented detectors open also other perspectives and applications. Two new modes of operation for segmented detectors are currently investigated at the IKP Cologne. The spectroscopy of high energetic radiation above 20 MeV utilizing the time over threshold techniques [11][12][91] implemented in the AGATA preamplifiers, could be used to measure the high energetic radiation that occurs at fast beam setups like the FRS at GSI or is produced from cosmic showers in the atmosphere. An energy calibration based on a pulser measurement and a measurement of muons from natural cosmic radiation was established up to an energy of 220 MeV. The corresponding energy loss spectrum is shown in figure 110. Considering the different size and geometry of the AGATA crystal, the measured data compares well with computer simulations presented in [92] and [93]. More details on the analysis and further applications of these type of measurements of high energetic charged particles are given in [94].

The second mode of operation exploits the gamma-ray tracking method to perform gamma-ray imaging [5]. Within the TRAKULA collaboration such a Compton camera is developed at the IKP. The Comp-

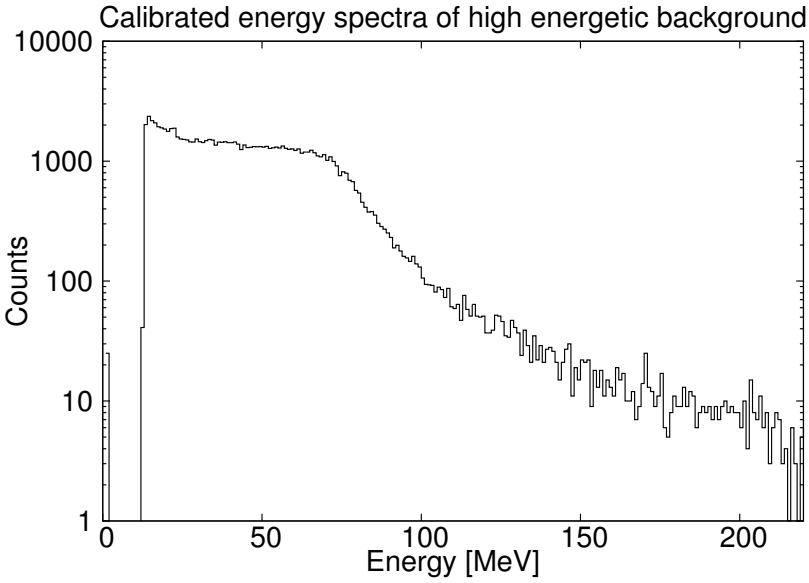

Figure 110: Calibrate energy spectrum of high energetic cosmic rays measured with an AGATA detector.

ton camera is based on a 36 fold segmented HPGe detector [95], a double-sided silicon strip detector DSSSD [96][97] and digital electronics [96][95]. The DSSSD is used as a position sensitive scattering detector that can be located at different distances with respect to the HPGe detector. The narrow pitch of the orthogonal rows of Si-strips provide a very good measurement of the first position of the Compton scattering location. The second interaction point in the position sensitive HPGe detector is determined like in all AGATA detector with the PSA and γ-ray tracking algorithm. For known γ-ray energies images of the position of the γ-ray emitting source is obtained from the intersection of all scattering cones which are the results of the the individual measurements. In this way gamma-ray images of radioactive sources are taken. Figure 111 shows a first picture of two radioactive sources separated by a distance of 7 cm demonstrating that the configuration can be applied for γ-ray imaging. Future applications of

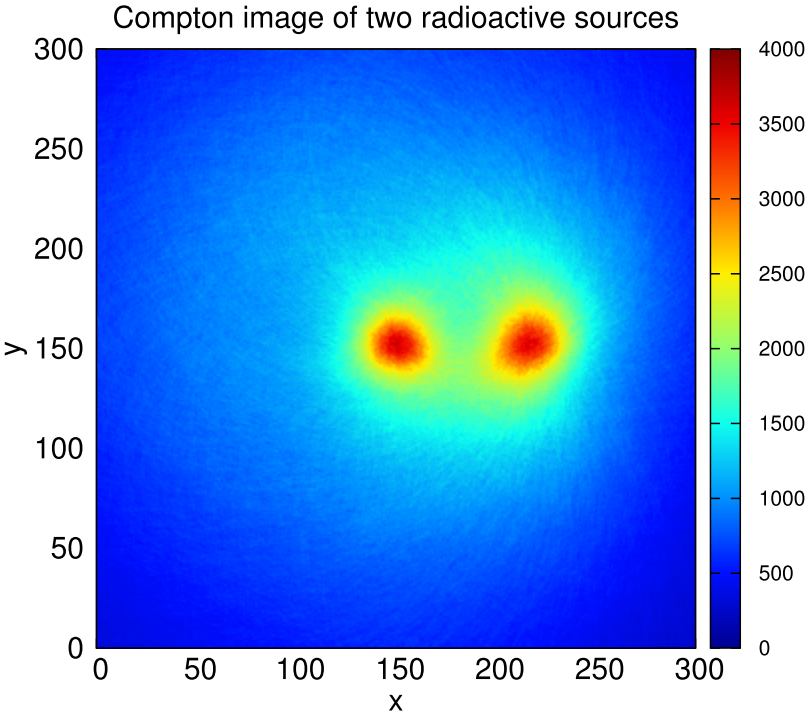

Figure 111: Compton image of a ^{22}Na (left) and a ^{137}Cs (right) source taken in coincidence between an AGATA crystal and a DSSSD

Compton cameras can be found for many different fields like nuclear waste management or medical applications.

The characterization of the AGATA crystals presented in the first chapter of this thesis is subject of future improvements. Although the achieved position resolution is well within the design goals of the AGATA system, developments are still under investigation. Different not yet fully understood effects like clustering of interaction points at the centre of a segment or an inhomogenous distribution of single interaction points in the grid are subject on ongoing studies and will improve the final position resolution. A comparison between the

calculated ADL pulses and a set of measured pulses from one of the AGATA scanning tables is of highest relevance to verify directly the ADL results by experimental data. This will then allow to study the effects close to the passivation volume at the back side of the detector volume and near segment boundaries. As the ADL comprises a versatile approach the methods developed for the ADL can be transferred for different geometries and materials. The ADL simulations could even be extended to new detector configurations or the simulations can be used to develop new shapes and geometries for HPGe detectors similar to the work described in [98].

The analysis of the experiment on neutron rich nuclei presented in this work focused on the neutron transfer reactions. In the Xenon and the Uranium isotopes a number of not yet reported gamma transitions were found that should be investigated further. The proton transfer and pickup channels are currently analyzed. Not only the actinide region from Thorium to Plutonium is interesting, but also the lighter beam like particles from Tellurium to Barium will be investigated. The results from the measurements will allow a thorough cross section measurement for the different multi-nucleon transfer channels. The combination with results from AGATA will allow to determine and constrain the survival probability of the heavy actinide reaction partners. In figure 112 the yields for the individual target like reaction partners are already shown. The grey scale is proportional to the number of events identified in PRISMA with at least one γ-ray registered in AGATA. Isotopes with less than 10000 events are not listed.

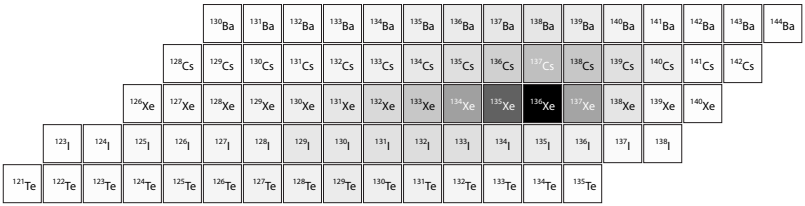

Figure 112: Yields of the investigated multi-nucleon transfer reaction channels. The grey scale is proportional to the number of events identified in PRISMA with at least one γ-ray registered by AGATA. Isotopes with less than 10000 events are not listed.

References

[1] Glenn F. Knoll. *Radiation Detection and Measurement*. John Wiley & Sons, fourth edition, 2010.

[2] J. Eberth and J. Simpson. From Ge(Li) detectors to gamma–ray tracking arrays — 50 years of gamma spectroscopy with germanium detectors. *Progress in Particle and Nuclear Physics*, 60:283–337, 2008.

[3] W.F. Mueller, J.A. Church, T. Glasmacher, D. Gutknecht, G. Hackman, P.G. Hansen, Z. Hu, K.L. Miller, and P. Quirin. Thirty-two-fold segmented germanium detectors to identify gamma-rays from intermediate-energy exotic beams. *Nuclear Instruments and Methods in Physics Research Section A: Accelerators, Spectrometers, Detectors and Associated Equipment*, 466(3):492 – 498, 2001.

[4] N. Warr, J. Walle, M. Albers, F. Ames, B. Bastin, C. Bauer, V. Bildstein, A. Blazhev, S. Bönig, N. Bree, B. Bruyneel, P.A. Butler, J. Cederkäll, E. Clément, T.E. Cocolios, T. Davinson, H. Witte, P. Delahaye, D.D. DiJulio, J. Diriken, J. Eberth, A. Ekström, J. Elseviers, S. Emhofer, D.V. Fedorov, V.N. Fedosseev, S. Franchoo, C. Fransen, L.P. Gaffney, J. Gerl, G. Georgiev, R. Gernhäuser, T. Grahn, D. Habs, H. Hess, A.M. Hurst, M. Huyse, O. Ivanov, J. Iwanicki, D.G. Jenkins, J. Jolie, N. Kesteloot, O. Kester, U. Köster, M. Krauth, T. Kröll, R. Krücken, M. Lauer, J. Leske, K.P. Lieb, R. Lutter, L. Maier, B.A. Marsh, D. Mücher, M. Münch, O. Niedermaier, J. Pakarinen, M. Pantea, G. Pascovici, N. Patronis, D. Pauwels, A. Petts, N. Pietralla, R. Raabe, E. Rapisarda, P. Reiter, A. Richter, O. Schaile, M. Scheck, H. Scheit, G. Schrieder, D. Schwalm, M. Seidlitz, M. Seliverstov, T. Sieber, H. Simon, K.-H. Speidel, C. Stahl, I. Stefanescu, P.G. Thirolf, H.-G. Thomas, M. Thürauf, P. Duppen, D. Voulot, R. Wadsworth, G. Walter, D. Weißhaar, F. Wenander, A. Wiens, K. Wimmer, B.H. Wolf, P.J. Woods, K. Wrzosek-Lipska, and K.O. Zell. The miniball spectrometer. *The European Physical Journal A*, 49(3):1–32, 2013.

[5] K Vetter, M Burks, and L Mihailescu. Gamma-ray imaging with position-sensitive HPGe detectors. *Nuclear Instruments and*

Methods in Physics Research Section A: Accelerators, Spectrometers, Detectors and Associated Equipment, 525(1–2):322 – 327, 2004. Proceedings of the International Conference on Imaging Techniques in Subatomic Physics, Astrophysics, Medicine, Biology and Industry.

[6] GRETA. Official website. http://greta.lbl.gov.

[7] AGATA. Official website. http://www-w2k.gsi.de/agata.

[8] S. Akkoyun, A. Algora, B. Alikhani, F. Ameil, G. de Angelis, L. Arnold, A. Astier, A. Ataç, Y. Aubert, C. Aufranc, A. Austin, S. Aydin, F. Azaiez, S. Badoer, D.L. Balabanski, D. Barrientos, G. Baulieu, R. Baumann, D. Bazzacco, F.A. Beck, T. Beck, P. Bednarczyk, M. Bellato, M.A. Bentley, G. Benzoni, R. Berthier, L. Berti, R. Beunard, G. Lo Bianco, B. Birkenbach, P.G. Bizzeti, A.M. Bizzeti-Sona, F. Le Blanc, J.M. Blasco, N. Blasi, D. Bloor, C. Boiano, M. Borsato, D. Bortolato, A.J. Boston, H.C. Boston, P. Bourgault, P. Boutachkov, A. Bouty, A. Bracco, S. Brambilla, I.P. Brawn, A. Brondi, S. Broussard, B. Bruyneel, D. Bucurescu, I. Burrows, A. Bürger, S. Cabaret, B. Cahan, E. Calore, F. Camera, A. Capsoni, F. Carrió, G. Casati, M. Castoldi, B. Cederwall, J.-L. Cercus, V. Chambert, M. El Chambit, R. Chapman, L. Charles, J. Chavas, E. Clément, P. Cocconi, S. Coelli, P.J. Coleman-Smith, A. Colombo, S. Colosimo, C. Commeaux, D. Conventi, R.J. Cooper, A. Corsi, A. Cortesi, L. Costa, F.C.L. Crespi, J.R. Cresswell, D.M. Cullen, D. Curien, A. Czermak, D. Delbourg, R. Depalo, T. Descombes, P. Désesquelles, P. Detistov, C. Diarra, F. Didierjean, M.R. Dimmock, Q.T. Doan, C. Domingo-Pardo, M. Doncel, F. Dorangeville, N. Dosme, Y. Drouen, G. Duchêne, B. Dulny, J. Eberth, P. Edelbruck, J. Egea, T. Engert, M.N. Erduran, S. Ertürk, C. Fanin, S. Fantinel, E. Farnea, T. Faul, M. Filliger, F. Filmer, Ch. Finck, G. de France, A. Gadea, W. Gast, A. Geraci, J. Gerl, R. Gernhäuser, A. Giannatiempo, A. Giaz, L. Gibelin, A. Givechev, N. Goel, V. González, A. Gottardo, X. Grave, J. Gre˛bosz, R. Griffiths, A.N. Grint, P. Gros, L. Guevara, M. Gulmini, A. Görgen, H.T.M. Ha, T. Habermann, L.J. Harkness, H. Harroch, K. Hauschild, C. He, A. Hernández-Prieto, B. Hervieu, H. Hess, T. Hüyük, E. Ince, R. Isocrate,

G. Jaworski, A. Johnson, J. Jolie, P. Jones, B. Jonson, P. Joshi, D.S. Judson, A. Jungclaus, M. Kaci, N. Karkour, M. Karolak, A. Kaşkaş, M. Kebbiri, R.S. Kempley, A. Khaplanov, S. Klupp, M. Kogimtzis, I. Kojouharov, A. Korichi, W. Korten, Th. Kröll, R. Krücken, N. Kurz, B.Y. Ky, M. Labiche, X. Lafay, L. Lavergne, I.H. Lazarus, S. Leboutelier, F. Lefebvre, E. Legay, L. Legeard, F. Lelli, S.M. Lenzi, S. Leoni, A. Lermitage, D. Lersch, J. Leske, S.C. Letts, S. Lhenoret, R.M. Lieder, D. Linget, J. Ljungvall, A. Lopez-Martens, A. Lotodé, S. Lunardi, A. Maj, J. van der Marel, Y. Mariette, N. Marginean, R. Marginean, G. Maron, A.R. Mather, W. Me˛czyński, V. Mendéz, P. Medina, B. Melon, R. Menegazzo, D. Mengoni, E. Merchan, L. Mihailescu, C. Michelagnoli, J. Mierzejewski, L. Milechina, B. Million, K. Mitev, P. Molini, D. Montanari, S. Moon, F. Morbiducci, R. Moro, P.S. Morrall, O. Möller, A. Nannini, D.R. Napoli, L. Nelson, M. Nespolo, V.L. Ngo, M. Nicoletto, R. Nicolini, Y. Le Noa, P.J. Nolan, M. Norman, J. Nyberg, A. Obertelli, A. Olariu, R. Orlandi, D.C. Oxley, C. Özben, M. Ozille, C. Oziol, E. Pachoud, M. Palacz, J. Palin, J. Pancin, C. Parisel, P. Pariset, G. Pascovici, R. Peghin, L. Pellegri, A. Perego, S. Perrier, M. Petcu, P. Petkov, C. Petrache, E. Pierre, N. Pietralla, S. Pietri, M. Pignanelli, I. Piqueras, Z. Podolyak, P. Le Pouhalec, J. Pouthas, D. Pugnére, V.F.E. Pucknell, A. Pullia, B. Quintana, R. Raine, G. Rainovski, L. Ramina, G. Rampazzo, G. La Rana, M. Rebeschini, F. Recchia, N. Redon, M. Reese, P. Reiter, P.H. Regan, S. Riboldi, M. Richer, M. Rigato, S. Rigby, G. Ripamonti, A.P. Robinson, J. Robin, J. Roccaz, J.-A. Ropert, B. Rossé, C. Rossi Alvarez, D. Rosso, B. Rubio, D. Rudolph, F. Saillant, E. Şahin, F. Salomon, M.-D. Salsac, J. Salt, G. Salvato, J. Sampson, E. Sanchis, C. Santos, H. Schaffner, M. Schlarb, D.P. Scraggs, D. Seddon, M. Şenyiğit, M.-H. Sigward, G. Simpson, J. Simpson, M. Slee, J.F. Smith, P. Sona, B. Sowicki, P. Spolaore, C. Stahl, T. Stanios, E. Stefanova, O. Stézowski, J. Strachan, G. Suliman, P.-A. Söderström, J.L. Tain, S. Tanguy, S. Tashenov, Ch. Theisen, J. Thornhill, F. Tomasi, N. Toniolo, R. Touzery, B. Travers, A. Triossi, M. Tripon, K.M.M. Tun-Lanoë, M. Turcato, C. Unsworth, C.A. Ur, J.J. Valiente-Dobon, V. Vandone, E. Vardaci, R. Venturelli, F. Veronese, Ch. Veyssiere, E. Viscione,

R. Wadsworth, P.M. Walker, N. Warr, C. Weber, D. Weisshaar, D. Wells, O. Wieland, A. Wiens, G. Wittwer, H.J. Wollersheim, F. Zocca, N.V. Zamfir, M. Zie˛bliński, and A. Zucchiatti. AGATA — Advanced GAmma Tracking Array. *Nuclear Instruments and Methods in Physics Research Section A: Accelerators, Spectrometers, Detectors and Associated Equipment*, 668(0):26 – 58, 2012.

[9] E. Farnea, F. Recchia, D. Bazzacco, Th. Kröll, Zs. Podolyák, B. Quintana, and A. Gadea. Conceptual design and monte carlo simulations of the AGATA array. *Nuclear Instruments and Methods in Physics Research Section A: Accelerators, Spectrometers, Detectors and Associated Equipment*, 621(1–3):331 – 343, 2010.

[10] Andreas Wiens, Herbert Hess, Benedikt Birkenbach, Bart Bruyneel, Jürgen Eberth, Daniel Lersch, Gheorghe Pascovici, Peter Reiter, and Heinz-Georg Thomas. The AGATA triple cluster detector. *Nuclear Instruments and Methods in Physics Research Section A: Accelerators, Spectrometers, Detectors and Associated Equipment*, 618(1–3):223 – 233, 2010.

[11] G. Pascovici, A. Pullia, F. Zocca, and B. Bruyneel. Low noise, dual gain preamplifier with built in spectroscopic pulser for highly segmented high-purity germanium detectors. In M. P. Brown and K. Austin, editors, *WSEAS Conference*, Bucharest, Romania, 2008.

[12] A. Pullia, F. Zocca, G. Pascovici, C. Boiano, and R. Bassini. An advanced preamplifier for highly segmented germanium detectors. *IEEE Transactions on Nuclear Science*, 53(5):2869–2875, 2006.

[13] Herbert Hess. *Aufbau und Inbetriebnahme des AGATA-Demonstrators*. PhD thesis, Institut für Kernphysik an Universität zu Köln, 2012.

[14] P.-A. Söderström, F. Recchia, J. Nyberg, A. Al-Adili, A. Ataç, S. Aydin, D. Bazzacco, P. Bednarczyk, B. Birkenbach, D. Bortolato, A.J. Boston, H.C. Boston, B. Bruyneel, D. Bucurescu, E. Calore, S. Colosimo, F.C.L. Crespi, N. Dosme, J. Eberth, E. Farnea, F. Filmer, A. Gadea, A. Gottardo, X. Grave, J. Grebosz, R. Griffiths, M. Gulmini, T. Habermann, H. Hess, G. Jaworski, P. Jones, P. Joshi, D.S. Judson, R. Kempley, A. Khaplanov, E. Legay, D. Lersch, J. Ljungvall, A. Lopez-Martens,

W. Meczynski, D. Mengoni, C. Michelagnoli, P. Molini, D.R. Napoli, R. Orlandi, G. Pascovici, A. Pullia, P. Reiter, E. Sahin, J.F. Smith, J. Strachan, D. Tonev, C. Unsworth, C.A. Ur, J.J. Valiente-Dobón, C. Veyssiere, and A. Wiens. Interaction position resolution simulations and in-beam measurements of the AGATA HPGe detectors. *Nuclear Instruments and Methods in Physics Research Section A: Accelerators, Spectrometers, Detectors and Associated Equipment*, 638(1):96 – 109, 2011.

[15] R. Venturelli and D. Bazzacco. Adaptive grid search as pulse shape analysis algorithm for γ-tracking and results. *LNL Annual Report*, 2004.

[16] Th. Kröll and D. Bazzacco. A genetic algorithm for the decomposition of multiple hit events in the gamma-ray tracking detector MARS. *Nuclear Instruments and Methods in Physics Research Section A: Accelerators, Spectrometers, Detectors and Associated Equipment*, 565(2):691 – 703, 2006.

[17] A. Olariu, P. Desesquelles, Ch Diarra, P. Medina, C. Parisel, and C.S.Obot.A. Collaboration. Pulse shape analysis for the location of the gamma-interactions in AGATA. *Nuclear Science, IEEE Transactions on*, 53(3):1028–1031, June 2006.

[18] M. Schlarb, R. Gernhäuser, S. Klupp, and R. Krücken. Pulse shape analysis for gamma-ray tracking (Part II): Fully informed particle swarm algorithm applied to AGATA. *The European Physical Journal A*, 47(10):1–9, 2011.

[19] L. Nelson, M.R. Dimmock, A.J. Boston, H.C. Boston, J.R. Cresswell, P.J. Nolan, I. Lazarus, J. Simpson, P. Medina, C. Santos, and C. Parisel. Characterisation of an AGATA symmetric prototype detector. *Nuclear Instruments and Methods in Physics Research Section A: Accelerators, Spectrometers, Detectors and Associated Equipment*, 573(1–2):153 – 156, 2007.

[20] A.J. Boston, M.R. Dimmock, C. Unsworth, H.C. Boston, R.J. Cooper, A.N. Grint, L.J. Harkness, I.H. Lazarus, M. Jones, P.J. Nolan, D.C. Oxley, J. Simpson, and M. Slee. Performance of an AGATA asymmetric detector. *Nuclear Instruments and Methods in Physics Research Section A: Accelerators, Spectrometers, Detectors and Associated Equipment*, 604(1–2):48 – 52, 2009.

[21] T.M.H. Ha, A. Korichi, F. Le Blanc, P. Désesquelles, N. Dosme, X. Grave, N. Karkour, S. Leboutelier, E. Legay, D. Linget, B. Travers, and P. Pariset. New setup for the characterisation of the AGATA detectors. *Nuclear Instruments and Methods in Physics Research Section A: Accelerators, Spectrometers, Detectors and Associated Equipment*, (0):–, 2012.

[22] F.C.L. Crespi, F. Camera, B. Million, M. Sassi, O. Wieland, and A. Bracco. A novel technique for the characterization of a HPGe detector response based on pulse shape comparison. *Nuclear Instruments and Methods in Physics Research Section A: Accelerators, Spectrometers, Detectors and Associated Equipment*, 593(3):440 – 447, 2008.

[23] C. Domingo-Pardo, N. Goel, T. Engert, J. Gerl, I. Kojouharov, H. Schaffner, F. Didierjean, G. Duchêne, and M.H. Sigward. A novel imaging method for the pulse-shape characterization of position sensitive semiconductor radiation detectors. *Nuclear Instruments and Methods in Physics Research Section A: Accelerators, Spectrometers, Detectors and Associated Equipment*, 643(1):79 – 88, 2011.

[24] N. Goel, C. Domingo-Pardo, T. Engert, J. Gerl, I. Kojouharov, and H. Schaffner. Spatial calibration via imaging techniques of a novel scanning system for the pulse shape characterisation of position sensitive hpge detectors. *Nuclear Instruments and Methods in Physics Research Section A: Accelerators, Spectrometers, Detectors and Associated Equipment*, 652(1):591 – 594, 2011. Symposium on Radiation Measurements and Applications (SORMA) XII 2010.

[25] P. Désesquelles. Determination of the hit locations in segmented hpge detectors without the use of simulations or scanning systems. *Nuclear Instruments and Methods in Physics Research Section A: Accelerators, Spectrometers, Detectors and Associated Equipment*, 654(1):324 – 329, 2011.

[26] P. Medina, C. Santos, and D. Villaume. A simple method for the characterization of HPGe detectors. In *Proceedings of the Twenty-first IEEE Instrumentation and Measurement Technology Conference*.

[27] M. Schlarb, R. Gernhäuser, S. Klupp, and R. Krücken. Pulse shape analysis for gamma-ray tracking (Part I): Pulse shape simulation with JASS. *The European Physical Journal A - Hadrons and Nuclei*, 47:1–14, 2011. 10.1140/epja/i2011-11132-2.

[28] W. Van Roosbroeck. *Bell System Technical Journal*, 29(560), 1950.

[29] *Semiconductor Radiation Detectors Device Physics.* Springer Berlin Heidelberg, 1999.

[30] G. Pausch, W. Bohne, and D. Hilscher. Particle identification in solid-state detectors by means of pulse-shape analysis — results of computer simulations. *Nuclear Instruments and Methods in Physics Research Section A: Accelerators, Spectrometers, Detectors and Associated Equipment*, 337(2–3):573 – 587, 1994.

[31] Bart Bruyneel, Peter Reiter, and Gheorghe Pascovici. Characterization of large volume HPGe detectors. Part I: Electron and hole mobility parameterization. *Nuclear Instruments and Methods in Physics Research Section A: Accelerators, Spectrometers, Detectors and Associated Equipment*, 569(3):764 – 773, 2006.

[32] Bart Bruyneel, Peter Reiter, and Gheorghe Pascovici. Characterization of large volume HPGe detectors. Part II: Experimental results. *Nuclear Instruments and Methods in Physics Research Section A: Accelerators, Spectrometers, Detectors and Associated Equipment*, 569(3):774 – 789, 2006.

[33] Bart Bruyneel. *Characterization of Segmented Large Volume, High Purity Germanium Detectors.* PhD thesis, Institut für Kernphysik an Universität zu Köln, 2006.

[34] E. Gatti, G. Padovini, and V. Radeka. Signal evaluation in multielectrode radiation detectors by means of a time dependent weighting vector. *Nuclear Instruments and Methods in Physics Research*, 193(3):651 – 653, 1982.

[35] William H. Press, Saul A. Teukolsky, William T. Vetterling, and Brian P. Flannery. *Numerical recipes in C: the art of scientific computing.* Cambridge University Press, 2 edition.

[36] B. Birkenbach, B. Bruyneel, G. Pascovici, J. Eberth, H. Hess, D. Lersch, P. Reiter, and A. Wiens. Determination of space

charge distributions in highly segmented large volume HPGe detectors from capacitance–voltage measurements. *Nuclear Instruments and Methods in Physics Research Section A: Accelerators, Spectrometers, Detectors and Associated Equipment*, 640(1):176 – 184, 2011.

[37] B. Bruyneel, B. Birkenbach, and P. Reiter. Space charge reconstruction in highly segmented HPGe detectors through capacitance-voltage measurements. *Nuclear Instruments and Methods in Physics Research Section A: Accelerators, Spectrometers, Detectors and Associated Equipment*, 641(1):92 – 100, 2011.

[38] B. Birkenbach, B. Bruyneel, A. Wiens, D. Bazzacco, M. Bellato, J. Eberth, E. Farnea, H. Hess, D. Mengoni, G. Pascovici, F. Recchia, and P. Reiter. Determination of the space charge distributions in the AGATA detectors. *LNL Annual Report 2010*, (1):68, 2010.

[39] B. Birkenbach. Raumladungsverteilungen in hochsegmentierten HPGe-Detektoren. Diplomarbeit, 2009.

[40] B. Bruyneel, B. Birkenbach, G. Pascovici, J. Eberth, H. Hess, D. Lersch, P. Reiter, A. Wiens, D. Bazzacco, E. Farnea, F. Recchia, and the AGATA collaboration. Determination of the crystal orientation of the AGATA detectors. *LNL Annual Report 2010*, (1):66 – 67, 2010.

[41] B. Bruyneel, B. Birkenbach, J. Eberth, H. Hess, Gh. Pascovici, P. Reiter, A. Wiens, D. Bazzacco, E. Farnea, C. Michelagnoli, and F. Recchia. Correction for hole trapping in AGATA detectors using pulse shape analysis. *The European Physical Journal A*, 49(5):1–9, 2013.

[42] F. Recchia, D. Bazzacco, E. Farnea, A. Gadea, R. Venturelli, T. Beck, P. Bednarczyk, A. Buerger, A. Dewald, M. Dimmock, G. Duchêne, J. Eberth, T. Faul, J. Gerl, R. Gernhaeuser, K. Hauschild, A. Holler, P. Jones, W. Korten, Th. Kröll, R. Krücken, N. Kurz, J. Ljungvall, S. Lunardi, P. Maierbeck, D. Mengoni, J. Nyberg, L. Nelson, G. Pascovici, P. Reiter, H. Schaffner, M. Schlarb, T. Steinhardt, O. Thelen, C.A. Ur, J.J. Valiente Dobon, and D. Weißhaar. Position resolution of the

prototype AGATA triple-cluster detector from an in-beam experiment. *Nuclear Instruments and Methods in Physics Research Section A: Accelerators, Spectrometers, Detectors and Associated Equipment*, 604(3):555 – 562, 2009.

[43] F. Recchia, D. Bazzacco, E. Farnea, R. Venturelli, S. Aydin, G. Suliman, and C.A. Ur. Performance of an AGATA prototype detector estimated by compton-imaging techniques. *Nuclear Instruments and Methods in Physics Research Section A: Accelerators, Spectrometers, Detectors and Associated Equipment*, 604(1–2):60 – 63, 2009.

[44] S. Klupp. A calibration experiment for the AGATA pulse shape analysis. Master's thesis, Technical University Munich, 2011.

[45] Enrico Farnea and Dino Bazzacco. The AGATA demonstrator array at LNL. *Nuclear Physics News*, 22(3):27–32, 2012.

[46] J F C Cocks, P A Butler, K J Cann, P T Greenlees, G D Jones, J F Smith, P M Jones, R Julin, S Juutinen, D Müller, M Piiparinen, A Savelius, R Broda, B Fornal, I Ahmad, D J Blumenthal, M P Carpenter, B Crowell, R V F Janssens, T L Khoo, T Lauritsen, D Nisius, S Asztalos, R M Clark, M A Deleplanque, R M Diamond, P Fallon, I Y Lee, A O Macchiavelli, R W MacLeod, F S Stephens, P Bhattacharyya, and C T Zhang. Multi-nucleon transfer reactions as a tool for spectroscopy of heavy nuclei. *Journal of Physics G: Nuclear and Particle Physics*, 26(1):23, 2000.

[47] A. Sobiczewski, I. Muntian, and Z. Patyk. Problem of "deformed" superheavy nuclei. *Phys. Rev. C*, 63:034306, Feb 2001.

[48] T. M. Shneidman, G. G. Adamian, N. V. Antonenko, and R. V. Jolos. Possible alternative parity bands in the heaviest nuclei. *Phys. Rev. C*, 74:034316, Sep 2006.

[49] J.-P. Delaroche, M. Girod, H. Goutte, and J. Libert. Structure properties of even–even actinides at normal and super deformed shapes analysed using the gogny force. *Nuclear Physics A*, 771(0):103 – 168, 2006.

[50] D. VRETENAR, T. NIKSIC, and P. RING. Relativistic nuclear energy density functionals. *International Journal of Modern Physics E*, 19(04):548–557, 2010.

[51] Jian-You Guo, Peng Jiao, and Xiang-Zheng Fang. Microscopic description of nuclear shape evolution from spherical to octupole-deformed shapes in relativistic mean-field theory. *Phys. Rev. C*, 82:047301, Oct 2010.

[52] Kenneth E. Gregorich, Kenton J. Moody, D. Lee, Wing K. Kot, Robert B. Welch, Philip A. Wilmarth, and Glenn T. Seaborg. Actinide production in 136xe bombardments of 249cf. *Phys. Rev. C*, 35:2117–2124, Jun 1987.

[53] T. Ishii, S. Shigematsu, M. Asai, A. Makishima, M. Matsuda, J. Kaneko, I. Hossain, S. Ichikawa, T. Kohno, and M. Ogawa. In-beam gamma-ray spectroscopy of ^{240}u using the (^{18}o, ^{16}o) reaction. *Phys. Rev. C*, 72:021301, Aug 2005.

[54] T. Ishii, H. Makii, M. Asai, H. Koura, S. Shigematsu, K. Tsukada, A. Toyoshima, M. Matsuda, A. Makishima, J. Kaneko, H. Toume, I. Hossain, T. Shizuma, S. Ichikawa, T. Kohno, and M. Ogawa. Ground-state bands of neutron-rich 236th and 242u nuclei and implication of spherical shell closure at N = 164. *Phys. Rev. C*, 76:011303, Jul 2007.

[55] Kerstin Geibel. *Search for Proton Emission in 54Ni and Multi-Nucleon Transfer Reactions in the Actinide Region.* PhD thesis, Institut für Kernphysik an Universität zu Köln, 2012.

[56] A.M. Stefanini, L. Corradi, G. Maron, A. Pisent, M. Trotta, A.M. Vinodkumar, S. Beghini, G. Montagnoli, F. Scarlassara, G.F. Segato, A. De Rosa, G. Inglima, D. Pierroutsakou, M. Romoli, M. Sandoli, G. Pollarolo, and A. Latina. The heavy-ion magnetic spectrometer prisma. *Nuclear Physics A*, 701(1–4):217 – 221, 2002. 5th International Conference on Radioactive Nuclear Beams.

[57] P. Mason, N. Marginean, G. Montagnoli, S. Beghini, F. Scarlassara, E. Farnea, C. A. Ur, A. Meroni, A. M. Stefanini, L. Corradi, E. Fioretto, I. V. Pokrovskiy, B. Guiot, A. Gadea, J. J. Valiente-Dobón, F. Della Vedova, R. Orlandi, E. Sahin, D. R. Napoli, L. Berti, N. Toniolo, S. Szilner, M. Trotta, M. Romoli, M. La Commara, D. Pierroutsakou, M. Sandoli, G. Pollarolo, and G. Benzoni. The heavy-ion magnetic spectrometer prisma. *The European Physical Journal Special Topics*, 150:359–361, 2007.

[58] J. J. Valiente-Dobon, A. Gadea, S. Brambilla, N. A. Kondratiev, S. Beghini, L. Corradi, G. De Angelis, F. Della Vedova, E. Farnea, E. Fioretto, E. M. Kozulin, S. Lunardi, N. Marginean, G. Montagnoli, D. R. Napoli, R. Orlandi, I. Pokrovsky, E. Sahin, A. M. Stefanini, S. Szilner, M. Trotta, and C. A. Ur. The new heavy-ion mcp-based ancillary detector dante for the clara-prisma setup. *AIP Conference Proceedings*, 853(1):202–207, 2006.

[59] A. Gadea, E. Farnea, J.J. Valiente-Dobón, B. Million, D. Mengoni, D. Bazzacco, F. Recchia, A. Dewald, Th. Pissulla, W. Rother, G. de Angelis, A. Austin, S. Aydin, S. Badoer, M. Bellato, G. Benzoni, L. Berti, R. Beunard, B. Birkenbach, E. Bissiato, N. Blasi, C. Boiano, D. Bortolato, A. Bracco, S. Brambilla, B. Bruyneel, E. Calore, F. Camera, A. Capsoni, J. Chavas, P. Cocconi, S. Coelli, A. Colombo, D. Conventi, L. Costa, L. Corradi, A. Corsi, A. Cortesi, F.C.L. Crespi, N. Dosme, J. Eberth, S. Fantinel, C. Fanin, E. Fioretto, Ch. Fransen, A. Giaz, A. Gottardo, X. Grave, J. Grebosz, R. Griffiths, E. Grodner, M. Gulmini, T. Habermann, C. He, H. Hess, R. Isocrate, J. Jolie, P. Jones, A. Latina, E. Legay, S. Lenzi, S. Leoni, F. Lelli, D. Lersch, S. Lunardi, G. Maron, R. Menegazzo, C. Michelagnoli, P. Molini, G. Montagnoli, D. Montanari, O. Möller, D.R. Napoli, M. Nicoletto, R. Nicolini, M. Ozille, G. Pascovici, R. Peghin, M. Pignanelli, V. Pucknell, A. Pullia, L. Ramina, G. Rampazzo, M. Rebeschini, P. Reiter, S. Riboldi, M. Rigato, C. Rossi Alvarez, D. Rosso, G. Salvato, J. Strachan, E. Sahin, F. Scarlassara, J. Simpson, A.M. Stefanini, O. Stezowski, F. Tomasi, N. Toniolo, A. Triossi, M. Turcato, C.A. Ur, V. Vandone, R. Venturelli, F. Veronese, C. Veyssiere, E. Viscione, O. Wieland, A. Wiens, F. Zocca, and A. Zucchiatti. Conceptual design and infrastructure for the installation of the first AGATA sub-array at LNL. *Nuclear Instruments and Methods in Physics Research Section A: Accelerators, Spectrometers, Detectors and Associated Equipment*, 654(1):88 – 96, 2011.

[60] G. Montagnoli, A.M. Stefanini, M. Trotta, S. Beghini, M. Bettini, F. Scarlassara, V. Schiavon, L. Corradi, B.R. Behera, E. Fioretto, A. Gadea, A. Latina, S. Szilner, L. Donà, M. Rigato, N.A. Kondratiev, A. Yu. Chizhov, G. Kniajeva, E.M. Kozulin, I.V.

Pokrovskiy, V.M. Voskressensky, and D. Ackermann. The large-area micro-channel plate entrance detector of the heavy-ion magnetic spectrometer prisma. *Nuclear Instruments and Methods in Physics Research Section A: Accelerators, Spectrometers, Detectors and Associated Equipment*, 547(2–3):455 – 463, 2005.

[61] S. Beghini, L. Corradi, E. Fioretto, A. Gadea, A. Latina, G. Montagnoli, F. Scarlassara, A.M. Stefanini, S. Szilner, M. Trotta, and A.M. Vinodkumar. The focal plane detector of the magnetic spectrometer prisma. *Nuclear Instruments and Methods in Physics Research Section A: Accelerators, Spectrometers, Detectors and Associated Equipment*, 551(2–3):364 – 374, 2005.

[62] X. Grave, R. Canedo, J.-F. Clavelin, S. Du, and E. Legay. Narval a modular distributed data acquisition system with ada 95 and rtai. In *Real Time Conference, 2005. 14th IEEE-NPSS*, pages 5 pp.–, 2005.

[63] O. Stezowski. AGATA data flow library. `http://agata.in2p3.fr/doc/ADF_DesignProposoal.pdf`.

[64] Bart Bruyneel, Peter Reiter, Andreas Wiens, Jürgen Eberth, Herbert Hess, Gheorghe Pascovici, Nigel Warr, Sezgin Aydin, Dino Bazzacco, and Francesco Recchia. Crosstalk corrections for improved energy resolution with highly segmented HPGe-detectors. *Nuclear Instruments and Methods in Physics Research Section A: Accelerators, Spectrometers, Detectors and Associated Equipment*, 608(1):99 – 106, 2009.

[65] J van der Marel and B Cederwall. Backtracking as a way to reconstruct compton scattered γ-rays. *Nuclear Instruments and Methods in Physics Research Section A: Accelerators, Spectrometers, Detectors and Associated Equipment*, 437(2–3):538 – 551, 1999.

[66] G.J. Schmid, M.A. Deleplanque, I.Y. Lee, F.S. Stephens, K. Vetter, R.M. Clark, R.M. Diamond, P. Fallon, A.O. Macchiavelli, and R.W. MacLeod. A γ-ray tracking algorithm for the GRETA spectrometer. *Nuclear Instruments and Methods in Physics Research Section A: Accelerators, Spectrometers, Detectors and Associated Equipment*, 430(1):69 – 83, 1999.

[67] A. Lopez-Martens, K. Hausschild, A. Korichi, J. Roccaz, and J-P. Thibaud. γ-ray tracking algorithms: a comparison. *Nuclear Inst. and Methods in Physics Research A*, 533:454–466, 2004.

[68] Ian Bird. Computing for the large hadron collider. *Annual Review of Nuclear and Particle Science*, 61(1):99–118, 2011.

[69] I. Antcheva, M. Ballintijn, B. Bellenot, M. Biskup, R. Brun, N. Buncic, Ph. Canal, D. Casadei, O. Couet, V. Fine, L. Franco, G. Ganis, A. Gheata, D. Gonzalez Maline, M. Goto, J. Iwaszkiewicz, A. Kreshuk, D. Marcos Segura, R. Maunder, L. Moneta, A. Naumann, E. Offermann, V. Onuchin, S. Panacek, F. Rademakers, P. Russo, and M. Tadel. ROOT — a C++ framework for petabyte data storage, statistical analysis and visualization. *Computer Physics Communications*, 180(12):2499 – 2512, 2009. 40 YEARS OF CPC: A celebratory issue focused on quality software for high performance, grid and novel computing architectures.

[70] Pär-Anders Söderström. *Collective Structure of Neutron-Rich Rare-Earth Nuclei and Development of Instrumentation for Gamma-Ray Spectroscopy.* PhD thesis, Uppsala University, Nuclear Physics, 2011.

[71] W.R. Leo. *Techniques for Nuclear and Particle Physics Experiments: A How-To Approach.* U.S. Government Printing Office, 1994.

[72] A. Vogt. Teilchenidentifikation für In-Beam-Gammaspektroskopie neutronenreicher Aktinide, 2012.

[73] T. Williams and C. Kelley. Gnuplot - an interactive plotting program. version 4.2 patchlevel 2.

[74] A. Georgiev and W. Gast. Digital pulse processing in high resolution, high throughput, gamma-ray spectroscopy. *Nuclear Science, IEEE Transactions on*, 40(4):770–779, Aug 1993.

[75] L. Arnold, R. Baumann, E. Chambit, M. Filliger, C. Fuchs, C. Kieber, D. Klein, P. Medina, C. Parisel, M. Richer, C. Santos, and C. Weber. Tnt digital pulse processor. *Nuclear Science, IEEE Transactions on*, 53(3):723–728, June 2006.

[76] D. Bazzacco. private communication.

[77] S.Y.F. Chu, L. P. Ekstroem, and R.B. Firestone. The Lund/LBNL Nuclear Data Search. Version 2.0.

[78] D. Bazzacco. Efficiency and P/T ratio for the AGATA demonstrator at legnaro. 13th AGATA week Ganil 2013, 2013.

[79] A. B. Brown, C. W. Snyder, W. A. Fowler, and C. C. Lauritsen. Excited states of the mirror nuclei, li^7 and be^7. *Phys. Rev.*, 82:159–181, Apr 1951.

[80] N. Braun, T. Kotthaus, and R. Schulze. HDTV - Nuclear Spectrum Analysis Tool, 2009.

[81] Brookhaven National Laboratory National Nuclear Data Center. Nudat (nuclear structure and decay data), March 18, 2008 2008.

[82] O.B. Tarasov and D. Bazin. LISE++ : design your own spectrometer. *Nuclear Physics A*, 746(0):411 – 414, 2004. Proceedings of the Sixth International Conference on Radioactive Nuclear Beams (RNB6).

[83] B. Alikhani, A. Givechev, A. Heinz, P.R. John, J. Leske, M. Lettmann, O. Möller, N. Pietralla, and C. Röder. Compton polarimetry with a 36-fold segmented HPGe-detector of the AGATA-type. *Nuclear Instruments and Methods in Physics Research Section A: Accelerators, Spectrometers, Detectors and Associated Equipment*, 675(0):144 – 154, 2012.

[84] R.B. Firestone and V.S. Shirley. *Table of Isotopes, 2 Volume Set*. Table of Isotopes. Wiley, 1997.

[85] Joa Ljungvall and Johan Nyberg. Neutron interactions in AGATA and their influence on gamma-ray tracking. *Nuclear Instruments and Methods in Physics Research Section A: Accelerators, Spectrometers, Detectors and Associated Equipment*, 550(1–2):379 – 391, 2005.

[86] Peter Möller, Arnold J. Sierk, Takatoshi Ichikawa, Akira Iwamoto, Ragnar Bengtsson, Henrik Uhrenholt, and Sven Åberg. Heavy-element fission barriers. *Phys. Rev. C*, 79:064304, Jun 2009.

[87] N. Fotiades, R. O. Nelson, M. Devlin, J. A. Cizewski, J. A. Becker, W. Younes, R. Krücken, R. M. Clark, P. Fallon, I. Y. Lee, A. O. Macchiavelli, T. Ethvignot, and T. Granier. High-spin states in xe-135. *Phys. Rev. C*, 75:054322, May 2007.

[88] A. Shrivastava, M. Caamaño, M. Rejmund, A. Navin, F. Rejmund, K. H. Schmidt, A. Lemasson, C. Schmitt, L. Gaudefroy, K. Sieja, L. Audouin, C. O. Bacri, G. Barreau, J. Benlliure, E. Casarejos, X. Derkx, B. Fernández-Domínguez, C. Golabek, B. Jurado, T. Roger, and J. Taieb. Prompt gamma-ray spectroscopy of isotopically identified fission fragments. *Phys. Rev. C*, 80:051305, Nov 2009.

[89] J. A. Becker and R. O. Nelson. New physics opportunities with GEANIE at LANSCE/WNR. *Nucl. Phys. News*, 7:11–14, 1997.

[90] J. M. Allmond, D. C. Radford, J. Pavan, K. Lagergren, C. Baktash, J. R. Beene, C. R. Bingham, L. Chaturvedi, M. Danchev, D. Fong, A. Galindo-Uribarri, P. A. Hausladen, J. K. Hwang, W. Krolas, J. F. Liang, E. Padilla-Rodal, W. Reviol, D. G. Sarantites, D. Seweryniak, D. Shapira, A. E. Stuchbery, J. P. Urrego-Blanco, R. L. Varner, X. Wang, C.-H. Yu, and S. Zhu. One-neutron transfer study of transfer study of 135te and 137xe by particle-gamma coincidence spectroscopy: The v1i13/2 state at n=83. *Phys. Rev. C*, 86:031307, Sep 2012.

[91] F. Zocca. *New technologies for low-noise wide-dynamic-range preamplification of HPGe segmented detector signals*. PhD thesis, Universita degli studi di Milano, 2007.

[92] R. Breier and P.P. Povinec. Simulation of background characteristics of low-level gamma-ray spectrometers using monte carlo method. *Applied Radiation and Isotopes*, 68(7–8):1231 – 1235, 2010. Proceedings of the 17th International Conference on Radionuclide Metrology and its Applications (ICRM 2009).

[93] Pavol Vojtyla. A computer simulation of the cosmic-muon background induction in a ge gamma-spectrometer using GEANT. *Nuclear Instruments and Methods in Physics Research Section B: Beam Interactions with Materials and Atoms*, 100(1):87 – 96, 1995.

[94] D. Schneiders. Analyse von kosmischer höhenstrahlung mit hilfe eines segmentierten HPGe-Detektors, 2011.

[95] T. Steinbach. Aufbau einer Compton-Kamera basierend auf einem hochsegmentierten HPGe-Detektor und digitaler Spektroskopieelektronik, 2011.

[96] B. Weiler. Development of a Compton camera using highly segmented semiconductor detectors. Diplomarbeit, 2009.

[97] L. Lewandowski. Koinzidenzmessung und Ortsbestimmung mit einer Compton-Kamera, 2012.

[98] R.J. Cooper, D.C. Radford, P.A. Hausladen, and K. Lagergren. A novel HPGe detector for gamma-ray tracking and imaging. *Nuclear Instruments and Methods in Physics Research Section A: Accelerators, Spectrometers, Detectors and Associated Equipment*, 665(0):25 – 32, 2011.

List of Tables

List of Figures

A. Example of an ADL simulation

```
//The ADL includes:
#include "ADL.h"
#include "SIMION_Array.h"
#include "SIMION_ReadWrite.h"

//Parameters for conversion
//From AGATA reference frame
//To the frame used in the weighting field arrays
#define Xoff 4.1 //[cm]
#define Yoff 4.1 //[cm]
#define Zoff 9.0 //[cm]

//Library step size:
//(Detector front is at Z=9cm!!!)
#define LibStep 0.2 //[cm]
#define LibXmin -5.025 //[cm]
#define LibXmax 5.025 //[cm]
#define LibYmin -5.025 //[cm]
#define LibYmax 5.025 //[cm]
#define LibZmin -0.025 //[cm]
#define LibZmax 10.025 //[cm]

int main(int argc, char **argv)
{
 char SetupFile[100];
 FILE *export;

 struct SIMION_PA *spy;
 struct ADL_EVENT *Sim;

 DOUBLE X,Y,Z,Check,P[4];
 DOUBLE sensity_e[2],sensity_h[2];
 INTEGER i,HitSeg,counter=0,number=0;
 INTEGER k,LastSample,LongestTrace = 0;

 //checking input arguments:
 if (argc != 3) {
  printf("ERROR: Need 2 arguments: \n - the detector number \
   (e.g. A001) \n - the output filename \n ");
```

```
 printf("argc: %d \n",argc);
 while(argc--) printf("%s\n", *argv++);
  return 0;
}

//Setup ADL using input argument:
sprintf(SetupFile,"SetupFiles/%s/%s.txt",argv[1],argv[1]);
ADL_Setup(SetupFile);
if (!ADL_G_DEBUG) ADL_Status();
//At this point ADL is setup, and ADL_G_NUMRES_XYZe
//should be defined, else problems:
if (ADL_G_NUMRES_XYZe==NULL){
 printf("\n>>> ERROR: ADL setup failed <<<\n");
 system("pause");
 return 1;
}
if (ADL_G_NUMRES_XYZh==NULL){
 printf("\n>>> ERROR: ADL setup failed <<<\n");
 system("pause");
 return 1;
}
//Opening file for export in TXT format:
printf("\n Output will be sent to file %s\n",argv[2]);
if ((export = fopen(argv[2],"w"))==NULL) {
 printf("\n ERROR: Cannot open file %s\n",argv[2]);
 exit(1);
}
//Create event:
Sim = new_event();
printf("\n**** END SETUP ****\n");
nspy = -1;
for (Z = LibZmin; Z<= LibZmax; Z+= LibStep){
 for (Y = LibYmin; Y<= LibYmax; Y+= LibStep){
  for (X = LibXmin; X<= LibXmax; X+= LibStep){
   nspy++;
   number++;
  //Check if in detector:
   P[1] = Xoff + X; P[2] = Yoff + Y; P[3] = Zoff - Z;
   if (!ADL_G_InDetector(P))
    continue;
   //Input for simulating event Sim:
```

```
    //contains the trigger time (in us) of core
    Sim->HP.T0 = 0.05;
    //contains the energy fraction deposited by
    //the nInt interactions
    Sim->HP.Eint[0] = 1.0;
    //This needs conversion from AGATA coordinate system to the
    //coordinate system used to describe the WEIGHTING FIELDS:
    Sim->HP.Pos[0][0] = Xoff + X;//x-position [cm]
    Sim->HP.Pos[0][1] = Yoff + Y;//y-position [cm]
    Sim->HP.Pos[0][2] = Zoff - Z;//z-position [cm]
    //Calculate the trace:
    ADL_G_CalculateTraces(Sim);
    //Check which segment was hit:
    HitSeg = -1;
    for (i=0;i<ADL_G_EVENT_NSEG;i++) if (Sim->TD.Eseg[i]>1e-5) {
     HitSeg = i;
     ADL_CalculateTrappingSensitivity(i,&(Sim->HP.Pos[0][0])\
     ,sensity_e,sensity_h);
    }
    //Write final results:
    if (HitSeg > -1){ //Only prints events in germanium:
     //This needs conversion from AGATA coordinate system to the
     //coordinate system used to describe the WEIGHTING FIELDS:
     Sim->HP.Pos[0][0] = 10*X;//x-position [mm]
     Sim->HP.Pos[0][1] = 10*Y;//y-position [mm]
     Sim->HP.Pos[0][2] = 10*(Zoff - Z);//z-position [mm]
     ADL_G_WriteEvent(export,Sim);
    }
   }
  }
 }
 fclose(export);
 return 0;
}
```

B. Template files for a simulation of detector A001

A001.txt

```
# This file is written for ADL version 3.0:
ADL_G_VERSION  3.0

# The debugin mode is switched off:
ADL_G_DEBUG 0

# Template for the event structure
# How many interactions maximum in an event,
# how many samples in the traces,
# how many segments...
ADL_EVENT templates/AGATA_EVENT.txt

# Template for convolution
# This setup file will invert channel 0 ("core")
ADL_CONVL_DUMMY templates/Invert_Core.txt

# Template for drift velocity parameters
# For Germanium, see:
# Bruyneel et al NIM A 569 (2006) 764-773
# Mihailescu et al NIM A 447 (2000) 350-360
ADL_DRIFT_GE templates/Template_Drift_GE.txt

# Template for field parameters
ADL_FIELDS_SIMION templates/A001_FIELDS.txt

# Template for read and write operations
ADL_READWRITE templates/READWRITE_TXT.txt

# Template for timing calculations (not needed)
# ADL_TIME_FAST templates/Template_TIME_FAST.txt

# Template of the path calculation
```

```
ADL_TRACES_NUMRES templates/Template_Traces_NUMRES.txt

# Template for the calculation of the trapping parameters
ADL_TRAPPING templates/Template_TRAPPING.txt
```

AGATA_EVENT.txt

```
# Maximum number interactions
ADL_G_EVENT_NINT  1
# Number of segments (including Core)
ADL_G_EVENT_NSEG  37
# Trace length [0...dimT]
ADL_G_EVENT_DIMT  119
# Sampling interval [us] (length per sample)
ADL_G_EVENT_DeltaT  0.005
```

Invert_Core.txt

```
# Segments to invert:
INVERT 0
```

Template_DRIFT_GE.txt

```
# LATTICE ORIENTATION PARAMETERS:
ADL_G_LatticePhi    0.7853981633
ADL_G_LatticeTheta 0.0
ADL_G_LatticePsi 0.0

# Electron Mobility Parameters:
# Mobility in 100:
ADL_G_E0e100 507.7
ADL_G_Be100 0.80422
ADL_G_Mu0e100 0.0371654
ADL_G_MuNe100 -0.0001447
# Intervalley Scattering rate:
ADL_G_LnNu0 0.459
```

```
ADL_G_LnNu1 0.0294
ADL_G_LnNu2 0.000054
ADL_G_E0 1200.0

# Hole Mobility Parameters:
# Mobility in 100:
ADL_G_E0h100 181.9
ADL_G_Bh100 0.73526
ADL_G_Muh100 0.062934
# Mobility in 111:
ADL_G_E0h111 143.9
ADL_G_Bh111 0.7488
ADL_G_Muh111 0.062383

# Other Parameters:
ADL_G_SmallField 1e-6
```

A001_FIELDS.txt

```
# Gridsize of the calculation
# [cm/gridunit] sets common dimension of arrays
ADL_G_SIMION_GridSize 0.05
# [V] Small potential, Defines e.g. ADL_In_Detector_SIMION
ADL_G_SIMION_SmallPot 1e-6

# Path to find the weighting potentials
ADL_G_Wpot SIMION/A001.pa%d

# Path to find the electrical potentials
ADL_G_Epot SIMION/charge_A001_%d.pa
# A list with scaling factors
# for the electrical potentials follow:
# (This depends on the meaning of the fields loaded)
# Bias voltage in [V]
ADL_SCALE_0 5000
# Scaling of the space charge
ADL_SCALE_1 0.5
```

```
ADL_SCALE_2 1.24
ADL_SCALE_3 0.5
ADL_SCALE_4 1.24
```

READWRITE_TXT.txt

```
# Read traces from TXT files
ADL_READ TXT
# Write traces to TXT files
ADL_WRITE TXT
```

Template_TRACES.txt

```
# RKQS error tolerance for integration
ADL_G_NUMRES_EPS 1e-6
# odeint maximum integration steps between 2 samples
ADL_G_NUMRES_MAXSTP 100000
# odeint small position difference [cm]
ADL_G_NUMRES_TINY 1e-5
# odeint minimum step size to take [us]
ADL_G_NUMRES_DTMIN  0.0
```

Template_TRAPPING

```
# SETTING TRAPPING RATE MODEL:
# For electrons
ADL_G_TRAPPING_ERATE ADL_ElectronTrappingRate_FIELD
# For holes
ADL_G_TRAPPING_HRATE ADL_HoleTrappingRate_FIELD

# SETTING NUMRES PARAMETERS for integration:
# RKQS error tolerance for integration
ADL_G_TRAPPING_EPS
# odeint maximum integration steps between 2 samples
ADL_G_TRAPPING_MAXSTP 100000
# odeint small position difference [cm]
```

```
ADL_G_TRAPPING_TINY 1e-5
# odeint minimum step size to take [us]
ADL_G_TRAPPING_DTMIN  0.0
```

C. Experiments of the LNL AGATA campaign

2010

February Coulomb excitation of the presumably deformed band in ^{42}Ca

May Neutron rich nuclei in the vicinity of ^{208}Pb

May Inelastic scattering as a tool to search for highly excited states up to the region of the Giant Quadrupole Resonance

June Lifetime measurements of the neutron-rich Cr isotopes

June Lifetime measurement in neutron-rich Ni, Cu, and Zn

July Lifetime measurement of the 6.792 MeV state in ^{15}O

2011

March Characterization of new structures in octupole-deformed radium and thorium nuclei

March Confirmation of the molecular structure of excited bands in ^{21}Ne

April Near and sub-barrier transfer reactions in ^{60}Ni +^{118}Sn

May Isospin mixing in N=Z nucleus ^{80}Zr at medium temperature

June Lifetimes of intruder states in N $\sim$ 20 sd-pf-shell neutron-rich nuclei

September Precision lifetime study in the neutron-rich N= 84 isotone ^{140}Ba from DSAM measurements following Coulomb-barrier alpha-transfer reactions on a ^{136}Xe

October Development of the nuclear structure of neutron–rich isotopes in the Z $>$ 38 region populated by heavy–ion induced fission

October RDDS lifetime measurement in the region of the neutron-rich doubly magic ^{132}Sn: Lifetime of the 6+ state in ^{136}Te.

October Spectroscopy of neutron rich Th and U nuclei after multi-nucleon reactions

October Collectivity at maximum nucleon valency: Investigation of ground-state rotation in the neutron-rich Dy, Er and Yb nuclei

November Structure beyond the N = 50 shell closure in neutron-rich nuclei in the vicinity of ^{78}Ni: The case of N = 51 nuclei

November Delayed shape transition in ^{196}Os

December Study of high-lying bound and unbound states in ^{124}Sn and ^{140}Ce via inelastic scattering of ^{17}O ions

D. Online spectra

The narval actors are generating for every run spectra in a simple binary format. This is useful to control, set up and debug the system. The spectra are documented in the source code of the actors. As this is not that practical an overview of the important spectra is given here as table.

Folder	Name and description
Global	`Oft__1-15-16384-UI__ES.spec`
	Sum-energy spectra (gain 1 keV / chan)
Global	`Oft__15-1000-UI__TC.spec`
	CFD trigger relative to beginning of trace (ns)
Global	`Oft__15-15-1000-UI__TS.spec`
	T-gamma-gamma from timestamp (samples)
Global	`Oft__15-15-1000-UI__TT.spec`
	T-gamma-gamma from CFD (ns)
Global	`Oft__15-15-UI__Fold.matr`
	number of gamma's versus number of crystals
Global	`Oft__2-10-16384-UI__EE.spec`
	input and tracked spectra
Global	`Oft__2-15-1000-UI__TA.spec`
	Difference of time stamps between crystals and ancillary
Global	`Oft__2-15-16384-UI__EA.spec`
	Core energy sorted by detector, in coincidence with ancillary
Global	`Oft__2-15-16384-UI__EC.spec`
	Core and sum Segs sorted by detector
Global	`Oft__2-256-4096-UI__Anc.spec`
	Projection of all Ancillary parameters
Global	`Oft__4-15-UI__Fold.spec`
	multiplicity of crystals
Global	`Oft__540-540-US__SGSG.matr`
	Segment-segment coincidences for all pairs
Crystal	`Prep__1000-44-100-S__Traces.samp`
	First traces sets

Table 38: Online spectra of the user libraries

Crystal	`Prep__2-10-16384-UI__Esum.spec` sum of energy of segments before and after Xtalk correction
Crystal	`Prep__2-1536-1536-US__EcTc.matr` Energy(keV)-Time(ns) for the triggering core
Crystal	`Prep__2-40-10000-UI__TT1.spec` Time spectra, before shifting traces
Crystal	`Prep__2-40-10000-UI__TT2.spec` Time spectra, after shifting traces
Crystal	`Prep__2-40-16384-UI__Ener.spec` calibrated energy spectrum of segments and core
Crystal	`Prep__3000-3000-US__TT1.matr` relative and absolute core-to-segment time, before shifting traces
Crystal	`Prep__3000-3000-US__TT2.matr` relative and absolute core-to-segment time, after shifting traces
Crystal	`Prep__36-36-US__EsEs.matr` Segment-segment energy for all pairs
Crystal	`Prep__40-1536-100-US__EeTr.matr` energy(keV)-T10-90 (samp)
Crystal	`Prod__100-42-100-S__Traces.samp` traces: 36segs + 2cores + 3empty
Crystal	`Prod__38-32768-UI__Ener.spec` Energy spectrum of segments and cores
Crystal	`Psa__1000-2-42-60-F__Traces.samp` The result of the first 1000 decompositions
Crystal	`Psa__10-100-100-100-US__XYZR.matr` XY, XZ, YZ, rZ hits and XY hits as function of Z
Crystal	`Psa__10-36-4-100-100-US__Seg.matr` hits in the segments
Crystal	`Psa__2-40-16384-UI__Ener.spec` Energy spectrum of segments and core (segment at mult 1)
Crystal	`Psa__40-100-UI__Stat.spec` Distribution of hits
Ancillary	`Anc__6-32-4096-UI__All.spec` Projection of all parameters
Ancillary	`Anc__6-32-4096-UI__Cal.spec` Calibrated projection of all parameters

Table 39: Online spectra of the user libraries

E. Glossary

ADC Analoge to Digital Converter

DAQ Data AcQuisition

DSSSD Double Sided Silicon Strip Detector

FET Field Effect Transistor

FWHM Full Width Half Maximum

GRT Gamma Ray Tracking

HPGe High Purity Germanium

IC Ionization Chamber

IO Input Output

MCP Micro Channel Plate

MWPPAC Multi Wire Parallel Plates Avalanche Counter

PA Potential Array

PSA Pulse Shape Analysis

TAC Time to Amplitude Converter

TOT Time Over Threshold

TOF Time Of Flight

Acknowledgement

First of all I want to thank Prof. Dr. Peter Reiter for the opportunity and the help to write this thesis. Without his support neither the experiments nor the presented work would have been possible.

Prof. Dr. Jan Jolie for being the co-examiners of my work.

Dr. Bart Bruyneel for always helping me, for the nice discussions and for the deep insights he shared with me on the basic working principle of semiconductor detectors.

The large group of system operators that I worked with namely, Dr. Ralf Schulze, Dr. Michael Pfeiffer, Dr. Stefan Heinze, Dr. Norbert Braun, Dr. Martin Ebert, Nima Saed–Samii, Dr. Gunnar Friesner and Moritz Dannhoff. Keep the system running!

Dr. Herbert Hess, Dr. Jürgen Eberth and Dr. Andreas Wiens for the never ending work with detectors and cryostats and the never ending discussions.

The bachelors that worked with me and contributed to this work: Andreas Vogt (special thanks for yield chart), Tim Steinbach, Lars Lewandowski, David Schneiders, Rouven Hirsch and Fabian Radeck.

My complete working group for listening to the many trial presentations and for the fruitful discussions.

The mechanical and electronic workshops of the IKP for their support and share of knowledge, especially Gheorge Pascovici for the discussions and help with the preamplifiers.

The complete AGATA community especially Dino Bazzacco, Caterina Michelagnoli, Enrico Farnea, Francesco Recchia, Jose Javier Valiente Dobon and Philip John for the fantastic support during and after the experiment 11.22.

My girlfriend Sabrina Scholz, my son Karl Birkenbach and the rest of my family for their never ending support and trust in me.

Publications

The following papers have been published in collaboration with other groups and scientists during my time at the Institut für Kernphysik at the University of Cologne.

2010

A. Wiens, H. Hess, B. Birkenbach, B. Bruyneel, J. Eberth, D. Lersch, G. Pascovici, P. Reiter, H.-G. Thomas
The AGATA triple cluster detector
Nucl. Instr. and Meth. A 618, (2010) 223-233

2011

P.-A. Söderström, F. Recchia, J. Nyberg, A. Al-Adili, A. Atac, S. Aydin, D. Bazzacco, P. Bednarczyk, B. Birkenbach, D. Bortolato, A.J. Boston, H.C. Boston, B. Bruyneel, D. Bucurescu, E. Calore, S. Colosimo, F.C.L. Crespi, N. Dosme, J. Eberth, E. Farnea, F. Filmer, A. Gadea, A. Gottardo, X. Grave, J. Grebosz, R. Griffiths, M. Gulmini, T. Habermann, H. Hess, G. Jaworski, P. Jones, P. Joshi, D.S. Judson, R. Kempley, A. Khaplanov, E. Legay, D. Lersch, J. Ljungvall, A. Lopez-Martens, W. Meczynski, D. Mengoni, x, C. Michelagnoli, P. Molini, D.R. Napoli, R. Orlandi, G. Pascovici, A. Pullia, P. Reiter, E. Sahin, J.F. Smith, J. Strachan, D. Tonev, C. Unsworth, C.A. Ur, J.J. Valiente-Dobon, C. Veyssiere, A. Wiens and The AGATA Collaboration
Interaction position resolution simulations and in-beam measurements of the AGATA HPGe detectors
Nucl. Instr. and Meth. A, Volume 638, Issue 1, 11 May 2011, Pages 96-109

B. Bruyneel, B. Birkenbach and P. Reiter
Space charge reconstruction in highly segmented HPGe detectors through Capacitance-voltage measurements
Nucl. Instr. and Meth. A, Volume 641, Issue 1, 11 June 2011, Pages 92-100

B. Birkenbach, B. Bruyneel, J. Eberth, H. Hess, D. Lersch, G. Pascovici, P. Reiter, A. Wiens
Determination of space charge distributions in highly segmented large volume HPGe detectors from capacitance-voltage measurements
Nucl. Instr. and Meth. A, Volume 640, Issue 1, 1 June 2011, Pages 176-184

D. Lersch, G. Pascovici, B. Birkenbach, B. Bruyneel, J. Eberth, H. Hess, P. Reiter, A. Wiens, H. G. Thomas
The LN2 level meter for the AGATA triple cluster detector
Nucl. Instr. and Meth. A, Volume 640, Issue 1, 1 June 2011, Pages 133-138

A. Gadea, E. Farnea, J.J. Valiente-Dobon, B. Million, D. Mengoni, D. Bazzacco, F. Recchia, A. Dewald, Th. Pissulla, W. Rother, G. de Angelis, A. Austin, S. Aydin, S. Badoer, M. Bellato, G. Benzoni, L. Berti, R. Beunard, B. Birkenbach, E. Bissiato, N. Blasi, C. Boiano, D. Bortolato, A. Bracco, S. Brambilla, B. Bruyneel, E. Calore, F. Camera, A. Capsoni, J. Chavas, P. Cocconi, S. Coelli, A. Colombo, D. Conventi, L. Costa, L. Corradi, A. Corsi, A. Cortesi, F.C.L. Crespi, N. Dosme, J. Eberth, S. Fantinel, C. Fanin, E. Fioretto, Ch. Fransen, A. Giaz, A. Gottardo, X. Grave, J. Grebosz, R. Griffiths, E. Grodner, M. Gulmini, T. Habermann, C. He, H. Hess, R. Isocrate, J. Jolie, P. Jones, A. Latina, E. Legay, S. Lenzi, S. Leoni, F. Lelli, D. Lersch, S. Lunardi, G. Maron, R. Menegazzo, C. Michelagnoli, P. Molini, G. Montagnoli, D. Montanari, O. Möller, D.R. Napoli, M. Nicoletto, R. Nicolini, M. Ozille, G. Pascovici, R. Peghin, M. Pignanelli, V. Pucknell, A. Pullia, L. Ramina, G. Rampazzo, M. Rebeschini, P. Reiter, S. Riboldi, M. Rigato, C. Rossi Alvarez, D. Rosso, G. Salvato, J. Strachan, E. Sahin, F. Scarlassara, J. Simpson, A.M. Stefanini, O. Stezowski, F. Tomasi, N. Toniolo, A. Triossi, M. Turcato, C.A. Ur, V. Vandone, R. Venturelli, F. Veronese, C. Veyssiere, E. Viscione, O. Wieland, A. Wiens, F. Zocca, A. Zucchiatti
Conceptual design and infrastructure for the installation of

the first AGATA sub-array at LNL
Nucl. Instr. and Meth. A, Volume 654, Issue 1, 21 October 2011, Pages 88-96

2012

G.Duchene, E.Farnea, A.Gadea, A.Korichi, J.Nyberg, P.Reiter, J.Simpson (corresponding authors)
AGATA Advanced GAmma Tracking Array
Nucl. Instr. and Meth. A 668 (2012) 26

P.-A. Söderström, F. Recchia, J. Nyberg, A. Gadea, S.M. Lenzi, A. Poves, A. Atac, S. Aydin, D. Bazzacco, P. Bednarczyk, D. Bortolato, A.J. Boston, H.C. Boston, B. Bruyneel, D. Bucurescu, E. Calore, S. Colosimo, F.C.L. Crespi, N. Dosme, E. Farnea, F. Filmer, A. Gottardo, M. Gulmini, G. Jaworski, P. Joshi, D.S. Judson, R.S. Kempley, A. Khaplanov, J. Ljungvall, W. Meczynski, D. Mengoni, C. Michelagnoli, P. Molini, D.R. Napoli, E. Sahin, J.F. Smith, D. Tonev, C. Unsworth, C.A. Ur, J.J. Valiente-Dobon, A. Wiens, M. Bellato, B. Birkenbach, B. Cederwall, L. Charles, J. Chavas, D.M. Cullen, P. Desesquelles, G. Duchene, J. Eberth, A. Görgen, J. Grebosz, H. Hess, T.A. Hughes, J. Jolie, A. Jungclaus, N. Karkour, M. Karolak, A. Maj, G. Maron, R. Menegazzo, P.J. Nolan, M. Norman, A. Obertelli, Zs. Podolyak, A. Pullia, B. Quintana, N. Redon, P.H. Regan, P. Reiter, A.P. Robinson, M.D. Salsac, J. Simpson, O. Stezowski, Ch. Theisen, N. Toniolo
High-spin structure in 40K
Phys. Rev. C 86, 054320 (2012)

2013

K. Hadynska-Klek, et al.
Towards the determination of superdeformation in 42Ca
Acta Physica Polonica B No 3 Vol. 44 (2013)

C. Louchart, A. Obertelli, A. Görgen, W. Korten, D. Bazzacco, B. Birkenbach, B. Bruyneel, E. Clement, P. J. Coleman-Smith, L. Corradi, D. Curien, G. de Angelis, G. de France, J.-P. Delaroche, A. Dewald, F. Didierjean, M. Doncel, G. Duchene, J. Eberth, M. N. Erduran, E. Farnea, C. Finck, E. Fioretto, C. Fransen, A. Gadea, M. Girod, A. Gottardo, J. Grebosz, T. Habermann, M. Hackstein, T. Huyuk, J. Jolie, D. Judson, A. Jungclaus, N. Karkour, S. Klupp, R. Krücken, A. Kusoglu, S. M. Lenzi, J. Libert, J. Ljungvall, S. Lunardi, G. Maron, R. Menegazzo, D. Mengoni1, C. Michelagnoli, B. Million, P. Molini, O. Möller, G. Montagnoli, D. Montanari, D. R. Napoli, R. Orlandi, G. Pollarolo, A. Prieto, A. Pullia, B. Quintana, F. Recchia, P. Reiter, D. Rosso, W. Rother, E. Sahin, M.-D. Salsac, F. Scarlassara, M. Schlarb, S. Siem, P. P. Singh, P.-A. Söderström, A. M. Stefanini, O. Stezowski, B. Sulignano1, S. Szilner, Ch. Theisen, C. A. Ur, J. J. Valiente-Dobon, M. Zielinska

Collective nature of low-lying excitations in 70,72,74 Zn from lifetime measurements using the AGATA spectrometer demonstrator

Physical Review C 87, 054302 (2013)

A. Wiens, B. Birkenbach, B. Bruyneel, J. Eberth, H. Hess, Gh. Pascovici, P. Reiter, D. Bazzacco, E. Farnea, C. Michelagnoli, F. Recchia

Improved energy resolution of highly segmented HPGe detectors by noise reduction

Eur. Phys. J. A (2013) 49:47

B. Bruyneel, B. Birkenbach, J. Eberth, H. Hess, Gh. Pascovici, P. Reiter, A. Wiens, D. Bazzacco, E. Farnea, C. Michelagnoli, F. Recchia for the AGATA collaboration

Correction for neutron damage in AGATA detectors using Pulse Shape Analysis

Eur. Phys. J. A (2013) 49: 61

V. Vandone, S. Leoni, G. Benzoni, N. Blasi, A. Bracco, S. Brambilla, C. Boiano, S. Bottoni, F. Camera, A. Corsi, F. C. L. Crespi, A. Giaz, B. Million, R. Nicolini, L. Pellegri, A. Pullia, O. Wieland, D. Bortolato, G. de Angelis, E. Calore, A. Gottardo, G. Maron, D. R. Napoli, D. Rosso, E. Sahin, J. J. Valiente-Dobon, D. Bazzacco, M. Bellato, E. Farnea, S. Lunardi, R. Menegazzo, D. Mengoni, P. Molini, C. Michelagnoli, D. Montanari, F. Recchia, C. A. Ur, A. Gadea, T. Hüyük, N. Cieplicka, A. Maj, M. Kmiecik, A. Atac, S. Akkoyun, A. Kaskas, P.-A. Söderström, B. Birkenbach, B. Cederwall, P. J. Coleman-Smith, D. M. Cullen, P. Desesquelles, J. Eberth, A. Görgen, J. Grebosz, H. Hess, D. Judson, A. Jungclaus, N. Karkour, P. Nolan, A. Obertelli, P. Reiter, M. D. Salsac, O. Stezowski, Ch. Theisen, M. Matsuo, E. Vigezzi

Global properties of K-hindrance probed by the g-decay of the warm rotating 174W nucleus

Phys. Rev. C 88, 034312 (2013)

V. Modamio, J. J. Valiente-Dobon, S. Lunardi, S. M. Lenzi, A. Gadea, D. Mengoni, D. Bazzacco, A. Algora, P. Bednarczyk, G. Benzoni, B. Birkenbach, A. Bracco, B. Bruyneel, A. Bürger, J. Chavas, L. Corradi, F. C. L. Crespi, G. de Angelis, P. Desesquelles, G. de France, R. Depalo, A. Dewald, M. Doncel, M. N. Erduran, E. Farnea, E. Fioretto, C. Fransen, K. Geibel, A. Gottardo, A. Görgen, T. Habermann, M. Hackstein, H. Hess, T. Huyuk, P. R. John, J. Jolie, D. Judson, A. Jungclaus, N. Karkour, R. Kempley, S. Leoni, B. Melon, R. Menegazzo, C. Michelagnoli, C. Mijatovic, B. Million, O. Möller, G. Montagnoli, D. Montanari, A. Nannini, D. R. Napoli, Zs. Podolyak, G. Pollarolo, A. Pullia, B. Quintana, F. Recchia, P. Reiter, D. Rosso, W. Rother, E. Sahin, M. D. Salsac, F. Scarlassara, K. Sieja, P. A. Soderstrom, A. M. Stefanini, O. Stezowski, S. Szilner, Ch. Theisen, B. Travers, C. A. Ur

Lifetime measurements on neutron-rich 63,65Co isotopes with the AGATA Demonstrator

Phys. Rev. C 88, 044326 (2013)

Erklärung

Ich versichere, dass ich die von mir vorgelegte Dissertation selbstständig angefertigt, die benutzten Quellen und Hilfsmittel vollständig angegeben und die Stellen der Arbeit – einschließlich Tabellen, Karten und Abbildungen –, die anderen Werken im Wortlaut oder dem Sinn nach entnommen sind, in jedem Einzelfall als Entlehnung kenntlich gemacht habe; dass diese Dissertation noch keiner anderen Fakultät oder Universität zur Prüfung vorgelegen hat; dass – abgesehen von unten angegebenen Teilpublikationen – noch nicht veröffentlicht worden ist sowie, dass ich eine solche Veröffentlichung vor Abschluss des Promotionsverfahrens nicht vornehmen werde.

Die Bestimmungen der Promotionsordnung sind mir bekannt. Die von mir vorgelegte Dissertation is von Prof. Dr. Peter Reiter betreut worden.

Köln, 4. März 2014

Benedikt Birkenbach

Teilveröffentlichungen

keine

Lebenslauf

Persönliche Details

Name:	Benedikt Birkenbach
[redacted]	[redacted]

Schulausbildung

1986 - 1990	Grundschule Eichenzell
1990 - 1999	Freiherr-vom-Stein Gymnasium Fulda (Abitur)

Zivildienst

1999 - 2000	Institut für Laboratoriumsmedizin der Städtischen Kliniken Fulda

Studium

2000 - 2002	Studium der Informatik an der Fachhochschule Fulda (ohne Abschluss)
2002 - 2009	Studium der Physik an der Universität zu Köln (Diplom)
Ab 2009	Promotion an der Universität zu Köln in experimenteller Physik

Arbeitsverhältnisse

2000 - 2002	Ibis Acam Fulda (Hilfskraft)
2002 - 2007	Regionales Rechenzentrum der Universität zu Köln (SHK)

2007 - 2009	Institut für Kernphysik der Universität zu Köln (SHK)
Ab 2010	Institut für Kernphysik der Universität zu Köln (wiss. Mit.)